Dissertation Thesis

Czech
Technical
University
in Prague

F4

Faculty of Nuclear Sciences and Physical Engineering
Department of Physics

Phenomenological studies of QCD at high energies

Marek Matas

Supervisor: prof. Jesús Guillermo Contreras Nuño, Ph.D.
Supervisor–specialist: Ing. Jan Čepila, Ph.D.
July 2020

Acknowledgements

I would like to thank prof. Jesús Guillermo Contreras Nuño, Ph.D. and Ing. Jan Čepila, Ph.D. for their kind and tireless help with supervising my work and facilitating my growth as a scientist. I could not have wished for better supervisors, thank you for everything.

I would also like to thank Dr. Cyrille Marquet for his offer to work with him on the topics addressed in this work. Thanks to the collaboration with him, I was able to travel to École Polytechnique, learn much about physics and understand how to become a true scientist.

Thanks to Christophe Royon, I was able to develop some of the missing pieces necessary for my work as well as get to the places where my research needed to be heard. Thank you.

I would also like to thank my family for their inexhaustible moral, financial and loving support without which I would have never been able to succeed. I want to give many thanks to my friend Milda, who supported me during the course of my studies and stood tirelessly by my side during the hard times that came with it.

Declaration

Prohlašuji, že jsem tuto práci vypracoval samostatně a použil jsem pouze podklady (literaturu, projekty, SW atd...) uvedené v přiloženém seznamu.

Nemám závažný důvod proti použití tohoto školního díla ve smyslu § 60 Zákona č. 121/2000 Sb. o právu autorském, o právech souvisejících s právem autorským a o změně některých zákonů (autorský zákon).

....

V Praze, Červenec 2020

Abstract

Quantum chromodynamics (QCD) is a field theory that governs our current understanding of the strong interaction which plays a decisive role in the realm of atomic nuclei. This theory comes along with a set of rules and tools that enable us to compute predictions for interactions of strongly charged particles. However, to understand and predict the behavior of an object as complex as a nucleon, we need to simplify the theory using well controlled approximations and supplement it with models of those aspects we do not know how to implement. One example is the dipole model along with the accompanying Balitsky-Kovchegov equation, which enables us to learn from the fundamental properties of QCD about the gluonic structure of protons and neutrons. I have used this formalism to extract information about the shape of the gluon distribution of protons and nuclei, its momentum dependence, transverse profile and distortion due to complex effects inside hadrons. I have used this knowledge to compute predictions for processes, which could possibly prove the existence of the long sought gluonic recombination effects inside hadrons, a phenomenon known as saturation.

Keywords: Quantum chromodynamics, Strong interaction, Balitsky-Kovchegov equation, Saturation

Supervisor: prof. Jesús Guillermo Contreras Nuño, Ph.D.

Supervisor–specialist: Ing. Jan Čepila, Ph.D.

Abstrakt

Kvantová chromodynamika (QCD) je polní teorie, která řídí naše současné chápání silných interakcí, jež hrají zásadní roli v říši atomových jader. Tato teorie nám dává sadu pravidel a nástrojů, které nám umožňují spočítat předpovědi pro jednotlivé interakce silně nabitých částic. Avšak pro porozumění a správné předpovědi chování objektů tak komplexních, jakými jsou například nukleony, je nezbytné sestavit a použít zjednodušující modely. Dipólový model spolu s doprovázející Balitsky-Kovchegovovou evoluční rovnicí nám umožňuje extrahovat z fundamentálních vlastností kvantové chromodynamiky informace o gluonové struktuře protonů. V této práci jsem použil dipólový model pro přepovězení tvaru protonových gluonových distribucí, jejich závislosti na hybnosti, příčném profilu a míře narušení vlivem komplexních jevů odehrávajících se uvnitř atomových jader. Tyto znalosti jsem použil k výpočtům předpovědí pro procesy, které mohou být použity k dokázání existence dlouho hledaných vlivů gluonové rekombinace na vlnovou funkci hadronů.

Klíčová slova: Kvantová chromodynamika, silná interakce, Balitsky-Kovchegovova rovnice, saturace

Překlad názvu: Fenomenologické studie kvantové chromodynamiky za vysokých energií

Contents

Chapter 1

Introduction

Quantum chromodynamics (QCD) is a quantum field theory describing the mechanisms of the strong interaction inside nucleons and nuclei. Its principles and properties have been intensively studied both theoretically and experimentally over the course of the past decades by a joint collaboration of the entire world.

In this theory nucleons, such as protons and neutrons, are constituted from fermion fields called quarks and of boson fields—that bind them together—called gluons. When working in the framework of quantum field theory (such as quantum electrodynamics), one usually takes advantage of perturbative expansions in the powers of the coupling constant associated with the strength of the interactions. This usual approach is more difficult for the purposes of QCD since the coupling (termed strong) reaches values ~ 1 and prevents us from omitting terms with higher powers of this constant. However, it has been shown, that the value of this coupling changes with energy and for highly energetic interactions, its value decreases low enough that the predictive powers of the series expansions are re-established [1, 2].

Going from the correct description of a single gluon-gluon interaction to a complete understanding of an object as complex as the proton is a colossal task. The proton consists not only of the three constituent quarks coined "valence", but also of an infinite pool of gluons and of a sea of quark-antiquark pairs, that interact with one another, exchange energy, spin, color and other quantum numbers making up this dynamical cluster of particles, that we call nucleon.

For the purpose of learning more about the full nucleon from simple rules for interactions, so-called evolution equations have been established [3–14]. These take a simple object and during the course of evolution apply the well-known single interactions over and over so that the sought complexity of the object arises.

One of the evolution equations, that has been established and used for the purpose of the description of the gluon populations inside nucleons is called the Balitsky-Kovchegov (BK) equation [15–19]. This evolution equation evolves the partonic population of the target in energy unlike the famous DGLAP equation [11, 12, 20, 21] that evolves in the scale of the process.

This work focuses on the use of the BK equation, that can be used to calculate, within perturbative QCD, the evolution of a color dipole [22–24] (quark-antiquark pair with total color zero) by adding a small amount of energy into the system. This dipole is considered as a probe in deep-inelastic scattering (DIS) events in virtual photon-proton collisions and with it, the QCD structure of the target can be obtained in the following way.

The BK equation "dresses" the initially bare dipole with a cloud of additional partons. Lorentz invariance of the cross section can be used to boost the entire system into a frame, where the dipole is at rest and thus stays bare. The energy evolution then has to go into the wavefunction of the proton (that the dipole is colliding with), which has acquired energy by the boost. This then gives birth to additional partons inside the proton.

This way, one can relate the scattering amplitude, that corresponds to the parton distribution of the dipole to the parton distribution of the target proton. This effect can be used to calculate distribution functions, that can be used to compute various processes within the factorized approach to the final cross section.

The BK equation is a differential equation that cannot be solved analytically so one has to use numerical methods to obtain a solution. At first, I have optimized its computation and used it to calculate structure functions of the proton with the commonly used initial conditions originating from the McLerran-Venugopalan (MV) [25] and Golec-Biernat Wüsthoff (GBW) [26] models.

Then I have used the BK equation and its solutions to calculate the Transverse Momentum Distributions (TMDs) [27] of proton and nuclei, with which I have computed the prediction for the di-jet events in the forward region in rapidity, that can serve as an ideal probe for the saturation effects inside nucleons [27]. These intensively sought effects are incorporated in the BK equation which, unlike the BFKL equation [13, 14, 28–30], incorporates non-linear terms that are responsible for gluon recombination.

I have found that the collinear resummation within the BK framework [31, 32] suppresses the parts of the phase space of the kernel of this equation where non-perturbative effects play an important role [33, 34]. This in turn enables us to solve this equation in the full impact-parameter dependent computation without the rise of non-perturbative tails in its amplitude (called Coulomb tails) and thus learn about the profile structure and evolution of the target.

I have generalized this approach to describe nuclear targets in order to gain more understanding of nuclear effects, such as shadowing, because of the planned facilities designed to perform such studies in the near future [35].

This work is organized as follows. In Chapter 2, I will introduce deep-inelastic scattering (DIS), which is an invaluable probe of the inner structure of the nucleons and nuclei. Then I will address, how the dipole model can be used to describe these processes on theoretical level. The overview of the BK equation as well as some of the key aspects of this formalism will be reviewed in Chapter 3. Saturation effects embedded in this equation as well as some of the possible ways to search for these effects will be outlined in Chapter 4 followed by a summary and finally, I include a reproduction of the articles produced during my Ph.D. work and submitted to high-impact journals as well as a list of the proceedings of international talks I gave on these subjects.

Chapter 2

Deep-inelastic scattering

2.1 Kinematics of DIS

Deep-inelastic scattering (DIS) is a key process for studying the internal structure of hadrons and therefore of the matter around us. This process (shown in Fig. 2.1) involves the interaction of a lepton with a target hadron. The passing lepton emits a gauge boson, which for the case of charged incoming leptons and small virtualities is normally a photon, and this then interacts with the target probing its internal structure and breaks it apart. Since the electromagnetic interaction is explicitly given by the rules of quantum electrodynamics (QED), electrons serve as an excellent probe of the structure of nuclei and nucleons.

In experiments at SLAC in 1968, deep inelastic scattering was the process that enabled the discovery of the constituent point-like particles inside nucleons (termed quarks) [36, 37] leading to the development of a quantum field theory of the strong interaction—quantum chromodynamics. These experiments have then been continued with great success in order to gain more information about QCD dynamics and the rules that govern strongly interacting particles e.g. at HERA [38, 39], SLAC [40] and CERN [41].

If we write this process symbolically as

$$e(l) + p(P) \to e^{'}(l^{'}) + X(P_x), \tag{2.1}$$

denoting the incoming electron as e, the incoming proton as p, the outgoing electron as $e^{'}$ and the outgoing fragmented hadron as X with their corresponding four-momenta in the parentheses next to them, we can define variables that are used to describe the kinematics of such processes as follows.

One of the most important variables for this process, the virtuality of the photon, defines the scale at which the target is being probed and is defined as

$$Q^2 = -q^2 = -(l - l^{'})^2. \tag{2.2}$$

This definition is chosen as such due to the fact, that in DIS, the interacting photon is considered to be an off-shell and space-like particle. Therefore, to obtain a positive and frame independent variable representing the scale of the process, one has to choose the negative square of its four-momenta.

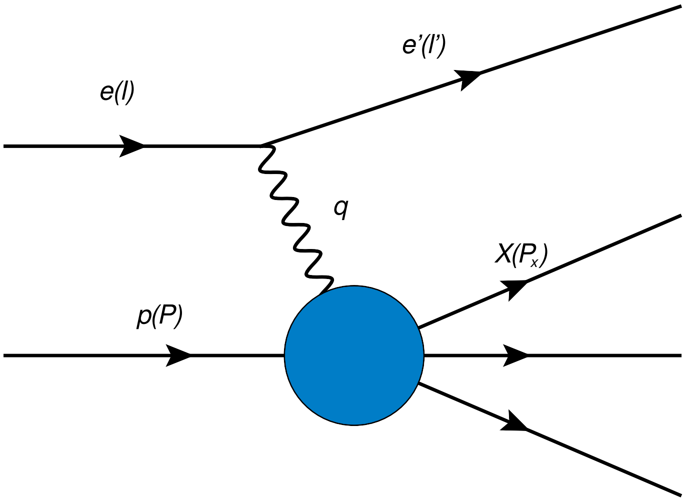

Figure 2.1: Schematic picture of deep inelastic electron-proton scattering.

Another important variable is the Bjorken x, which in the infinite momentum frame corresponds to the fraction of the momentum carried by the struck parton with respect to the total momentum of the proton and is defined as

$$x = \frac{Q^2}{2P \cdot q} = \frac{Q^2}{Q^2 + W^2 - m_N^2}, \tag{2.3}$$

where m_N is the mass of the nucleon (in this case a proton). A convenient variable used for one of the definitions of x is W^2, the total energy that is transferred to the hadron in the CMS frame, which is given by

$$W^2 = (P + q)^2. \tag{2.4}$$

The inelasticity of the collision y is defined as

$$y = \frac{q \cdot P}{l \cdot P}, \tag{2.5}$$

and represents the fraction of energy lost by the incoming electron because of the collision. The last kinematic variable that will be addressed here, denoted as s, is given by expression

$$s = (l + P)^2 \tag{2.6}$$

and gives us the squared center-of-mass energy of the lepton-hadron collision.

2.2 Cross sections in DIS

The kinematic variables introduced above are used in DIS to describe the totally inclusive cross section for the process schematically shown in Fig. 2.1 as

$$\frac{d^2\sigma_\pm}{dxdQ^2} = \frac{4\pi\alpha_{em}^2}{xQ^4} \left[\left(1 - y + \frac{y^2}{2}\right) F_2(x,Q^2) - \frac{y^2}{2} F_L(x,Q^2) \mp \left(y - \frac{y^2}{2}\right) F_3(x,Q^2)\right], \tag{2.7}$$

where α_{em} is the QED coupling and is usually set to $1/137$. This cross section is expressed in terms of the so-called structure functions $F_2(x,Q^2)$, $F_L(x,Q^2)$ and $F_3(x,Q^2)$. The structure function $F_3(x,Q^2)$ takes into account parity-violating effects depending on the chosen projectile particle (an electron or a positron) and is negligible for values of Q^2 smaller than the scale of the mass of the Z^0 boson.

The longitudinal structure function can be expressed in terms of the standard structure functions $F_1(x,Q^2)$ and $F_2(x,Q^2)$ as

$$F_L(x,Q^2) = F_2(x,Q^2)\left(1 + \frac{4M_N^2 x^2}{Q^2}\right) - 2xF_1(x,Q^2), \tag{2.8}$$

where M_N is the mass of the target nucleon. Therefore (after omitting the parity-violating term $F_3(x,Q^2)$) Eq. (2.7) becomes

$$\frac{d^2\sigma}{dxdQ^2} = \frac{4\pi\alpha_{em}^2}{Q^4}\left[\left(1 - y - \frac{M_N^2 y^2}{Q^2}\frac{F_2(x,Q^2)}{x} + y^2 F_1(x,Q^2)\right)\right]. \tag{2.9}$$

The proof, that the proton, in fact, contains point-like constituent particles (called partons [42]) came from satisfying of the so-called Bjorken scaling, which implies that the structure functions should depend only on one variable, Bjorken-x [43], which can be expressed as

$$F_2(x,Q^2) \to F_2(x), \qquad F_1(x,Q^2) \to F_1(x). \tag{2.10}$$

This behavior was later observed in data, proving that the proton is made of constituent point-like particles (see Fig. 2.2)

The evidence, that the constituting partons are, in fact, spin-$1/2$ particles comes from satisfying the Callan-Gross relation [45], that reads

$$2xF_1(x) = F_2(x). \tag{2.11}$$

This relation has then been verified experimentally, determining the spin of the partons probed by the DIS process (see Fig. 2.3).

2.3 The parton model

If we boost to a frame, where the proton carries infinite momentum in one direction, all of the transverse components of the momentum of its constituents as well as their masses will be negligible. In this frame, and during the short

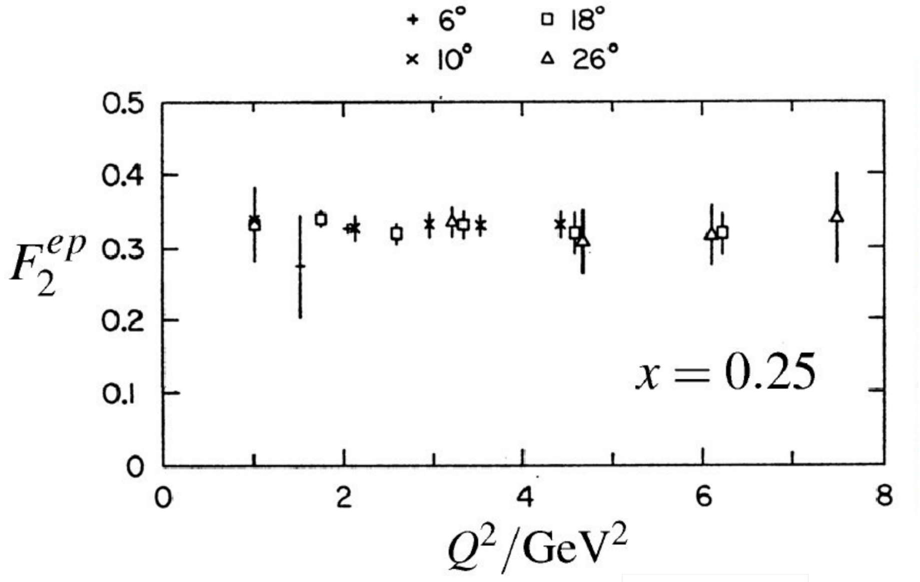

Figure 2.2: Manifestation of the Bjorken scaling in the data (figure taken from [44]).

time that the interaction lasts, you can treat the partons as quasi-free particles that the virtual photon scatters off (see Fig. 2.4).

In this framework, the structure function of the proton can be written in terms of the so-called parton distribution functions (PDFs) as

$$F_2(x, Q^2) = x \sum_f e_{q_f}^2 \left[q_f(x, Q^2) + \bar{q_f}(x, Q^2) \right], \tag{2.12}$$

where f denotes the chosen flavor, e_{q_f} is the charge of the considered quark, $q_f(x, Q^2)$ is the quark PDF and $\bar{q_f}(x, Q^2)$ is the anti-quark PDF. These PDFs have a stochastic interpretation and they give us the information about the probability of a parton existing inside of a proton within a specific energy interval. Furthermore, since quarks emit gluons and those can fluctuate into more quarks, a picture of the proton consisting only of three static quarks is too simplistic. The population of quarks that originates from these gluonic fluctuations is called the "sea" distribution and the total quark densities for u and d quarks are then given as

$$u(x) = u_v(x) + u_s(x), \qquad d(x) = d_v(x) + d_s(x). \tag{2.13}$$

Here subscript v denotes the valence-quark distribution and subscript s denotes the sea-quark distribution.

The fact, that there are two valence u-quarks and one valence d-quark in the proton translates into these distributions as a condition

$$\int_0^1 u_v(x) = 2, \qquad \int_0^1 d_v(x) = 1. \tag{2.14}$$

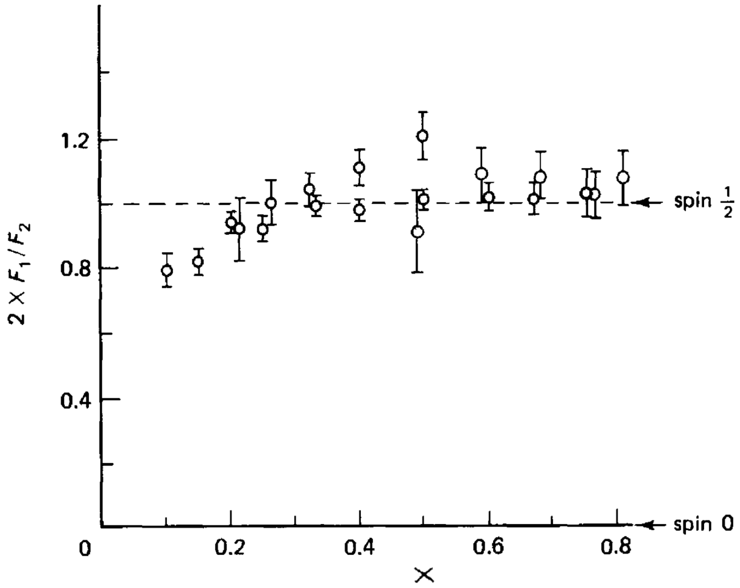

Figure 2.3: Manifestation of the Callan-Gross relation in the data (figure taken from [46]).

Since there are no valence anti-quarks in the proton, we can relate the quark sea distributions to the anti-quark distributions as

$$\bar{u}_s(x) = \bar{u}(x) = u_s(x), \qquad \bar{d}_s(x) = \bar{d}(x) = d_s(x). \tag{2.15}$$

From the form of the relation for the structure function (2.12) and the assumption, that all sea-quark distributions for the light quarks (u, d and s) are equal

$$S(x) \equiv \bar{u}_s(x) = \bar{d}_s(x) = \bar{s}_s(x) = u_s(x) = u_s(x) = u_s(x) \tag{2.16}$$

we can construct the structure functions for the proton and neutron as

$$F_2^{ep}(x) = x\left[\frac{4}{9}u_v(x) + \frac{1}{9}d_v(x) + \frac{4}{3}S(x)\right] \tag{2.17}$$

and

$$F_2^{en}(x) = x\left[\frac{4}{9}d_v(x) + \frac{1}{9}u_v(x) + \frac{4}{3}S(x)\right]. \tag{2.18}$$

These expressions follow that due to the isospin symmetry, $u_v^p(x) = d_v^n(x)$ and $d_v^p(x) = u_v^n(x)$. Then we also decide to keep the convention of $u(x) \equiv u^p(x)$, $d(x) \equiv d^p(x)$. The superscripts p and n denote the proton and neutron, respectively.

Therefore one can construct the ratio of the two structure functions and probe it at various values of x. Since the sea-quarks come from gluonic emissions, which are more probable at regions where gluons are abundant—the low-x region—the sea-quarks dominate the distributions and for low values of x

$$\frac{F_2^{ep}(x)}{F_2^{en}(x)} \to 1. \tag{2.19}$$

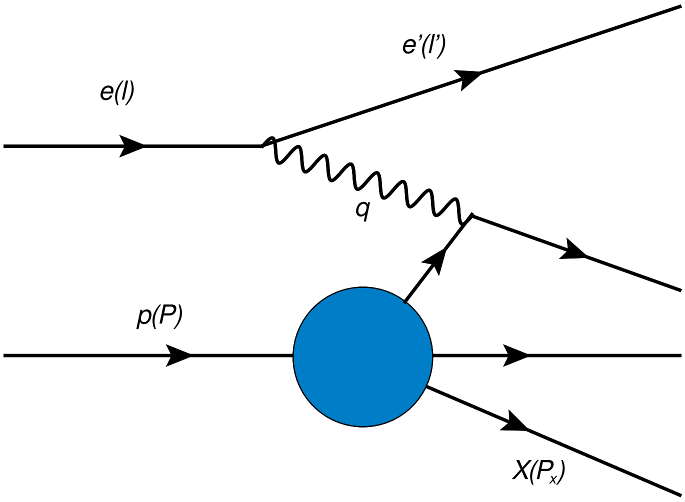

Figure 2.4: Schematic picture of the lepton-proton scattering where the virtual photon scatters of a point-like quasi-free parton.

At other regions where sea-distributions are negligible, you can determine the ratio of the valence u and d distributions by measuring the ratio of these structure functions.

If we measure the total momentum carried by the quark distributions as

$$T_q = \int_0^1 xu(x) + xd(x), \tag{2.20}$$

we find out, that these quarks carry just about 50% of the total momentum of the proton. The rest is carried by electromagnetically neutral particles called gluons. A useful framework for determining the gluonic structure of protons and nuclei is the dipole model.

2.4 The dipole model

The dipole model addresses the interaction of a virtual photon with the target hadron. In DIS, we are studying the effects of strong interaction, although, the interacting photon emitted by the projectile lepton (see Fig.2.1) does not carry color charge. In order for the photon to interact strongly, it needs to fluctuate into one of its composing Fock-states. The minimal partonic Fock state, that the photon can fluctuate into and that could interact strongly with the target is a quark-antiquark pair forming a color dipole.

In the dipole picture to DIS [22–24], the incoming virtual photon firstly fluctuates into a color dipole, which then exchanges a colorless object with the target proton (see Fig. 2.5). This colorless object is in the first approximation represented by a pair of gluons, even though in reality, its structure is far more complicated.

The dipole interacting with the target proton is characterized by several variables defining its properties. These are the transverse size $\vec{r}$, impact

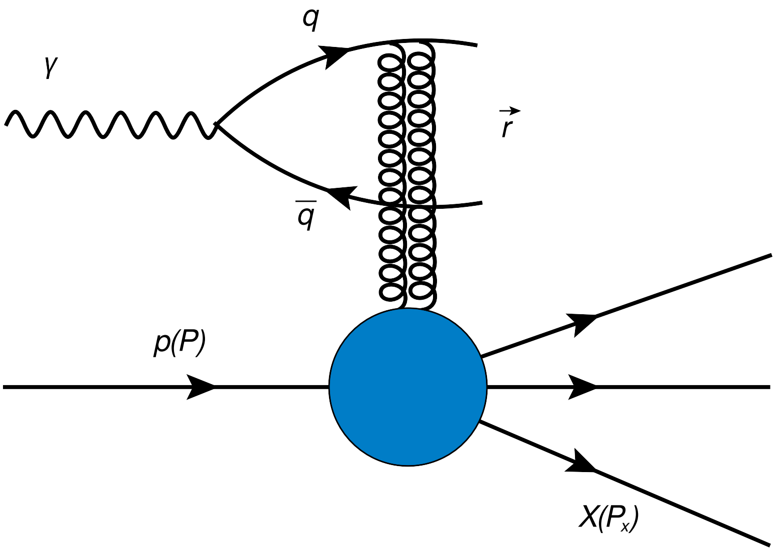

Figure 2.5: DIS in the color dipole model. The virtual photon first fluctuates into a color dipole and this then scatters off a target breaking it apart.

parameter of the interaction $\vec{b}$ (as shown in Fig. 2.6) and energy, in our case represented via its rapidity Y since

$$Y \sim \ln\left(\frac{1}{x}\right) \tag{2.21}$$

and

$$x \sim \frac{1}{\sqrt{s}}. \tag{2.22}$$

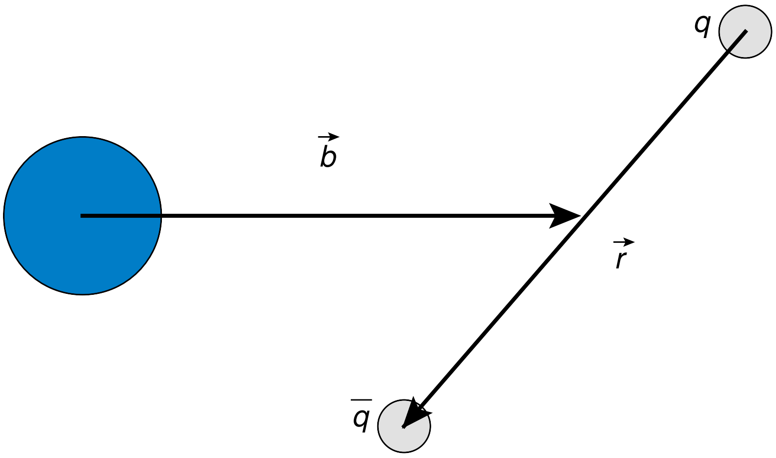

Figure 2.6: Schematic view of the variables describing a color dipole in the transverse plane.

Due to the fact that the dipole lives much longer than the typical interaction time, we can factorize the total cross section of the DIS process into two separate terms.

1. Formation of the color dipole.
2. Interaction of the dipole with the target hadron.

The first of the factorized terms then are the wave functions, that represent the probability of a virtual photon splitting into a quark-antiquark dipole. They read [26]

$$\mid \Psi_T^f(z,\vec{r},Q^2) \mid^2 = \frac{3\alpha_{em}}{2\pi^2} e_{q_f}^2 ((z^2+(1-z)^2)\epsilon^2 K_1^2(\epsilon r) + m_{q_f}^2 K_0^2(\epsilon r)) \tag{2.23}$$

and

$$\mid \Psi_L^f(z,\vec{r},Q^2) \mid^2 = \frac{3\alpha_{em}}{2\pi^2} e_{q_f}^2 (4Q^2 z^2 (1-z)^2 K_0^2(\epsilon r)), \tag{2.24}$$

for the transverse and longitudinal polarization of the virtual photon respectively.

Here z is the fraction of the total momentum carried by the quark, K_0 and K_1 are the MacDonald functions, Q^2 is the virtuality of the probing photon, e_{qf} is the fractional charge (in units of elementary charge) of a quark carrying flavor f, $\alpha_{em} = 1/137$ and

$$\epsilon^2 = z(1-z)Q^2 + m_{q_f}^2, \tag{2.25}$$

where m_{q_f} is the mass of the considered quark. We denote the sum of the two polarized wave functions as

$$\mid \Psi_{T,L}^f(z,\vec{r}) \mid^2 = \mid \Psi_T^f(z,\vec{r}) \mid^2 + \mid \Psi_L^f(z,\vec{r}) \mid^2 . \tag{2.26}$$

The second factorized term is the cross section of the dipole-hadron interaction denoted as $\mathrm{d}\sigma^{q\bar{q}}(\vec{r},\tilde{x})/\mathrm{d}\vec{b}$. This variable contains all the information about the QCD processes of the interaction and contains both the perturbative and non-perturbative contributions to the collision and can be computed with various models and approximations. We will discuss it in detail in the following section at a fixed energy and address its evolution in energy in the next chapters.

The structure function of the proton is then proportional to the integral of the photon-dipole wavefunction and the cross section of the quark-antiquark dipole scattering of the proton target over all transverse dipole sizes $\vec{r}$, all possible values of impact parameter $\vec{b}$ and over all possible values of the fractional momentum of photon z (which goes from 0 to 1) as

$$F_2(x,Q^2) = \frac{Q^2}{4\pi^2\alpha_{em}} \int \sum_f d\vec{r} d\vec{b} dz \mid \Psi_{T,L}^f(z,\vec{r}) \mid^2 \frac{\mathrm{d}\sigma^{q\bar{q}}(\vec{r},\tilde{x})}{\mathrm{d}\vec{b}}. \tag{2.27}$$

Furthermore, it is usual to shift the value of the x at which the structure function and reduced cross section is computed according to the photoproduction kinematic shift [26]

$$\tilde{x} = x\left(1 + \frac{4m_{q_f}^2}{Q^2}\right), \tag{2.28}$$

where m_{q_f} is the mass of the considered quark and Q^2 is the virtuality.

The reduced cross section, that can also be measured, is obtained from the relation [47]

$$\sigma_{red}(x,y,Q^2) = F_2(x,Q^2) - \frac{y^2}{1+(1-y)^2} F_L(x,Q^2), \tag{2.29}$$

where the inelasticity y is obtained from $y = Q^2/sx$ and $\sqrt{s}$ is the center-of-mass (CMS) collision energy as discussed in previous sections and

$$F_L(x,Q^2) = \frac{Q^2}{4\pi^2\alpha_{em}} \int \sum_f d\vec{r} d\vec{b} dz \mid \Psi_L^f(z,\vec{r}) \mid^2 \frac{\mathrm{d}\sigma^{q\bar{q}}(\vec{r},\tilde{x})}{\mathrm{d}\vec{b}}, \tag{2.30}$$

where similarly as above, z goes from 0 to 1. One can also compute the reduced cross section only for a single-quark contribution (c-quark $\sigma_{red}^{charm}(x,y,Q^2)$ for instance) by including only the desired flavor instead of the sum over i in the computation of the structure function $F_2(x,Q^2)$ and longitudinal structure function $F_L(x,Q^2)$. Since the structure function $F_1(x,Q^2)$ is given by

$$2xF_1(x,Q^2) = \frac{Q^2}{4\pi^2\alpha_{em}} \int \sum_f d\vec{r} d\vec{b} dz \mid \Psi_T^f(z,\vec{r}) \mid^2 \frac{\mathrm{d}\sigma^{q\bar{q}}(\vec{r},\tilde{x})}{\mathrm{d}\vec{b}}, \tag{2.31}$$

we can relate these three structure functions as

$$F_2(x,Q^2) - 2xF_1(x,Q^2) = F_L(x,Q^2). \tag{2.32}$$

Another important process in the color dipole framework is the diffractive production of vector mesons as a function of the four-momentum t transferred at the hadron vertex. This process, where the virtual photon interacts with a target proton diffractively, produces a vector meson but leaves the target intact. It is especially important since the transferred four-momentum is a Fourier-related variable to the impact parameter b and therefore by measuring this cross section, we are, in fact, probing the impact-parameter profile of the target. This cross section can be written as

$$\left.\frac{\mathrm{d}\sigma^{\gamma^* p\to \mathrm{V}p}}{\mathrm{d}|t|}\right|_{T,L} = \frac{(1+\beta^2)\left(R_g^{T,L}\right)^2}{16\pi} |\mathcal{A}_{T,L}|^2, \tag{2.33}$$

where $\mathcal{A}_{T,L}$ is the amplitude of the process, $(1+\beta^2)$ is a correction for the fact that in the derivation of this amplitude we considered only its imaginary part (for more details see [48]). $R_g^{T,L}$ is called the skewedness correction and corrects for the fact that we did not use an off-diagonal gluon distribution for the vector meson production (see [49]).

The amplitude of this process is given by

$$\mathcal{A}_{T,L}(x,Q^2,\vec{\Delta}) = \tag{2.34}$$
$$i\int \mathrm{d}\vec{r} \int_0^1 \frac{\mathrm{d}z}{4\pi} \int \mathrm{d}\vec{b} |\Psi_{\mathrm{V}}^* \Psi_{\gamma^*}|_{T,L} \exp\left[-i\left(\vec{b}-(1-z)\vec{r}\right)\vec{\Delta}\right] \frac{\mathrm{d}\sigma^{q\bar{q}}}{\mathrm{d}\vec{b}},$$

where Ψ_{γ^*} is a photon wave function that reflects the probability of it splitting into a color dipole and Ψ_{V} is the wave function of the outgoing vector meson. Subscript T, L denotes a sum over their longitudinal and transverse polarizations. The square of the transferred four-momentum is here denoted as $\vec{\Delta}^2 \equiv -t$. The x for this process is then computed as

$$x = \frac{Q^2 + M^2}{W_{\gamma\mathrm{p}}^2 + Q^2}, \tag{2.35}$$

where M is the mass of the considered vector meson and $W_{\gamma\mathrm{p}}$ is the center-of-mass energy between the photon and proton. The convolution of the wave functions takes the form

$$\begin{split} |\Psi_{\mathrm{V}}^* \Psi_{\gamma^*}|_T = \\ \hat{e}_f e \frac{N_c}{\pi z(1-z)} \left[m_f^2 K_0(\epsilon r) \phi_T(r,z) - \left(z^2 + (1-z)^2 \right) \epsilon K_1(\epsilon r) \partial_r \phi_T(r,z) \right], \end{split} \tag{2.36}$$

and

$$|\Psi_{\mathrm{V}}^* \Psi_{\gamma^*}|_L = \hat{e}_f e \frac{N_c}{\pi} 2Qz(1-z) K_0(\epsilon r) \left[M \phi_L(r,z) + \delta \frac{m_f^2 - \nabla_r^2}{Mz(1-z)} \phi_L(r,z) \right]. \tag{2.37}$$

Here δ was fixed to one and for the scalar part of the vector meson wave function $\phi_{T,L}(r,z)$, we used the boosted Gaussian model as in [50–52]. The variable $\hat{e}_f$ is the effective quark charge and other variables are defined similarly as for Eq. (2.26).

2.5 The dipole-proton cross section

When addressing the dipole-proton cross section, that we need to compute for the DIS-related processes, we can take use of the optical theorem that identifies it with the dipole scattering amplitude by

$$\frac{\mathrm{d}\sigma^{q\bar{q}}(\vec{r}, x)}{\mathrm{d}\vec{b}} = 2N(\vec{r}, \vec{b}, x). \tag{2.38}$$

This relation is especially useful to us, since N can be obtained from various models (such as MV or GBW) or closer to pQCD obtained as a solution of the Balitsky-Kovchegov evolution equation as will be discussed in the following chapters.

For a moment, let us omit the dependence of the dipole-proton cross section (or equivalently of the scattering amplitude) on the impact parameter $\vec{b}$ and focus solely on its behavior with respect to the transverse dipole size $\vec{r}$ and energy represented by x. This omitted dependence will be reintroduced in various ways in the following chapters and is not necessary for the initial consideration of such cross sections.

This simplification can then be rewritten as

$$N(\vec{r}, \vec{b}, x) \to N(\vec{r}, x). \tag{2.39}$$

There are many models, that predict the behavior of this form of the scattering amplitude at a fixed energy and we can then take it and use it as a starting point for the energy evolution of the Balitsky-Kovchegov equation.

We will choose a commonly used model called McLerran-Venugopalan (MV) [25] to illustrate how one can arrive to an expression for such cross section. This model simplifies the picture of the proton as consisting of a few highly-energetic partons, that generate a soft gluonic field that is then treated as classical for the purposes of this computation and is derived within the Color Glass Condensate model (CGC). For a review and more information on CGC see [53–55].

If we try to express how a single quark, passing through such medium would be affected, assuming a Gaussian distribution of the color sources and zero-momentum exchange during the collision, we arrive to an object that describes the color rotation occurring during this interaction, is called the Wilson line, and can be expressed as

$$V(x_T) = P \exp\left[ig \int dx^+ A^{c-}(x^+, x_T) t^c\right]. \tag{2.40}$$

Here P denotes path ordering in the integral, $A^{c-}(x^+, x_T)$ is the color field that approximates our target, t^c is the Gell-Mann color matrix and g is the interaction coupling. We have used the light-cone notation to describe the four-vectors that enter these expressions, which for a four-vector $x = (x^0, x^1, x^2, x^3)$ is defined as

$$x^\pm = \frac{1}{\sqrt{2}}(x^0 \pm x^3), \qquad\qquad x_T = (x^1, x^2). \tag{2.41}$$

If we then take two Wilson lines to model the effects of such collision on a quark-antiquark pair, we are able to construct a scattering matrix for a color dipole interacting with a target depending on its transverse size r at a fixed energy given by $x = x_0$ as

$$S = \frac{1}{N_c} \mathrm{Tr} V(x_T) V_T^\dagger(y_T), \tag{2.42}$$

where N_c is the number of colors, $V(x_T)$ stands for the quark-contribution to the scattering, the conjugated $V_T^\dagger(y_T)$ for the antiquark-contribution and the transverse size of the dipole is given by $r = |x_T - y_T|$. The corresponding scattering amplitude is then constructed as

$$N^{MV} = 1 - \frac{1}{N_c} \mathrm{Tr} V(x_T) V_T^\dagger(y_T). \tag{2.43}$$

After the evaluation of the trace over colors one arrives to an expression

$$N^{MV}(r, x = x_0) = 1 - \exp\left(-\frac{(r^2 Q_0^2)^\gamma}{4} \ln\left(\frac{1}{r\Lambda} + e\right)\right), \tag{2.44}$$

where the constants that emerge in this computation are the saturation scale Q_0^2, the anomalous dimension γ, the Landau pole Λ and Euler's number e. Values for some of them can vary depending on which fit one chooses to follow or for the description of which processes they are used and they will be addressed in greater detail in the following chapters.

There is of course a wide variety of models that can be used for predicting the scattering amplitude at a fixed energy and then used for the BK evolution. We will address each one before making the use of it in the following chapters, but the methodology sketched out above for the case of the MV model can be used as a possible way when thinking about the construction of such cross sections in the color-dipole formalism.

Chapter 3

The Balitsky-Kovchegov evolution equation

3.1 The dipole picture of the BK equation

In the previous chapter, we have sketched how one can arrive to an expression for the cross section of a bare color-dipole interacting with a target. This cross section has been shown to be important for the DIS processes in the color-dipole formalism. However, the interacting dipole does not necessarily have to be bare (that is constituting solely of a quark-antiquark pair). When increasing the energy of the interaction, it emits additional gluons making the interaction far more complex than what we previously described. That is why in order to take into account these gluonic emissions, one can make the use of the so-called evolution equations.

The Balitsky-Kovchegov evolution equation (BK) is one of the equations describing the evolution of the scattering amplitude N towards higher energies by subsequent emissions of gluons from one of the quarks forming the color dipole. It was derived from the JIMWLK evolution equations in the limit of large number of colors N_c [19, 24, 56–60] and, unlike the BFKL equation, accounts for the nonlinear effects of gluon recombination (see Eq. (3.7)) [61,62].

Following Mueller's derivation [24] of the BK equation, in order to compute the energy evolution of the scattering amplitude, one has to first boost into a frame, where the dipole has minimal energy. Then its wave function consists solely of the quark-antiquark pair Fig. 3.1 (left). If we want to add a bit of energy to the system, we boost a bit further away from this frame which manifests itself as an emission of a gluon from one of the quarks forming the color dipole Fig. 3.1 (right). This gluon can be (in the limit of the infinite number of colors) represented as a quark-antiquark pair, which then forms two independent so-called "daughter" dipoles within the original "mother" dipole Fig. 3.2 (left).

This way, we can add energy bit by bit into the system until we dress the original bare dipole with a cloud of additional dipoles, that get emitted as we add energy by boosting into a frame, where the dipole is not at rest Fig. 3.2 (right).

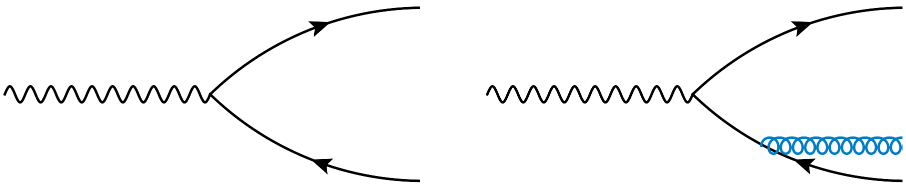

Figure 3.1: Diagram for the bare color dipole consisting solely of quark-antiquark pair (left) and the color dipole after a bit of energy is added to the system and one of the quarks emits a gluon (right).

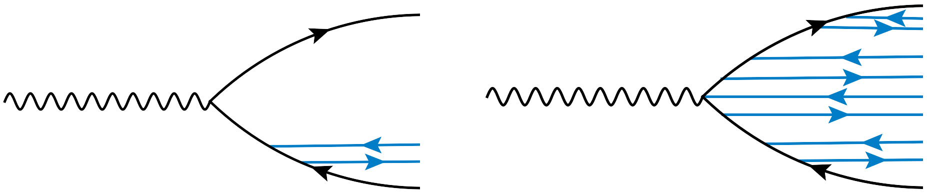

Figure 3.2: Diagram for the color dipole after the emitted gluon splits into a quark-antiquark pair in the limit of high number of colors and two daughter dipoles are formed (left). Diagram for the color dipole after it is dressed with a cloud of additional dipoles (right).

Mathematically, the BK equation reads [61, 63]

$$\begin{aligned}\frac{\partial N(\vec{r},\vec{b},Y)}{\partial Y} &= \int d\vec{r_1} K(r,r_1,r_2)\Big(N(\vec{r_1},\vec{b_1},Y)+N(\vec{r_2},\vec{b_2},Y)-N(\vec{r},\vec{b},Y)\\ &\quad -N(\vec{r_1},\vec{b_1},Y)N(\vec{r_2},\vec{b_2},Y)\Big), \qquad (3.1)\end{aligned}$$

where $K(r,r_1,r_2)$ is the kernel of the equation, reflects the probability of a quark emitting a gluon, and is derived with the use of perturbative QCD. $N(\vec{r_i},\vec{b_i},Y)$ denotes the scattering amplitude with $\vec{r}$, $\vec{r_1}$ and $\vec{r_2}$ being the transverse sizes of the mother and daughter dipoles respectively, where $\vec{r}=\vec{r_1}+\vec{r_2}$ holds. Impact parameters of the considered dipoles are denoted with $\vec{b_i}$. We follow the notation of $|\vec{r}|=r$ and similarly for impact-parameter vectors. The BK equation can be equivalently formulated in momentum space [62] although, throughout this work, we will stick to the outlined formulation in position space.

Since the total cross section is a variable invariant under a Lorenz boost, we can relate the two cases (bare dipole at rest and dressed boosted dipole) by assuming, that the compensating variable, that fixes the Lorenz invariance of the cross section, is the gluon distribution of the proton that the dipole interacts with. This then allows us to relate the dipole gluon distribution with the gluon distribution of the target proton and make the use of the BK equation when describing the structure of nucleons.

3.2 Simplifying the solution of the BK equation

The BK evolution equation is usually solved in the b-independent scheme [47], for which we have also sketched the derivation of the MV initial condition in the previous chapter.

In this scheme, we assume the impact parameter dependence of the scattering amplitude to factorize from the transverse size and rapidity dependence as

$$N(\vec{r}, \vec{b}, Y) \cong T(\vec{b}) N(\vec{r}, Y), \tag{3.2}$$

where we have moved from using x as the variable describing the energy of the collision to rapidity Y, which is connected to it by the relation

$$Y = \ln\left(\frac{x_0}{x}\right). \tag{3.3}$$

The parameter x_0 is a free parameter that defines the value of x, where we decide to start our evolution.

The integral over the impact parameter of the scattering amplitude can be parametrized under this factorization with a variable σ_0, which remains constant throughout the evolution and can be fitted to data. The formula for the computation of the dipole cross section integrated over the impact-parameter plane then reduces to

$$\sigma^{q\bar{q}}(\vec{r}, Y) = 2 \int d\vec{b} N(\vec{r}, \vec{b}, Y) = \sigma_0 N(\vec{r}, Y). \tag{3.4}$$

It is also convenient to assume that the size of the target proton is very big and completely homogeneous. If we assume a proton with infinite size, no matter, how large impact parameter or transverse size we choose, the dipole will always interact with the target. This strong approximation simplifies the situation a lot, because then we are able to neglect the dependence of the scattering amplitude on the impact parameter not only in its integration to get the inclusive cross section, but also in the BK evolution itself. In other words, under the assumption of an infinite proton size and factorizable b-dependence, the scattering amplitude reduces to

$$N(\vec{r}, \vec{b}, Y) \cong N(\vec{r}, Y). \tag{3.5}$$

In this approach, we neglect the angular asymmetries of the infinitely large target and the scattering amplitude can be further simplified as

$$N(\vec{r}, Y) \cong N(r, Y). \tag{3.6}$$

Under these assumptions, we may rewrite the BK evolution equation as

$$\begin{aligned} \frac{\partial N(r, Y)}{\partial Y} = \int d\vec{r_1} K(r, r_1, r_2)(N(r_1, Y) + N(r_2, Y) - N(r, Y) \\ - N(r_1, Y) N(r_2, Y)). \end{aligned} \tag{3.7}$$

There is a wide pallet of kernels $K(r, r_1, r_2)$ that one can choose for the BK evolution. Because this term reflects the perturbative calculation that accounts for the emission of a gluon from one of the quarks, it can be carried out under various approximations, orders and schemes. One of the usual choices for such calculation is the running coupling kernel $K^{run}(r, r_1, r_2)$ that can be expressed as [61, 63, 64]

$$K^{run}(r, r_1, r_2) = \frac{N_c \alpha_s(r^2)}{2\pi^2} \left(\frac{r^2}{r_1^2 r_2^2} + \frac{1}{r_1^2} \left(\frac{\alpha_s(r_1^2)}{\alpha_s(r_2^2)} - 1 \right) + \frac{1}{r_2^2} \left(\frac{\alpha_s(r_2^2)}{\alpha_s(r_1^2)} - 1 \right) \right). \tag{3.8}$$

Here N_c is the number of colors, α_s denotes the strong coupling that will be discussed in more detail later on, and r, r_1 and r_2 are the dipole transverse sizes. A clear picture of the geometric orientation of the mother-daughter dipoles and their relation in the evolution can be seen in Fig. 3.3 in the transverse plane. This kernel incorporates some of the NLO effects into the evolution and differs from a pure LO version of the equation [65–67].

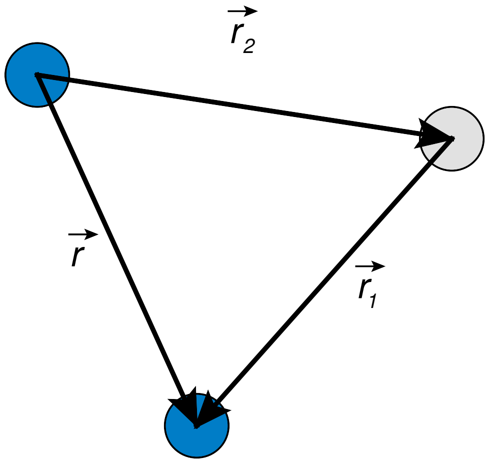

Figure 3.3: Schematic view of the mother and daughter dipoles in transverse space for the BK evolution.

The Balitsky-Kovchegov equation unfortunately does not have an analytic solution, so it has to be solved numerically [47, 64, 68]—more recently for more complicated kernels in the work described in this thesis and in [33–35]. A usual way of solving this equation involves the Simpson method for integration, a linear interpolation for acquiring values of $N(r, Y)$ for intermediate positions in a predefined grid in the size of dipoles r and the Runge-Kutta method for solving the differential equation.

Solving this equation numerically can be CPU-time demanding and it is necessary to develop methods to improve the speed of the computation in order to be able to calculate predictions for more complicated approaches (such as for the b-dependent computations). Throughout this work, we follow and extend on the approach, that we implemented in my Diploma thesis [69, 70].

fit	Q_0^2 [GeV^2]	C	Λ [GeV]	γ	σ_0 [mb]
GBW	0.241	2.46	0.241	0.971	32.357
MV	0.165	$\sqrt{6.5}$	0.241	1.13	32.895

Table 3.1: Possible values of the initial condition and running coupling parameters [47].

This approach consists of optimizing the grid spacing (in rapidity, transverse dipole size and its angle in integration) for maintaining constant error-to-precision ratio, rewriting the Runge-Kutta method of fourth order, so that it needs just one step in computation, rather than four [71], and choosing the correct scale for the variables, that are iterated over (logarithmic scale for the transverse size and linear for its angular dependence has proven to be an optimal choice).

In order to solve the Balitsky-Kovchegov evolution equation and to get a prediction for the associated observables, one must start with a certain initial condition. One of the frequently used initial conditions is the GBW initial condition [26]

$$N^{GBW}(r, Y=0) = 1 - \exp\left(-\frac{(r^2 Q_0^2)^\gamma}{4}\right). \tag{3.9}$$

Another typical initial condition (as discussed in the previous chapter) for the BK equation is the MV initial condition [25] that reads

$$N^{MV}(r, Y=0) = 1 - \exp\left(-\frac{(r^2 Q_0^2)^\gamma}{4} \ln\left(\frac{1}{r\Lambda} + e\right)\right). \tag{3.10}$$

Here Λ is called the Landau pole and represents the infrared cutoff of the dipole cross section [72], Q_0^2 determines the typical gluon momentum where the target starts to be saturated (see next chapter for more details) and is called the saturation scale. Parameter γ is called the anomalous dimension and e is the Euler's number. Some of the typical values for the parameters used in these two initial conditions are shown in Tab. 3.1.

3.3 Running coupling in the variable n_f scheme

In the kernel of the BK equation, the strong running coupling plays an essential role. A common choice for the coupling constant in this approach is to use the running coupling with variable number of flavors n_f. In this framework, the number of flavors that are active in the evolution changes with the considered size of the original dipole that emitted the two daughter dipoles. The running coupling is then given by

$$\alpha_{s,n_f}(r^2) = \frac{4\pi}{\beta_{0,n_f} \ln\left(\frac{4C^2}{r^2\Lambda_{n_f}^2}\right)}, \tag{3.11}$$

where n_f corresponds to the number of flavors that are active, C^2 is the uncertainty coming from the Fourier transform that was used to derive this result and is usually fit to data [72] (Tab. 3.1) and

$$\beta_{0,n_f} = 11 - \frac{2}{3} n_f. \tag{3.12}$$

$\Lambda^2_{n_f}$ is called the QCD scale parameter and its value depends on the value of n_f in the variable n_f scheme. When heavier quark flavors are active (e.g. charm and beauty quarks, Eq. (3.14)), its value needs to be calculated from the relation [47]

$$\Lambda_{n_f-1} = (m_f)^{1-\frac{\beta_{0,n_f}}{\beta_{0,n_f-1}}} (\Lambda_{n_f})^{\frac{\beta_{0,n_f}}{\beta_{0,n_f-1}}}. \tag{3.13}$$

We need to fix this recursive relation at one point in order to be able to solve it. For this, it is standard to choose the value of Λ_5, which we obtain by solving the running coupling relation (3.11) at the scale of Z^0 boson mass with the value of the coupling that has been measured experimentally. For this we use the measured value of $\alpha_s(M_Z) = 0.1196 \pm 0.0017$ at the Z^0 mass of $M_Z = 91.18\,\mathrm{GeV/c^2}$ [73].

The number of active flavors n_f is set depending on the transverse size of the mother dipole. The condition that governs this relates the mass of the heaviest quark considered to the values of r^2. This condition can be expressed as

$$r^2 < \frac{4C^2}{m_f^2}. \tag{3.14}$$

Since all dipole sizes are accounted for in the BK evolution equation, there is a need to freeze the coupling at a set value α_0 after a certain dipole size is reached [47, 72]. This value differs depending on the chosen parametrization and is one of the free parameters that enters the computation.

3.4 Solutions without impact-parameter dependence

Let us now conclude the necessary introduction to the theory of the dipole model and the BK equation and move to the results that I have computed. This section and sections 3.6 and 3.8 are reproduction of previous works and aim for development of tools necessary for investigation and improvement of the problems of those approaches. From Sec. 3.9 onward I present our original results published in peer-reviewed journals.

If we now solve the simplified BK equation as was sketched above (Eq. (3.7)), we arrive to a scattering amplitude (Fig. 3.4), that approaches zero in the region of low-values of the transverse dipole size r, which corresponds to color-transparency of the probing dipole [74–76], and reaches one in the region of high values of r, which is a consequence of the infinite-target approximation as well as of the saturation effects of the non-linear term in the equation.

Without this non-linear term, at high regions in r, the scattering amplitude would not be stopped at 1, but would continue growing. Figure 3.5 depicts the integrand of the structure function of the DIS process (2.27). It serves for gaining the notion of which regions in r are mostly important for these inclusive cross sections. This then turns out to be from about 0.02 to 4 GeV^{-1}.

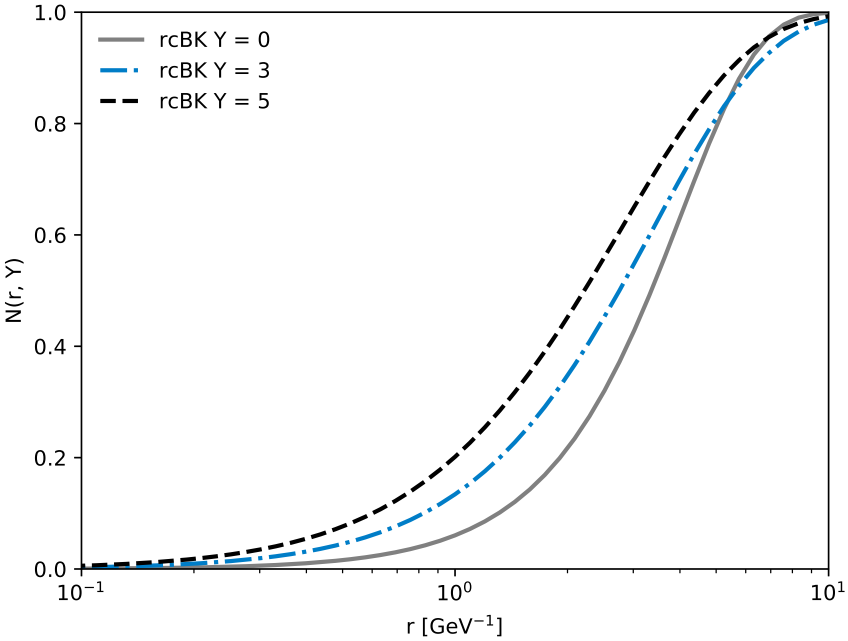

Figure 3.4: Scattering amplitude as a solution of the approximated BK equation (3.7) with factorized impact parameter.

Figure 3.6 shows the computed structure function confronted with data from the HERA experiment [39]. The initial condition for this computation was chosen to be the MV model with parameters obtained from [47] Tab. 1, row e, where the masses of the considered u, d and s quarks were set to be 140 MeV/c^2. The running coupling was frozen at a value of 0.7 and the heavier quark masses were set to $m_c = 1.3\,\mathrm{GeV/c^2}$ and $m_b = 4.5\,\mathrm{GeV/c^2}$.

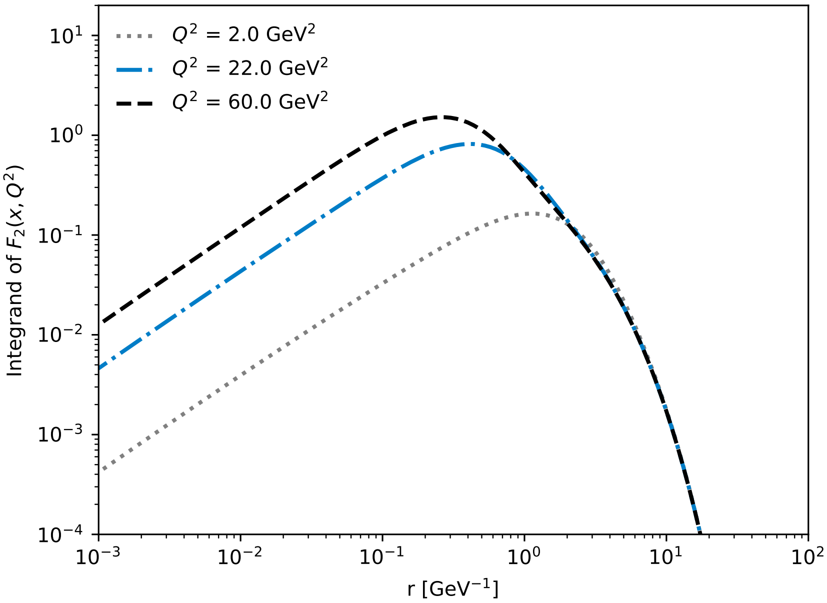

Figure 3.5: Integrand of the structure function (Eq. (2.27)) - virtual photon wave function $\mid \psi_{T,L} \mid^2$ (2.26) multiplied by the scattering amplitude $N(r, Y)$, corresponding Jacobian and factors. This plot is used to illustrate the region of r that contributes the most to the inclusive processes in DIS.

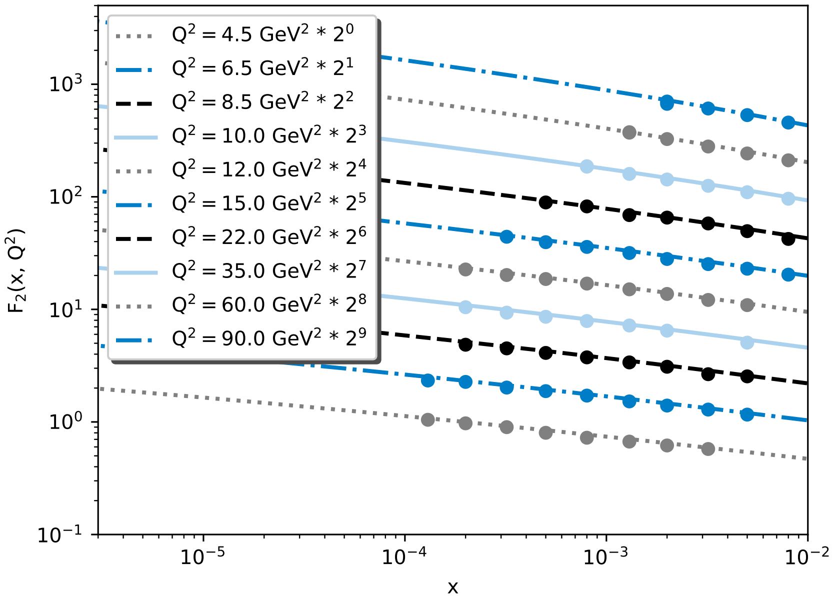

Figure 3.6: The dependence of the proton structure function $F_2(Y, Q^2)$ computed from the impact-parameter independent BK equation on Y and compared with data from HERA [39].

3.5 Impact parameter dependent BK equation

In the previous chapters, we have demonstrated how one can obtain solutions of the BK equation under the approximation of factorizable impact-parameter dependence. This approach was very successful in the past, but now we would like to lift this simplification and solve for a scattering amplitude containing a non-trivial dependence on the impact parameter. The proton will no longer be "an infinite homogeneous object", but we will allow it to have finite-size and non-trivial structure.

The full BK evolution equation without neglecting the impact parameter dependence reads

$$\begin{aligned}\frac{\partial N(\vec{r},\vec{b},Y)}{\partial Y} = \int d\vec{r_1} K^{run}(r,r_1,r_2)(N(\vec{r_1},\vec{b_1},Y) + N(\vec{r_2},\vec{b_2},Y) - \\ - N(\vec{r},\vec{b},Y) - N(\vec{r_1},\vec{b_1},Y)N(\vec{r_2},\vec{b_2},Y)). \quad (3.15)\end{aligned}$$

Let us assume (as in [77–79]), that the hadronic target is rotationally symmetric and therefore we omit the dependence on the angle Φ (as shown in Fig. 3.7).

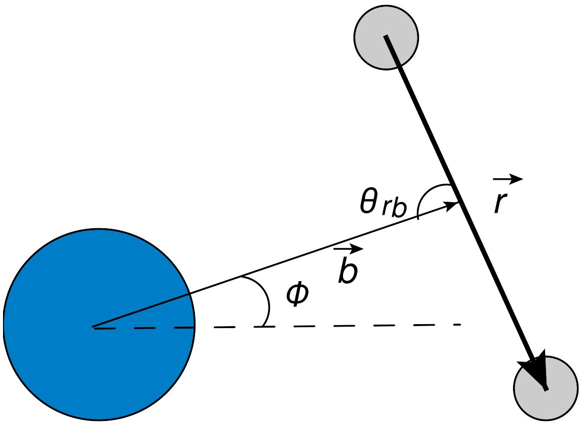

Figure 3.7: Schematic view of the dipole interacting with a proton in the impact parameter dependent scheme.

The equation in this approach becomes independent of the rotational angle as

$$\begin{aligned}\frac{\partial N(\vec{r},b,Y)}{\partial Y} = \int d\vec{r_1} K^{run}(r,r_1,r_2)(N(\vec{r_1},b_1,Y) + N(\vec{r_2},b_2,Y) - \\ - N(\vec{r},b,Y) - N(\vec{r_1},b_1,Y)N(\vec{r_2},b_2,Y)). \quad (3.16)\end{aligned}$$

All variables that enter this equation can be derived from the geometry of the three dipoles, which is defined by the knowledge of at least one impact parameter vector and two dipole size vectors. In the usual approach, the known vectors are $\vec{r}$, $\vec{b}$ and $\vec{r_1}$ and we can then compute the remaining variables that enter this equation as

$$r_2 = \sqrt{r^2 + r_1^2 - 2rr_1 cos(\theta_{rr_1})}, \tag{3.17}$$

$$\theta_{rr_2} = arccos\left(\frac{r_2^2 + r^2 - r_1^2}{2rr_2}\right), \tag{3.18}$$

$$b_1 = \left|\vec{b} + \frac{\vec{r_2}}{2}\right| = \sqrt{b^2 + \frac{r_2^2}{4} + br_2 cos(\theta_{br_2})}, \tag{3.19}$$

and

$$b_2 = \left|\vec{b} - \frac{\vec{r_1}}{2}\right| = \sqrt{b^2 + \frac{r_1^2}{4} - br_1 cos(\theta_{br_1})}. \tag{3.20}$$

Here the variable θ_{xy} denotes the angle between vectors x and y. Furthermore, for the angles θ_{br_1} and θ_{br_2} holds

$$\theta_{br_1} = \theta_{br} + \theta_{rr_1} \tag{3.21}$$

and

$$\theta_{br_2} = \theta_{br} + \theta_{rr_2}, \tag{3.22}$$

as is illustrated in Fig. 3.8.

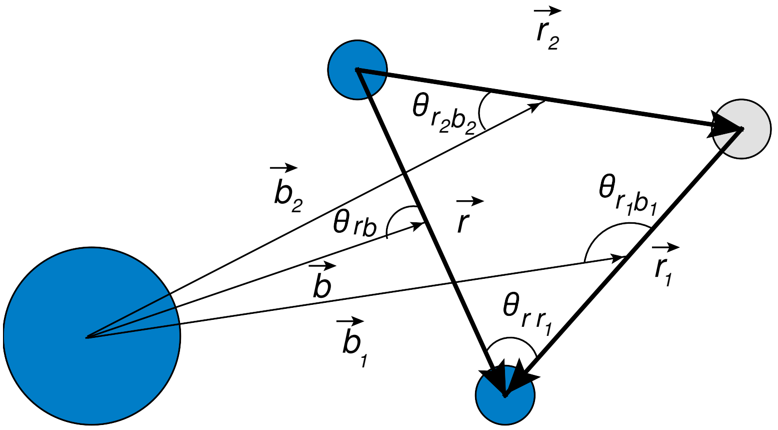

Figure 3.8: Schematic view of the mother and daughter dipoles along with all the associated variables defining the evolution.

The scattering amplitude in this framework has two more dimensions with respect to the previously considered case without the impact-parameter dependence: the size of the vector $\vec{b}$ and its orientation relative to the transverse size vector, θ_{br}. Let us simplify the situation by assuming that the dependence on this angle is weak and that we are solely interested in the influence of the distance from the center of the proton on the scattering amplitude. This effectively means

$$N(\vec{r}, b, Y) \rightarrow N(r, b, Y), \tag{3.23}$$

transforming the BK equation into

$$\frac{\partial N(r,b,Y)}{\partial Y} = \int d\vec{r_1} K^{run}(r,r_1,r_2)(N(r_1,b_1,Y) + N(r_2,b_2,Y) - \\ - N(r,b,Y) - N(r_1,b_1,Y)N(r_2,b_2,Y)). \quad (3.24)$$

3.6 Coulomb tails

When trying to solve the impact-parameter dependent BK equation, one has to modify the initial condition to incorporate this behavior. A possible choice is to combine the GBW model (Gaussian profile in the transverse dipole size) with a Gaussian distribution for modelling the transverse profile of the proton [77]

$$N(r,b,Y=0) = 1 - \exp[-cr^2 \exp(-db^2)]. \quad (3.25)$$

The values for the parameters that were used for this initial condition are $c = 0.0643\,\mathrm{GeV}^2$ and $d = 1/8\,\mathrm{GeV}^2$.

The Runge-Kutta formulas have to be adapted to the new dimensionality of the problem. The original way of writing the method [71] was such that it allowed for a straight forward generalization. In this approach, one can then simply add the extra dimension to the scattering amplitude, at each step of the evolution calculate the corresponding daughter-dipole impact parameters b_1 and b_2 as illustrated in Fig. 2.6 and solve the BK equation in a similar manner as for the previous case without the impact-parameter dependence.

The numerical computation can be quite demanding on hardware resources due to a very large phase space that needs to be covered in each step of the evolution. However, CPU time is not the only problem that one encounters. When one tries to evolve the scattering amplitude to higher rapidities in this framework, it is observed, that the initial exponentially falling dependence of the scattering amplitude in b gets distorted quickly and that the evolution changes this exponential fall-off into a power-law (as shown in Fig. 3.9). This behavior was first observed in [79] using a kernel with a constant α_s. As we can see from Fig. 3.9, the inclusion of the running coupling does not change the qualitative picture.

The resulting size of the proton therefore grows rapidly, as we evolve the scattering amplitude towards higher rapidities superseding the Martin-Froissart bound (a theoretical limit on the speed of the growth of a cross section emerging from quantum mechanics [80–82]) and making the data description impossible (see Fig. 3.10 and 3.11).

This unphysical behavior emerges from the fact, that the BK equation was postulated in perturbative QCD, where a small value of the strong coupling constant α_s is assumed. When we reach the region of large b, the corresponding coupling constant is too large and we reach a non-perturbative region, where this equation loses validity [83]. In other words, when the BK equation was derived, the effects of confinement were not taken into account, which manifests itself by producing unphysical results.

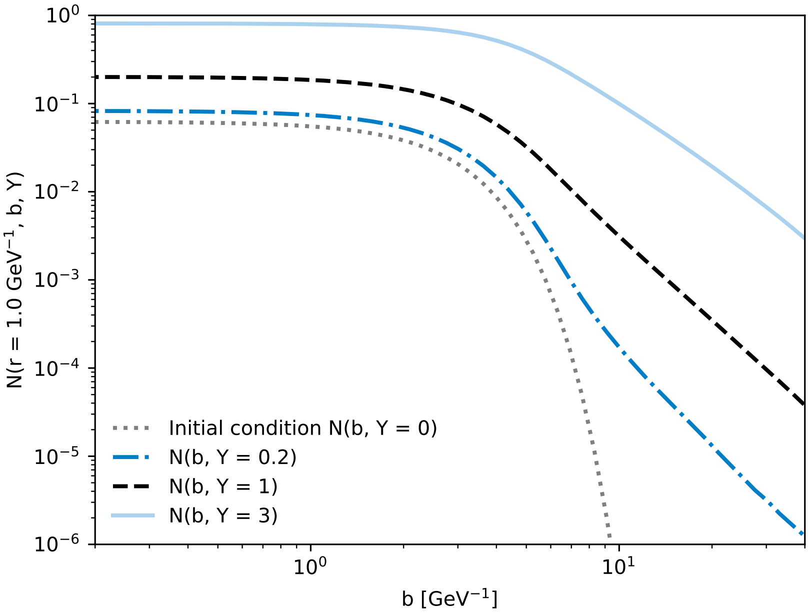

Figure 3.9: The dependence of the b-dependent running-coupling BK equation with respect to the impact parameter. We can see, that the initial exponential decrease of the scattering amplitude is changed to a power law with evolution.

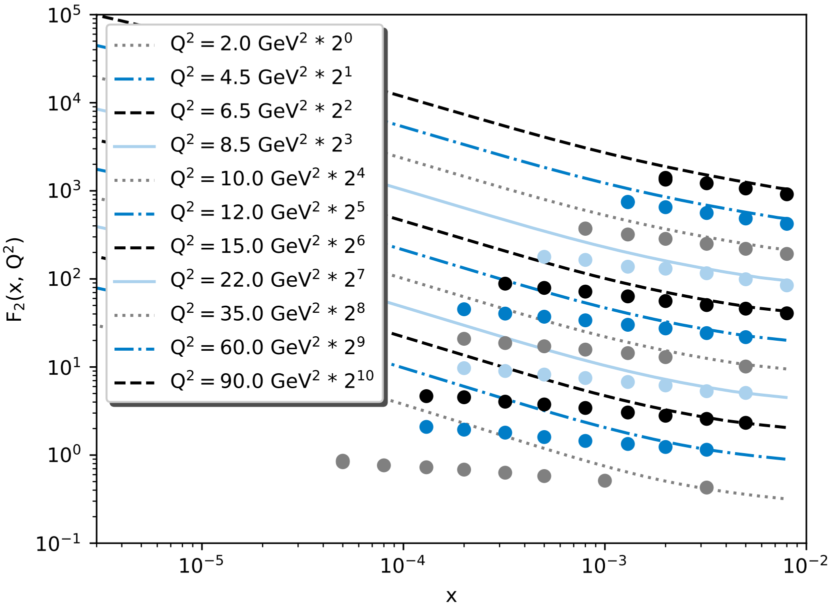

Figure 3.10: Structure function of the proton computed from the b-dependent BK equation with the running coupling kernel compared to data from HERA [39]. For this evolution, the initial condition (3.39) was used since it describes data at the initial condition without any additional parameters.

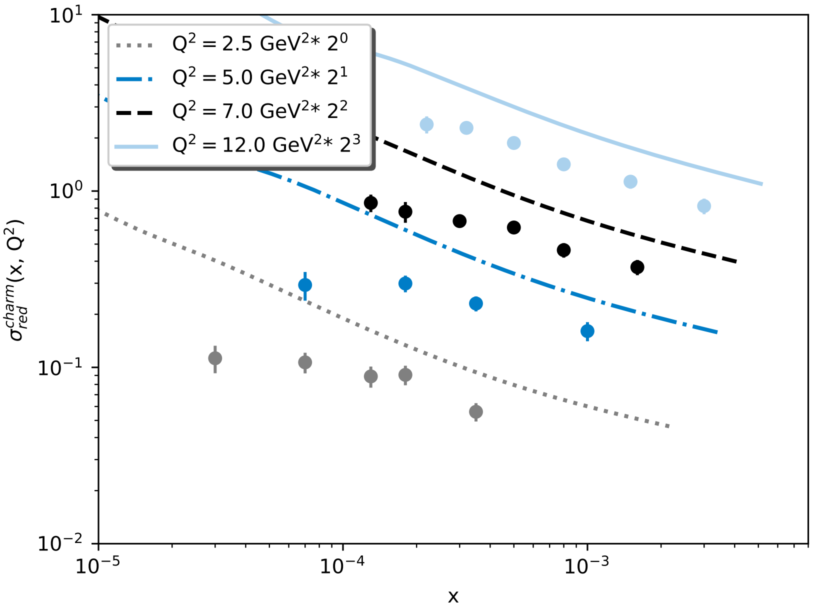

Figure 3.11: The comparison of the prediction for the reduced cross section for the charm quark with respect to x for the running coupling b-dependent BK equation. Data are from the accelerator HERA [39].

3.7 Origin of the non-perturbative contribution

In the previous section, we have shown how the b-dependent computation makes the scattering amplitude grow so fast, that it makes correct data description impossible. If we try to determine, which part of the phase-space of the evolution is responsible for the onset of non-perturbative effects, one has to look at a single step of the evolution at the initial condition in a region, where b is very large (as shown in Fig. 3.12).

Here, the mother dipole is far away from the proton that is depicted as a grey blob in the center of the figure. Since we are starting at the initial condition, the scattering amplitude at large-b region is exponentially suppressed. This means, that all $N(r, b, Y)$ terms in the Eq. (3.24) will be essentially zero. In this figure, we see that the first daughter dipole has also an impact-parameter vector, that puts it outside of the target and therefore terms with $N(r_1, b_1, Y)$ will be zero as well.

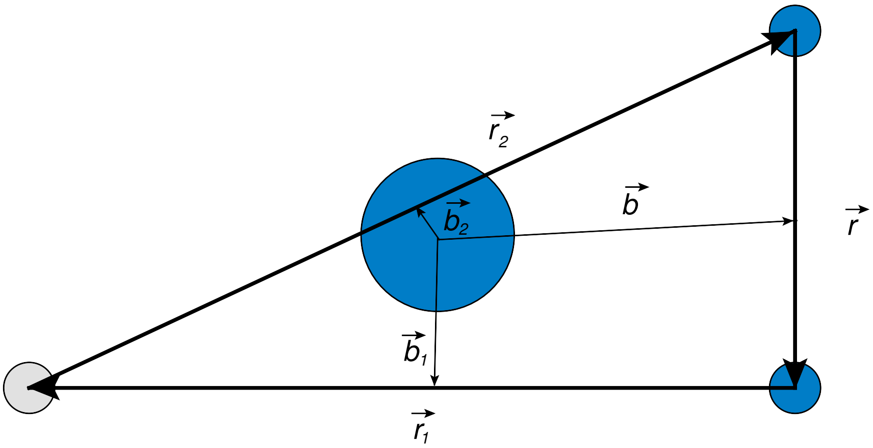

Figure 3.12: Geometrical orientation of the mother and daughter dipoles that contributes to the rise of Coulomb tails. The region that contributes the most is the one where transverse sizes of the daughter dipoles r_1 or r_2 are large. See text for more details.

However, the third dipole $N(r_2, b_2, Y)$ has an impact parameter small enough, so that it could hit the target, resulting in a large value of the scattering amplitude. We can see, that in the integration over the daughter-dipole size r_1, the term $N(r_2, b_2, Y)$ is going to be the only non-zero term and comes with a positive sign. This term will be the one responsible for the growth of the scattering amplitude at high values of b.

The only way, how one can obtain a small value for b_1 or b_2 for computations at large distances from the center of the target is when the corresponding daughter-dipole sizes are very large, namely

$$r_{1,2} \sim 2b. \tag{3.26}$$

Therefore, the growth of the scattering amplitude at large distances—and thus the growth of the Coulomb tails—stems from the configurations, where daughter-dipole sizes are very large.

3.8 Scale-dependent cutoff as a remedy for the Coulomb tails

If we now try to fix the unphysical growth of the scattering amplitude and restore its ability to correctly describe data, an obvious choice is to suppress the regions responsible for these divergences. We can achieve this regularization by imposing a scale-dependent cutoff of the daughter-dipole size into the kernel of the equation as

$$\frac{\partial N(r,\vec{b},Y)}{\partial Y} = \int d\vec{r_1} K^{run}(r,r_1,r_2)\Theta\left(\frac{1}{m^2}-r_1^2\right)\Theta\left(\frac{1}{m^2}-r_2^2\right)$$
$$(N(r_1,\vec{b_1},Y)+N(r_2,\vec{b_2},Y)-N(r,\vec{b},Y)-N(r_1,\vec{b_1},Y)N(r_2,\vec{b_2},Y)), \quad (3.27)$$

In this section, we will follow the work of [78], where the cutoff parameter m was set to be $0.35\,\mathrm{GeV}$.

Of course, since we have imposed a cutoff for large-$r_{1,2}$ regions into the kernel of the equation, we need to impose the same cutoff into the initial condition in order to stay consistent with our scattering amplitude, which then becomes

$$N(r,b,Y=0) = 1-\exp[-cr^2\exp(-db^2)]\Theta\left(\frac{1}{m^2}-r^2\right). \quad (3.28)$$

This initial condition was then used for evolution with the kernel, that incorporates confinement effects via the mass-dependent cutoff (3.27). See Fig. 3.13 for the scattering amplitude cut in r for various values of rapidity and Fig. 3.14 for the scattering amplitude cut in b.

After we include this regularization parameter, that tries to mimic the effects of confinement, we can run the evolution again and compare the resulting scattering amplitude (Fig. 3.14) with the non-regularized version (Fig. 3.9). We can see, that the mass-dependent cutoff (sometimes termed "gluon mass") suppresses the Coulomb tails and restores the exponential falloff of the scattering amplitude in the impact-parameter region even after several units of rapidity. This regularization however comes at a cost of an extra free parameter that needs to be fitted to data. Since this parameter cuts a part of the phase space away from the evolution, the resulting scattering amplitude is especially sensitive to its value.

Figure 3.13 shows the behaviour of this amplitude with respect to the transverse dipole size r. Notice, that the cutoff in this plane occurs at twice the distance as the chosen gluon mass dictates. This occurs because, in fact, $\vec{r}=\vec{r_1}+\vec{r_2}$ and therefore the evolution does not suppress r until the value of $2/m$ is reached.

If we now use the formalism described above and produce the related scattering amplitude, we will not get a good data description (see Fig. 3.15).

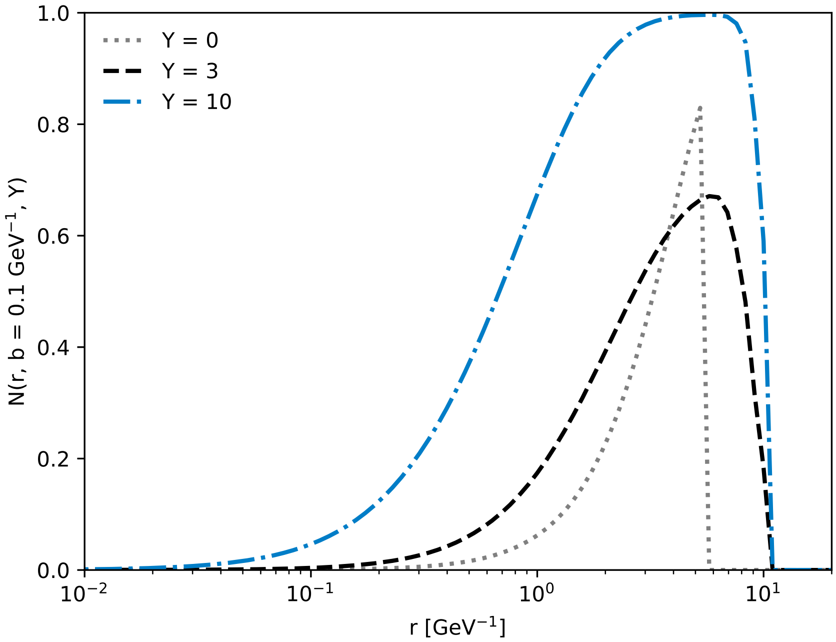

Figure 3.13: Scattering amplitude as a function of r for $b = 0.1\,\mathrm{GeV}^{-1}$ for various values of rapidity for the impact-parameter dependent BK equation with the massive cutoff as Eq.(3.27).

As was reported in the work of [78], the used cutoff that regulates the large-b behavior of the scattering amplitude is too strong and cuts off some of the important parts of the large-$r_{1,2}$ phase space that are necessary for a correct description of the inclusive F_2 data. In order to make up for this loss, one has to come up with an additional phenomenological term dubbed F_2^{soft} [84]. This correction is computed as

$$F_2^{soft} = \frac{Q^2}{2\pi\alpha_{em}}\sigma_0 \int_{\frac{1}{m}} rdr \int_0^1 dz(|\Psi_L|^2 + |\Psi_T|^2), \tag{3.29}$$

where $\sigma_0 = 75.98\,\mathrm{GeV}^{-2}$. This addition effectively means, that we are assuming the scattering amplitude to be unity for dipole sizes $r > 1/m$. Since this inclusion of large dipoles lacks the b-dependence, it has to be normalized with a constant σ_0 just as was done for the impact-parameter independent BK equation and this parameter needs to be again fitted to data. The total structure function is then computed as

$$F_2 = F_2^{BK} + F_2^{soft}, \tag{3.30}$$

where by F_2^{BK} we mean the structure function obtained by the BK computation (Eq. (2.27)).

If we now compute the scattering amplitude with these corrections (see Fig. 3.16 and 3.17), we can see that we obtain a description of the data as

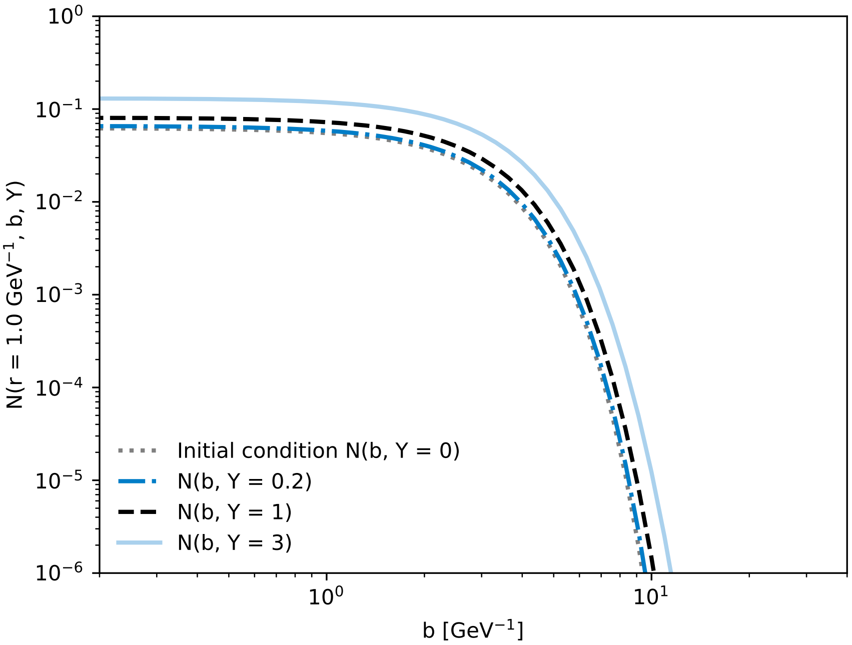

Figure 3.14: The dependence of the b-dependent BK equation with respect to the impact parameter. The confinement cut was considered in this computation, which fixed the large-b behavior of the scattering amplitude (see Eq. (3.27)).

measured at HERA. This description however comes at a significant cost, since we needed to introduce a number of additional free parameters and phenomenological terms (m, F_2^{soft}, σ_0) into the computation. If we try to quantify how much the soft correction contributes to the final structure function (see Fig. 3.18), we can see that, especially in the high-x region, its contribution plays a significant role in the final value of the cross section. The dependence of the scattering amplitude on so many free parameters, that have a strong impact on its final shape and the associated observables, spoils its predictive powers. The fact that we needed them in order to describe the inclusive DIS cross section suggests that when we try to apply this equation for other processes (as well as for predicting processes that have not yet been measured), it will give incorrect results. That is why in the next section, we will investigate other possibilities for the kernel regularization without the need for additional ad hoc corrections.

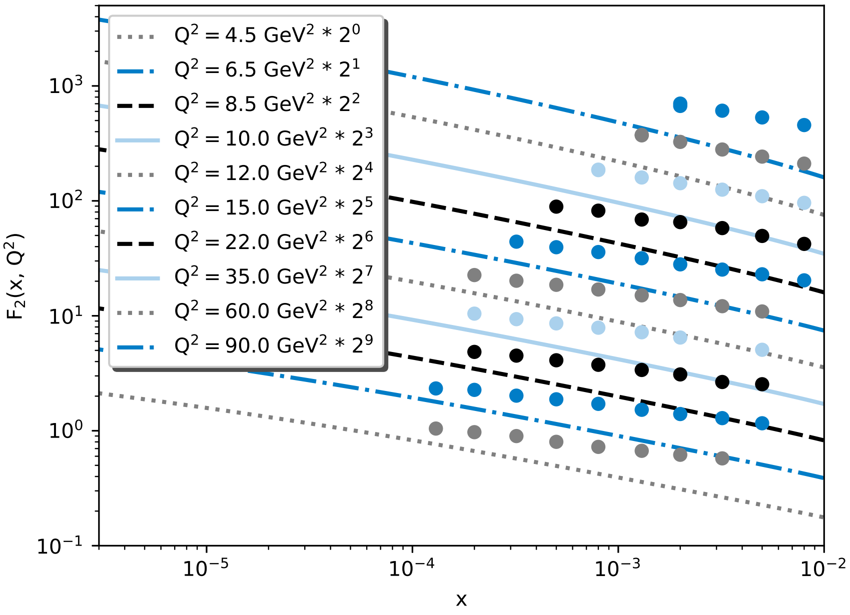

Figure 3.15: Comparison of the prediction for the structure function F_2 with data from HERA [39] at various Q^2 for the b-dependent BK evolution equation after the mass-dependent cutoff has been imposed to the kernel as in [78].

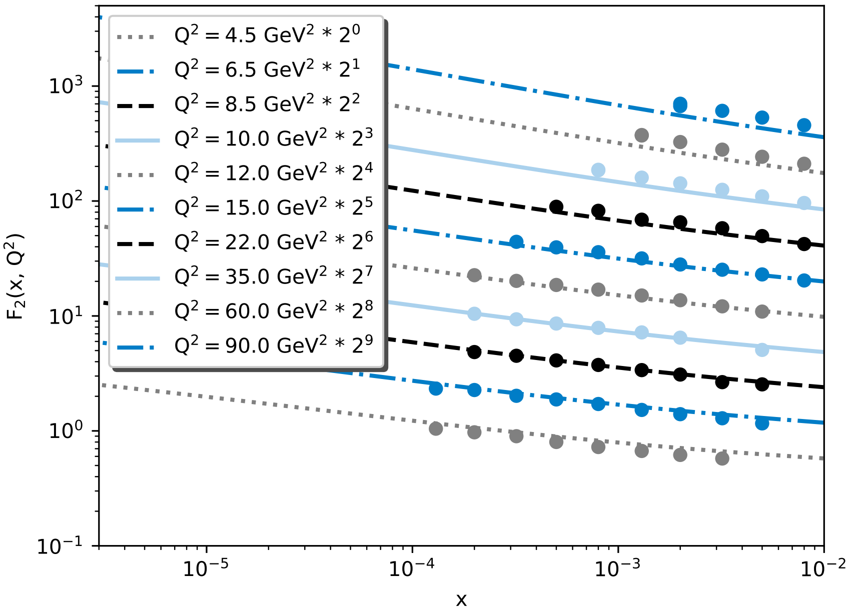

Figure 3.16: Comparison of the prediction for the structure function F_2 with data from HERA [39] at various Q^2 for the b-dependent BK evolution equation with the F_2^{soft} correction.

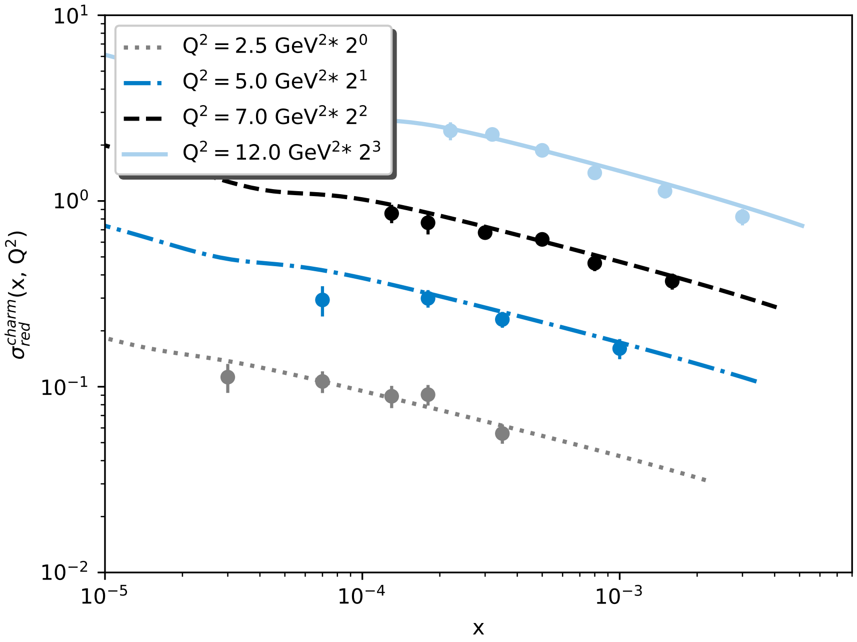

Figure 3.17: Comparison of the prediction for the reduced cross section for the charm quark with respect to x for the regularized b-dependent BK equation. Data are from HERA [39].

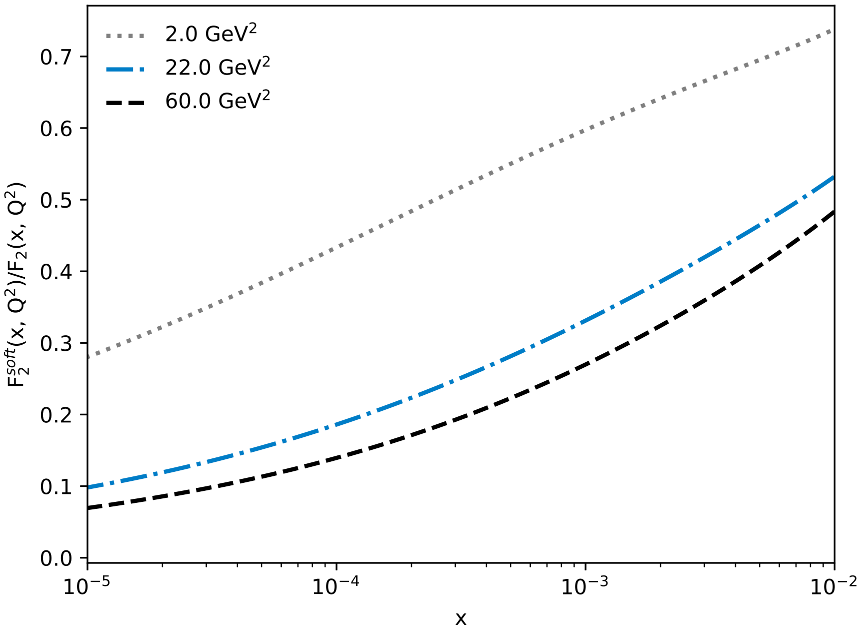

Figure 3.18: Evaluation of the fractional soft contribution F_2^{soft}/F_2 to the final structure function at various Q^2 for the b-dependent BK evolution equation.

3.9 Collinear resummation and its implications to the b-BK equation

In the previous section, we have shown how the regularization of the kernel of the b-dependent BK equation can lead to the restoration of the exponential fall off of the scattering amplitude. We have shown, that this approach also introduces additional undesirable free parameters and phenomenological corrections into the computation. In this section, we will explore the properties of the collinearly improved kernel [31, 32, 85–88], that resumms some of the divergences that the running coupling kernel omitted, and we will show how it can be used for the suppression of the Coulomb tails instead of the massive kernel regularization.

Inclusion of the running coupling into the LO BK equation managed to add some of the large perturbative corrections crucial for a more complete description of the dipole-related processes [61]. However, there are other corrections that should be included such as large single or double transverse logarithms. These logarithms arise from collinear radiative corrections in higher orders of α_s and they were first included into the equation in [31]. These corrections come at play in the case, when the size of the dipole is small and the scattering weak. In this approach, the collinearly improved BK equation reads [32]

$$\frac{\partial N(r,b,Y)}{\partial Y} = \frac{\overline{\alpha}_s}{2\pi}\int d\vec{r}_1 \frac{r^2}{r_1^2 r_2^2}\left[\frac{r^2}{\min(r_1^2,r_2^2)}\right]^{\pm\overline{\alpha}_s A_1} K_{DLA}(\sqrt{|L_{r_1r}L_{r_2r}|})$$
$$(N(r_1,b_1,Y)+N(r_2,b_2,Y)-N(r,b,Y)-N(r_1,b_1,Y)N(r_2,b_2,Y)), \quad (3.31)$$

where

$$K_{DLA}(\rho) = \frac{J_1(2\sqrt{\overline{\alpha}_s\rho^2})}{\sqrt{\overline{\alpha}_s}\rho}, \quad (3.32)$$

J_1 is the Bessel function, the anomalous dimension $A_1 = 11/12$ and

$$L_{r_ir} = \ln\left(\frac{r_i^2}{r^2}\right). \quad (3.33)$$

The sign factor in the exponent $\pm\overline{\alpha}_s A_1$ takes the value of the plus sign when

$$r^2 < \min(r_1^2.r_2^2) \quad (3.34)$$

and a negative sign otherwise. For the running coupling

$$\overline{\alpha}_s = \alpha_s\frac{N_c}{\pi}, \quad (3.35)$$

the smallest dipole prescription was used according to

$$\alpha_s = \alpha_s(r_{\min}), \quad (3.36)$$

where

$$r_{\min} = \min(r, r_1, r_2). \quad (3.37)$$

This version of the BK equation allows us to resum large collinear logarithms as well as incorporates the running coupling in its kernel.

In this approach, it is usual to include the contribution of the heavier quarks to the structure function F_2. The mass of the charm quark was set, as in [32], to $m_c = 1.3\,\mathrm{GeV/c^2}$ and the mass of the bottom quark as $m_b = 4.5\,\mathrm{GeV/c^2}$. The masses of the light quarks u, d and s were set to $100\,\mathrm{MeV/c^2}$ (it has been shown that the solutions are insensitive to the chosen value of the light-quark mass [32]).

The contribution of the massive quarks to the dipole cross section makes the computation more complicated due to the fact, that the mass affects the value of x, for which the structure function is computed according to the photoproduction kinematic shift [26]

$$\tilde{x} = x\left(1 + \frac{4m_f^2}{Q^2}\right). \tag{3.38}$$

In this computation, we have incorporated the contribution from the charm quark and neglected the one from the bottom quark. The mass of the bottom quark was therefore used just for the correct computation of the running coupling.

Since before we were assuming the quark masses of the u, d and s quarks to be identical, the inclusion of this correction shifts the value of x, for which we compute the F_2 for heavier quarks. Therefore, it is necessary to compute both the wave function and structure function for these quarks separately and then interpolate and add the two structure functions together.

The collinear resummation embedded in the kernel of the equation (3.31) imposes time-ordering in the lifetime of the subsequent color dipoles. This time-ordering suppresses the emission of large-sized daughter dipoles since those would then live longer than the original mother dipole. This large daughter-dipole suppression is crucial not only for the collinear resummation itself, but as we have shown in the previous section, also should suppress the onset of non-perturbative effects to the scattering amplitude.

The magnitude of this suppression is studied in Fig. 3.19. Here we can see that for large values of daughter-dipole size, value of the collinearly improved kernel drops by a factor of $\sim 10^4$ with respect to that of the running coupling kernel. This then in turn mimics the behavior of the previously postulated mass-dependent cutoffs (3.27) without the need to fix the suppression at a predefined scale, since that is given in a natural way by the life-time ordering of the collinear resummation.

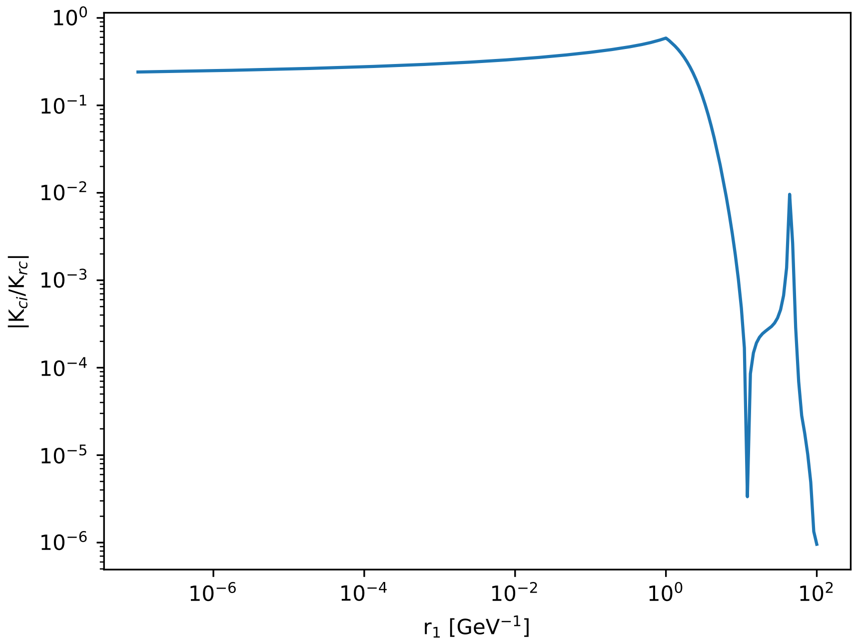

Figure 3.19: Absolute value of the ratio of the collinearly improved kernel $K_{\rm ci}$ (Eq. (3.31)) and running couling kernel $K_{\rm rc}$ (Eq. (3.8)) at a fixed dipole size $r = 1\,{\rm GeV}^{-1}$ and orientation with respect to the daughter dipole $\theta_{rr_1} = \pi/2$ as a function of the daughter dipole size (Fig. taken from [33]).

3.10 Proposing a new initial condition for the collinearly improved b-BK equation

The collinearly improved kernel has been shown to suppress the emission of large-daughter dipoles and to mimic the mass-dependent cutoff in the kernel of the BK equation (3.19). It is however also necessary to adjust the initial condition of the equation to properly take into account the geometry of the b-dependent computation.

In order to include the finite-size of the target proton, we have proposed a new family of initial conditions [34] that include the contribution of the quarks constituting the bare dipole at the initial condition separately, based on their distance from the center of the target b_{q_i} as shown in Fig. 3.20. The initial condition combines the Gaussian shape of the proton profile with the GBW dependence for the behavior of the scattering amplitude with respect to dipole size as

$$N(r, b, Y = 0) = 1 - \exp\left(-\frac{1}{2}\frac{Q_s^2}{4}r^2 T(b_{q_1}, b_{q_2})\right), \tag{3.39}$$

where b_{q_i} are the impact parameters of the quark and anti-quark forming the dipole and

$$T(b_{q_1}, b_{q_2}) = \left[\exp\left(-\frac{b_{q_1}^2}{2B_G}\right) + \exp\left(-\frac{b_{q_2}^2}{2B_G}\right)\right]. \tag{3.40}$$

This equation introduces two free parameters, where one is the saturation scale Q_s^2 and the other B_G defines the size of the proton. In order to establish a value for these two free parameters, we have used the inclusive structure function at $x = 0.008$ for the determination of the saturation scale as $Q_s^2 = 0.496$ GeV^2 and then exclusive J/ψ vector meson production at a fixed value of Y to fit the value of the proton-profile parameter as $B_G = 3.2258$ GeV^{-2}.

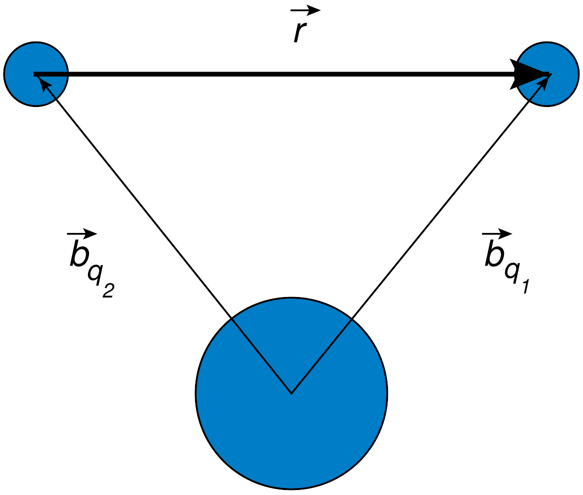

Figure 3.20: Schematic picture of the variables that enter the initial condition presented in Eq. (3.39).

Such initial condition then reflects the fact, that a dipole too large will not hit the proton (even for $b = 0$, for sufficiently large r, we will get large $b_{q_{1,2}}$ and therefore low value of N). There is no need to include a mass-dependent regularization in the initial condition as in (3.28), since this form is naturally suppressed as shown in Fig. 3.21.

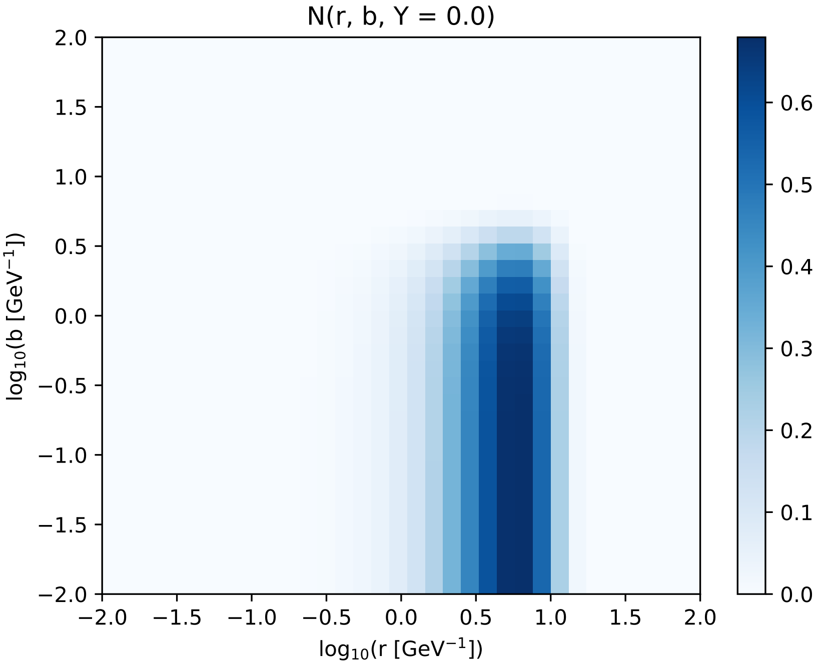

Figure 3.21: Modified initial condition for the b-dependent BK equation (3.39). This form of the initial condition is naturally suppressed at high values of r without a mass-dependent regularization. Figure adapted from [33].

3.11 Solutions of the collinearly improved b-BK equation

Combining the newly proposed initial condition (3.39) with the collinearly improved BK equation (3.31), we proceeded to solve the BK equation (for details see [33]). As we can see from Fig. 3.22, which shows the b-dependent evolution for the collinearly improved kernel, the collinear resummation suppresses the onset of Coulomb tails when compared to the running coupling evolution shown in Fig. 3.9. The fact, that the large-$r_{1,2}$ part of the phase space is suppressed in the collinearly improved case retards the onset of Coulomb tails but does not fully suppress them. If we now ask ourselves whether the suppression is sufficient enough to restore the description of data for the b-dependent case, we can compute the inclusive structure function and reduced cross section (see Fig. 3.23 and 3.24). These observables were computed without any other phenomenological constant or modification to the equation other than a modified initial condition and running coupling.

The modified structure function is sensitive to the overall integral of the scattering amplitude weighted with the photon wave-function (2.26) in the r-region. If we want to study in detail the computed impact-parameter profile of the target and compare it to data, we can focus on vector meson production with respect to the transferred four-momentum t (see Fig. 3.25). This variable

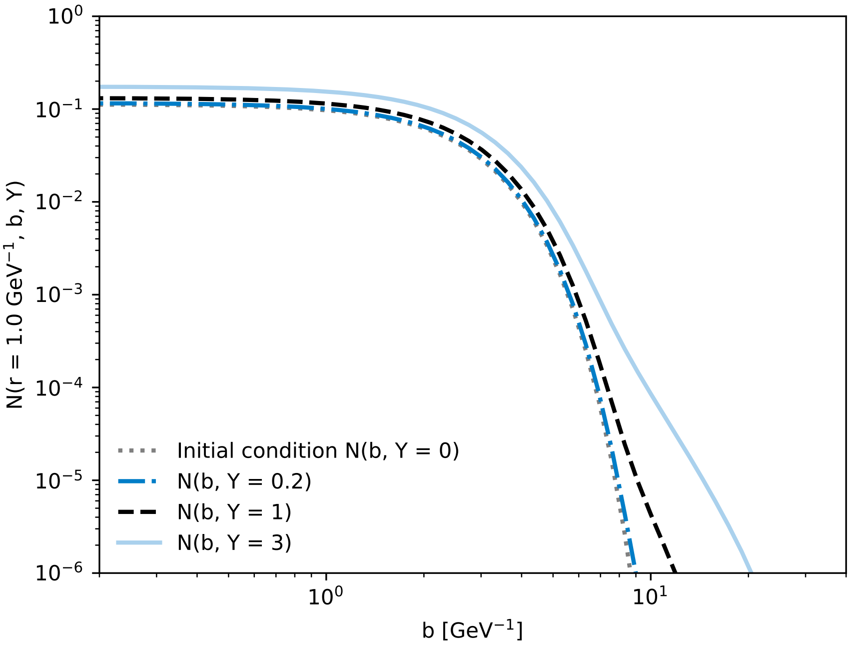

Figure 3.22: Dependence of the collinearly-improved scattering amplitude with respect to the impact parameter at different rapidities for a dipole of size $r = 1$ GeV^{-1}. Figure adapted from [33].

is Fourier-related to the impact parameter and therefore a correct description of these observables in t points to a correct slope and shape of the scattering amplitude in b.

The fact that in this approach, we get a good description of the structure function as well as of the vector meson production is a strong signal pointing to the fact, that we can rely on the predictive powers of this scattering amplitude and use it for computation of various other processes of interest.

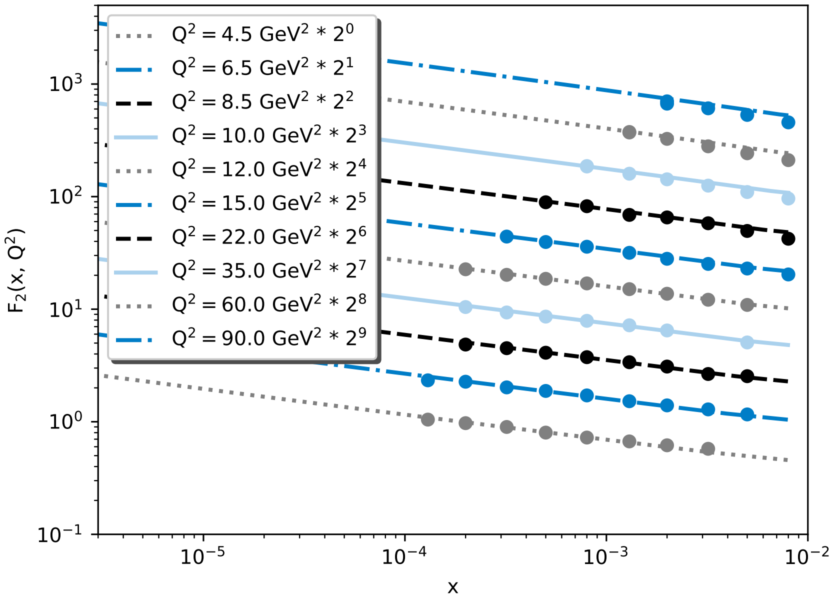

Figure 3.23: Comparison of the structure function data from HERA [39] with the solutions to the collinearly improved b-dependent BK equation. Figure adapted from [33].

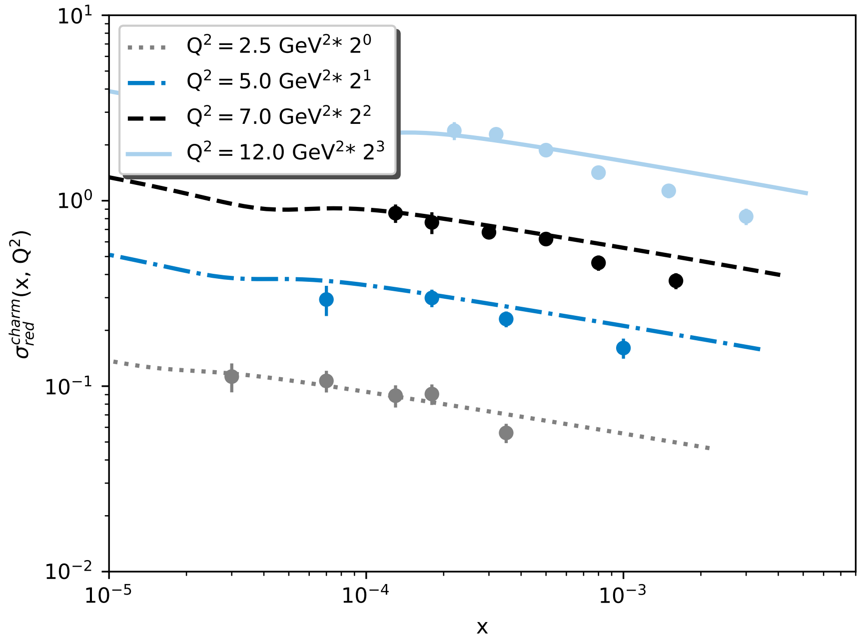

Figure 3.24: The comparison of the prediction for the reduced cross section for the charm quark with respect to x for the collinearly improved b-dependent BK equation. Data are from HERA [39]. Figure adapted from [33].

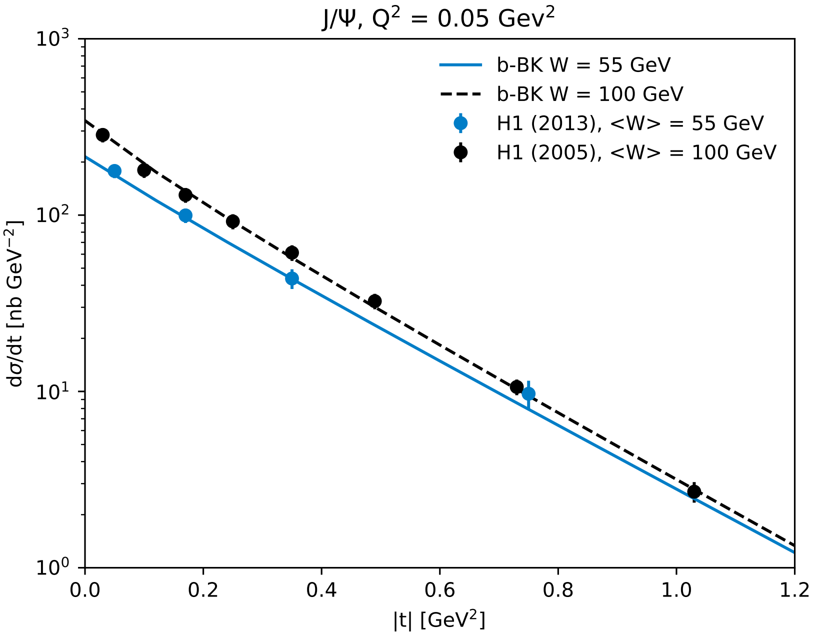

Figure 3.25: Comparison of the computation for the $|t|$ dependence of the cross section with data from HERA for the exclusive photoproduction of J/ψ vector mesons off protons. The data is from the H1 Collaboration at HERA at $\langle W\rangle =$ 55 GeV [89] and $\langle W\rangle = 100$ GeV [90]. Figure adapted from [34].

3.12 Nuclear collinearly improved b-BK equation

In the previous sections, we have shown how the formalism of collinearly improved BK equation can be shown to restore the predictive powers of the b-dependent version of this equation. Now we will generalize this formalism to compute predictions not only for protons as targets, but also for nuclei. These results can then be used for computing effects of nuclear shadowing [91], structure functions, and other observables that will be extensively studied at future facilities, such as [92, 93].

In order to make a transition towards nuclear targets, we need to adjust the initial condition. Each considered nucleus will have a different profile in the impact-parameter space, which is modelled by the corresponding Woods-Saxon distribution. The form of this distribution is

$$\rho_A(x, y, z) = \rho_0 \frac{1}{\exp\left[(r - \mathrm{R})/\mathrm{a}\right] + 1}, \tag{3.41}$$

(where $r \equiv \sqrt{x^2 + y^2 + z^2}$) and x, y and z are Cartesian spatial coordinates. Since we are interested in the nuclear density in the impact parameter space, we need to integrate over the longitudinal spatial coordinate as

$$T_A(b) = \int\limits_{-\infty}^{+\infty} dz \rho_A(x, y, z). \tag{3.42}$$

Table 3.2 shows the parameters for the Woods-Saxon distribution for various nuclei, which is then normalized as $\int \mathrm{d}^2\vec{b}\, T_A(b) = A$. However, nuclear density is not the desired variable for the exponent of the initial condition since, just as in the proton case, we want the initial condition to saturate at ~ 1 for the cases when the dipole hits the target and then fall off proportionally to the density of the target for more peripheral interactions of the dipole. That is why we need to normalize this function so that it would reach unity for central values of b with a factor k as

$$T_A^{norm}(b_{q_1}, b_{q_2}) = k\left[T_A(b_{q_1}) + T_A(b_{q_2})\right], \tag{3.43}$$

where the k is defined simply so that $kT_A(0) = 1$. Then we can rewrite the previously proposed collinearly improved initial condition (3.39) as

$$N^A(r, b, Y = 0) = 1 - \exp\left(-\frac{1}{2}\frac{Q_{s0}^2(A)}{4} r^2 T_A^{norm}(b_{q_1}, b_{q_2})\right), \tag{3.44}$$

where the values of the saturation scale will depend on the atomic number of the considered nucleus and will need to be fit to data again. In order to fit the values of the saturation scale, we have used the EPPS16 nuclear PDF fit [94] to compute the structure function of the considered nucleus at the initial value of $x = 0.008$ and then chose the saturation scale optimizing for the best possible description of the EPPS16 data there. The values obtained

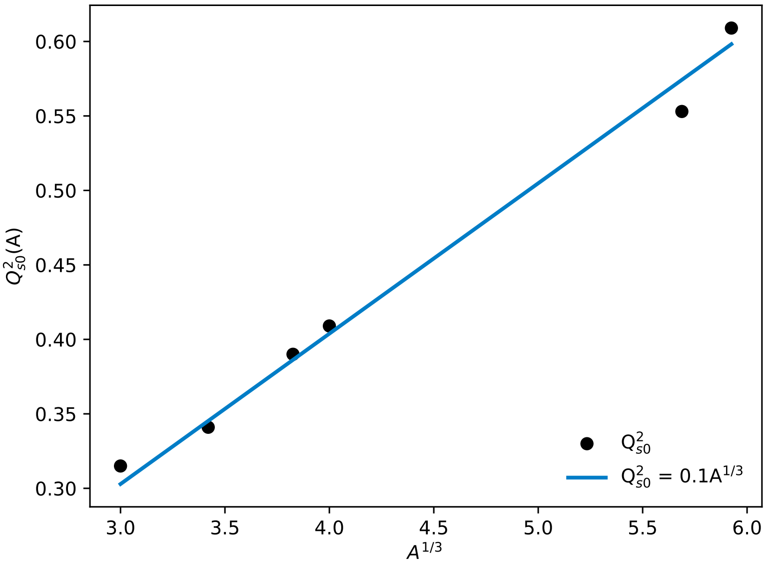

Figure 3.26: Dependence of the $Q^2_{s0}(A)$ parameter as a function of $A^{1/3}$ (solid bullets) compared with a linear function (blue line). Figure adapted from [35].

Nucleus	A	R (fm)	a (fm)	ρ_0 (fm^{-3})	$Q^2_{s0}(A)$ (GeV^2)
Al	27	2.84	0.569	0.2015	0.315
Ca	40	3.51	0.563	0.17611	0.341
Fe	56	3.980	0.569	0.17655	0.390
Cu	64	4.2	0.569	0.1746	0.409
W	184	6.510	0.535	0.1493	0.553
Pb	208	6.624	0.549	0.16	0.609

Table 3.2: Values of the parameters of the Wood-Saxon distribution, see Eq. (3.41), used in the computations reported in this text, and the value of the $Q^2_{s0}(A)$ parameter obtained as explained in the text. The Wood-Saxon parameters are taken from [95], Table taken from [35].

by the fit are shown in Tab. 3.2 as well as in Fig. 3.26. The technical details of the fitting procedure are discussed in more detail in [35].

An alternative prescription for the scattering amplitude for the nuclear case can be obtained in the Glauber-Gribov approach with the use of the evolved scattering amplitude of the proton [96] as

$$N^A(r,b,Y) = \Big[1 - \exp\Big(-\frac{1}{2}T_A(b)\sigma_{q\bar{q}}(Y,r)\Big)\Big], \tag{3.45}$$

with

$$\sigma_{q\bar{q}}(Y,r) = \int \mathrm{d}\vec{b}2N^p(r,b,Y), \tag{3.46}$$

where $N^p(r,b,Y)$ is in our case the solution of the collinearly-improved BK equation for the proton (as discussed in previous sections). We will denote

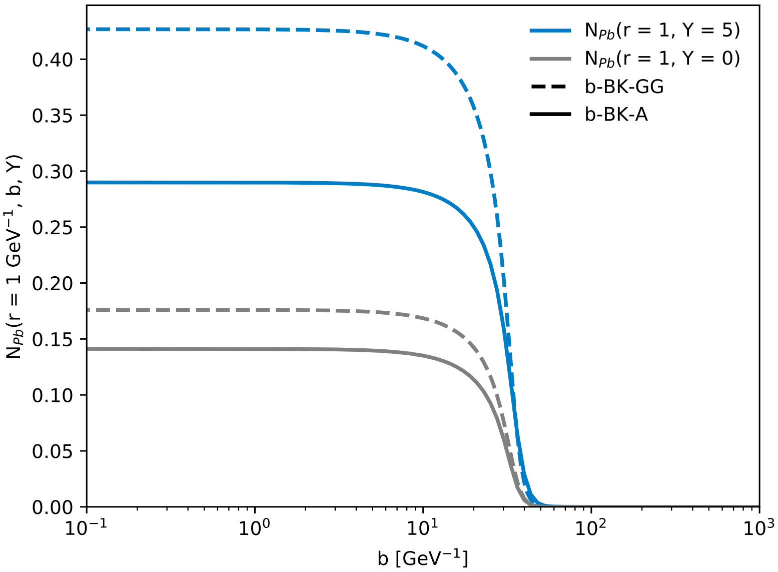

Figure 3.27: Comparison of the dipole scattering amplitudes computed for b-BK-A (solid line) with the b-BK-GG approach (dashed line). The comparisons are done at $Y = 0$ and $Y = 5$ for lead as a function of the impact parameter for a dipole size $r = 1\,\mathrm{GeV}^{-1}$. Figure adapted from [35].

solutions obtained by this approach as b-BK-GG and the ones with evolved initial condition (3.44) as b-BK-A. The two resulting scattering amplitudes for the case of lead are shown in Figs. 3.27 and 3.28.

For both approaches, we have computed the evolved scattering amplitudes, structure functions and from them the nuclear modification factor as

$$R_{pA} \equiv \frac{F_2^A(x, Q^2)}{A\ F_2^p(x, Q^2)}, \tag{3.47}$$

where $F_2^p(x, Q^2)$ is the structure function of the proton computed as discussed in the previous sections within the impact-parameter dependent framework (see Fig. 3.29 for its dependence on atomic number A). The results were then confronted with the data measured at Fermilab by the E665 collaboration [97] and with the b-BK-GG approach (Fig. 3.30). After verifying that we obtain a good description of the data, we have produced predictions for the observables that will be measured at future facilities [35].

Furthermore, the influence of the non-linear term in the BK equation on the nuclear modification factor was also studied in order to estimate the amount of saturation effects present in these measurable observables [98]. This was done by carrying out the computation in the same manner as was discussed above but with the non-linear term in the Eq. (3.31) set to zero. The comparison of the two nuclear modification factors along with measured data [97] can be seen in Fig. 3.31.

It is expected that the BFKL-like scattering amplitude will grow faster

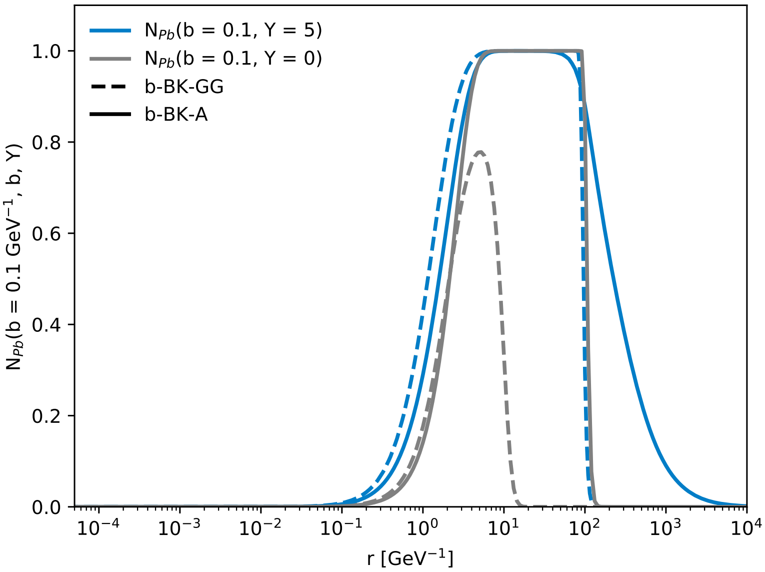

Figure 3.28: Comparison of the dipole scattering amplitudes computed for b-BK-A (solid line) with the b-BK-GG approach (dashed line). The comparisons are done at $Y = 0$ and $Y = 5$ for lead as a function of the dipole size for an impact parameter $b = 0.1\,\text{GeV}^{-1}$. Figure adapted from [35].

than the one that includes non-linear terms responsible for saturation effects. However, from this comparison we can see that the BFKL-like version of the BK equation produces nuclei that grow even faster than the sum of individual non-saturated protons. That is a prediction that could impact the measurement of such observables in the future planned facilities such as [92, 93] and help us with determining the validity of saturation-driven models in low-x physics.

Another good variable for testing the validity of the two approaches (b-BK-GG and b-BK-A) is the vector meson production, as described in Eq. (2.33) and below. The vector meson production was evaluated for coherent J/ψ production at the LHC for both cases [99] and Fig. 3.32 shows that the position of the diffractive minima shifts, which has been reported as a signal of saturation effects [100, 101]. On one hand, the b-BK-GG model uses a simple addition of the individual protons and thus the b-BK-A approach (which runs the BK evolution for entire nuclei) is expected to yield more saturation and show a displacement of these minima. On the other hand, the fact that the displacement is larger than in models that incorporate no saturation casts a warning on using solely this observable as a clear indicator of the presence of saturation effects.

The fact that the nuclear scattering amplitude computed from the BK equation with nuclear initial condition gets saturated sooner than the one computed with the use of the proton scattering amplitude and Glauber model results into a suppression of the differential coherent photoproduction of

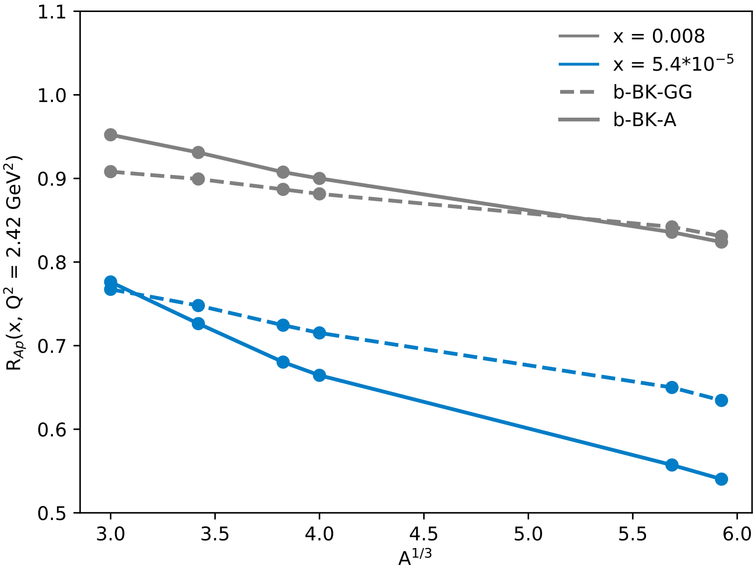

Figure 3.29: Nuclear modification factor at two values of the photon virtuality $Q^2 = 2.42$ GeV^2 as a function of A at different fixed values of x. Figure adapted from [35].

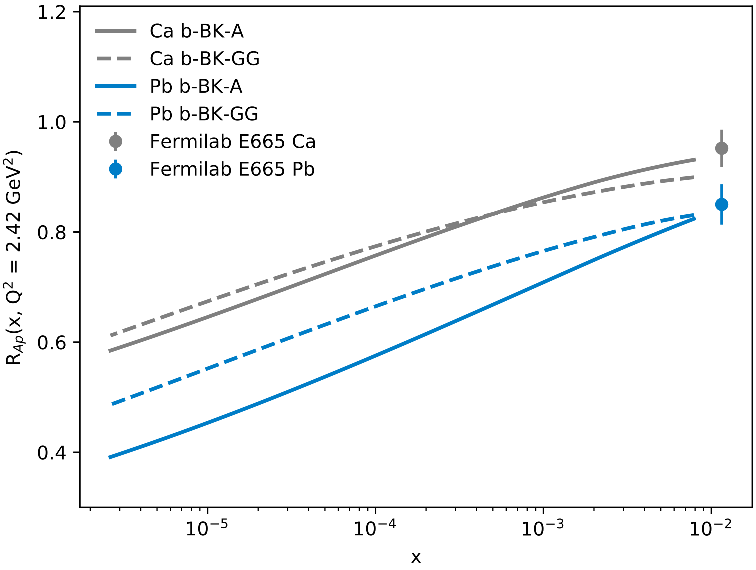

Figure 3.30: Nuclear modification factor at two values of the photon virtuality $Q^2 = 2.42$ GeV^2 as a function of x for Ca and Pb. The predictions are compared with data from [97]. Figure adapted from [35].

vector mesons.

Currently there is no dedicated photon-nucleus collider, but ultra-peripheral

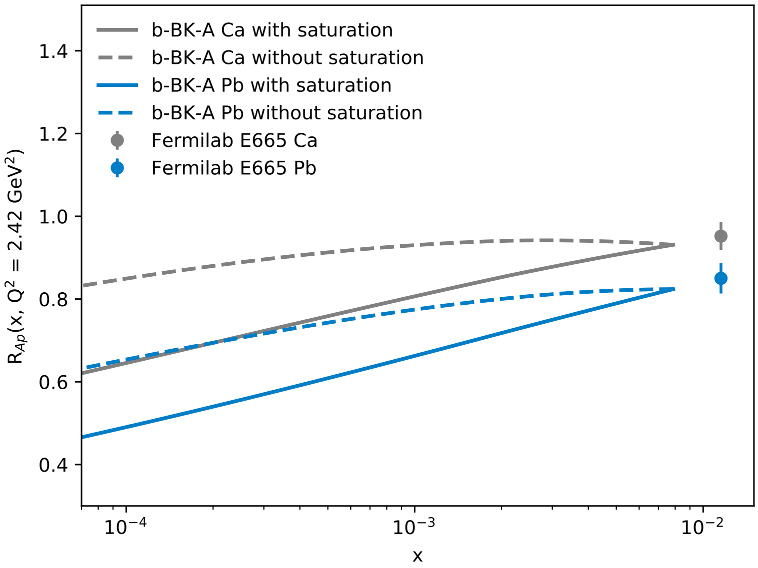

Figure 3.31: Nuclear modification factor computed for Ca and Pb with and without saturation effects for $Q^2 = 2.42$ GeV^2. The predictions are compared with data from [97]. Figure adapted from [98].

collisions [102–105] in a hadron collider offer a possibility to explore this process using the strong electromagnetic field of the circulating ions.

The differential cross section in rapidity for the coherent J/ψ production (at the LHC) reads:

$$\frac{d\sigma}{dy} = n_\gamma(y)\sigma_{\gamma\mathrm{Pb}}(y) + n_\gamma(-y)\sigma_{\gamma\mathrm{Pb}}(-y), \tag{3.48}$$

where the rapidity y of the J/ψ vector meson can be related to the photon-nucleus collision energy $W_{\gamma\mathrm{Pb}}$ by the relation

$$W^2_{\gamma\mathrm{Pb}} = \sqrt{s_{\mathrm{NN}}} M_{\mathrm{J}/\psi} e^{-y}. \tag{3.49}$$

Here $\sqrt{s_{\mathrm{NN}}}$ is the center-of-mass energy of the collision, $M_{\mathrm{J}/\psi}$ is the mass of the J/ψ meson, $\sigma_{\gamma\mathrm{Pb}}(y)$ is the cross section of the virtual photon with a lead nucleus, and the flux of photons $n_\gamma(y)$ that comes from it is computed as described in [106].

Figure 3.33 illustrates this suppression and matches it to data. It shows that the coherent photoproduction of J/ψ in Pb-Pb collisions from the LHC Run 1 strongly favors the b-BK-A approach when confronted with data from ALICE and CMS. As discussed in [99], Run 2 data do not show such a strong favor toward either of the models due to discrepancies between ALICE and LHCb data as well as due to large errorbars on this data. Future experiments should provide us with a clear answer on the validity of the two models and their applicability for phenomenology.

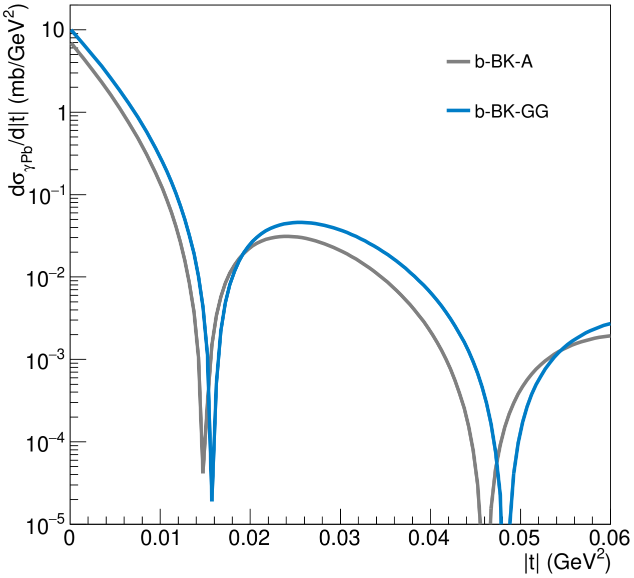

Figure 3.32: Cross section for the coherent photoproduction of a J/ψ vector meson off a Pb target as a function of $|t|$ at a centre-of-mass energy of the γPb system $W_{\gamma\text{Pb}} = 121$ GeV. Figure adapted from [99].

Since a conclusive evidence for the presence of saturation effects in the data has proven to be difficult to obtain due to the fact that we need to probe a region of very low x (high energy of the collision), in the next section an alternative way of getting information about the presence of such phenomena will be discussed with the help of di-jet events in the forward region in rapidity.

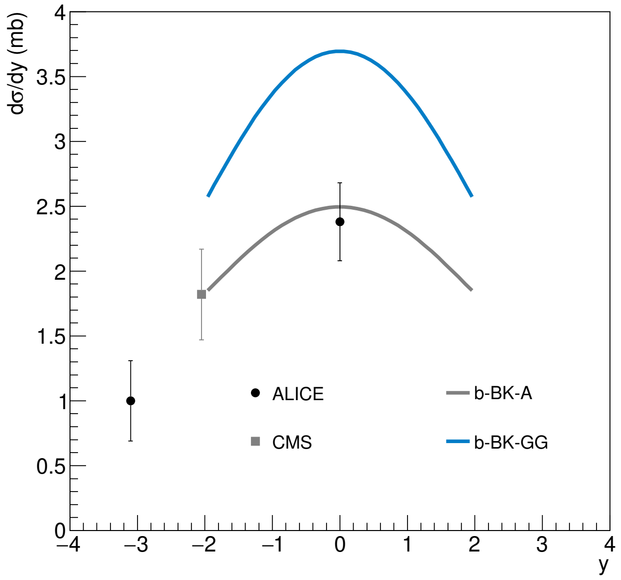

Figure 3.33: Cross section for the coherent photoproduction of a J/ψ vector meson in ultra-peripheral Pb–Pb collisions at $\sqrt{s_{\rm NN}} = 2.76$ TeV corresponding to LHC energies during the the Run 1 period. The predictions are compared with data from the ALICE [102, 103] and CMS [105] collaborations. Figure adapted from [99].

Chapter 4

Saturation

4.1 The origin of saturation and where it is relevant

It is well known that since gluons (unlike photons) carry color charge, they can undergo the process of gluon splitting. This means, that a gluon can—with a certain probability—radiate other gluons. Each of these gluons has smaller energy than their predecessor and each has a probability of further splitting (see Fig. 4.1). This effect then increases the number of partons inside hadrons and nuclei when we move toward regions of smaller x.

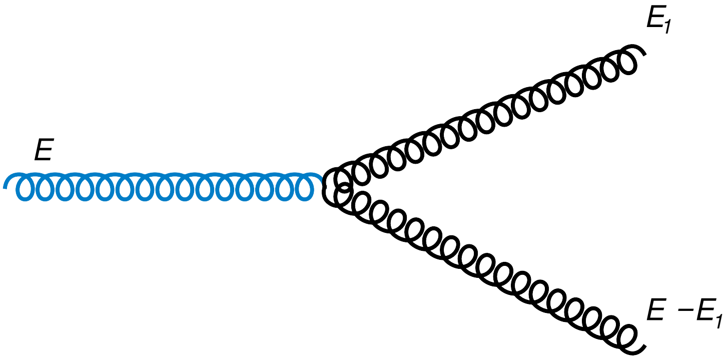

Figure 4.1: A schematic diagram of gluon splitting.

The number of gluons keeps growing until the opposite process (gluon recombination) becomes important. This is a process of two gluons merging into one Fig. 4.2. The resulting gluon has bigger energy, than the two original gluons due to energy conservation and therefore this process reduces the number of gluons with smaller momenta. Gluon recombination becomes more and more probable as there are more gluons in the nucleon and therefore plays a crucial role in the regions of small x. The dynamical balance between gluon splitting and recombination is called saturation.

Models including saturation predict correctly some specific effects, that have been observed in the data. Some of the most convincing results have been obtained at RHIC [107,108] in the forward di-hadron production; these results

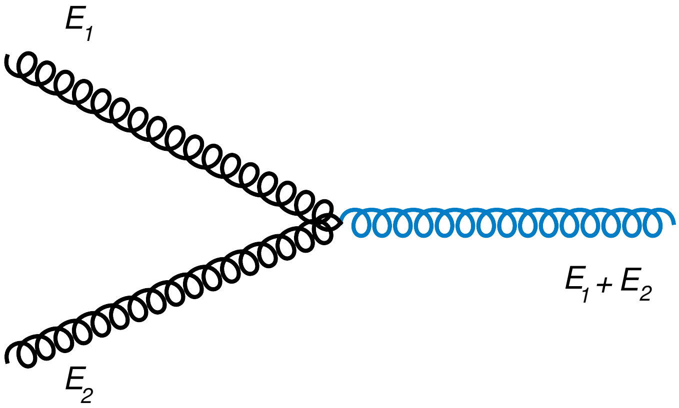

Figure 4.2: A schematic diagram of gluon recombination.

have been adequately described with the use of the Color Glass Condensate (CGC) framework [109–111].

It is very important to understand these observations and to look for other processes, that would verify (or disprove) the existence of saturation effects. This can be challenging, because the suppression in the cross section in the region of low x can be alternatively described by other approaches rather than by saturation and the measurements have not yet been completely decisive.

If we take a look at the parton distribution functions (PDFs), as they were measured at HERA [38], we can see, that the gluon distribution grows as we move toward the region of low x, which is the effect of gluon splitting (see Fig. 4.3).

To search for signatures of saturation effects can be difficult due to the fact, that these become dominant in regions of very low x, beyond the scope of Fig. 4.3 (and possibly of today's accelerators). Reaching lower regions of x would require us to further increase the energy of the interaction (which we are unable to do in an existing collider), go to more forward rapidities or decrease the typical transverse momentum of the process, since [27]

$$x \sim \frac{k_t}{\sqrt{s}}. \tag{4.1}$$

Here k_t is the typical transverse momentum of the considered process and s is the Mandelstamm variable that corresponds to the energy of the collision.

4.2 Saturation scale and its properties

Saturation is typically described by a variable Q_s, the saturation scale. This variable determines the region, where saturation becomes dominant. If we plot a transverse momentum distribution (TMD) $k_t\Phi(x, k_t^2)$ with respect to k_t, saturation scale is the value of transverse momentum where this distribution reaches its maximal value [27] (as can be seen from Fig. 4.4).

The reason, why we chose to plot this distribution multiplied by the transverse momentum is that the TMD would grow indefinitely even if

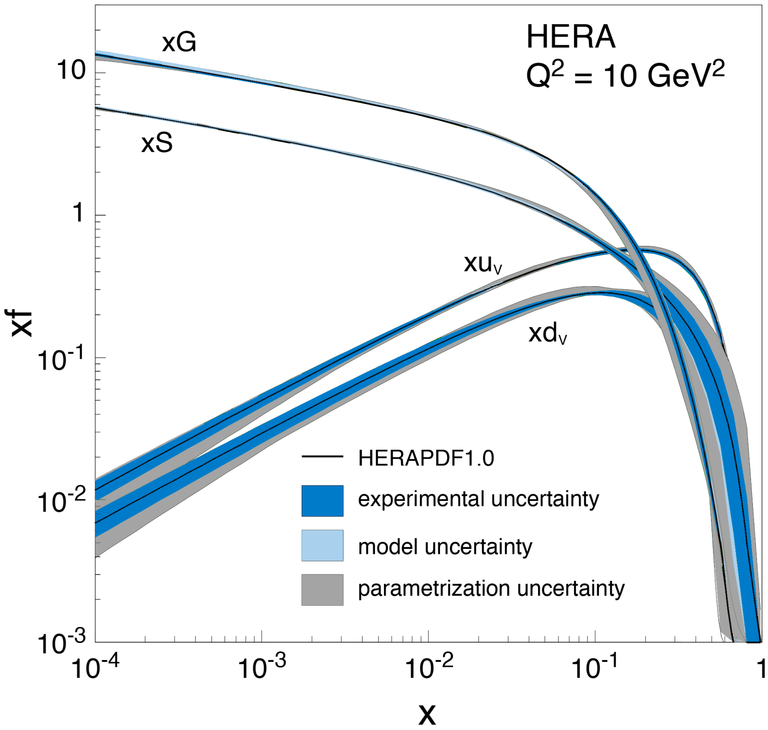

Figure 4.3: Parton Distribution Functions measured at HERA [112] with their uncertainties.

we include the saturation effects into its computation. However, since it would grow logarithmically, after multiplying it with a factor of k_t, the logarithmic increase is suppressed and the distribution decreases at low transverse momenta.

One additional feature of saturation will be used in this chapter, that its effects are stronger in nuclei than in nucleons. The saturation scale of a nucleus Q^2_{sA} is expected to be roughly proportional to that of the proton via

$$Q^2_{sA} \sim A^{1/3} Q^2_{sp} \tag{4.2}$$

due to the Lorentz boost of the system and the overlapping of parton wavefunctions (see Fig. 4.5).

This phenomenon can be used to determine the presence of saturation effects in measurements. If we compare the cross sections for protons and for nuclei, we can observe a suppression in nuclei with respect to those of in protons due to the fact, that in nuclei, the value of saturation scale is greater and therefore saturation processes become dominant sooner. Stronger saturation effects decrease the distribution functions of nuclei faster than those of protons which results in lower cross sections.

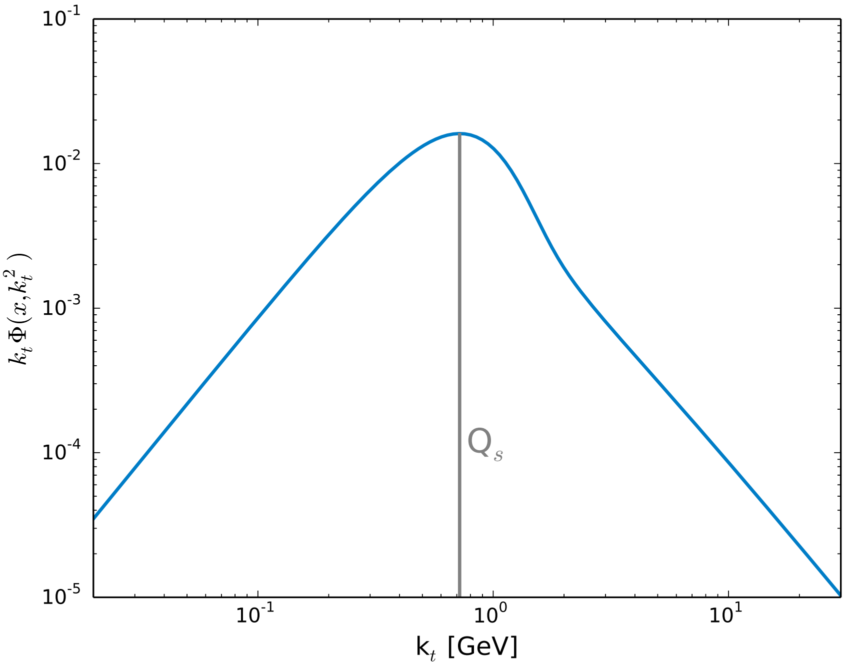

Figure 4.4: Weiszacker-Williams gluon distribution (here as $\Phi(x, k_t^2)$) weighted with momentum k_t with depicted saturation scale as a gray vertical line.

4.3 Dijet production and saturation

The detection of saturation effects in data has proven to be difficult due to the inaccessibility of the region of very low x for processes with a perturbative energy scale. In order to use the previously discussed BK equation and to use its predictions for the detection of saturation, one has to focus on processes that are energetically and kinematically reachable within current experiments. One of such processes, that is both reachable by current measurements and that shows a signature of saturation effects, is the one shown in Fig. 4.6–the production of back-to-back jets in the forward region of rapidity.

We need to focus on back-to-back events due to the fact, that in our collision, we would like to access the region of low-x values as well as be able to detect the outgoing particles with enough precision. Since

$$x \sim \frac{k_t}{\sqrt{s}}, \tag{4.3}$$

the way to reach low values of x is to either increase the energy of the collision or decrease the typical transverse momentum of the considered process. Because we are working with experiments at the frontier of their energy reach, we can increase our reach in x solely by decreasing the typical transverse momentum of the process.

In these dilute-dense collisions, the projectile particle is described by the usual collinear parton distribution functions, that have no transverse

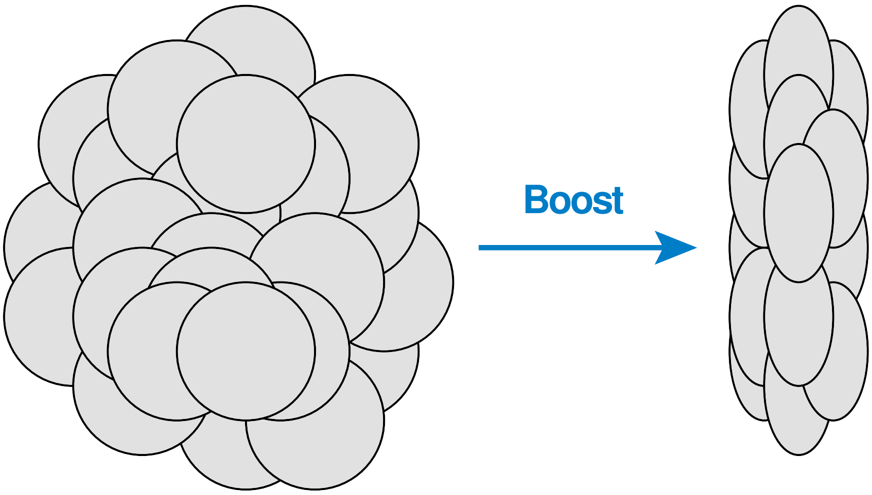

Figure 4.5: Lorentz contraction of the proton enhances the color density and shifts saturation scale to higher values.

momentum dependence. The only transverse momentum, that enters the process is the one carried by the interacting gluon in the target particle, that is described by the TMDs (See Fig.4.6). The outgoing jet pair then carries the total transverse momentum, that this gluon was carrying prior to the collision.

When these two jets are back-to-back (and of the same magnitude) in the transverse momentum plane, their transverse momenta cancel out and the total transverse momentum of the process is small due to the fact that

$$k_t = |\vec{p_{1t}} + \vec{p_{2t}}|, \tag{4.4}$$

where $\vec{p_{1t}}$ and $\vec{p_{2t}}$ are the momenta of the two outgoing jets.

We want to reach low values of k_t of the process with high p_t of the jets, since jets with low p_t are difficult to detect and it is not simple to obtain their corresponding matrix elements. When we have dijet events as in Fig. 4.6, with the jets being back-to-back in the transverse momentum plane, we can fulfill this constraint [27].

Furthermore, we want to reach a region, where x_1 is large (the projectile particle) and x_2 is small (the target particle). $x_2 << 1$ is necessary to detect saturation effects and large x_1 is required because in this region of x, we can use collinear parton distribution functions that are known with great precision from previous experiments to describe the projectile particle. Collisions with such imbalance in x_1 and x_2 are then called dilute-dense collisions. Since [27]

$$\begin{aligned} x_1 &= \frac{1}{\sqrt{s}}\Big(p_{1t}\ e^{y_1} + p_{2t}\ e^{y_2}\Big), \\ x_2 &= \frac{1}{\sqrt{s}}\Big(p_{1t}\ e^{-y_1} + p_{2t}\ e^{-y_2}\Big), \end{aligned} \tag{4.5}$$

we can achieve both conditions by imposing y_1 and y_2 to be large. That is why, to detect saturation effects, we shall focus on back-to-back dijet events

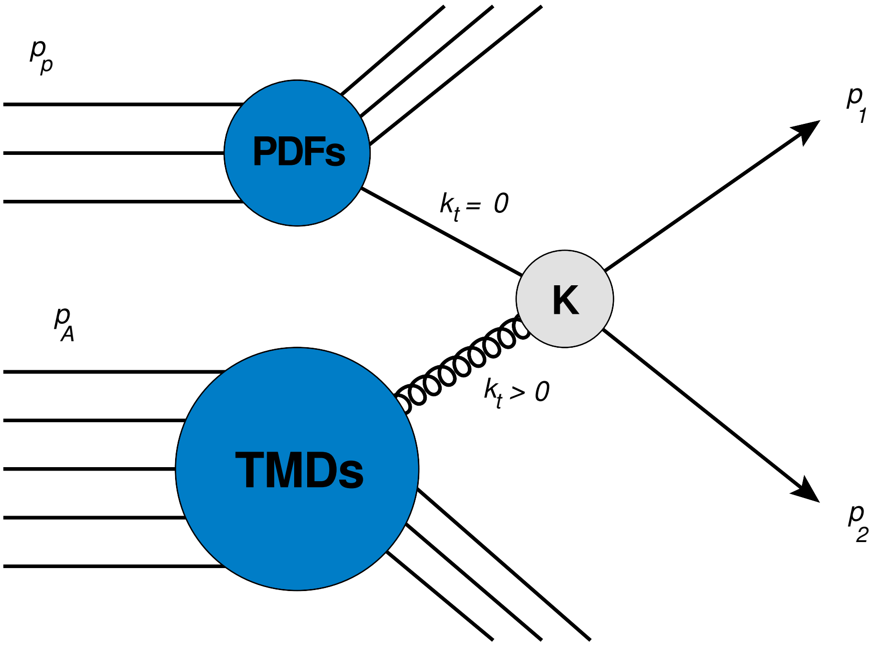

Figure 4.6: A schematic picture of the dilute-dense proton-nucleus collision with dijet production.

in the forward region of rapidity.

4.4 Cross section of dijet events in the factorized scheme

The cross section for the process discussed in Sec. 4.3 can be expressed in the factorized approach as [27]

$$\frac{d\sigma^{pA\to dijets+X}}{d^2P_t d^2k_t dy_1 dy_2} = \frac{\alpha_s^2}{(x_1x_2s)^2} \sum_{a,c,d} x_1 f_{a/p}(x_1) \sum_i \frac{1}{1+\delta_{cd}} K^{(i)}_{ag*\to cd}(P_t,k_t)\Phi^{(i)}_{ag}(x_2,k_t). \tag{4.6}$$

Here x_1 and x_2 correspond to the projectile and target particle respectively, δ_{cd} is a variable, that triggers a combinatorical factor of $1/2$ when the outgoing particles are indistinguishable, s corresponds to the CMS energy of the collision and α_s is the coupling of the interaction. The variable $x_1 f_{a/p}(x_1)$ is the collinear structure function that describes the projectile particle and is obtained from data. $K^{(i)}_{ag*\to cd}(P_t,k_t)$ are the 2 to 2 matrix elements with non-zero k_t computed in [27], that are shown in Tab. 4.1. y_1 and y_2 are the rapidities of the two jets and k_t is the transverse momentum of the jet pair.

i	1	2
$K^{(i)}_{gg^*\to gg}$	$2\frac{(\overline{s}^4+\overline{t}^4+\overline{u}^4)(\overline{u}\hat{u}+\overline{t}\hat{t})}{\overline{t}\hat{t}\overline{u}\hat{u}\overline{s}\hat{s}}$	$-\frac{(\overline{s}^4+\overline{t}^4+\overline{u}^4)(\overline{u}\hat{u}+\overline{t}\hat{t}-\overline{s}\hat{s})}{\overline{t}\hat{t}\overline{u}\hat{u}\overline{s}\hat{s}}$
$K^{(i)}_{gg^*\to q\overline{q}}$	$\frac{1}{2N_c}\frac{(\overline{t}^2+\overline{u}^2)(\overline{u}\hat{u}+\overline{t}\hat{t})}{\hat{t}\hat{u}\overline{s}\hat{s}}$	$\frac{1}{2N_c^3}\frac{(\overline{t}^2+\overline{u}^2)(\overline{u}\hat{u}+\overline{t}\hat{t}-\overline{s}\hat{s})}{\hat{t}\hat{u}\overline{s}\hat{s}}$
$K^{(i)}_{qg^*\to qg}$	$-\frac{\overline{u}(\overline{s}^2+\overline{u}^2)(\overline{u}\hat{u}+\overline{t}\hat{t})}{2\overline{t}\hat{t}\hat{s}}$	$-\frac{\overline{s}(\overline{s}^2+\overline{u}^2)(\overline{u}\hat{u}+\overline{t}\hat{t})}{2\overline{t}\hat{t}\hat{s}}$

Table 4.1: The values of matrix elemets for the forward dijet events.

Here the Mandelstamm variables are computed as

$$\begin{aligned} \hat{s} &= \frac{P_t^2}{z(1-z)}, & \overline{s} &= \frac{P_t^2}{z(1-z)} + k_t^2, \\ \hat{t} &= \frac{-p_{t2}^2}{1-z}, & \overline{t} &= -z\overline{s}, \\ \hat{u} &= \frac{-p_{t1}^2}{z}, & \overline{u} &= -(1-z)\overline{s}, \end{aligned}$$

where

$$\vec{P_t} = \frac{p_2^+\vec{p_1} - p_1^+\vec{p_2}}{p_1^+ + p_2^+}. \tag{4.7}$$

The transverse momentum k_t can be expressed as

$$k_t = \sqrt{p_{t1}^2 + p_{t2}^2 + 2p_{t1}p_{t2}cos(\Delta\phi)}, \tag{4.8}$$

where $\Delta\phi$ is the angle between the two jets in the transverse momentum plane as shown in Fig. 4.7.

Furthermore, z can be expressed as

$$z = \frac{p_{t1}e^{y_1}}{p_{t1}e^{y_1} + p_{t2}e^{y_2}}, \tag{4.9}$$

and p_i^+ as

$$p_i^+ = p_{ti}e^{y_i}/\sqrt{2}. \tag{4.10}$$

The distributions $\Phi_{ag}^{(i)}(x_2, k_t)$ [27] are the TMDs, that can be computed from the BK equation and will be discussed in more detail in Sec 4.6.

With all these ingredients, we can compute the cross section for the production of dijet events in the forward region in rapidity by integrating over the correct part of phase space.

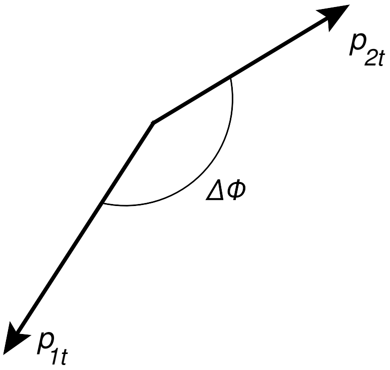

Figure 4.7: Schematic picture of the two outgoing jets in the transverse momentum plane.

4.5 Nuclear modification factor and saturation

The fact that these events are sensitive to saturation effects is however by itself not enough to observe them. In order to detect the presence of saturation effects, we will furthermore exploit the fact, that they are stronger in nuclei than in nucleons [27]. If we take a look at the nuclear modification factor

$$R_{pPb} = \frac{\frac{d\sigma^{p+Pb}}{dO}}{A\frac{d\sigma^{p+p}}{dO}}, \tag{4.11}$$

where O denotes an arbitrary observable sensitive to saturation, we should observe its suppression when the saturation effects become dominant because there will be fewer partons per nucleon available for the interaction in lead than there will be in a proton.

In order to predict the behavior of the nuclear modification factor, one has to compute the cross section both for protons and for nuclei. The sole difference in these two computations lies in the TMDs, since these distributions are used to describe the target.

They are obtained from the BK equation and to distinguish between the computation of lead and protons a different saturation scale in the initial condition was chosen. How to choose the correct value for saturation scale of protons and nuclei, as well as the computation of those TMDs will be discussed more in Sec. 4.6.

If we then plot the nuclear modification factor with respect to the angle $\Delta\phi$, that denotes the angle between the two jets in the transverse momentum plane, we should see a decrease as we approach the region, where $\Delta\phi \sim \pi$ and the two momenta of jets cancel each other out.

This way, we can use the nuclear modification factor to depict the onset of saturation effects in nuclei and to determine their presence in data.

4.6 Transverse momentum distributions in the dipole picture

Now, since we have addressed some of the main features of the BK equation and of the scattering amplitude, we can use these to compute the TMDs, that would be related to the events with a dijet pair at forward rapidity (shown in Fig. 4.6) in order to determine the presence of saturation effects in nuclei as was described in the previous sections.

The following text and numerical solutions will be based on the non-impact-parameter dependent BK equation with the running coupling kernel. We have used numerical solutions of this equation, Fourier-transformed them into momentum space and then convoluted them with themselves to obtain the TMDs relevant for the dijet processes. A similar approach was considered in [27], where analytical solution of the GBW model was used instead of the BK evolution.

Then, the derived hard-process matrix elements have been implemented (Tab. 4.1) and combined with a macro, that uses the data measured at HERA for the description of the projectile particle. In order to be able to predict the onset of saturation effects, we need to carry out this computation for protons and for lead separately to obtain the two cross sections and from them the nuclear modification factor. This modification factor shows the effects of saturation on the dijet events and can be measured experimentally at the LHC.

To start with this computation, first we have to calculate the Fourier transform of the impact-parameter independent scattering amplitude $N(x_2, \vec{r})$ as

$$F(x_2, k_t) = \int \frac{d\vec{r}}{(2\pi)^2} e^{-ik_t \cdot \vec{r}} [1 - N(x_2, \vec{r})]. \tag{4.12}$$

Then, we need to calculate two universal (process independent) unintegrated gluon distributions within the dipole model [27]–the dipole gluon distribution and the Weiszacker-Williams gluon distribution (for more information about the universality of these two distributions see [113]). Fig. 4.8 shows the two distributions and their dependence on k_t at $Y = 0$. These two gluon distributions are given by the following relations

$$x_2 G^{(1)}(x_2, k_t) = \frac{N_c S_\perp}{4\alpha_s \pi^4} \int d^2b \int \frac{d\vec{r}}{\vec{r}^2}\, e^{-ik_t \cdot \vec{r}} \left\{1 - [1 - N(x_2, \vec{r})]^2\right\} \tag{4.13}$$

and

$$x_2 G^{(2)}(x_2, k_t) = \frac{N_c\, k_t^2\, S_\perp}{2\pi^2 \alpha_s} F(x_2, k_t), \tag{4.14}$$

where $S_\perp$ is a constant that describes the transverse size of the proton and is fitted to data. Since in our approach, we are interested in a ratio of two cross sections, this constant cancels out. Then we need to convolute the gluon distributions to obtain the non-universal, process dependent TMDs, that

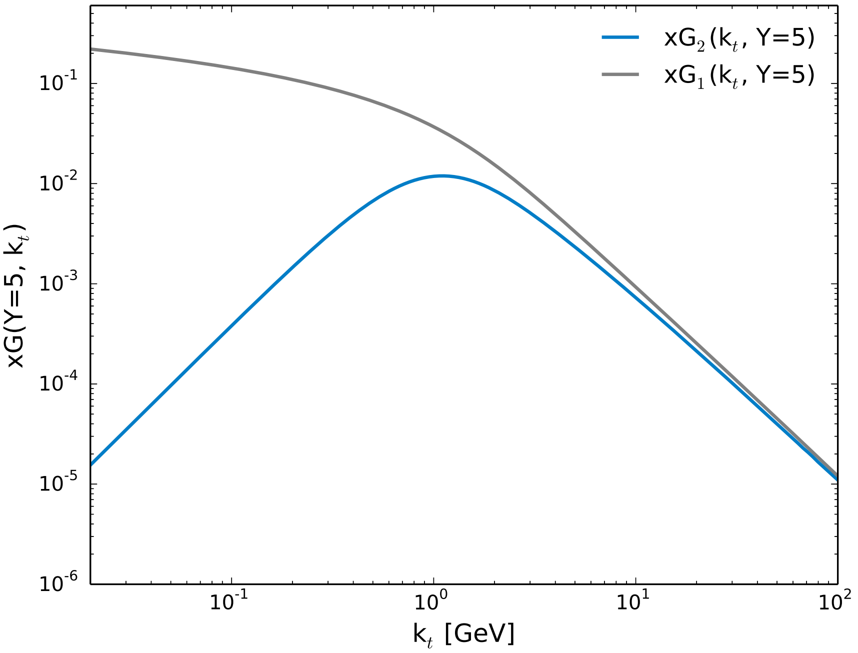

Figure 4.8: The WW (blue) and dipole (gray) gluon distributions computed with the use of the BK equation.

come in the computation of the actual dijet cross section [27]. The resulting TMDs are shown in Fig. 4.9.

$$\begin{aligned}
\mathcal{F}_{qg}^{(1)}(x_2, k_t) &= \frac{N_c\ k_t^2\ S_\perp}{2\pi^2\alpha_s} F(x_2, k_t)\,, && (4.15)\\
\mathcal{F}_{qg}^{(2)}(x_2, k_t) &= \int d^2q_t\, x_2 G^{(1)}(x_2, q_t) F(x_2, k_t - q_t)\,, && (4.16)\\
\mathcal{F}_{gg}^{(1)}(x_2, k_t) &= \int d^2q_t\, x_2 G^{(2)}(x_2, q_t) F(x_2, k_t - q_t)\,, && (4.17)\\
\mathcal{F}_{gg}^{(2)}(x_2, k_t) &= -\int d^2q_t \frac{(k_t - q_t)\cdot q_t}{q_t^2} x_2 G^{(2)}(x_2, q_t) F(x_2, k_t - q_t)\,, && (4.18)\\
\mathcal{F}_{gg}^{(6)}(x_2, k_t) &= && (4.19)\\
& \int d^2q_t d^2q_t'\, x_2 G^{(1)}(x_2, q_t) F(x_2, q_t') F(x_2, k_t - q_t - q_t')\ .
\end{aligned}$$

The last step then is to redefine the TMDs in the limit of high number of

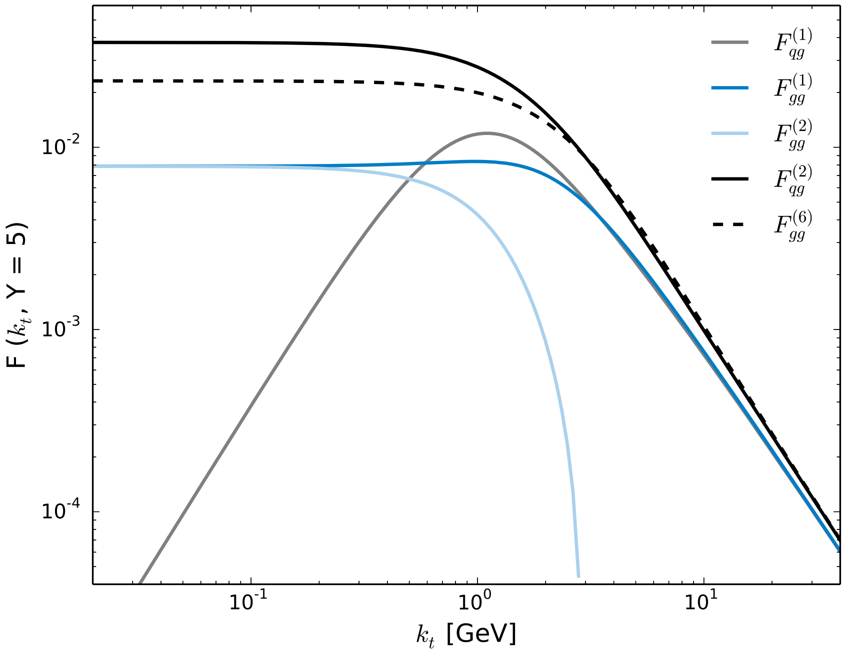

Figure 4.9: The non-universal TMDs that contribute to the dijet production in the forward region in rapidity.

colors, so that they correspond to the considered matrix elements as [27]

$$\Phi^{(1)}_{qg\to qg} = \mathcal{F}^{(1)}_{qg}\,, \tag{4.20}$$

$$\Phi^{(1)}_{gg\to\bar{q}q} = \mathcal{F}^{(1)}_{gg}\,, \tag{4.21}$$

$$\Phi^{(1)}_{gg\to gg} = \frac{1}{2}(\mathcal{F}^{(1)}_{gg} + \mathcal{F}^{(6)}_{gg})\,, \tag{4.22}$$

$$\Phi^{(2)}_{qg\to qg} = \mathcal{F}^{(2)}_{qg}\,, \tag{4.23}$$

$$\Phi^{(2)}_{gg\to q\bar{q}} = -N_c^2\mathcal{F}^{(2)}_{gg}\,, \tag{4.24}$$

$$\Phi^{(2)}_{gg\to gg} = \mathcal{F}^{(2)}_{gg} + \mathcal{F}^{(6)}_{gg}\,. \tag{4.25}$$

Since the scattering amplitude that is the starting ingredient in this computation does not have an analytic solution, we have to compute its value on a predetermined grid via numerical methods [47, 64, 68, 71]. Then we have to use similar methods for the computation of the WW and dipole gluon distributions and finally for the convolution to obtain the TMDs. These TMDs are the ones that contain the information about the saturation effects, since the parton distribution, that was used to describe the projectile particle is probed at much higher values of x, where these effects are negligible.

The TMDs shown in Fig. 4.9 represent the non-universal distributions, that enter the calculation of the cross section for dijet events in the forward region in rapidity, that we have mentioned in previous sections.

These distributions enable us to calculate the cross section for protons. To compute the TMDs for lead, we need to compute the scattering amplitude for the interaction of dipoles and lead. In order to do this, one has to change the value of the saturation scale Q_{s0}^2 in the initial conditions of BK equation (in the impact parameter independent framework).

The value of the saturation scale for protons was obtained from a fit to single-hadron production as $Q_{s0p}^2 = 0.2\,\mathrm{GeV}^2$ [114]. For nuclei, this value was obtained from a fit to minimum-bias d+Au data at RHIC. The fit resulted in the value of $0.4\,\mathrm{GeV}^2$ and to obtain the saturation scale for central collisions for nuclei, the Woods-Saxon distribution was assumed, which predicted a factor of 1.5 with respect to the minimum-bias events. The saturation scale for lead then was determined to be $Q_{s0Pb}^2 = 0.6\,\mathrm{GeV}^2$ [114].

With this setup, we can compute the cross section for dijet events for both p-p collisions as well as for p-Pb collisions, which enables us to compute the nuclear modification factor (NMF) for this interaction.

4.7 Dijet events in the forward region in rapidity

With the use of the TMDs calculated in Sec. 4.6, we can calculate the cross section for dijet events, that would show a signature of saturation effects which we would like to study. We have used the formula (4.6) for the computation of the factorized cross section for the process shown in Fig. 4.6.

The kinematic region, that was considered for our computation was $y_1, y_2 \in [3.4, 4.5]$ (since we have imposed the condition of forward rapidity for both jets because of our constraints on x_1 and x_2) and $p_{t1}, p_{t2} > 20\,\mathrm{GeV}$. This kinematic region could be experimentally covered by the CMS or ATLAS experiments at the LHC.

Since we are interested in the ratio of the two cross sections, the running coupling cancels out in Eq. (4.6). As was mentioned before, x_1 and x_2 correspond to the projectile and target particle respectively and s is the energy of the collision.

$x_1 f_{a/p}(x_1)$ is the parton distribution function obtained from data measured at the HERA experiment. We use the MSTW data set at leading order from the year 2008 (MSTW2008lo90cl) to describe the projectile particle.

$K_{ag*\to cd}^{(i)}(P_t, k_t)$ are the 2 to 2 matrix elements with non-zero k_t computed in [27] and $\Phi_{ag}^{(i)}(x_2, k_t)$ [27] are the TMDs computed in the previous section.

The nuclear modification factor was then computed as a ratio of the cross section for proton and for lead. The difference between the two is that the impact-parameter-independent initial condition (3.10), that goes to the computation of the BK equation was used with the value of saturation scale of $0.6\,\mathrm{GeV}^2$ for lead and $0.2\,\mathrm{GeV}^2$ for proton, as was discussed in the previous section. These two initial conditions were then evolved, Fourier-transformed, convoluted and used to obtain the two cross sections.

In order to normalize the two processes to take multiplicity into an account, the asymptotic equivalence of the two cross sections was assumed in the region of large k_t. If we take the limit of the NMF for the MV model, we find out that this normalization reduces to a factor of Q^2_{s0p}/Q^2_{s0n}, see Appendix B in [27], which for our case is 1/3. After including this last piece, we can calculate the NMF prediction from the BK equation and the dipole model.

The NMF never completely reaches unity even at large k_t in our prediction. This is given by the fact, that evolution to higher values of rapidity spoils the originally assumed normalization of 1/3, that was carried out at Y=0.

The resulting nuclear modification factor is shown in Fig. 4.10, and we can see, that it is suppressed when the two jets become back-to-back in the transverse momentum region, which is a signature of the saturation effects since as we move towards the region of back-to-back jets, the two momenta cancel each other out and the total transverse momentum of the jet pair is comparable to the saturation scale of lead

$$k_t \sim Q_{sPb}. \tag{4.26}$$

This approach produces results completely different from those of the nuclear distribution functions approach because these do not include the k_t dependence and therefore, in this approach all regions of the angle between the two jets in the transverse momentum plane (denoted as $\Delta\phi$) would show the NMF to be at unity (Fig. 4.10 - grey line).

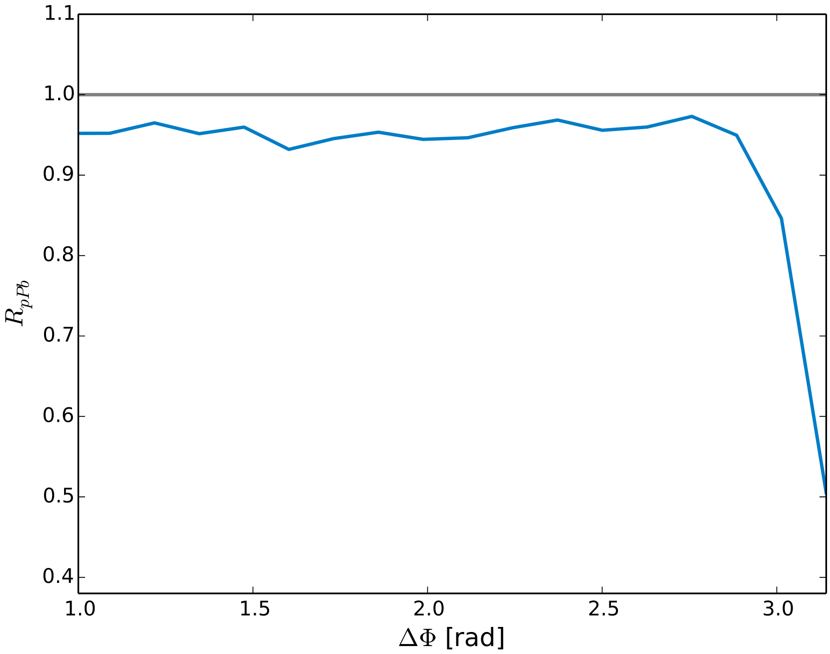

Figure 4.10: Nuclear modification factor as a function of the angle between the two outgoing jets in the transverse momentum plane. The gray line represents the results, that would be seen in the nuclear PDFs approach and the suppression at $\Delta\Phi \sim \pi$ is due to saturation effects in nuclei.

Chapter 5

Summary

Quantum chromodynamics (QCD) is a fundamental theory describing the strong interaction within the framework of a relativistic quantum field theory. It allows us to compute particle-particle interactions in the high-energy limit, where we can make use of the fact that strong coupling decreases at large scales of the processes. Then we can expand the amplitudes we are computing into a perturbative power-series and omit the higher-order terms. In order to obtain predictions for objects more complicated than single particles, we need to build models that simplify the situation and allow us to use the information about single-particle interaction to build complex structures.

One of these models is the so-called dipole model which together with the BK equation allows us to compute the gluonic structure of protons and nuclei and compare them with various experimentally measurable processes such as DIS, diffractive vector meson production, and dijet production at forward rapidities.

This work presents a review of the color dipole formalism used for the evolution equations in QCD starting with a brief review of the DIS process, parton model and then how some observables-of-interest can be expressed in terms of color dipole variables (e.g. the scattering amplitude). Then we have shown how the BK equation can be used to compute these observables within such framework in the impact parameter-independent approach. We have shown how the impact parameter dependence introduces the non-perturbative effects into the scattering amplitude resulting in a growth of the scattering amplitude at the large-b region (the so-called Coulomb tails). We have linked this growth with the emissions of large daughter dipoles and showed two approaches to taming this growth.

1. Introducing a mass-dependent cut-off into the kernel of the equation that stops the evolution for large daughter dipoles.

2. Using a collinearly improved kernel for the evolution that suppresses the emission of large daughter dipoles due to built-in lifetime ordering of the subsequent dipoles.

We have explored the second approach in greater detail and matched its solutions to data in order to test the validity of the assumption that the

Coulomb tails are suppressed to such extent that the description of data is restored.

We have then used this approach to obtain predictions for nuclear targets and to compute the nuclear shadowing effects arising from the non-linear BK evolution. We have also explained how the BK evolution incorporates saturation effects, and how these can be studied with the use of dijet events in the forward region in rapidity. We have obtained predictions for these events in the impact-parameter independent framework for both protons and lead as targets and computed the nuclear modification factor, that shows a significant suppression due to saturation effects when the two jets become back-to-back and the typical transverse momentum of the process decreases low enough so that we reach the saturation region.

The works [33] and [34] study the collinearly improved resummation for the BK equation and how it suppresses the emissions of large daughter dipoles (due to the life-time ordering imposed by this resummation). In these papers we study the suppression of the Coulomb tails and how it affects the predictive powers of this equation. We show that with this approach a successful description of DIS data as well as of vector meson photoproduction cross sections is achieved.

In works [35], [99], and [98], we have shown how to generalize this equation to describe nuclear targets, proposed a new family of initial conditions and then produced solutions, that were successfully compared to existing data as well as used for obtaining predictions for future measurements.

Work [115] is dedicated to the dijet events in the forward region in rapidity and how the information about the presence of saturation effects can be accessed through this channel, where we can access low-values of x while still being able to measure these events by current experiments.

Chapter 6

Published results

6.1 List of Publications

Original articles and letters submitted to impacted journals

1. Albacete, J. L., Giacalone, G., Marquet, C. and Matas, M. (2019). “Forward di-hadron back-to-back correlations in p-A collisions”. In:Phys. Rev.D99.1,p. 014002.doi:10.1103/ PhysRevD.99.014002. arXiv:1805.05711 [hep-ph].

2. Bendova, D., Cepila, J., Contreras, J. G. and Matas, M. (2019). “Solution to the Balitsky-Kovchegov equation with the collinearly improved kernel including impact-parameter dependence”. In:Phys. Rev.D100.5,p. 054015.doi:10.1103/ PhysRevD. 100.054015. arXiv:1907.12123 [hep-ph].

3. Cepila, J., Contreras, J. G. and Matas, M. (2019). “Collinearly improved kernel suppresses Coulomb tails in the impact- parameter dependent Balitsky-Kovchegov evolution”. In:Phys. Rev.D99.5, p. 051502.doi: 10.1103/ PhysRevD.99.051502. arXiv:1812.02548 [hep-ph].

4. Bendova, D., Cepila, J., Contreras, J. G. and Matas, M. (2020). “Predictions for nuclear structure functions from the impact-parameter dependent Balitsky-Kovchegov equation”. arXiv:2002.11056 [hep-ph].

5. Bendova, D., Cepila, J., Contreras, J. G. and Matas, M. (2020). “Photonuclear J/ψ production at the LHC: proton-based versus nuclear dipole scattering amplitudes”. arXiv:2006.12980 [hep-ph].

6. Cepila, J. and Matas, M. (2020). “Contribution of the non-linear term in the Balitsky-Kovchegov equation to the nuclear structure functions”. arXiv:2006.16136 [hep-ph].

Proceedings from conferences

1. Cepila, J., Contreras, J. G. and Matas, M. (2016). “Numerical precision of the solution to the running-coupling Balitsky-Kovchegov equation”. In:EPJ WebConf.112, p.02008.doi:10.1051/epjconf/ 201611202008.
2. Matas, M. and Marquet, C. (2018). “Forward di-jets in p+A collisions in the ITMD framework”. In:PoS DIS2018,p. 055.doi:10.22323.
3. Cepila, J., Contreras, J. G. and Matas, M. (2019). “Collinearly improved impact-parameter dependent Balitsky-Kovchegov evolution”. In:PoS DIS2019, p. 255. doi:10.22323/ 1.352.0255.
4. Bendova, D., Cepila, J., Contreras, J. G. and Matas, M. (2020). “Collineraly improved Balitsky-Kovchegov evolution and its suppression of the large-impact-parameter Coulomb tails”. PoS(LC2019)064.

PHYSICAL REVIEW D **99,** 051502(R) (2019)

Rapid Communications

Collinearly improved kernel suppresses Coulomb tails in the impact-parameter dependent Balitsky-Kovchegov evolution

J. Cepila, J. G. Contreras, and M. Matas

Faculty of Nuclear Sciences and Physical Engineering, Czech Technical University in Prague, Czech Republic

(Received 10 December 2018; published 29 March 2019)

We solved the impact-parameter dependent Balitsky-Kovchegov equation with the recently proposed collinearly improved kernel. We find that the solutions do not present the Coulomb tails that have affected previous studies. We also show that once choosing an adequate initial condition it is possible to obtain a reasonable description of HERA data on the structure function of the proton, as well as on the cross section for the exclusive production of a J/ψ vector meson off proton targets. As a further application of the solutions, we computed the impact-parameter dependent Weizsäcker-Williams gluon distribution.

DOI: 10.1103/PhysRevD.99.051502

I. INTRODUCTION

The high-energy, or equivalently small Bjorken-x, limit of perturbative quantum chromodynamics (pQCD) has received significant attention in recent years. From the experimental side, this has been driven by the precise measurements from HERA [1], the large kinematic reach of the LHC [2], and the proposal of new electron-ion facilities [3,4]. In particular, the precise measurement of the $F_2(x, Q^2)$ structure function of the proton at HERA and its interpretation within pQCD [5,6] shows that the gluon distribution grows rapidly with decreasing x for a fixed Q^2, where x is fractional momentum of the struck parton and Q^2 is the negative squared four-momentum transferred between the lepton and the nucleon. This growth has to be tamed at some high energy in order to respect unitarity.

In this limit, integro-differential equations are a powerful tool to compute and predict observables related to the dynamics of pQCD where the nonperturbative contributions are typically incorporated into an initial condition. In the seminal work [7], it was shown that the inclusion of a nonlinear term in these so-called evolution equations would limit the growth of the gluon distribution, a phenomenon known as saturation, see e.g., [8] and references therein. In this context, the Balitsky-Kovchegov (BK) equation [9,10] has been quite successful for phenomenological studies. This equation was derived independently in the formalism of the operator product expansion in [9] and within the dipole approach in [11,12]. It can also be obtained within the color glass condensate model as a limit of the so-called Jalilian-Marian-Iancu-McLerran-Weigert-Leonidov-Kovner (JIMWLK) equation [10,13–18].

The BK equation describes the evolution with rapidity, Y, of the dipole-target scattering amplitude, $N(\vec{r}, \vec{b}, Y)$, where $\vec{r}$ is the transverse size of the dipole, $\vec{b}$ the impact parameter, and $Y = \ln(x_0/x)$ with x_0 being the x value at the start of the evolution. Solutions obtained under the assumption that there is no dependence on the impact parameter describe quite well the $F_2(x, Q^2)$ data [19]. This equation has also been solved including the impact parameter dependence [20,21], where it was found out that the solutions acquired a so-called Coulomb tail, meaning that the contribution at large impact parameters grew too fast. This behavior was curbed by introducing an extra term to the kernel; furthermore, it was necessary to include an extra, so-called *soft*, contribution in order to describe $F_2(x, Q^2)$ data [22]. With this approach it was also possible to describe the exclusive production of vector mesons in deeply inelastic scattering [23]. These studies were based on a BK equation with a kernel including running coupling corrections [24,25]. Recently, a new kernel including collinear corrections was proposed and shown to describe correctly HERA data on $F_2(x, Q^2)$ in an impact-parameter independent BK equation [26,27].

In this work we study the BK equation including the dependence on the impact parameter using the collinearly improved kernel. We find that the Coulomb tails are strongly suppressed with respect to the running coupling case. Furthermore, we show that when using an appropriate initial condition a good description of experimental data is directly obtained; that is, without having to modify the kernel nor having to add extra soft contributions.

The improved treatment of the impact parameter dependence provides a new tool for phenomenology. This tool is

---

particularly important for the EIC facilities being currently under design and which have as one of their main goals a tomographic study of the structure of nucleons and nuclei [3,4].

II. THE BALITSKY-KOVCHEGOV EQUATION

We assume a rotational symmetry of the target which implies that the scattering amplitude depends on the magnitude of the impact parameter, b, but not on its orientation. Furthermore, we assume the scattering amplitude to be independent of the angle between the vectors $\vec{r}$ and $\vec{b}$. In this case, the BK equation reads

$$\begin{aligned}\frac{\partial N(r,b,Y)}{\partial Y} = \int d\vec{r_1} K(r,r_1,r_2)(N(r_1,b_1,Y)\\ + N(r_2,b_2,Y) - N(r,b,Y)\\ - N(r_1,b_1,Y)N(r_2,b_2,Y)),\end{aligned} \tag{1}$$

where $\vec{r_2} = \vec{r} - \vec{r_1}$, $|\vec{r}| \equiv r$ with similar definitions for r_1 and r_2, while b_1 and b_2 are the magnitudes of the impact parameters of the respective dipoles. The collinearly improved kernel [26–28] is given by

$$K(r,r_1,r_2) = \frac{\bar{\alpha}_s}{2\pi}\frac{r^2}{r_1^2 r_2^2}\left[\frac{r^2}{\min(r_1^2,r_2^2)}\right]^{\pm\bar{\alpha}_s A_1}\frac{J_1(2\sqrt{\bar{\alpha}_s\rho^2})}{\sqrt{\bar{\alpha}_s\rho}}. \tag{2}$$

It constitutes of four factors. The factors $\bar{\alpha}_s/2\pi$ and $r^2/r_1^2 r_2^2$ are present already at the LO, the factor in square brackets represents the contribution of single collinear logarithms and factor $J_1(2\sqrt{\bar{\alpha}_s\rho^2})/\sqrt{\bar{\alpha}_s\rho}$ resums double collinear logarithms to all orders. Parameter $A_1 = 11/12$ and the sign in the third factor is positive when $r^2 < \min(r_1^2, r_2^2)$ and negative otherwise. J_1 is the Bessel function, $\rho \equiv \sqrt{L_{r_1 r} L_{r_2 r}}$ and $L_{r_i r} \equiv \ln(r_i^2/r^2)$. For the running coupling, $\bar{\alpha}_s \equiv \alpha_s N_c/\pi$ with N_c the number of colors, we use the smallest dipole prescription: $\alpha_s = \alpha_s(r_{\min})$, where $r_{\min} = \min(r_1, r_2, r)$. This prescription has been used in previous studies, where it was compared to other prescriptions at a phenomenological level [27]; it has also been advocated to be the correct prescription for the BK equation at next-to-leading order (NLO) [29].

To be consistent with the computations leading to the BK equation the form of the running coupling is given by

$$\alpha_s(r) = \frac{4\pi}{\beta_{0,n_f}\ln(\frac{4C^2}{r^2\Lambda_{n_f}^2})}, \tag{3}$$

where n_f denotes the number of flavors that are active at the scale r and β_{0,n_f} is the leading order coefficient of the QCD beta-series. The value of $\Lambda_{n_f}^2$ depends on the number of active flavors and was computed in the same manner as in [19]. Two parameters control the infrared behavior of α_s: α_{fr} and C^2. For very large dipoles the perturbative form of α_s given by Eq. (3) is not anymore valid. Following the procedure used in previous studies [19] (see also discussion in Sec II. C of [30]) we freeze the value of α_s to $\alpha_{fr} = 1.0$ for all dipole sizes that would produce a larger value of α_s when using Eq. (3). This is a purely phenomenological approach, which roughly describes the behavior found in more theoretical studies of α_s in the nonperturbative regime [31,32]. Finally, the parameter C^2 also contributes to regulate the infrared behavior and takes into account the potential effect of the approximations made when computing the Fourier transform to coordinate space [29,33].

III. SOLVING THE BK EQUATION

For the initial condition we use a combination of the Golec-Biernat and Wusthoff (GBW) model [34] for the dependence on the dipole size r and a Gaussian distribution for the impact parameter dependence. A similar approach has been considered in [35]. We use the following functional form

$$N(r,b,Y=0) = 1 - \exp\left(-\frac{1}{2}\frac{Q_s^2}{4}r^2 T(b_{q_1}, b_{q_2})\right), \tag{4}$$

where b_{q_i} are the impact parameters of the quark and antiquark forming the dipole and

$$T(b_{q_1}, b_{q_2}) = \left[\exp\left(-\frac{b_{q_1}^2}{2B}\right) + \exp\left(-\frac{b_{q_2}^2}{2B}\right)\right]. \tag{5}$$

Both Q_s^2 and B are parameters to be adjusted. These parameters have a clear interpretation: the scale at which nonlinear effects become important, known as the saturation scale, is given by Q_s^2; while B is related to the effective radius of the Gaussian distribution in impact parameter space that represents the target profile by $2B = \langle b^2 \rangle$. $T(b_{q_1}, b_{q_2})$ suppresses contributions from dipoles that are large with respect to the size of the target. Such suppression of large dipole sizes, which makes sense from the phenomenological point of view, has also been used in previous approaches [22] in order to describe the data.

Parameter B was chosen to obtain a reasonable description of the cross section for J/ψ photoproduction off protons as a function of $|t|$ ($-t$ is the square of the momentum transferred at the proton vertex) at a fixed center-of-mass energy of the photon–proton system ($W = 100$ GeV), while Q_s^2 was simultaneously chosen to describe $F_2(x, Q^2)$ data at $x_0 = 0.008$ and $Q^2 \in (3.5, 27)$ GeV^2. That is, the fixing of Q_s^2 does not involve an evolution in Y, while that of B requires evolving the dipole scattering amplitude to $x \approx 0.001$. (This value is obtained from $x = (M_{J/\psi}/W)^2$ where $M_{J/\psi}$ is the mass of the J/ψ). These two conditions uniquely fix the value of these two parameters, since the structure function

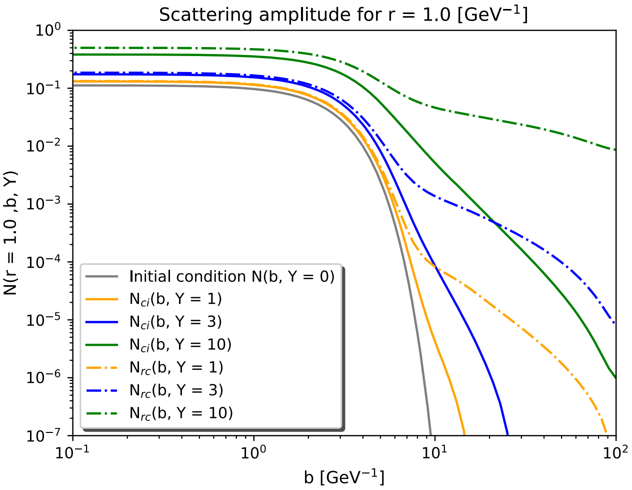

FIG. 1. Dependence of the dipole scattering amplitude with respect to the impact parameter at different rapidities for a dipole of size $r = 1$ GeV^{-1}. The dashed-dotted lines represent solutions obtained with the running-coupling kernel (N_{rc}), while solid lines represent solutions with the collinearly improved kernel (N_{ci}).

is sensitive to an overall integral of the scattering amplitude and vector meson production is sensitive to the b-dependence of it. The values we use in the following are $Q_s^2 = 0.49$ GeV^2 and $B = 3.22$ GeV^{-2}. The value of C^2 used in the computation of $\alpha_s(r)$ was chosen to regulate the evolution speed of the dipole scattering amplitude and set to $C = 9$.

The BK equation is solved numerically using the Runge-Kutta method of order four with the algorithm described in [36,37], extended to include the b-dependence. The grids in $\log_{10}(r)$ and $\log_{10}(b)$ are of the same size and cover the range from 10^{-7} to 10^2 1/GeV for both r and b. A linear interpolation in $\log_{10}(r)$ and $\log_{10}(b)$ is used to find the value of the dipole scattering amplitude outside the points in the grids. The step in rapidity was 0.01. The integrals are performed with the Simpson method.

Using the procedure just described we obtained the solutions presented in Fig. 1, which shows the impact-parameter dependence of the dipole scattering amplitude for a dipole of size $r = 1$ GeV^{-1} at different rapidities for two computations: using the collinearly improved or the running-coupling kernel. In both cases we use the same initial condition.

We show results for rapidities which are relevant for phenomenology at current and planned facilities, but have checked that such a behavior is still present even at $Y = 10$, which is beyond the reach of foreseeable accelerators. The evaluation of $\alpha_s(r)$ for the running coupling case is done as in [19]. Figure 1 shows that the Coulomb tails are strongly suppressed when using the collinearly improved kernel. A similar pattern is observed for all dipole sizes. The suppression of the amplitude at large values of b observed when using the collinearly improved kernel instead of the running coupling kernel is due to two reasons: (i) the different treatment of the $r^2/r_1^2 r_2^2$ factor, which in the running coupling kernel appears accompanied by other additive terms, and (ii) the new corrections introduced in the collinearly improved kernel. When comparing the original LO with the collinearly improved kernel, there are three factors contributing to the suppression: the use of a running coupling constant instead of a fixed α_s, the contribution of single collinear logarithms, and the resummation of double collinear logarithms. This last term is numerically the most important. A detailed discussion of the properties of the solutions found with our approach is outside the scope of this work and will be presented elsewhere [38].

IV. APPLICATIONS

As a first use of the solutions to the b-dependent BK equation we compute the $F_2(x, Q^2)$ structure function and compare the result with HERA data. In the dipole model the structure function is related to the dipole scattering amplitude by

$$F_2(x, Q^2) = \frac{Q^2}{4\pi^2 \alpha_{\mathrm{em}}} \sum_f \int \mathrm{d}\vec{r}\mathrm{d}\vec{b}\mathrm{d}z \times |\Psi^f_{T,L}(z, \vec{r})|^2 \frac{\mathrm{d}\sigma^{q\bar{q}}(\vec{r}, x_f)}{\mathrm{d}\vec{b}}, \tag{6}$$

where α_{em} is the electromagnetic coupling constant, $\Psi^f_{T,L}(z, \vec{r})$ is the convolution of the wave functions for a photon to split into a quark-antiquark dipole of flavor f and for the dipole to return to the photon state—see e.g., [39] for a detailed discussion—z is the fraction of the dipole energy carried by the quark, and the cross section is related to the dipole scattering amplitude by

$$\frac{\mathrm{d}\sigma^{q\bar{q}}(\vec{r}, x)}{\mathrm{d}\vec{b}} = 2N(\vec{r}, \vec{b}, x). \tag{7}$$

As it is customary, we use $x_f = x(1 + (4m_f^2)/Q^2)$ with m_f an effective quark mass set to 100 MeV/c^2 for light quarks. The description of data shown below does not depend strongly on the value of m_f and remains the same if a value of 10 MeV/c^2 is used. Similar observations were made in [27]. In the future, it would be interesting to match this prescription with a more formal description of dressed quarks as e.g., in [40]. Mass of the charm quark was fixed to 1.3 GeV/c^2; these values are the same as used in [27].

Figure 2 shows the comparison of the computation with the measured data [5] for several different values of Q^2 as a function of x. The average percentile difference between data and theory is 3.7% for data with $Q^2 \in [3.5, 35]$ GeV^2. We would like to emphasize that this level of agreement was obtained without the need to include *ad hoc* corrections to the kernel and without the addition of soft contributions.

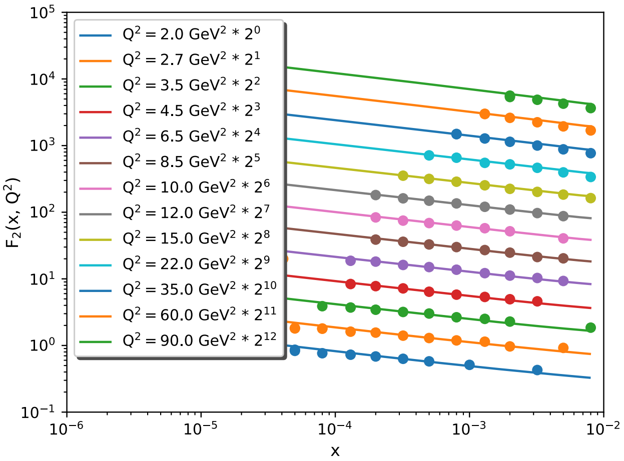

FIG. 2. Comparison of the structure function data from HERA [5] with the computation based on solutions to the collinearly improved b-dependent BK equation.

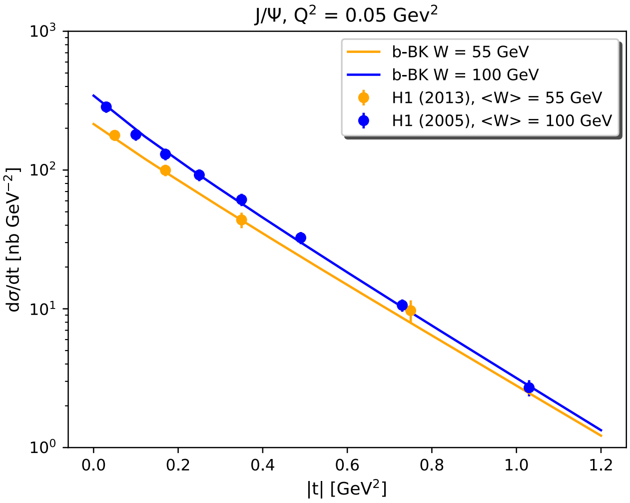

FIG. 3. Comparison of the computation for the $|t|$ dependence of the cross section for the exclusive photoproduction of J/ψ vector mesons off protons with data from the H1 Collaboration at HERA at $\langle W\rangle = 55$ GeV [44] and $\langle W\rangle = 100$ GeV [45].

As a further application we computed the $|t|$ dependence of cross section for the exclusive photoproduction of J/ψ vector mesons off protons at fixed values of W. The amplitude for this process is given by (see e.g., [39])

$$A(x, Q^2, \vec{\Delta})_{T,L} = i \int \mathrm{d}\vec{r} \int_0^1 \frac{\mathrm{d}z}{4\pi} (\Psi^* \Psi_{J/\psi})_{T,L} \times \int \mathrm{d}\vec{b} e^{-i(\vec{b}-(1-z)\vec{r})\cdot\vec{\Delta}} \frac{\mathrm{d}\sigma^{q\bar{q}}}{\mathrm{d}\vec{b}}, \quad (8)$$

where $-t \equiv \vec{\Delta}^2$, T and L represent transverse and longitudinal photons, respectively, and $\Psi_{J/\psi}$ is the wave function of the transition from the dipole into a J/ψ vector meson. We use the boosted Gaussian wave functions [41,42] with parameters as determined in [39].

The $|t|$-differential cross section is given by the square of the amplitude divided by 16π. The contributions from the longitudinal and transverse photons are added. As it is customary (see discussion in Sec. III of [39]), we correct the cross section for two effects: (i) to take into account the contribution of the real part of the dipole scattering amplitude that was not considered when deriving the form of the amplitude in Eq. (8), and (ii) the fact that in a two-gluon exchange the gluons have different momentum, which is known as the skewedness correction [43]. The correction has been computed using the derivative of the amplitude as in [39]. The correction in this context has to be understood as a phenomenological ingredient that contributes up to a value of 30% to the total cross section.

The comparison of the computation with data from the H1 Collaboration [44,45] is shown in Fig. 3. Note that the data at $\langle W\rangle = 100$ GeV were used to set the value of the parameter B, but the computation for $W = 50$ GeV is a prediction. The agreement is at the level of 10%.

As a final application of the dipole scattering amplitude solutions to the b-dependent BK equation with the collinearly improved kernel we turn to TMD (transverse momentum dependent) distributions. The measurement of these distributions is one of the goals of future facilities which are being currently designed [3,4]. There are also recent ideas on how to access this kind of distributions, and how to apply them to phenomenology, using LHC data, see e.g., [46–48]. Here, as an example of the potential of the solutions we found, we compute the impact-parameter dependent Weizsäcker-Williams gluon distribution $G^{(1)}$.

This gluon distribution can be interpreted as the number density of gluons at certain x and with a given transverse momentum, k_t, at a distance b from the center of the proton. Its relation to the dipole scattering amplitude as given in [46] is (see e.g., [49])

$$\alpha_s x G^{(1)}(x, k_t, b) = \frac{N_c}{4\pi^4} \int \frac{\mathrm{d}\vec{r}}{r^2} e^{-i\vec{k}_t\cdot\vec{r}} \times \{1 - [1 - N(x, r, b)]^2\}. \quad (9)$$

Figure 4 shows the impact-parameter dependent Weizsäcker-Williams gluon distribution computed with the dipole scattering amplitude obtained as a solution to the b-dependent BK equation with the collinearly improved kernel. The distribution is shown at a rapidity $Y = 2$. The figure also shows the integrals of this distribution over $\vec{k}_t$ and over $\vec{b}$. Integrals of this distribution feature reasonable size in impact parameter and fast-falling dependence on k_t (with an asymptotic behavior close to a power-like fall off with a power of -2, which was also reported in [46]),

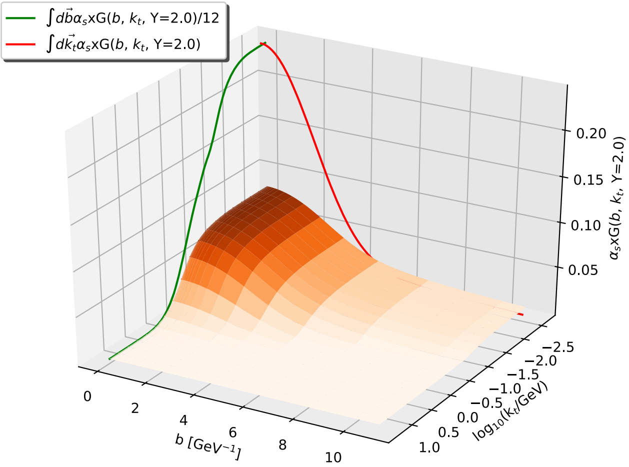

FIG. 4. The impact-parameter dependent Weizsäcker-Williams gluon distribution computed from the solution to the BK equation with the collinearly improved kernel. The red and green lines represent the integral of this distribution over the transverse momentum $\vec{k}_t$ or over the impact parameter $\vec{b}$, respectively.

suggesting that these distributions are ready to be used for phenomenological studies.

V. SUMMARY AND OUTLOOK

In this work we obtained the dipole scattering amplitude as a solution to the impact-parameter dependent Balitsky-Kovchegov equation using the collinearly improved kernel. We find that the Coulomb tails that have affected previous studies are strongly suppressed when using this kernel. Furthermore, we show that choosing specific initial conditions we obtain a good description of data on the $F_2(x,Q^2)$ structure function of the proton and on the cross section for the $|t|$ dependence of exclusive photoproduction of J/ψ vector mesons off protons. The agreement with data is obtained without the need of adding any extra term to the kernel and without any soft contribution. The success of these dipole scattering amplitudes in the description of data makes them valuable tools for phenomenological studies either using existing HERA and LHC data or to predict observables for future colliders. In this context we presented first results on the impact-parameter dependent Weizsäcker-Williams gluon distribution.

As a last remark, we would like to point out that there have been important advances in the computation of the BK equation at the next order in perturbation theory. The new equation, presented in [29], has been solved in [50] using the collinearly improved kernel, but without considering the impact parameter dependence. Furthermore, the tools to be able to use this equation for phenomenological applications are being developed, see e.g., [51–54]. Our results indicate that solutions of the NLO-BK equation including the collinearly improved kernel and considering the impact-parameter dependence may be useful to understand better the properties of pQCD in the high-energy limit.

The dipole scattering amplitudes computed in this work are publicly available in the website https://hep.fjfi.cvut.cz/.

ACKNOWLEDGMENTS

We would like to thank Dagmar Bendová, Heikki Mäntysaari and Cyrille Marquet for fruitful discussions. Our work has been partially supported by Grant No. 17-04505S of the Czech Science Foundation, GAČR and the COST Action CA15213 THOR. Computational resources were provided by the Czech Education and Scientific Network (CESNET) LM2015042 grant and the CERIT Scientific Cloud LM2015085, provided under the program "Projects of Large Research, Development, and Innovations Infrastructures."

---

[1] P. Newman and M. Wing, Rev. Mod. Phys. **86**, 1037 (2014).
[2] K. Akiba *et al.* (LHC Forward Physics Working Group), J. Phys. G **43**, 110201 (2016).
[3] A. Accardi *et al.*, Eur. Phys. J. A **52**, 268 (2016).
[4] J. A. Fernandez *et al.* (LHeC Study Group), J. Phys. G **39**, 075001 (2012).
[5] F. D. Aaron *et al.* (ZEUS and H1 Collaborations), J. High Energy Phys. 01 (2010) 109.
[6] H. Abramowicz *et al.* (ZEUS and H1 Collaborations), Eur. Phys. J. C **75**, 580 (2015).
[7] L. V. Gribov, E. M. Levin, and M. G. Ryskin, Phys. Rep. **100**, 1 (1983).
[8] J. L. Albacete and C. Marquet, Prog. Part. Nucl. Phys. **76**, 1 (2014).
[9] I. Balitsky, Nucl. Phys. **B463**, 99 (1996).
[10] J. Jalilian-Marian, A. Kovner, A. Leonidov, and H. Weigert, Phys. Rev. D **59**, 014014 (1998).
[11] Y. V. Kovchegov, Phys. Rev. D **60**, 034008 (1999).
[12] Y. V. Kovchegov, Phys. Rev. D **61**, 074018 (2000).
[13] J. Jalilian-Marian, A. Kovner, and H. Weigert, Phys. Rev. D **59**, 014015 (1998).
[14] H. Weigert, Nucl. Phys. **A703**, 823 (2002).
[15] E. Iancu, A. Leonidov, and L. D. McLerran, Nucl. Phys. **A692**, 583 (2001).
[16] E. Iancu, A. Leonidov, and L. D. McLerran, Phys. Lett. B **510**, 133 (2001).
[17] E. Ferreiro, E. Iancu, A. Leonidov, and L. McLerran, Nucl. Phys. **A703**, 489 (2002).

[18] H. Mntysaari and B. Schenke, Phys. Rev. D **98**, 034013 (2018).

[19] J. L. Albacete, N. Armesto, J. G. Milhano, P. Quiroga-Arias, and C. A. Salgado, Eur. Phys. J. C **71**, 1705 (2011).

[20] K. J. Golec-Biernat and A. M. Stasto, Nucl. Phys. **B668**, 345 (2003).

[21] J. Berger and A. Stasto, Phys. Rev. D **83**, 034015 (2011).

[22] J. Berger and A. M. Stasto, Phys. Rev. D **84**, 094022 (2011).

[23] J. Berger and A. M. Stasto, J. High Energy Phys. 01 (2013) 001.

[24] I. Balitsky, Phys. Rev. D **75**, 014001 (2007).

[25] Y. V. Kovchegov and H. Weigert, Nucl. Phys. **A784**, 188 (2007).

[26] E. Iancu, J. D. Madrigal, A. H. Mueller, G. Soyez, and D. N. Triantafyllopoulos, Phys. Lett. B **744**, 293 (2015).

[27] E. Iancu, J. D. Madrigal, A. H. Mueller, G. Soyez, and D. N. Triantafyllopoulos, Phys. Lett. B **750**, 643 (2015).

[28] L. Motyka and A. M. Stasto, Phys. Rev. D **79**, 085016 (2009).

[29] I. Balitsky and G. A. Chirilli, Phys. Rev. D **77**, 014019 (2008).

[30] J. L. Albacete, N. Armesto, J. G. Milhano, and C. A. Salgado, Phys. Rev. D **80**, 034031 (2009).

[31] D. Binosi, C. Mezrag, J. Papavassiliou, C. D. Roberts, and J. Rodriguez-Quintero, Phys. Rev. D **96**, 054026 (2017).

[32] S. J. Brodsky, G. F. de Teramond, and A. Deur, Phys. Rev. D **81**, 096010 (2010).

[33] J. L. Albacete and Y. V. Kovchegov, Phys. Rev. D **75**, 125021 (2007).

[34] K. J. Golec-Biernat and M. Wusthoff, Phys. Rev. D **59**, 014017 (1998).

[35] L. D. McLerran and R. Venugopalan, Phys. Lett. B **424**, 15 (1998).

[36] J. Cepila and J. G. Contreras, arXiv:1501.06687.

[37] M. Matas, J. Cepila, and J. G. C. Nuno, EPJ Web Conf. **112**, 02008 (2016).

[38] J. Cepila, J. G. Contreras, and M. Matas (to be published).

[39] H. Kowalski, L. Motyka, and G. Watt, Phys. Rev. D **74**, 074016 (2006).

[40] M. S. Bhagwat, M. A. Pichowsky, C. D. Roberts, and P. C. Tandy, Phys. Rev. C **68**, 015203 (2003).

[41] J. Nemchik, N. N. Nikolaev, and B. G. Zakharov, Phys. Lett. B **341**, 228 (1994).

[42] J. Nemchik, N. N. Nikolaev, E. Predazzi, and B. G. Zakharov, Z. Phys. C **75**, 71 (1997).

[43] A. G. Shuvaev, K. J. Golec-Biernat, A. D. Martin, and M. G. Ryskin, Phys. Rev. D **60**, 014015 (1999).

[44] C. Alexa *et al.* (H1 Collaboration), Eur. Phys. J. C **73**, 2466 (2013).

[45] A. Aktas *et al.* (H1 Collaboration), Eur. Phys. J. C **46**, 585 (2006).

[46] A. van Hameren, P. Kotko, K. Kutak, C. Marquet, E. Petreska, and S. Sapeta, J. High Energy Phys. 12 (2016) 034.

[47] Y. Hagiwara, Y. Hatta, R. Pasechnik, M. Tasevsky, and O. Teryaev, Phys. Rev. D **96**, 034009 (2017).

[48] J. L. Albacete, G. Giacalone, C. Marquet, and M. Matas, Phys. Rev. D **99**, 014002 (2019).

[49] C. Marquet, E. Petreska, and C. Roiesnel, J. High Energy Phys. 10 (2016) 065.

[50] T. Lappi and H. Mntysaari, Phys. Rev. D **93**, 094004 (2016).

[51] G. Beuf, Phys. Rev. D **89**, 074039 (2014).

[52] G. Beuf, Phys. Rev. D **96**, 074033 (2017).

[53] B. Duclou, H. Hnninen, T. Lappi, and Y. Zhu, Phys. Rev. D **96**, 094017 (2017).

[54] H. Hnninen, T. Lappi, and R. Paatelainen, Ann. Phys. (Amsterdam) **393**, 358 (2018).

PHYSICAL REVIEW D **99,** 014002 (2019)

Editors' Suggestion

Forward dihadron back-to-back correlations in *pA* collisions

Javier L. Albacete,[1] Giuliano Giacalone,[2,3] Cyrille Marquet,[3] and Marek Matas[4]
[1]*CAFPE and Departamento de Física Teórica y del Cosmos, Universidad de Granada, E-18071 Campus de Fuentenueva, Granada, Spain*
[2]*Institut de physique théorique, Université Paris Saclay, CNRS, CEA, F-91191 Gif-sur-Yvette, France*
[3]*CPHT, École Polytechnique, CNRS, Université Paris Saclay, Route de Saclay, 91128 Palaiseau, France*
[4]*Czech Technical University in Prague, FNSPE, Břehová 7, 11519 Prague, Czech Republic*

(Received 23 May 2018; published 2 January 2019)

We study the disappearance of the away-side peak of the di-hadron correlation function in $\mathrm{p}+\mathrm{A}$ vs $\mathrm{p}+\mathrm{p}$ collisions at forward rapidities, when the scaterring process presents a manifest dilute-dense asymmetry. We improve the state-of-the-art description of this phenomenon in the framework of the color glass condensate (CGC), for hadrons produced nearly back to back. In that case, the gluon content of the saturated nuclear target can be described with transverse-momentum-dependent gluon distributions, whose small-x evolution we calculate numerically by solving the Balitsky-Kovchegov equation with running coupling corrections. We first show that our formalism provides a good description of the disappearance of the away-side azimuthal correlations in $\mathrm{d}+\mathrm{Au}$ collisions observed at BNL Relativistic Heavy Ion Collider (RHIC) energies. Then, we predict the away-side peak of upcoming $\mathrm{p}+\mathrm{Au}$ data at $\sqrt{s}=200$ GeV to be suppressed by about a factor 2 with respect to $\mathrm{p}+\mathrm{p}$ collisions, and we propose to study the rapidity dependence of that suppression as a complementary strong evidence of gluon saturation in experimental data.

DOI: 10.1103/PhysRevD.99.014002

I. INTRODUCTION

Azimuthal correlations of particles in the final states of hadronic collisions serve as a powerful tool for experimental tests of the color glass condensate (CGC) [1–3], the effective theory of protons and nuclei in the nonlinear regime of quantum chromodynamics. A special role in the phenomenology of the CGC is played by correlations of particles in $\mathrm{p}+\mathrm{A}$ collisions probed in the region of fragmentation of the protons [4–11], where the rapidities of the correlated particles are large and positive (forward rapidity region). Such configurations are ideal for testing the CGC theory, because they induce a dilute-dense asymmetry in the problem: The projectile proton is probed at large values of Bjorken x, and is thus a dilute object, amenable to a description in terms of well-known parton distribution functions (PDFs). The nuclear target is instead seen as dense state of low x gluons, a regime in which the *saturation* of the gluon densities is manifest, so that the CGC description applies. This dilute-dense asymmetry, hence, minimizes our uncertainty in the knowledge of the projectile and provides the cleanest possible environment for the study of phenomenological signatures of gluon saturation in the target.

In this paper, we deal with a salient prediction of the CGC theory: The disappearance of the away-side peak ($\Delta\phi=\pi$) of the two-particle correlation function of dilute-dense collisions (i.e., forward $\mathrm{p}+\mathrm{A}$ collisions). Following [12], let us provide an intuitive picture of this phenomenon. A valence parton interacting with a CGC (i.e., a large classical Yang-Mills background field) undergoes multiple scattering with low-x gluons, either before or after splitting into a pair of back-to-back partons, which eventually produce the jets or hadrons observed in the final state. The pair of partons is put on shell via the interaction with the target, and this occurs through a transverse momentum exchange of order of the saturation scale of the target, Q_s, which is typically much larger than the transverse momentum of the parent valence parton. The back-to-back correlation of the final-state particles, which would not be affected by an interaction with a gluon of zero transverse momentum, is therefore altered, and this induces a depletion of the correlation function around $\Delta\phi=\pi$. Hence, the away-side peak observed in $\mathrm{p}+\mathrm{A}$ collisions is expected to be suppressed with respect to that of $\mathrm{p}+\mathrm{p}$ collisions, because the target nuclei are denser and more saturated. Moreover, since Q_s grows with the inverse of x probed in the targets, one expects stronger suppression of back-to-back correlations if particles are correlated at large rapidity, $y=\ln(1/x)$.

Experimentally, the validity of this picture is strongly supported by Relativistic Heavy-Ion Collider (RHIC) data, as both the STAR and the PHENIX Collaborations reported a visible suppression of the away-side peak when comparing $\mathrm{p}+\mathrm{p}$ collisions to central $\mathrm{d}+\mathrm{Au}$ collisions [13,14]. These data, though, suffer from large uncertainties. More accurate tests of the CGC prediction may nevertheless become possible with the advent of data from the recent 200 GeV $\mathrm{p}+\mathrm{Au}$ run performed at RHIC. As we shall see, one of the goals of this paper is to provide predictions for the away-side peak in these collisions.

On the theory side, first calculations of forward two-particle production in $\mathrm{p}+\mathrm{A}$ collisions within the CGC framework date back more than ten years [4,15]. The cross section for the production of two particles is intrinsically difficult to evaluate, because it involves multipoint correlators of Wilson lines. Over the years, different levels of approximation have been employed to perform calculations and obtain predictions, as reviewed in Ref. [12]. The simplest option is to disregard nonlinear effects and recover the so-called k_t factorization (or high-energy factorization) framework [5,16]; the cross section is then obtained from a single two-point correlator, but that approximation is not applicable in the away-side peak region. In Ref. [6], the multipoint correlators are evaluated using the so-called Gaussian approximation of the nonlinear QCD evolution; however, only the *elastic* contributions are kept, and it turns out that the neglected contributions are also sizable in the away-side peak region. In Ref. [8], the complete Gaussian expressions are used; however, due to the complexity of the problem, only quark-initiated channels could be included.

A crucial step was the realization that the cross section simplifies dramatically if one considers the production of partons which are nearly back to back [17,18]. In this limit, the dense part of the scattering (the nucleus) is characterized by transverse-momentum-dependent (TMD) gluon distributions whose small x evolution is easily affordable to numerical implementations, because the multipoint correlators of Wilson line [19] involve only two distinct transverse positions. This framework has been employed in a number of applications [7,10,11,19–22], and was recently reviewed in [23].[1] In the case of forward di-hadron production, it has only been used together with Golec-Biernat Wusthoff (GBW) type parameterizations for the gluon TMDs [7], which suffer from unphysical exponential tails at large gluon transverse momentum. The goal of our work is to improve on this by obtaining the TMD gluon distributions from numerical solutions of the QCD nonlinear evolution.

In [19,20], the gluon TMDs and their small-x evolution were obtained from the full QCD evolution at leading logarithmic accuracy, i.e., from the Jalilian-Marian–Iancu–McLerran–Weigert–Leonidov–Kovner (JIMWLK) equation. Since the implementation of running-coupling corrections in this context has not been performed yet, we prefer to work within the Gaussian approximation of JIMWLK evolution and obtain the gluon TMDs from the Balitsky-Kovchegov (BK) equation with running coupling corrections (rcBK), because we expect running-coupling corrections to be much more important than corrections to the Gaussian approximation. In addition, the rcBK solutions are well constrained from deep inelastic scattering data [25], so that the final expression of the cross section of two-parton production turns out to be essentially free from tunable parameters. We shall derive this cross section, and convolute it with fragmentation functions to present state-of-the-art results on azimuthal correlations of di-hadrons in forward $\mathrm{p}+\mathrm{A}$ and $\mathrm{p}+\mathrm{p}$ collisions at RHIC energies. We both test our theory against existing data and make predictions for future back-to-back correlations of hadrons.

The paper is organized as follows. In Sec. II, we briefly review the theoretical formalism of nearly back-to-back forward di-hadron production in $\mathrm{p}+\mathrm{A}$ collisions in the CGC framework, and we present the fully differential cross section for the production of di-hadrons, specifically, two neutral pions. In the cross section we shall introduce the TMD gluon distributions which characterize the dense component of the scattering process. In Sec. III, we explain in detail how such quantities are obtained from rcBK evolution, and we show their behavior as function of the kinematic variables. Calculations of the away-side peak are eventually given in Sec. IV. The per-trigger-yield cross section is calculated as a function of the relative azimuthal angle of the two hadrons. We first calculate it in $\mathrm{d}+\mathrm{Au}$ and $\mathrm{p}+\mathrm{p}$ collisions, and we compare our results to existing RHIC data. Then, we compute several predictions for the away-side peak in upcoming $\mathrm{p}+\mathrm{Au}$ collisions at $\sqrt{s}=$ 200 GeV. In Sec. V, we make predictions for the evolution with rapidity of the suppression of the away-side peak, and we compare our results with calculations performed using an alternative implementation of the rcBK evolution for nuclei. Section VI is left for conclusive remarks.

II. COLOR GLASS CONDENSATE IN THE BACK-TO-BACK REGION: TMD FACTORIZATION

We study the production of pairs of hadrons in forward $\mathrm{p}+\mathrm{A}$ collisions. We display this process in Fig. 1. Working in light-cone coordinates, $(+,\ \perp,\ -)$, the Feynman-x variables associated with the projectile parton moving along the $+$ direction and with the target gluon coming from the $-$ direction are, respectively, given by

---

[1] Note that an improved version of the TMD formalism (dubbed ITMD) was introduced in Ref. [24]. This framework allows one to relax the condition $\Delta\phi\sim\pi$, and was applied in calculations of forward di-jet production in Refs. [10,11]. However, in this paper we do not employ the improved framework because it is strictly equivalent to the original TMD formulation as long as back-to-back particles are considered.

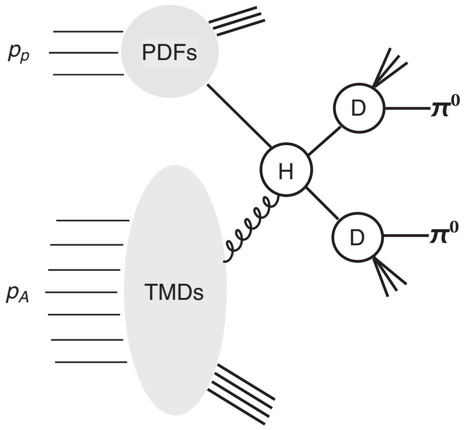

FIG. 1. The $pA \to \pi^0\pi^0 X$ process. See the text for details about the displayed quantities.

$$x_1 = \frac{k_1^+ + k_2^+}{p_p^+} = \frac{1}{\sqrt{s}}\left(\frac{p_{1t}}{z_1}e^{y_1} + \frac{p_{2t}}{z_2}e^{y_2}\right),$$
$$x_2 = \frac{k_1^- + k_2^-}{p_A^-} = \frac{1}{\sqrt{s}}\left(\frac{p_{1t}}{z_1}e^{-y_1} + \frac{p_{2t}}{z_2}e^{-y_2}\right), \qquad (1)$$

where the k_i's refer to the outgoing partons and the p_i's refer to the final-state hadrons. We have introduced their transverse momenta, $p_{1t} = z_1 k_{1t}$ and $p_{2t} = z_2 k_{2t}$, and rapidities, y_1 and y_2, while $\sqrt{s}$ denotes the invariant mass of the scattering process. Equation (1) shows that when both y_1 and y_2 are large and positive, we probe a large-x parton in the projectile, and a small-x gluon inside the target nucleus. In experiments at RHIC, one can reach $y \sim 4$, leading to $x_1 \sim 0.5$, and $x_2 \sim 10^{-3}$: This realizes the anticipated dilute-dense asymmetry of forward particle production, which is essential for the applicability of our formalism.

Now, following [18,19], we dub

$$z = \frac{k_1^+}{k_1^+ + k_2^+} = \frac{p_1^+/z_1}{p_1^+/z_1 + p_2^+/z_2}, \qquad (2)$$

and we introduce the following variables

$$k_t = k_{1t} + k_{2t}, \qquad P_t = (1-z)k_{1t} - zk_{2t}. \qquad (3)$$

If we stick to a limit in which the produced particles are back to back, i.e., their relative azimuthal angle, $\Delta\phi$, is close to π, then the total transverse momentum of the di-hadron pair is much smaller than the transverse momentum of the single hadrons, i.e., $|k_t| \ll |P_t|$ [18].

Following the exhaustive derivations of [19], the advantage of this limit is that it allows to write the cross section of the scattering process as an expansion in powers of $1/P_t$. Keeping only the leading order terms in this expansion, the dense component of the scattering is given by a combination of transverse momentum dependent gluon distributions (TMDs in short), which are CGC correlators of traces of Wilson lines. Summing over all production channels ($qg \to qg$, $gg \to q\bar{q}$, $gg \to gg$), the cross section for the production of two partons can be written in the following compact notation [19]

$$\frac{d\sigma^{pA\to hhX}}{d^2k_{1t}d^2k_{2t}dy_1dy_2} = \frac{\alpha_s^2}{(x_1x_2s)^2}\sum_{a,c,d} x_1 f_{a/p}(x_1,\mu^2)$$
$$\times \sum_i \frac{1}{1+\delta_{cd}} H^{(i)}_{ag\to cd}(z,P_t)$$
$$\times \mathcal{F}^{(i)}_{ag}(x_2,k_t), \qquad (4)$$

where we note the manifest factorization of the cross section into a dilute component, characterized by collinear parton distribution functions $f_{a/p}(x_1,\mu^2)$, evaluated at a factorization scale μ^2, and a channel-dependent dense component, characterized by hard factors [18], $H(z,P_t)$, and the TMD gluon distributions, $\mathcal{F}^{(i)}(x_2,k_t)$, specified below.

To turn Eq. (4) into a tool enabling us to compute predictions for di-hadron production, we convolute it with fragmentation functions. Considering u quarks, d quarks and gluons in the projectile proton, and considering only their fragmentation into pions, and neglecting all terms which are suppressed by $1/N_c^2$, the full expression of the cross section reads

$$\frac{d\sigma^{pA\to\pi^0\pi^0X}}{dy_1dy_2d^2p_{1t}d^2p_{2t}} = \frac{\alpha_s^2}{2C_F}\int_{p_{t1}\frac{e^{y_1}}{\sqrt{s}}/(1-p_{t2}\frac{e^{y_2}}{\sqrt{s}})}^1 \frac{dz_1}{z_1^2}\int_{p_{t2}\frac{e^{y_2}}{\sqrt{s}}/(1-\frac{p_{t1}}{z_1}\frac{e^{y_1}}{\sqrt{s}})}^1 \frac{dz_2}{z_2^2}\frac{z(1-z)}{P_t^4}$$
$$\times \{D_{\pi^0/g}(z_1,\mu^2)[x_1u(x_1,\mu^2)D_{\pi^0/u}(z_2,\mu^2) + x_1d(x_1,\mu^2)D_{\pi^0/d}(z_2,\mu^2)]P_{gq}(z)$$
$$\times [(1-z)^2\mathcal{F}^{(1)}_{qg}(x_2,k_t) + \mathcal{F}^{(2)}_{qg}(x_2,k_t)] + D_{\pi^0/g}(z_2,\mu^2)[x_1u(x_1,\mu^2)D_{\pi^0/u}(z_1,\mu^2)$$
$$+ x_1d(x_1,\mu^2)D_{\pi^0/d}(z_1,\mu^2)]P_{gq}(1-z)[z^2\mathcal{F}^{(1)}_{qg}(x_2,k_t) + \mathcal{F}^{(2)}_{qg}(x_2,k_t)]$$
$$+ 2[D_{\pi^0/u}(z_1,\mu^2)D_{\pi^0/u}(z_2,\mu^2) + D_{\pi^0/d}(z_1,\mu^2)D_{\pi^0/d}(z_2,\mu^2)]x_1g(x_1,\mu^2)P_{qg}(z)$$
$$\times [\mathcal{F}^{(1)}_{gg}(x_2,k_t) - 2z(1-z)(\mathcal{F}^{(1)}_{gg}(x_2,k_t) - \mathcal{F}^{(2)}_{gg}(x_2,k_t))]$$
$$+ D_{\pi^0/g}(z_1,\mu^2)D_{\pi^0/g}(z_2,\mu^2)x_1g(x_1,\mu^2)P_{gg}(z)$$
$$\times [\mathcal{F}^{(1)}_{gg}(x_2,k_t) - 2z(1-z)(\mathcal{F}^{(1)}_{gg}(x_2,k_t) - \mathcal{F}^{(2)}_{gg}(x_2,k_t)) + \mathcal{F}^{(6)}_{gg}(x_2,k_t)]\}, \qquad (5)$$

where we have denoted by $D_{\pi^0/a}(z_i, \mu^2)$ the fragmentation of a parton a into a neutral pion at the factorization scale μ^2, and the notation used for the distributions $\mathcal{F}_{ag}^{(i)}(x_2, k_t)$ is the same as in [19]. In Sec. IV we shall make use of Eq. (5) to compute azimuthal correlations of neutral pions at RHIC. Let us first describe, in the following section, the rcBK formalism developed for the small x_2 evolution of the TMD distributions which appear in the cross section.

III. EVOLUTION OF THE TMD GLUON DISTRIBUTIONS TOWARDS SMALL *x*

In order to complete our formulation of the cross section, Eq. (5), we discuss now the x_2 evolution of the TMD gluon distributions, $\mathcal{F}_{ag}^{(i)}(x_2, k_t)$. The starting point is the evolution of the impact parameter (b) independent fundamental–dipole scattering amplitude, which we denote in a standard notation $N_F(x, r)$. As it is customarily done in the literature, we assume that the b dependence of N_F factorizes, and that it does not mix with the evolution. The evolution equation of the dipole amplitude, known as the Balitsky-Kovchegov equation [26,27], supplemented with running coupling corrections (rcBK equation), reads ($r_i = |\mathbf{r_i}|$)

$$\frac{\partial N_F(r,x)}{\partial \ln(x_0/x)} = \int d^2 r_1 K^{\rm run}(\mathbf{r}, \mathbf{r_1}, \mathbf{r_2})[N_F(r_1, x) + N_F(r_2, x) - N_F(r,x) - N_F(r_1,x)N_F(r_2,x)], \tag{6}$$

with $\mathbf{r_2} \equiv \mathbf{r} - \mathbf{r_1}$, and where x_0 is some initial value for the evolution (usually chosen to be $x_0 = 0.01$). $K^{\rm run}$ is the evolution kernel including running coupling corrections. Different prescriptions have been proposed in the literature for $K^{\rm run}$. As shown in [28], Balitsky's prescription minimizes the role of higher *conformal* corrections:

$$K^{\rm run}(\mathbf{r}, \mathbf{r_1}, \mathbf{r_2}) = \frac{N_c \alpha_s(r^2)}{2\pi^2}\left[\frac{1}{r_1^2}\left(\frac{\alpha_s(r_1^2)}{\alpha_s(r_2^2)} - 1\right) + \frac{r^2}{r_1^2 r_2^2} + \frac{1}{r_2^2}\left(\frac{\alpha_s(r_2^2)}{\alpha_s(r_1^2)} - 1\right)\right]. \tag{7}$$

The rcBK evolution is independent of whether the target is a proton or a nucleus. That is accounted for in the initial condition. We use the so-called McLerran-Venugopalan (MV) model:

$$N_F(r, x = x_0) = 1 - \exp\left[-\frac{r^2 Q_{s0}^2}{4}\ln\left(\frac{1}{\Lambda r} + e\right)\right], \tag{8}$$

with $\Lambda = 0.241$ GeV, and where Q_{s0} denotes the saturation scale at the initial value x_0. We use $x_0 = 0.01$ and $Q_{s0}^2 = 0.2$ GeV^2 for a proton target, which are known to provide a good description of single-inclusive forward hadron RHIC data [29]. For a target nucleus, things are more uncertain, as we are interested only in central collisions, i.e., collisions at small impact parameter. Motivated by previous studies [6], we keep $x_0 = 0.01$, and we choose $Q_{s0}^2 = 0.6$ GeV^2, i.e., a factor 3 larger than the Q_{s0}^2 with a target proton.

Now, the simplest gluon TMD distribution, $\mathcal{F}_{qg}^{(1)}(x_2, k_t)$, is related to the Fourier transform of the fundamental dipole amplitude, $N_F(x_2, \mathbf{r})$, and is given by

$$\mathcal{F}_{qg}^{(1)}(x_2, k_t) = \frac{N_c}{\alpha_s \pi (2\pi)^3}\int d^2 b \int d^2\mathbf{r} e^{-ik_t\cdot\mathbf{r}} \nabla_{\mathbf{r}}^2 N_F(x_2, \mathbf{r}) = \frac{N_c k_t^2 S_\perp}{2\pi^2 \alpha_s} F(x_2, k_t), \tag{9}$$

where

$$F(x_2, k_t) = \int \frac{d^2\mathbf{r}}{(2\pi)^2} e^{-ik_t\cdot\mathbf{r}}[1 - N_F(x_2, \mathbf{r})], \tag{10}$$

and with $S_\perp$ denoting the transverse area of the target.

In full generality, none of the other gluon TMDs can be obtained in such a straightforward manner, directly from N_F, or its Fourier transform F. To move forward, we resort to a mean-field type approximation: we shall utilize the so-called Gaussian approximation of the CGC [4,30–35]. The essence of this approximation is to consider all the color charge correlations in the target to stay Gaussian throughout the evolution. This approximation, along with the large N_c-limit, ensures the factorization of CGC expectation values into single-trace expectation values, and allows to calculate $\mathcal{F}_{gg}^{(1)}$ and $\mathcal{F}_{gg}^{(2)}$ from F [18]:

$$\mathcal{F}_{gg}^{(1)}(x_2, k_t) = \int d^2 q_t \mathcal{F}_{qg}^{(1)}(x_2, q_t) F(x_2, k_t - q_t), \tag{11}$$

$$\mathcal{F}_{gg}^{(2)}(x_2, k_t) = -\int d^2 q_t \frac{(k_t - q_t)\cdot q_t}{q_t^2}\mathcal{F}_{qg}^{(1)}(x_2, q_t) \times F(x_2, k_t - q_t), \tag{12}$$

We note that the difference,

$$\mathcal{F}_{gg}^{(1)}(x_2, k_t) - \mathcal{F}_{gg}^{(2)}(x_2, k_t) = \int d^2 q_t \frac{k_t\cdot q_t}{q_t^2}\mathcal{F}_{qg}^{(1)}(x_2, q_t) F(x_2, k_t - q_t) \tag{13}$$

$$= \frac{k_t^2}{2}\int \frac{d^2 q_t}{q_t^2}\mathcal{F}_{qg}^{(1)}(x_2, q_t) F(x_2, k_t - q_t), \tag{14}$$

which enters the cross section (5), is related to the adjoint-dipole scattering amplitude N_A in the same way that $\mathcal{F}_{qg}^{(1)}$ was related to the fundamental dipole scattering amplitude. Indeed, if we introduce

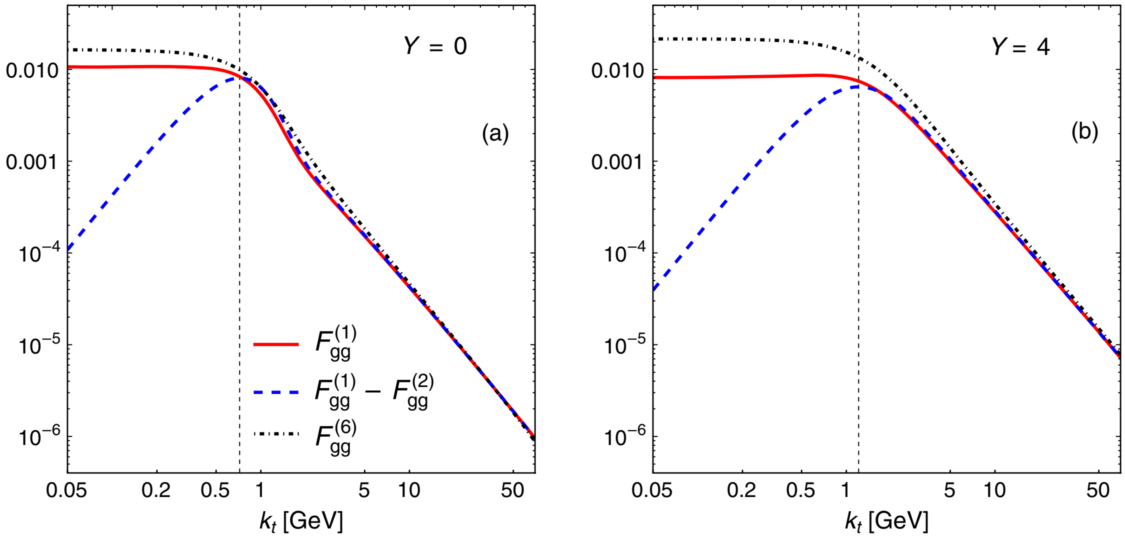

FIG. 2. This figure presents the x_2 evolution of three TMDs appearing in the cross section of Eq. (5), for a target proton. In panel (a), the initial conditions at $x_2 = 0.01$ are presented. We show $\mathcal{F}_{gg}^{(1)}$ (solid line), $\mathcal{F}_{gg}^{(1)} - \mathcal{F}_{gg}^{(2)}$ (dashed line), and $\mathcal{F}_{gg}^{(6)}$ (dot-dashed line). The vertical dotted lines represent the saturation scale at the given value of x_2. In the figure, $Y = \ln(0.01/x_2)$. The plotted quantities do not include the factor $S_\perp/\alpha_s$ in Eq. (9), common to all the gluon TMDs.

$$\mathcal{F}_{\mathrm{adj}}(x_2, k_t) = \frac{C_F}{\alpha_s \pi (2\pi)^3} \int d^2b \int d^2\mathbf{r} e^{-ik_t\cdot\mathbf{r}} \nabla_{\mathbf{r}}^2 N_A(x_2, \mathbf{r}) = \frac{C_F k_t^2 S_\perp}{2\pi^2 \alpha_s} \tilde{F}(x_2, k_t), \tag{15}$$

where

$$\tilde{F}(x_2, k_t) = \int \frac{d^2\mathbf{r}}{(2\pi)^2} e^{-ik_t\cdot\mathbf{r}} [1 - N_A(x_2, \mathbf{r})], \tag{16}$$

then one has $\mathcal{F}_{gg}^{(1)} - \mathcal{F}_{gg}^{(2)} = \mathcal{F}_{\mathrm{adj}}$. This identify is true in full generality, beyond the Gaussian and large-N_c approximations (for which $1 - N_A = [1 - N_F]^2$) used here, as was first noticed in [20].

Finally, the two remaining gluon TMDs need to be computed from the Weizsäcker-Williams (WW) gluon distribution [18], which we denote $\mathcal{F}_{WW}$, and which should be obtained from the quadrupole operator $\langle \mathrm{Tr}[A(\mathbf{x})A(\mathbf{y})] \rangle_{x_2}$ where $A(\mathbf{x}) = U^\dagger(\mathbf{x}) \partial_{\mathbf{x}} U(\mathbf{x})$ with U denoting a Wilson line. Again, this quantity is in general not related to the solution of the BK equation, $F(x_2, k_t)$, but using the Gaussian approximation one can write (in the large N_c limit)[2]:

$$\mathcal{F}_{WW}(x_2, k_t) = \frac{C_F}{2\alpha_s \pi^4} \int d^2b \int \frac{d^2\mathbf{r}}{r^2} \times e^{-ik_t\cdot\mathbf{r}} \{1 - [1 - N_F(x_2, \mathbf{r})]^2\}. \tag{17}$$

which allows to calculate the remaining two gluon TMDs needed in the cross section as follows [18]:

$$\mathcal{F}_{gg}^{(2)}(x_2, k_t) = \int d^2q_t \mathcal{F}_{WW}(x_2, q_t) F(x_2, k_t - q_t), \tag{18}$$

$$\mathcal{F}_{gg}^{(6)}(x_2, k_t) = \int d^2q_t d^2q_t' \mathcal{F}_{WW}(x_2, q_t) F(x_2, q_t') \times F(x_2, k_t - q_t - q_t'). \tag{19}$$

We have now expressed all the needed gluon TMDs in terms of $F(x_2, k_t)$, the solution of the BK equation.

We show in Fig. 2 some of those gluon distributions for a target proton, as function of k_t, and for two values of x_2. We do not show $\mathcal{F}_{gg}^{(2)}$ explicitly, but rather the difference $\mathcal{F}_{gg}^{(1)} - \mathcal{F}_{gg}^{(2)}$, which effectively plays a role in Eq. (5). The TMD distributions present three specific features, fully characterizing the dense component of our scattering. Starting from the region where $k_t \gg 1$ GeV, we note that all the curves approach the same asymptotic behavior, i.e., an inverse power law, precisely equal to k_t^{-2} at $x_2 = x_0$ [panel (a)], with a smaller absolute slope after x_2 evolution [panel (b)]. As k_t becomes of order 1 GeV, the TMD distributions start to separate, and quickly change their slope at a specific k_t, which corresponds approximately to the location of the maximum of $F_{gg}^{(1)} - F_{gg}^{(2)}$. This is the value of the saturation scale, Q_s, which we indicate in both panels with a vertical dotted line.[3] Note that the small-x_2 evolution

---

[2] Strictly speaking, the $1/r^2$ factor—which we shall keep in our numerical computation—should be replaced by a more complicated function of N_F, equal to $1/r^2$ only in the MV model at $x_2 = x_0$.

[3] More specifically, the maximum of $\mathcal{F}_{\mathrm{adj}}$ corresponds to the *adjoint* saturation scale, which is 1.5 times bigger than Q_s, the *fundamental* saturation scale which corresponds to the maximum of $F_{gg}^{(1)}$. This explains why the vertical line in Fig. 2(a) does not correspond to $Q_{s0} = \sqrt{0.2}$ GeV.

has the effect of shifting the saturation scale to larger values. Eventually, below the value of Q_s the distributions become flat, and saturation is manifest. The difference $\mathcal{F}_{gg}^{(1)} - \mathcal{F}_{gg}^{(2)}$ goes to zero at $k_t = 0$, consistently with Eq. (14).

IV. THE AWAY-SIDE PEAK FROM rcBK EVOLUTION: RESULTS AND PREDICTIONS

We can eventually employ the theoretical formalism introduced in the previous sections to compute azimuthal correlations of two hadrons in p + p and p + A collisions at $\sqrt{s} = 200$ GeV. We integrate Eq. (5) over the momenta and rapidities of the produced hadrons, and study the behavior of the cross section as function of relative azimuthal angle, $\Delta\phi$. In the notation of [6], the observable we want to calculate is

$$N_{\mathrm{pair}}(\Delta\phi) = \int \frac{d\sigma^{pA\to\pi^0\pi^0 X}}{d\Delta\phi dy_1 dy_2 dp_{t1}^2 dp_{t2}^2} dy_1 dy_2 dp_{t1}^2 dp_{t2}^2. \tag{20}$$

The experimentally measured quantity is not directly given by Eq. (20). Experimentalists normalize $N_{\mathrm{pair}}(\Delta\phi)$ with the total number of hadrons that trigger the correlations, i.e.,

$$N_{\mathrm{trig}} = \int \frac{d\sigma^{pA\to\pi^0+X}}{dy dp_t^2} dy dp_t^2, \tag{21}$$

in which we have introduced the cross section for single hadron production [29]

$$\begin{aligned}\frac{d\sigma^{pA\to\pi^0+X}}{dy dp_t^2} = &\int_{p_t\frac{e^y}{\sqrt{s}}}^1 \frac{dz}{z^2}\{[x_1 u(x_1,\mu^2)D_{\pi^0/u}(z,\mu^2)\\ &+ x_1 d(x_1,\mu^2)D_{\pi^0/d}(z,\mu^2)]F(x_2,k_t)\\ &+ x_1 g(x_1,\mu^2)D_{\pi^0/g}(x_2,\mu^2)\tilde{F}(x_2,k_t)\},\end{aligned} \tag{22}$$

where F and $\tilde{F}$ are computed from the rcBK evolution equation as explained in the previous section. The final observable is dubbed *coincidence probability* by the STAR Collaboration, and is given by

$$CP(\Delta\phi) = N_{\mathrm{pair}}(\Delta\phi)/N_{\mathrm{trig}}. \tag{23}$$

Before showing our results, let us list all the details about the quantities needed in the calculation of $CP(\Delta\phi)$:

(i) The parton distribution functions (PDFs) describing the projectile are taken from the NLO MSTW2008 fits [36];

(ii) The fragmentation functions (FFs) used are the recent DSS14 NLO sets [37];

(iii) The strong coupling constant appearing in Eq. (5) is calculated at NLO, and is given by the following expression

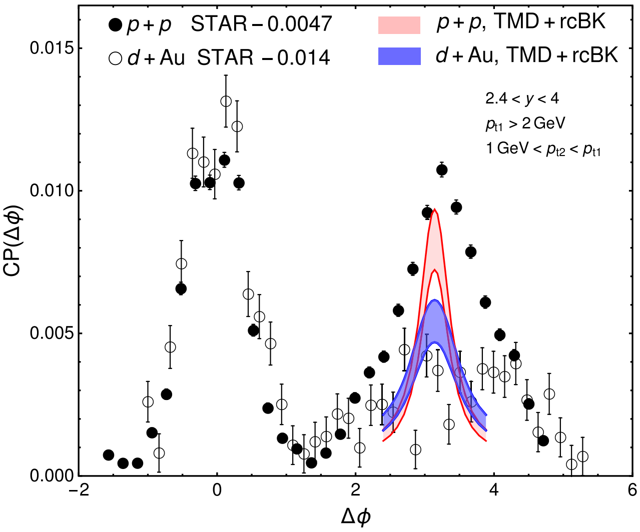

FIG. 3. The figure shows STAR data on azimuthal π^0 correlations at forward rapidity, in p + p collisions (circles) and central d + Au collisions (triangles) at $\sqrt{s} = 200$ GeV. To remove fake two particle correlations which are essentially due to pileup effects, an arbitrary offset is added to push the STAR measurements close to 0 at the minimum of the correlation functions. Calculations of $CP(\Delta\phi)$ in our TMD + rcBK framework are shown as shaded bands. Light-shaded band: p + p collisions. Dark-shaded band: d + Au collisions. The meaning of the shaded bands is discussed in the text.

$$\alpha_s(\mu^2) = \frac{4\pi}{(11 - \frac{2}{3}N_f)\ln(\frac{\mu^2}{\Lambda^2})}, \tag{24}$$

where we take $N_f = 4$, and $\Lambda = 197$ MeV. For μ^2, we use the same scale employed in the PDFs and in the FFs (see item below);

(iv) The PDFs, the FFs, and α_s are computed at the scale $\mu^2 = p_{t1}^2$, i.e., at the transverse momentum of the leading hadron.

A. Comparison with run-8 d + Au RHIC data

Saturation effects are expected to yield a larger $CP(\Delta\phi)$ in pp collisions than in pA collisions, when $\Delta\phi$ is in the vicinity of π. STAR data on $CP(\Delta\phi)$ [13] for neutral pion correlations are shown as symbols in Fig. 3. Data present a visible suppression of the correlation in d + Au collisions, suggesting that saturation effects may be effectively at play. The outcome of integrating Eq. (5) over the STAR kinematics in both p + p and d + Au collisions[4] is shown as shaded bands, in the nearby of $\Delta\phi = \pi$. The shaded bands represent the uncertainty in the choice of the factorization scale, μ^2, in Eq. (5). The upper limit of the

---

[4] Note that Eq. (5) is suitable only for proton-nucleus collisions. A slightly different combinations of the PDFs and FFs at play is used to obtain the same cross section in the deuteron-nucleus case.

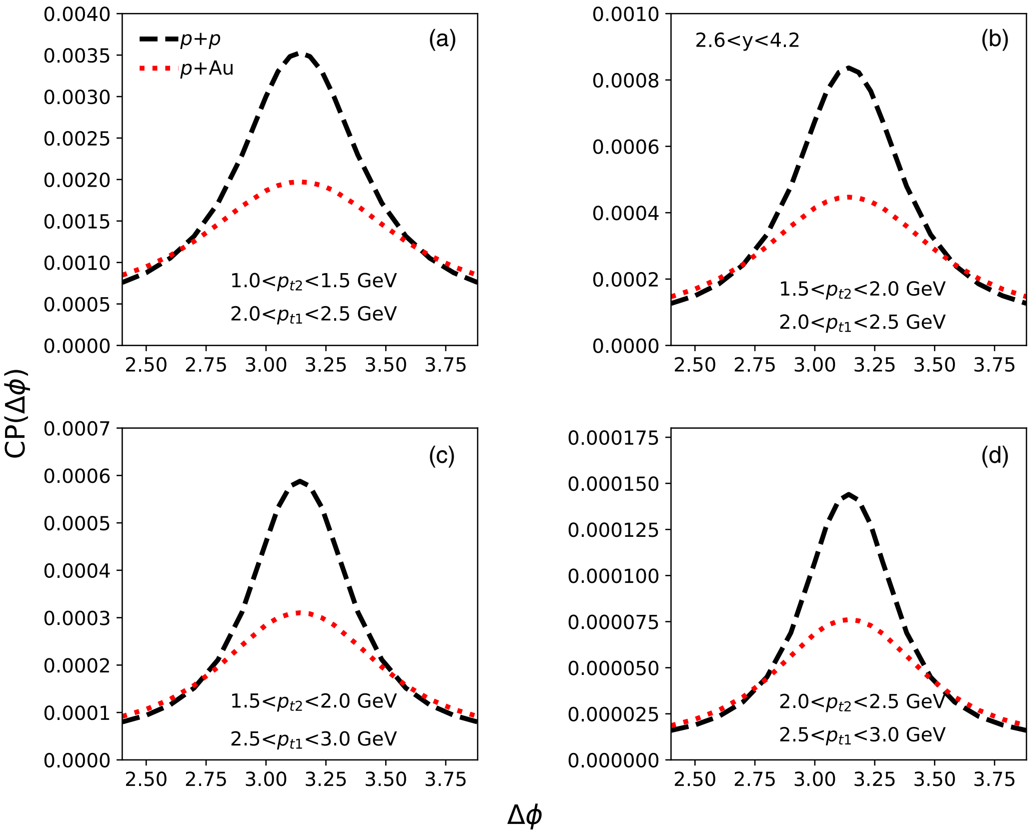

FIG. 4. In this figure we show predictions for azimuthal correlation of forward neutral pions in p + p (dashed line) and p + Au (dotted line) collisions at $\sqrt{s} = 200$ GeV. Different panels correspond to different p_t cuts applied to the cross section.

bands is obtained with $\mu^2 = p_{t1}^2$, and the shaded area is obtained by taking a scale larger by 50%.[5] In the following, we shall therefore always employ $\mu^2 = p_{t1}^2$, which should provide the best agreement with data.

Figure 3 shows that the suppression of the away-side peak provided by our calculation is in agreement with the data, although robust conclusions are impossible to draw due to the large uncertainties in d + Au collisions. We also notice that our calculation reasonably captures the magnitude of $CP(\Delta\phi)$ at the away-side peak of p + p collisions. What we fail in reproducing, though, is the width of the measured correlation in p + p, which appears to be broader than our result. This has a simple explanation: in our calculation we are not supplementing the cross section with Sudakov factors; i.e., we do not take into account the radiation of soft gluons in both the initial and the final state, which would naturally provide a broadening of the correlation function. This was done in Ref. [38], using GBW-type parametrization for the gluon TMDs, but it remains to be done with the rcBK gluon TMDs. An attempt of such Sudakov resummation in the case of di-jet production was made within the Kutak-Sapeta (KS) approach [39] (see Sec. V), and the results are promising, in the sense that one observes a clear broadening around $\Delta\phi = \pi$ when Sudakov resummation is included. We finally note that the correlation function shown in Fig. 3 is somewhat less flat than the one obtained in [29]. By comparison, our formalism is valid in a narrower window near $\Delta\phi = \pi$, but it is more accurate there.

B. Predictions for p + Au collisions

In Fig. 4, we present predictions for the away-side peak of neutral pions in p + p and p + Au collisions at $\sqrt{s} = 200$ GeV. This is achieved by integrating Eq. (5) over the kinematic cuts used by the STAR collaboration in their new analysis. We predict that the away-side peak is suppressed in p + Au by a factor close to 2. We find this conclusion to be rather independent of the p_t window chosen for the measurement.

V. RAPIDITY DEPENDENCE OF THE SUPPRESSION AND COMPARISON WITH THE KUTAK-SAPETA APPROACH

A generic prediction of the CGC framework is that any effect due to gluon saturation should become less visible if we move towards more central rapidities; i.e., in our case, if

---

[5] We cannot test values of μ^2 lower than p_{t1}^2, as they would lead to unreasonably small values of the factorization scale.

we reduce the dilute-dense asymmetry by probing larger values of x in the nuclei. Consequently, the suppression of the away-side peak in $\mathrm{p+A}$ collisions relative to $\mathrm{p+p}$ should essentially fade away if we correlate particles in more central rapidity intervals. It is important to stress that the dependence on rapidity is a very specific feature of the saturation framework, which is not predicted by typical competing effects, e.g., conservation of total transverse momentum [40], or other energy-momentum conservation corrections which are relevant in the proximity of $x_1 \to 1$ [41,42]. Another competing description is that reported by Kang *et al.* [43], who manage to describe the suppression of the away-side peak without resorting to a CGC description, but solely from (cold) nuclear transverse-momentum broadening effects. Such models do not predict a specific dependence on the rapidity, so that the CGC interpretation would be strongly favored if such dependence is observed in data. Let us stress that the away-side peak in different rapidity intervals could be easily measured at the STAR or at the LHCb detectors, which present wide rapidity coverages.

Let us show, then, what our formalism predicts for the rapidity dependence of the suppression of the away-side peak. For reasons which will appear clear in the following discussion, it is very instructive to perform calculations and show results using both our rcBK formalism and the alternative Kutak-Sapeta (KS) approach [16], which we briefly review below.

In the KS approach, the momentum space version of the BK equation is used (written below for $\mathcal{F}_p = \pi\mathcal{F}_{qg}^{(1)}$, for a target proton):

$$\mathcal{F}_p(x,k^2) = \mathcal{F}_p^{(0)}(x,k^2) + \frac{\alpha_s N_c}{\pi}\int_x^1 \frac{dz}{z}\int_{\mu^2}^{\infty} \frac{dl^2}{l^2}\left\{\frac{l^2\mathcal{F}_p(\frac{x}{z},l^2) - k^2\mathcal{F}_p(\frac{x}{z},k^2)}{|l^2-k^2|} + \frac{k^2\mathcal{F}_p(\frac{x}{z},k^2)}{|4l^4+k^4|^{\frac{1}{2}}}\right\}$$
$$-\frac{2\alpha_s^2}{R^2}\left[\left(\int_{k^2}^{\infty}\frac{dl^2}{l^2}\mathcal{F}_p(x,l^2)\right)^2 + \mathcal{F}_p(x,k^2)\int_{k^2}^{\infty}\frac{dl^2}{l^2}\ln\left(\frac{l^2}{k^2}\right)\mathcal{F}_p(x,l^2)\right]. \quad (25)$$

This way of writing the BK equation is convenient as it allows to include relatively easily some higher-order corrections, and in particular running-coupling corrections [44]. To write down the nonlinear term of Eq. (25) (last line in the equation) for the impact-parameter-integrated gluon distribution, it is assumed that integration over impact parameter yields $\int d^2b = \pi R^2$, where R is the radius of the target proton. The evolution of the gluon TMD in the case of a nucleus, $\mathcal{F}_A$, is then obtained through the following formal substitution in Eq. (25),

$$\frac{1}{R^2} \to c\,\frac{A}{R_A^2}, \quad \text{where } R_\mathrm{A}^2 = R^2A^{2/3}. \quad (26)$$

In the above equation, R_A is the nuclear radius, A is the mass number ($A = 208$ for Pb), and c is a parameter that is supposed to vary between 0.5 and 1, to assess the uncertainty related to the nonlinear term. The density $\mathcal{F}_A$ obtained from Eq. (25) with the substitution above is the nuclear gluon density normalized to the number of nucleons in the nuclei.

The KS evolution in Eq. (25) is A-dependent through the nonlinear term (it has to be so, since $\mathcal{F}_A$ is an impact parameter integrated distribution), but the prescription for the initial condition is to choose the same in the nuclear case as in the proton case, i.e., $\mathcal{F}_A(x_0,k^2) = \mathcal{F}_p(x_0,k^2)$. This is the major difference with respect to the approach presented in Sec. III, where an A-dependent initial condition and an A-independent evolution were used.

Figure 5 shows an illustration of the effect due to this difference between the rcBK and the KS approaches, which are both based on the same small-x evolution. In the figure we show $\mathcal{F}_{gg}^{(1)}$ for a target nucleus divided by the same quantity for a target proton,[6] for different values of rapidity Y, which is defined as $Y = \ln(0.01/x_2)$. On the left, the rcBK distributions predict the same amount of suppression at each value of Y in the fully saturated region, $k_t \sim 0$, because the small-x evolution is A independent. This is not the case in panel (b), where the ratio in the KS scheme is equal to unity for $Y = 0$ (not shown), and the difference in the evolution of the nucleus with respect to the proton is manifest already at $k_t = 0$. Note that the plot is drawn for $c = 0.5$, but we stress that the qualitative picture is essentially independent of the choice of this constant.

This difference shown in Fig. 5 has a non-negligible impact on the rapidity dependence of the suppression of the away-side peak, which is the subject under study in this section. To show this, we calculate the ratio $CP(\Delta\phi)$ in $\mathrm{p+Au}$ over the same quantity in $\mathrm{p+p}$ using both the standard rcBK approach and the KS alternative proposal,[7] and we look at its dependence with rapidity. We keep the old STAR kinematics of Fig. 3 for the p_t of the produced hadrons, and we compute $CP(\Delta\phi)_{pA}/CP(\Delta\phi)_{pp}$, with an obvious meaning of the notation, around $\Delta\phi = \pi$ in different intervals of rapidity. Results are shown in Fig. 6.

---

[6] The factor 3 appearing in the denominator of the rcBK ratio corresponds to the initial value of the ratio $Q_s^2[\mathrm{A}]/Q_s^2[\mathrm{pp}]$, as introduced in Sec. III.

[7] The KS implementation we have in mind is not directly the one performed in [16] which involves a single gluon TMD, but rather an adaptation of it to the away-side peak region, involving the several gluon TMDs needed just as in (5).

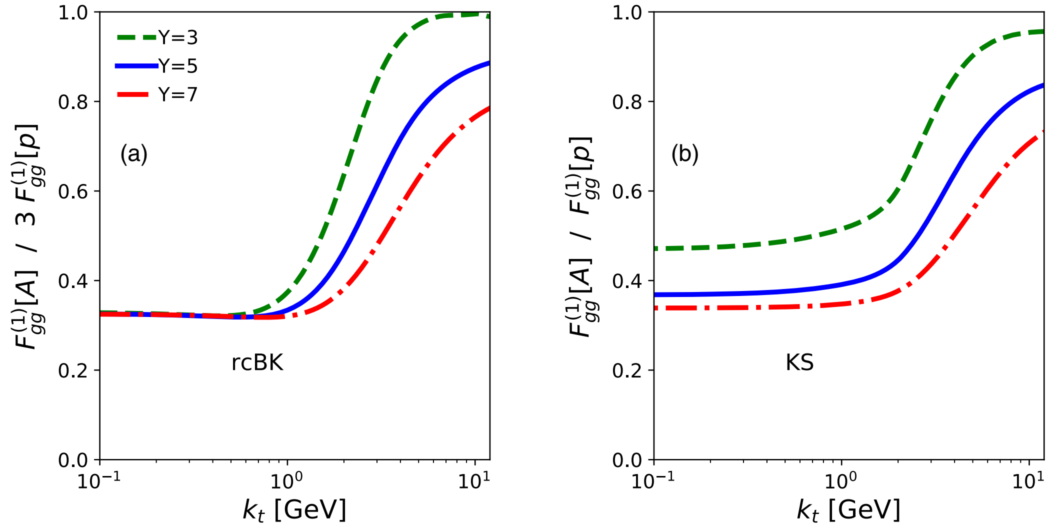

FIG. 5. The figure shows $\mathcal{F}_{gg}^{(1)}$ for a target nucleus divided by the same quantity for a target proton, as function of k_t. Results are shown within two different evolution schemes, namely rcBK [panel (a)] and KS approximation [panel (b)]. The ratio is taken at different values of x_2, indicated with different line styles. In the figure, $Y = \ln(0.01/x_2)$.

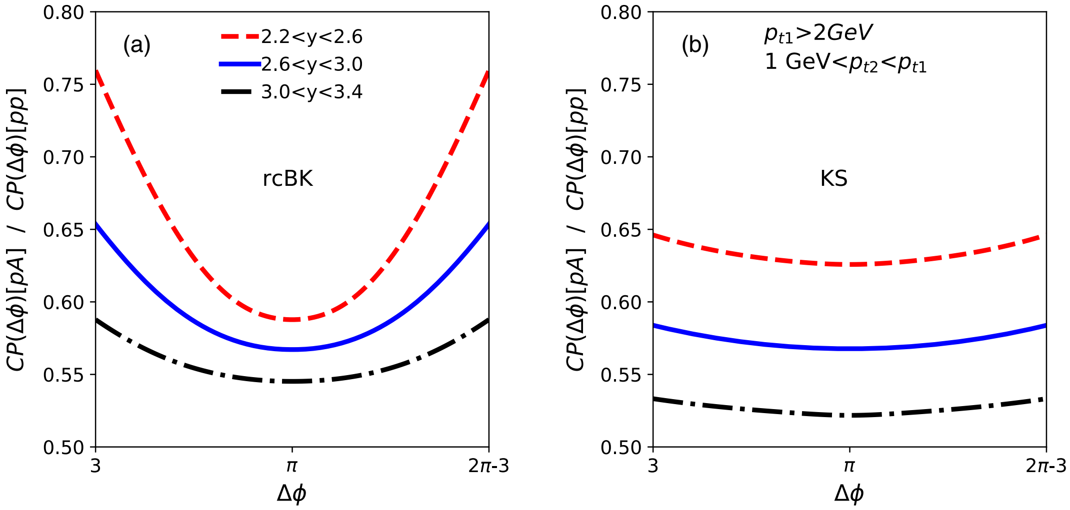

FIG. 6. The figure shows the ratio $CP(\Delta\phi)_{pA}/CP(\Delta\phi)_{pp}$ around $\Delta\phi = \pi$. Different line styles represent different rapidity intervals. Panel (a) shows results with gluon TMDs obtained as described in Sec. III. In panel (b) the TMDs are obtained using the KS scheme, with $c = 0.5$.

We find that both schemes provide a hierarchy as function of rapidity expected in the saturation framework: Larger values of the ratio around $\Delta\phi = \pi$ correspond to more central rapidities, i.e., less suppression at the away-side peak. We stress that this is a peculiar feature of the saturation framework, and we strongly encourage measurements of this ratio in different rapidity intervals, which could provide, arguably, the strongest possible evidence in favor of the saturation picture. In addition, we expect such quantity to be almost unaffected by the uncertainties on the factorization scale (which turned out to be quite large in Fig. 3), as they are likely to cancel in the ratio.

Besides confirming the generic prediction of the CGC framework, precise measurements in p + Au collisions might as well shed light on the very validity of the approaches taken for the small-x evolution of the dense targets. In Fig. 6 we observe two notable differences between rcBK and KS. First, the dependence on rapidity at $\Delta\phi = \pi$ is about twice stronger in the KS approach [panel (b)]: This results from having a small-x evolution at low k_t (Fig. 5). Second, the rcBK case presents ratios which grow towards unity much faster as we move away from the back-to-back region. Specifically, the ratio at $\Delta\phi = 3$ is larger by 15% in the rcBK scheme. Such visible differences are expected to be sizable in the upcoming data, and would help improve significantly our understanding of the evolution equations of QCD in the nonlinear small-x regime.

VI. CONCLUSION

We have calculated the production of back-to-back pions in $\mathrm{p+A}$ and $\mathrm{p+p}$ collisions at RHIC energies, using the state-of-the-art CGC framework, i.e., the cross section reported in Eq. (5). We have developed a novel approach for the small-x evolution of the TMD gluon distributions $\mathcal{F}_{ag}^{(i)}$, in which they are obtained from the BK evolution with an evolution kernel that includes running coupling corrections. The evolution is identical for proton and nuclear targets, the only difference being the value of Q_s^2 at the initial condition. The validity of our framework is confirmed by the good agreement observed between the available data and our results in Fig. 3.

We thus derived genuine predictions of the CGC theory. The away-side peak in upcoming $\mathrm{p+Au}$ data is suppressed by about a factor 2 with respect to $\mathrm{p+p}$ collisions (Fig. 4), and this suppression tends to disappear as we reduce the dilute-dense asymmetry of the problem (Fig. 6). We stress, once more, that the combination of these two effects is a much stronger probe of gluon saturation than the suppression of the away-side peak alone. We have further compared the expectation of our framework to those of another state-of-the-art rcBK implementation, namely, the KS approach. Using the observable proposed in Fig. 6, $\mathrm{p+Au}$ data will potentially allow us to make a data-driven distinction between these two schemes of small-x evolution.

Before concluding, we stress that our calculation lacks an important ingredient: The inclusion of the soft gluon resummation, i.e., of Sudakov factors attached to the cross section which could potentially solve our problem of a too narrow correlation peak around $\Delta\phi = \pi$ (Fig. 3). This improvement of our formalism will be presented in an upcoming publication.

ACKNOWLEDGMENTS

The work of C. M. was supported in part by the Agence Nationale de la Recherche under Project No. ANR-16-CE31-0019-02. The work of M. M. has been supported by Grant No. 17-04505S of the Czech Science Foundation (GACR) and has been performed in the framework of COST Action CA15213 THOR. Computational resources were provided by the CESNET LM2015042 and the CERIT Scientific Cloud LM2015085, provided under the program “Projects of Large Research, Development, and Innovations Infrastructures.”

[1] F. Gelis, E. Iancu, J. Jalilian-Marian, and R. Venugopalan, Annu. Rev. Nucl. Part. Sci. **60**, 463 (2010).
[2] F. Gelis, Int. J. Mod. Phys. A **28**, 1330001 (2013).
[3] J. P. Blaizot, Rep. Prog. Phys. **80**, 032301 (2017).
[4] C. Marquet, Nucl. Phys. **A796**, 41 (2007).
[5] K. Tuchin, Nucl. Phys. **A846**, 83 (2010).
[6] J. L. Albacete and C. Marquet, Phys. Rev. Lett. **105**, 162301 (2010).
[7] A. Stasto, B. W. Xiao, and F. Yuan, Phys. Lett. B **716**, 430 (2012).
[8] T. Lappi and H. Mantysaari, Nucl. Phys. **A908**, 51 (2013).
[9] A. Ayala, M. Hentschinski, J. Jalilian-Marian, and M. E. Tejeda-Yeomans, Phys. Lett. B **761**, 229 (2016).
[10] A. van Hameren, P. Kotko, K. Kutak, C. Marquet, E. Petreska, and S. Sapeta, J. High Energy Phys. 12 (2016) 034.
[11] P. Kotko, K. Kutak, S. Sapeta, A. M. Stasto, and M. Strikman, Eur. Phys. J. C **77**, 353 (2017).
[12] J. L. Albacete and C. Marquet, Prog. Part. Nucl. Phys. **76**, 1 (2014).
[13] E. Braidot (STAR Collaboration), arXiv:1005.2378.
[14] A. Adare *et al.* (PHENIX Collaboration), Phys. Rev. Lett. **107**, 172301 (2011).
[15] J. Jalilian-Marian and Y. V. Kovchegov, Phys. Rev. D **70**, 114017 (2004); **71**, 079901(E) (2005).
[16] K. Kutak and S. Sapeta, Phys. Rev. D **86**, 094043 (2012).
[17] F. Dominguez, B. W. Xiao, and F. Yuan, Phys. Rev. Lett. **106**, 022301 (2011).
[18] F. Dominguez, C. Marquet, B. W. Xiao, and F. Yuan, Phys. Rev. D **83**, 105005 (2011).
[19] C. Marquet, E. Petreska, and C. Roiesnel, J. High Energy Phys. 10 (2016) 065.
[20] C. Marquet, C. Roiesnel, and P. Taels, Phys. Rev. D **97**, 014004 (2018).
[21] D. Boer, P. J. Mulders, J. Zhou, and Y. j. Zhou, J. High Energy Phys. 10 (2017) 196.
[22] T. Altinoluk, N. Armesto, A. Kovner, M. Lublinsky, and E. Petreska, J. High Energy Phys. 04 (2018) 063.
[23] E. Petreska, Int. J. Mod. Phys. E **27**, 1830003 (2018).
[24] P. Kotko, K. Kutak, C. Marquet, E. Petreska, S. Sapeta, and A. van Hameren, J. High Energy Phys. 09 (2015) 106.
[25] J. L. Albacete, N. Armesto, J. G. Milhano, P. Quiroga-Arias, and C. A. Salgado, Eur. Phys. J. C **71**, 1705 (2011).
[26] I. Balitsky, Nucl. Phys. **B463**, 99 (1996).
[27] Y. V. Kovchegov, Phys. Rev. D **60**, 034008 (1999).
[28] J. L. Albacete and Y. V. Kovchegov, Phys. Rev. D **75**, 125021 (2007).
[29] J. L. Albacete and C. Marquet, Phys. Lett. B **687**, 174 (2010).
[30] H. Fujii, F. Gelis, and R. Venugopalan, Nucl. Phys. **A780**, 146 (2006).

[31] Y. V. Kovchegov, J. Kuokkanen, K. Rummukainen, and H. Weigert, Nucl. Phys. **A823**, 47 (2009).

[32] C. Marquet and H. Weigert, Nucl. Phys. **A843**, 68 (2010).

[33] A. Dumitru, J. Jalilian-Marian, T. Lappi, B. Schenke, and R. Venugopalan, Phys. Lett. B **706**, 219 (2011).

[34] E. Iancu and D. N. Triantafyllopoulos, J. High Energy Phys. 04 (2012) 025.

[35] M. Alvioli, G. Soyez, and D. N. Triantafyllopoulos, Phys. Rev. D **87**, 014016 (2013).

[36] A. D. Martin, W. J. Stirling, R. S. Thorne, and G. Watt, Eur. Phys. J. C **63**, 189 (2009).

[37] D. de Florian, R. Sassot, M. Epele, R. J. Hernndez-Pinto, and M. Stratmann, Phys. Rev. D **91**, 014035 (2015).

[38] A. Stasto, S. Y. Wei, B. W. Xiao, and F. Yuan, Phys. Lett. B **784**, 301 (2018).

[39] A. van Hameren, P. Kotko, K. Kutak, and S. Sapeta, Phys. Lett. B **737**, 335 (2014).

[40] N. Borghini, Eur. Phys. J. C **30**, 381 (2003).

[41] B. Z. Kopeliovich, J. Nemchik, I. K. Potashnikova, M. B. Johnson, and I. Schmidt, Phys. Rev. C **72**, 054606 (2005).

[42] L. Frankfurt and M. Strikman, Phys. Lett. B **645**, 412 (2007).

[43] Z. B. Kang, I. Vitev, and H. Xing, Phys. Rev. D **85**, 054024 (2012).

[44] K. Kutak and J. Kwiecinski, Eur. Phys. J. C **29**, 521 (2003).

PHYSICAL REVIEW D **100,** 054015 (2019)

Solution to the Balitsky-Kovchegov equation with the collinearly improved kernel including impact-parameter dependence

D. Bendova, J. Cepila, J. G. Contreras, and M. Matas

Faculty of Nuclear Sciences and Physical Engineering, Czech Technical University in Prague, 115 19 Prah, Czech Republic

(Received 5 August 2019; published 16 September 2019)

The solution to the impact-parameter dependent Balitsky-Kovchegov equation with the collinearly improved kernel is studied in detail. The solution does not present the phenomenon of Coulomb tails at large impact parameters that have affected previous studies. The origin of this behavior is explored numerically. It is found to be linked to the fact that this kernel suppresses large daughter dipoles. Solutions based on a physics motivated form of the initial condition are used to compute predictions for structure functions of the proton and the exclusive photoproduction and electroproduction of vector mesons. A reasonable agreement is found when comparing to HERA and LHC data.

DOI: 10.1103/PhysRevD.100.054015

I. INTRODUCTION

Evolution equations are powerful tools to study the high-energy, equivalently, small-x limit of quantum chromodynamics (QCD) [1–3]. The availability of quality data from HERA [4] and the LHC [5] as well as the need for reliable phenomenology for the proposal of new electron-ion facilities [6,7] have given an extra impulse to the development of these tools.

In this work, the emphasis is placed on the Balitsky-Kovchegov (BK) evolution equation derived independently in the operator-product-expansion formalism by Balitsky [8], and by Kovchegov [9,10] within the color dipole approach [11–13]. It corresponds to the large-number-of-colors limit of the Jalilian-Marian-Iancu-McLerran-Weigert-Leonidov-Kovner (JIMWLK) evolution equations [14–19]. The BK equation describes the evolution with rapidity, Y, of the dipole-target scattering amplitude, $N(\vec{r}, \vec{b}, Y)$, where $\vec{r}$ is the transverse size of the dipole and $\vec{b}$ the impact parameter of the interaction.

Soon after its introduction, the kernel of the leading order BK equation was modified to include corrections that take into account the running of the coupling constant [20–23]. The resulting equation, referred to as rcBK below, when combined with appropriate initial conditions—embodying nonperturbative properties of the hadronic targets—and disregarding the impact-parameter dependence, produces solutions that have been successfully used to describe a wide variety of phenomena. In particular, the structure function data of the proton as measured at HERA was successfully described [24–27]. A few other applications of these solutions are, for example, gluon production in heavy-ion collisions [28], single particle [29] and J/ψ production in pp and pA collisions [30], dihadron correlations in p-Pb interactions [31] and even the flux of atmospheric neutrinos [32,33].

As already mentioned, these comparisons of rcBK-based predictions to data disregarded the impact-parameter dependence of the dipole amplitude. The reason is that earlier studies of solutions including the impact parameter found that the amplitude developed a powerlike dependence on $b \equiv |\vec{b}|$, the so-called Coulomb tails, which generate an unphysical growth of the cross section [34]. Nonetheless attempts were made to modify the kernel to solve this problem, for example, by adding an *ad hoc* cutoff for large sizes of the daughter dipoles [35]. The solutions found had no more Coulomb tails, but needed an extra, so-called *soft*, contribution to be able to describe HERA data on structure functions [36]. (A similar conclusion also holds for the solutions of the impact-parameter dependent JIMWLK equation [37].) Nonetheless, this approach did a good job when confronted with HERA data on exclusive vector meson production [38].

Recently, the kernel of the leading order equation has been improved by including the resummation of all double collinear logarithms [39] as well as two classes of single logarithmic corrections [40]. (See also early work on this direction in the context of the Balitsky-Fadin-Kuraev-Lipatov (BFKL) equation in [41].) Using this kernel and disregarding the dependence on the impact parameter, it was also possible to obtain a good description of HERA

---

data on the structure function of the proton. Finally, in the rapid communication [42], we have demonstrated that solutions of the BK equation with the collinearly improved kernel and an appropriate initial condition describe correctly the HERA data on structure functions and the t dependence of the exclusive photoproduction of J/ψ at one energy without the need of any additional *ad hoc* parameter or correction.

In this contribution the studies reported in [42] are extended to discuss in depth the behavior of the collinearly improved kernel and of the solutions of the corresponding BK equation, comparing them to the rcBK case. In addition, more details on the comparison to HERA structure function data are presented, and comparison of our predictions to relevant HERA and LHC data on exclusive vector meson photoproduction and electroproduction is provided. In all cases, the agreement between model and measurements is satisfactory.

The rest of this contribution is organized as follows: In Sec. II the formalism used throughout this work is reviewed. In Sec. III the technical details to solve the collinearly improved impact-parameter dependent BK equation are addressed. In Sec. IV the origin of the suppression at large impact parameters is discussed, the behavior of the solution is contrasted with solutions of the rcBK case, and the shape of the amplitude is shown at different values of rapidity, dipole size and impact parameter. In Secs. V and VI our predictions are confronted with structure function data measured at HERA, and to data for cross sections of exclusive photoproduction and electroproduction of ϕ, J/ψ, $\psi(2S)$, and $\Upsilon(1S)$ vector mesons measured both at HERA and at the LHC, respectively. Section VII contains a brief summary of our findings and presents our conclusions.

II. REVIEW OF THE FORMALISM

A. The Balitsky-Kovchegov equation

The BK evolution equation reads [21,22]

$$\begin{aligned}\frac{\partial N(\vec{r},\vec{b},Y)}{\partial Y} = \int d\vec{r}_1 K(r,r_1,r_2)(N(\vec{r}_1,\vec{b}_1,Y) \\ + N(\vec{r}_2,\vec{b}_2,Y) - N(\vec{r},\vec{b},Y) \\ - N(\vec{r}_1,\vec{b}_1,Y)N(\vec{r}_2,\vec{b}_2,Y)),\end{aligned} \tag{1}$$

where $r \equiv |\vec{r}|$, $r_1 \equiv |\vec{r}_1|$, and $r_2 \equiv |\vec{r}_2| \equiv |\vec{r}-\vec{r}_1|$ are the sizes of the original dipole and of the two daughter dipoles, respectively. Note that these are two-dimensional vectors in the same plane as the impact parameter. The magnitudes of the corresponding impact parameters are $b \equiv |\vec{b}|$, $b_1 \equiv |\vec{b}_1|$, $b_2 \equiv |\vec{b}_2|$. The kernel $K(r,r_1,r_2)$ is discussed below.

In this work, the solution to the BK equation is obtained under the assumption that the scattering amplitude $N(\vec{r},\vec{b},Y)$ depends solely on the sizes of the dipoles and of the impact parameter vectors. In practice, this means to solve the equation

$$\begin{aligned}\frac{\partial N(r,b,Y)}{\partial Y} = \int d\vec{r}_1 K(r,r_1,r_2)(N(r_1,b_1,Y) \\ + N(r_2,b_2 Y) - N(r,b,Y) \\ - N(r_1,b_1,Y)N(r_2,b_2,Y)),\end{aligned} \tag{2}$$

subjected to the condition that the angle between $\vec{r}$ and $\vec{b}$ is fixed. We chose to fix this angle at zero, meaning that these vectors are parallel.

B. Kernels of the Balitsky-Kovchegov equation

Several functional forms for the kernel of the BK equation have been proposed. The ones that are mentioned in this work are presented in the following.

The leading order kernel is given by

$$K_{\mathrm{LO}}(r,r_1,r_2) = \frac{\alpha_s^{\mathrm{nr}}}{2\pi}\frac{r^2}{r_1^2 r_2^2}, \tag{3}$$

where the nonrunning coupling, α_s^{nr}, is fixed to a constant value.

The running coupling kernel $K_{\mathrm{rc}}(r,r_1,r_2)$ reads [21]

$$\begin{aligned}K_{\mathrm{rc}}(r,r_1,r_2) = \frac{N_c\alpha_s(r^2)}{2\pi^2}\left(\frac{r^2}{r_1^2r_2^2} + \frac{1}{r_1^2}\left(\frac{\alpha_s(r_1^2)}{\alpha_s(r_2^2)} - 1\right)\right. \\ \left. + \frac{1}{r_2^2}\left(\frac{\alpha_s(r_2^2)}{\alpha_s(r_1^2)} - 1\right)\right),\end{aligned} \tag{4}$$

where N_c is the number of colors and α_s is the running coupling, which is further discussed in Sec. II C.

The running coupling kernel with a cutoff to tame the Coulomb tails generated by the evolution in the impact parameter is given by [36]

$$K_{\mathrm{rc}}^{\mathrm{bdep}}(r,r_1,r_2) = K_{\mathrm{rc}}(r,r_1,r_2)\Theta\left(\frac{1}{m^2} - r_1^2\right)\Theta\left(\frac{1}{m^2} - r_2^2\right), \tag{5}$$

where Θ is the Heaviside function and m a parameter to limit the size of daughter dipoles.

Finally, the collinearly improved kernel is [40]

$$\begin{aligned}K_{\mathrm{ci}}(r,r_1,r_2) \\ = \frac{\bar{\alpha}_s}{2\pi}\frac{r^2}{r_1^2r_2^2}\left[\frac{r^2}{\min(r_1^2,r_2^2)}\right]^{\pm\bar{\alpha}_s A_1} K_{\mathrm{DLA}}(\sqrt{L_{r_1 r}L_{r_2 r}}),\end{aligned} \tag{6}$$

where [41]

$$K_{\mathrm{DLA}}(\rho) = \frac{J_1(2\sqrt{\bar{\alpha}_s \rho^2})}{\sqrt{\bar{\alpha}_s \rho}}, \tag{7}$$

J_1 is the Bessel function (the inclusion of the Bessel function into the BK kernel has been previously discussed in [43]), the anomalous dimension is $A_1 = 11/12$, and

$$L_{r_i r} = \ln\left(\frac{r_i^2}{r^2}\right). \tag{8}$$

The sign factor in the exponent $\pm\bar{\alpha}_s A_1$ takes the value of the plus sign when $r^2 < \min(r_1^2, r_2^2)$ and the negative sign otherwise. For the running coupling

$$\bar{\alpha}_s = \alpha_s \frac{N_c}{\pi}, \tag{9}$$

the smallest dipole prescription is used throughout the computation according to

$$\alpha_s = \alpha_s(r_{\min}), \tag{10}$$

where $r_{\min} = \min(r_1, r_2, r)$. This prescription was compared to other prescriptions in [40], where it was found to work adequately in this context. This prescription has also been suggested as the natural option for the BK equation at next-to-leading order (NLO) [44].

C. Treatment of the coupling constant

In this work the running coupling is computed in the variable-number-of-flavors scheme, implemented according to

$$\alpha_{s,n_f}(r^2) = \frac{4\pi}{\beta_{0,n_f} \ln\left(\frac{4C^2}{r^2 \Lambda_{n_f}^2}\right)}, \tag{11}$$

where n_f corresponds to the number of flavors that are active, C^2 is an infrared regulator that takes into account the approximations made for the computation of the Fourier transform into the position space and is usually fit to data [25]. The variable β_{0,n_f} is the leading order coefficient of the QCD beta series and is given by relation

$$\beta_{0,n_f} = 11 - \frac{2}{3} n_f. \tag{12}$$

The value of the QCD scale parameter $\Lambda_{n_f}^2$ depends on the number of active flavors. When heavier quarks are active (charm and beauty quarks), its value is obtained from the relation [26]

$$\Lambda_{n_f - 1} = (m_f)^{1 - \frac{\beta_{0,n_f}}{\beta_{0,n_f-1}}} (\Lambda_{n_f})^{\frac{\beta_{0,n_f}}{\beta_{0,n_f-1}}}. \tag{13}$$

This recursive relation needs to be fixed at one point and for this the usual choice is to take the value of the running coupling at the scale of the mass of the Z^0 boson. In this way, Λ_5 is set with the use of the experimentally measured value of $\alpha_s(M_Z) = 0.1196 \pm 0.0017$, where the Z^0 mass is $M_Z = 91.18\ \mathrm{GeV}/c^2$ [45]. The number of active flavors is set depending on the transverse size of the mother dipole. The condition that governs this relates the mass of the heaviest quark considered to the values of the dipole size r. This condition can be expressed as

$$r^2 < \frac{4C^2}{m_f^2}. \tag{14}$$

Since all dipole sizes are accounted for in the BK evolution equation, there is a need to freeze the coupling at a set value after a certain dipole size is reached [25]. In this work, the coupling is frozen at $\alpha_s^{\mathrm{sat}} = 1$ as in [39].

The value of the parameter C affects the description of data by modifying the speed of the evolution and effectively changes the slope of the structure function. The higher value of this parameter the more the running of the coupling is suppressed and, consequently, the slope in the structure function F_2 is less steep. Figure 1 compares the running of α_s for two values of C: the one used here, $C = 9$, and the one used in [39], $C = 2.586$. The value $C = 9$ was set heuristically and since the solutions reproduce correctly the data, as shown below, it has not been further optimized.

III. IMPACT-PARAMETER SOLUTION TO THE BALITSKY-KOVCHEGOV EQUATION

A. Initial condition

The initial condition, already introduced in [42], depends on the impact parameter; it is suppressed in the regions

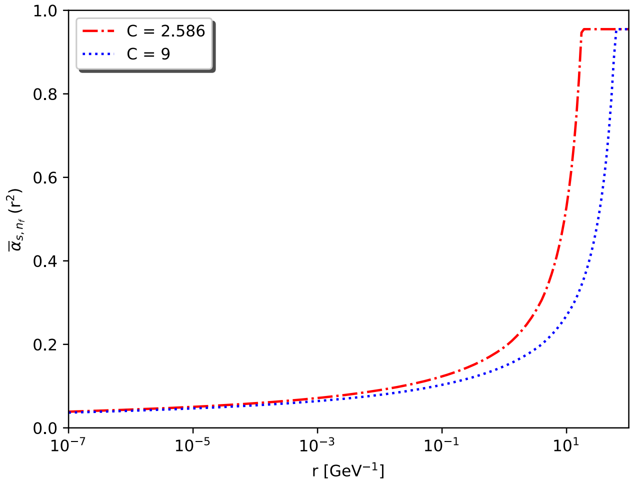

FIG. 1. Comparison between the behavior of $\bar{\alpha}_s$ computed from Eqs. (9) and (11) with $C = 2.586$ (red) and C = 9 (blue).

where r or b reaches large values, in order to respect the geometric nature of the dipole-proton interaction. The shape of its functional form is a combination of the expected behavior in r, which is obtained from the Golec-Biernat Wüsthoff (GBW) model [46], and the impact-parameter dependence, which uses a Gaussian distribution to reflect the expected profile of the proton. Such an approach has been used in similar forms in the past; e.g., in [47–51]. The main new ingredient with respect to the initial condition used in the previous studies [20,35,36,38] is the explicit separation of the contribution from the individual quark and antiquark forming the dipole. The initial condition is given by

$$N(r,b,Y=0) = 1 - \exp\left(-\frac{1}{2}\frac{Q_s^2}{4}r^2 T(b_{q_1},b_{q_2})\right), \qquad (15)$$

where b_{q_i} are the impact parameters of the quark and antiquark forming the dipole and

$$T(b_{q_1},b_{q_2}) = \left[\exp\left(-\frac{b_{q_1}^2}{2B_G}\right) + \exp\left(-\frac{b_{q_2}^2}{2B_G}\right)\right]. \qquad (16)$$

As a first attempt, the angle between $\vec{r}$ and $\vec{b}$ was fixed as shown schematically in Fig. 2. As the results obtained with this initial condition are satisfactory, no further optimization has been considered.

The parameters appearing in this initial condition, Q_s^2 and B_G, have a clear physical interpretation as the saturation scale and as the variance of the Gaussian distribution of the target in impact parameter, respectively. The value of the Q_s^2 parameter is chosen to be 0.496 GeV^2, such that the $F_2(x,Q^2)$ data are correctly described at the rapidity of the initial condition. The relation between x and rapidity is $Y = \ln(x_0/x)$, where $x_0 = 0.008$. The parameter B_G is set to 3.2258 GeV^{-2} in order to describe the data for exclusive photoproduction of J/ψ off protons at a photon–proton center-of-mass energy $\langle W_{\gamma p}\rangle = 100$ GeV, where as customary $x = (M^2+Q^2)/(W_{\gamma p}^2+Q^2)$ is used; here, M represents the mass of the vector meson.

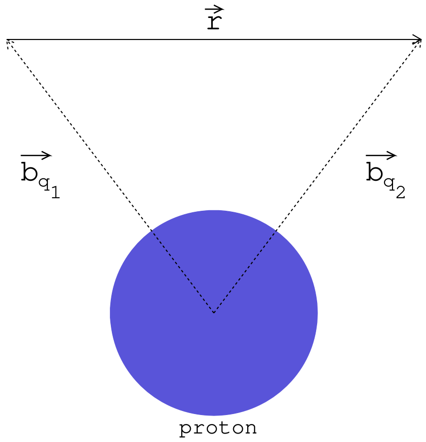

FIG. 2. Schematic picture of the variables that enter the initial condition presented in Eq. (15).

B. Setup for the numerical solution to the equation

The BK evolution equation does not have an analytic solution and therefore has to be solved numerically. The procedure used by us in [27,52] was extended to the case of the impact-parameter dependent BK equation [42] and the solution is evolved in rapidity with a step of $\Delta Y = 0.01$.

Fixed grids are used for r and b. They are logarithmic grids of base 10 with 25 evenly spaced points per order of magnitude, spanning the range from 10^{-7} to 10^4 GeV^{-1} for both the r and b variables. The integration over $\vec{r_1}$ is performed in polar coordinates, where r_1 is evaluated in the same grid as r and the polar angle, denoted by θ_{rr_1}, is evaluated in a fixed grid with 21 points separated by a constant step. The numerical integrations are performed applying Simpson's method.

Since the transverse dipole vectors are related as $\vec{r} = \vec{r_1} + \vec{r_2}$, by fixing the values of r and r_1 to the predefined grid, the values of r_2 are in general off the grid. Whenever this happens, linear interpolation in the $\log_{10}$ space is used to get the desired value of $N(r_2,b_2,Y)$. A similar approach is used for obtaining the value of the scattering amplitude whenever the value of b_1 or b_2 is off the grid.

The values of b_1 and b_2 are then computed from the relations $\vec{b_1} = \vec{b} + \vec{r_2}/2$ and $\vec{b_2} = \vec{b} - \vec{r_1}/2$ assuming a fixed angle between $\vec{r}$ and $\vec{b}$. As mentioned above, this angle is set to zero for the results presented below.

The solution to the BK equation has been implemented independently using C++ and the Intel Fortran Compiler. Both implementations have similar performance, with the Fortran version being slightly faster. In a standard personal computer, the program performs the evolution of the dipole amplitude in one unit of rapidity, that is 100 steps for the settings described above, in a bit less than one hour for one set of parameters.

To test the numerical stability of the selection of the grid, the setup was modified and the scattering amplitude was compared at $Y = 3$, $r = 1/\mathrm{GeV}$ and all values of b. We have changed the step in rapidity from 0.01 to 0.02, the number of steps in r and b per order of magnitude from 25 to 15 and the size of the grid in the polar angle from 21 to 16 and 31 points. Except for the change to 16 points in the grid for polar angles, all other changes produced a difference below the per-mil level. The use of the spare grid in polar angle produced changes almost at one percent level. In summary, with the chosen settings a numerical precision at the percent level, or even below it, is expected.

IV. THE SOLUTION TO THE BK EQUATION

A. Behavior of the collinearly improved kernel

As was shown in [42], the solutions to the BK equation do not exhibit Coulomb tails when using the collinearly improved kernel. This behavior is related to the suppression of this kernel for large values of the size of the daughter dipoles. As an illustration, Fig. 3 shows the ratio of the collinearly improved kernel, see Eq. (4), to the running-coupling kernel, see Eq. (6). (The parameter C for the running coupling in this kernel was chosen to be $C = 9$ just as in the collinearly improved kernel for the sake of a valid comparison.) The ratio is computed at $r = 1\ \mathrm{GeV}^{-1}$ and $\theta_{rr_1} = \pi/2$. Other values produce a similar picture. The figure shows that for large sizes of the daughter dipole the collinearly improved kernel is orders of magnitude smaller than the running-coupling one.

To follow up in more detail the origin of this behavior the kernels are divided into three parts. For the collinearly improved kernel, they are

$$K_{\mathrm{ci}}^{1} = \frac{\bar{\alpha}_s}{2\pi} \frac{r^2}{r_1^2 r_2^2}, \tag{17}$$

$$K_{\mathrm{ci}}^{2} = \left[\frac{r^2}{\min(r_1^2, r_2^2)}\right]^{\pm\bar{\alpha}_s A_1}, \tag{18}$$

$$K_{\mathrm{ci}}^{3} = K_{\mathrm{DLA}}\left(\sqrt{L_{r_1 r} L_{r_2 r}}\right). \tag{19}$$

The first term, K_{ci}^{1}, is present already at the leading order if one considers a fixed value of the running coupling, K_{ci}^{2} takes into account the contribution from the single collinear logarithms, and K_{ci}^{3} resums double collinear logarithms to all orders. The entire collinearly improved kernel is then given by the multiplication of all these factors as

$$K_{\mathrm{ci}} = K_{\mathrm{ci}}^{1} K_{\mathrm{ci}}^{2} K_{\mathrm{ci}}^{3}. \tag{20}$$

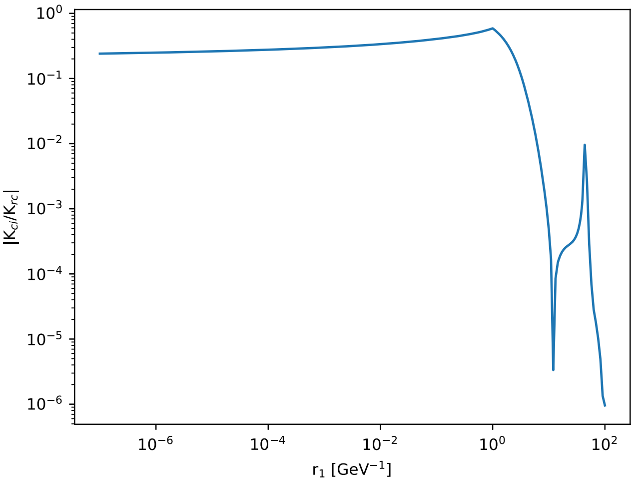

FIG. 3. Absolute value of the ratio $K_{\mathrm{ci}}/K_{\mathrm{rc}}$ at a fixed dipole size $r = 1\ \mathrm{GeV}^{-1}$ and orientation with respect to the daughter dipole $\theta_{rr_1} = \pi/2$ as a function of the daughter dipole size.

For the running coupling BK kernel, the separation in three parts is as follows:

$$K_{\mathrm{rc}}^{1} = \frac{N_c \alpha_s(r^2)}{2\pi^2} \frac{r^2}{r_1^2 r_2^2}, \tag{21}$$

$$K_{\mathrm{rc}}^{2} = \frac{N_c \alpha_s(r^2)}{2\pi^2} \frac{1}{r_1^2} \left(\frac{\alpha_s(r_1^2)}{\alpha_s(r_2^2)} - 1\right), \tag{22}$$

$$K_{\mathrm{rc}}^{3} = \frac{N_c \alpha_s(r^2)}{2\pi^2} \frac{1}{r_2^2} \left(\frac{\alpha_s(r_2^2)}{\alpha_s(r_1^2)} - 1\right), \tag{23}$$

whereas the running coupling kernel is then given by the addition of these constituent terms as

$$K_{\mathrm{rc}} = K_{\mathrm{rc}}^{1} + K_{\mathrm{rc}}^{2} + K_{\mathrm{rc}}^{3}. \tag{24}$$

The contribution of the three terms is shown in Fig. 4 at $r = 1\ \mathrm{GeV}^{-1}$ and $\theta_{rr_1} = \pi/2$ for each of the two kernels. The fact that the three terms are added in K_{rc}, but multiplied in K_{ci} explains numerically the suppression. Even though the first term is essentially the same for both kernels, the additive character of K_{rc} makes it deviate from the collinearly improved kernel at large r_1 values as shown in Fig. 4. There, we can see that even though the kernels are comparable in the low-r_1 region, at large r_1 values, the K_{rc}^{2} and K_{rc}^{3} terms become dominant, whereas in the collinearly improved kernel, the K_{ci}^{1} term suppresses the total value.

The physical reason of this suppression can be traced back to the fact that large daughter dipoles do not follow the time-ordering prescription (that is, they would live longer than the parent dipole) built in when setting up the resummation that leads to the collinearly improved kernel [40,53].

B. Contribution of the kernel terms to the evolution

The suppression for large sizes of the daughter dipole in the kernel is translated as a suppression of the amplitude at large b in the evolution. In this region only large $r_{1,2}$ contribute to the total integral in Eq. (2). This is true because a large impact parameter means that the probing dipole is far away from the target proton and the amplitude is therefore (at the initial condition) exponentially suppressed. Only dipoles with r_1 (r_2) $\sim 2b$ can be oriented so that their impact parameters b_1 (b_2) are small, such that they contribute to the evolution. But, since K_{ci} is suppressed in this region, the integral will be suppressed as well and the scattering amplitude will not grow fast at large b.

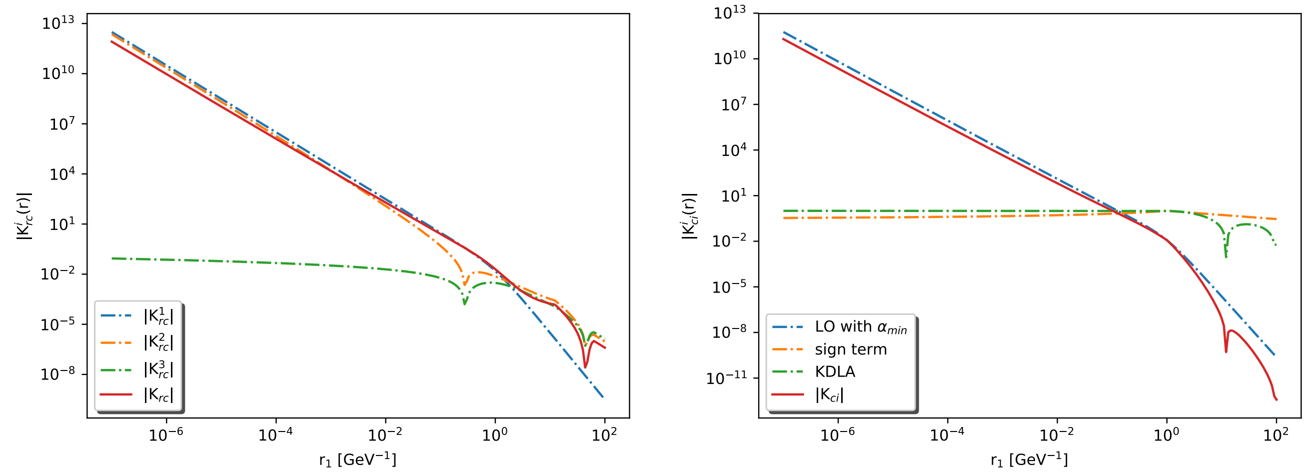

FIG. 4. The three constituent terms of the BK kernel for the running coupling (left) and collinearly improved cases (right) at a fixed dipole size $r = 1$ GeV^{-1} and orientation with respect to the daughter dipole $\theta_{rr_1} = \pi/2$.

This can be numerically studied by computing the contribution to the evolution of the three terms in the collinearly improved kernel. Figure 5 shows the scattering amplitude after evolution to $Y = 3$ using each time a kernel formed with different constituents. It is clearly seen that the impact parameter profile is mostly influenced by the inclusion of the $K^3_{\rm ci}$ term with the Bessel functions. This term originates from resumming double collinear logarithms. Note that also the term $K^2_{\rm ci}$, resumming single collinear logarithms, suppresses the large b region.

C. Behavior of the solution to the BK equation

The evolution of the scattering amplitude as a function of r for different fixed values of b is shown in the upper panels of Fig. 6, while the lower panels of the same figure show the evolution as a function of b for two fixed values of r. A two-dimensional view of the amplitude at two stages of the evolution is shown in Fig. 7. The amplitude decreases fast for small dipole sizes as expected. The suppression of large dipole sizes imposed in the initial condition is lifted with evolution. Similar behavior was observed in previous studies, e.g., [35]. Nonetheless, in the case of the collinearly improved kernel the growth at the largest dipole sizes is not as fast and a shoulder appears, after which the amplitude is again suppressed. The behavior as a function of impact parameter has been discussed above; the profile impact parameter grows, but the development of Coulomb tails is suppressed. Recently, a similar finding has been reported for the case of NLO BFKL equations at large impact parameters [54].

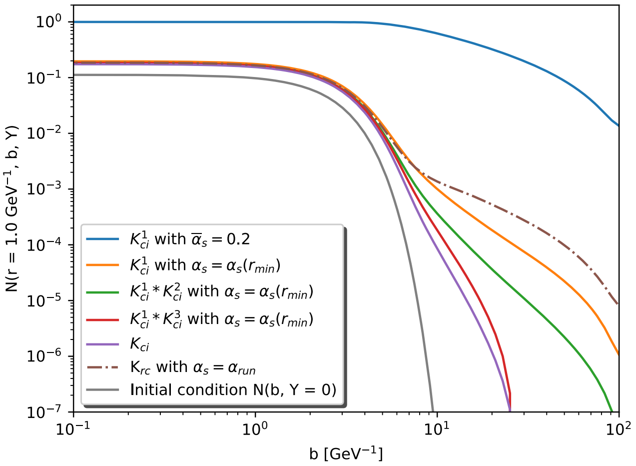

FIG. 5. The scattering amplitude evolved to $Y = 3$ with various kernels illustrates the effect of the different terms in the evolution and demonstrates that the computation based on the $K_{\rm ci}$ kernel does not develop the Coulomb tails seen when the $K_{\rm rc}$ kernel is used.

Finally, Fig. 8 shows $N(r, Y)$, defined as

$$N(r, Y) = \int d^2\vec{b} N(r, b, Y), \tag{25}$$

for different dipole sizes and for two kernels, the running coupling and the collinearly improved. For small dipoles the difference is larger and it grows with rapidity. At larger dipole sizes the difference between both kernels is smaller. Note that for the comparisons to data discussed below, the main numerical contribution comes from the region of relatively large dipoles. For the case of the structure function the main contribution for virtualities between 1 and 10 GeV^2 comes from dipoles of sizes on the range around 0.1/GeV to 10/GeV, see e.g., the lower panel of Fig. 4 in [27].

Another interesting observation is that $N(r, Y)$ is related to the σ_0 parameter introduced in studies based on the rcBK equation without impact-parameter dependence. Basically, σ_0 corresponds to the scale of $N(r, Y)$. Standard values

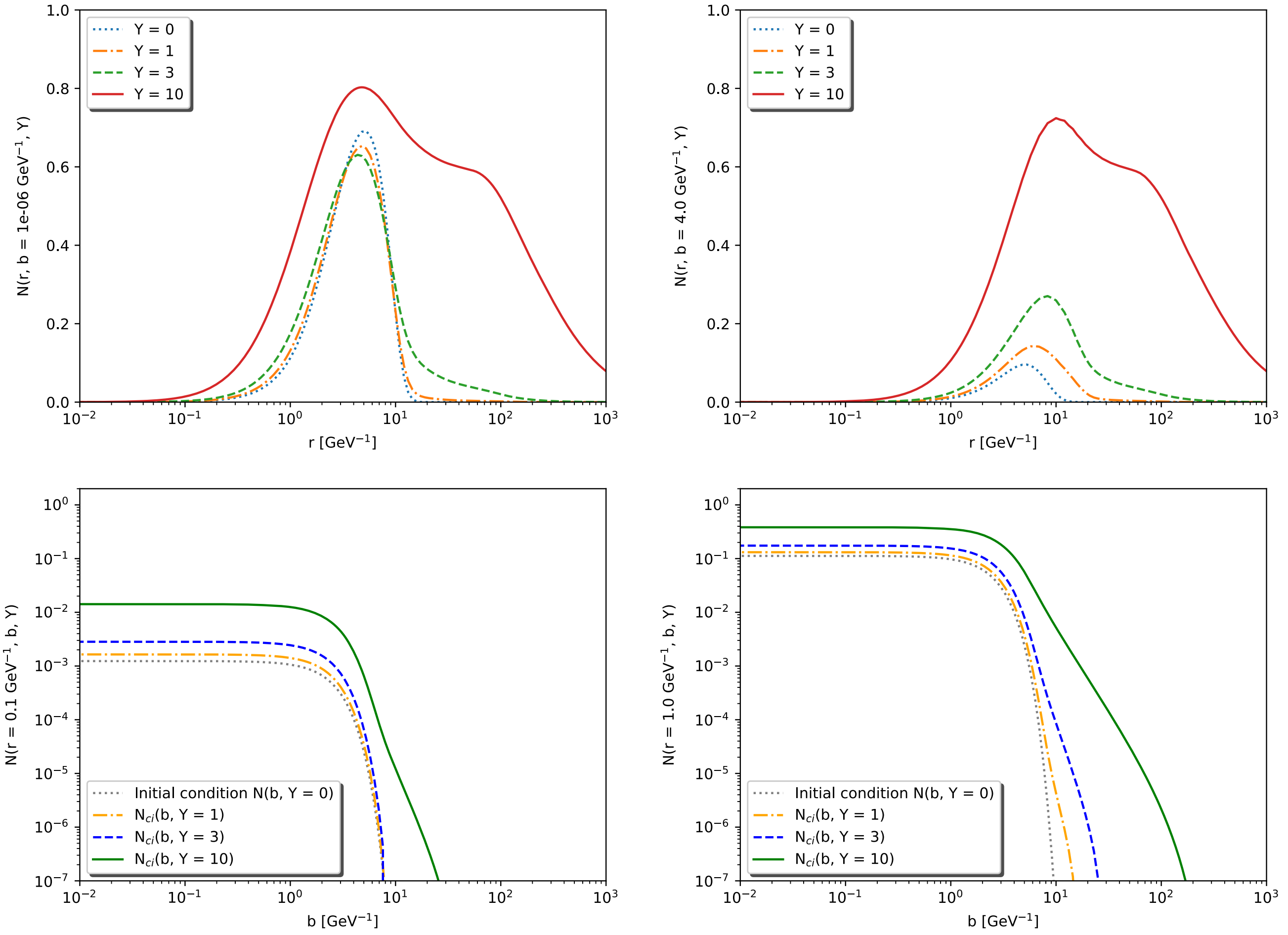

FIG. 6. The scattering amplitude as a solution to the BK equation with the collinearly improved kernel as a function of r for $b = 10^{-6}$ GeV^{-1} (upper left) and $b = 4$ GeV^{-1} (upper right), and as a function of b at $r = 0.1$ GeV^{-1} (lower left) and at $r = 1$ GeV^{-1} (lower right).

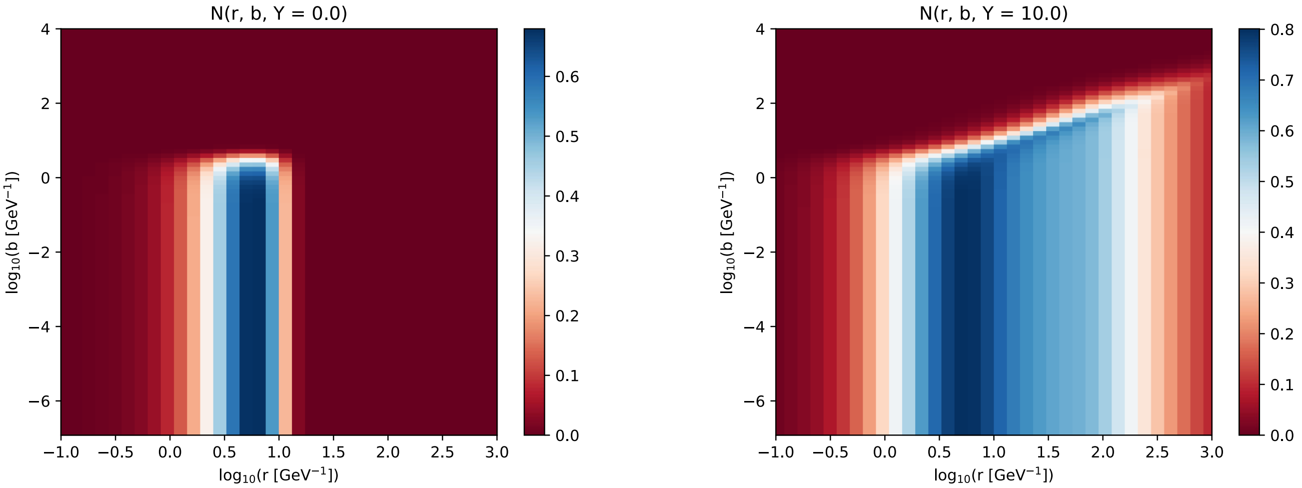

FIG. 7. Evolution of the scattering amplitude from the initial condition at $Y = 0$ (left) to $Y = 10$ (right).

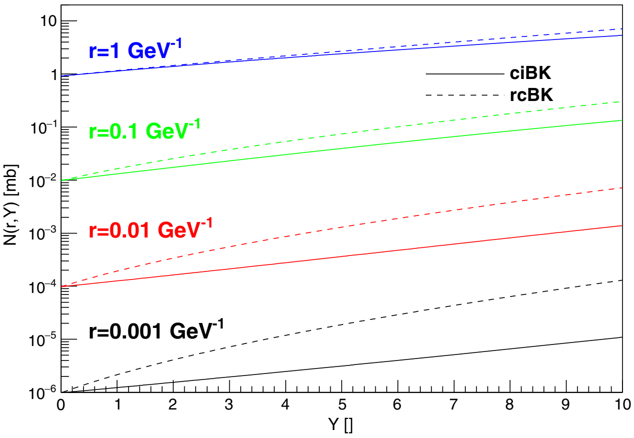

FIG. 8. Growth of the dipole-target amplitude integrated over impact parameter as a function of rapidity for solutions of the BK equations with the running coupling and the collinearly improved kernel.

found for this parameter are a few tens of mb, see e.g., Table I in [26]. Figure 8 justifies the order of magnitude of these values from the perspective of an impact-parameter dependent computation.

V. DEEP INELASTIC SCATTERING

A. Structure function and reduced cross section

Due to the fact that the dipole lives much longer than the typical interaction time, the computation of the total deep-inelastic scattering (DIS) cross section can be written as the convolution of separate terms. One of them is the wave function representing the probability of a virtual photon splitting into a quark-antiquark dipole. Here formulas and notation of [46] are used:

$$|\Psi^i_T(z,\vec{r},Q^2)|^2 = \frac{3\alpha_{\rm em}}{2\pi^2} e^2_{q_i}((z^2+(1-z)^2)\epsilon^2 K_1^2(\epsilon r) + m^2_{q_i} K_0^2(\epsilon r)), \tag{26}$$

and

$$|\Psi^i_L(z,\vec{r},Q^2)|^2 = \frac{3\alpha_{\rm em}}{2\pi^2} e^2_{q_i}(4Q^2 z^2(1-z)^2 K_0^2(\epsilon r)) \tag{27}$$

for the transverse and longitudinal polarization of the incoming photon, respectively, where z is the fraction of the total longitudinal momentum of the photon carried by the quark, K_0 and K_1 are the MacDonald functions, Q^2 is the virtuality of the probing photon, e_{qi} is the fractional charge (in units of elementary charge) of quark i, $\alpha_{\rm em} = 1/137$ and

$$\epsilon^2 = z(1-z)Q^2 + m^2_{q_i}, \tag{28}$$

where m_{q_i} is the mass of the considered quark, which is set to 100 MeV$/c^2$ for light quarks and 1.3 GeV$/c^2$ for charm quark and 4.5 GeV$/c^2$ for bottom quark. Note that the computed structure function does not depend strongly on the value of the mass of the light quarks (as was reported in [40]); this has been checked by also using $m_{u,d,s} = 10$ MeV$/c^2$, which did not influence the description of data. The total wave function then is

$$|\Psi^i_{T,L}(z,\vec{r})|^2 = |\Psi^i_T(z,\vec{r})|^2 + |\Psi^i_L(z,\vec{r})|^2. \tag{29}$$

According to the optical theorem, one can link the dipole-target cross section to the scattering amplitude by

$$\frac{d\sigma^{q\bar{q}}(\vec{r},x)}{d\vec{b}} = 2N(\vec{r},\vec{b},x). \tag{30}$$

Furthermore, it is usual to shift the value of the x at which the structure function and reduced cross section are computed according to the photoproduction kinematic shift [46],

$$\tilde{x} = x\left(1+\frac{4m^2_{q_i}}{Q^2}\right). \tag{31}$$

Using these ingredients, the relation for the computation of the structure function in the dipole model framework is

$$F_2(x,Q^2) = \frac{Q^2}{4\pi^2\alpha_{\rm em}} \int \sum_i d\vec{r} d\vec{b} dz |\Psi^i_{T,L}(z,\vec{r})|^2 \frac{d\sigma^{q\bar{q}}(\vec{r},\tilde{x})}{d\vec{b}}, \tag{32}$$

and the reduced cross section is computed as

$$\sigma_{\rm red}(y,x,Q^2) = F_2(x,Q^2) - \frac{y^2}{1+(1-y)^2} F_L(x,Q^2), \tag{33}$$

where $y = Q^2/(sx)$ is the inelasticity of the process, s is the squared of the center-of-mass energy of the collision and $F_L(x,Q^2)$ is given by the relation

$$F_L(x,Q^2) = \frac{Q^2}{4\pi^2\alpha_{\rm em}} \int \sum_i d\vec{r} d\vec{b} dz |\Psi^i_L(z,\vec{r})|^2 \frac{d\sigma^{q\bar{q}}(\vec{r},\tilde{x})}{d\vec{b}}. \tag{34}$$

B. Comparison to HERA data

The predictive power of this model is evaluated by confronting it with data from HERA on the $F_2(x,Q^2)$ structure function [55] in Fig. 9. A closer look is given in Fig. 10 for two values of the photon virtuality. To quantify

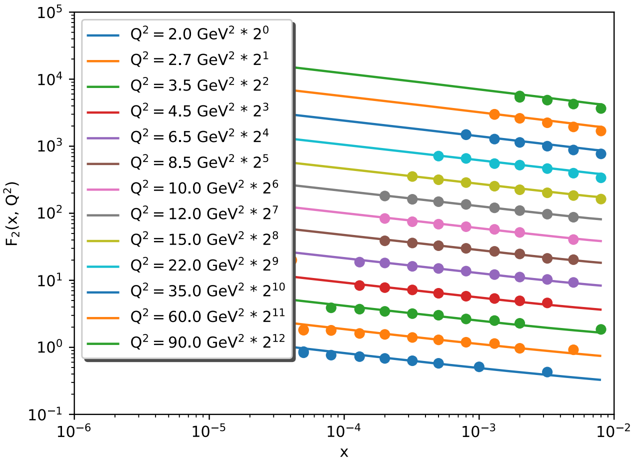

FIG. 9. Comparison of the structure function data from HERA [55] (solid circles) to the prediction of the impact-parameter dependent BK equation with the collinearly improved kernel (lines).

the level of agreement between data and model, Fig. 11 presents the percentage pulls associated with the structure function, which are given by

$$d_{\%} = 100 \frac{F_2^{\mathrm{BK}}(x,Q^2) - F_2^{\mathrm{HERA}}(x,Q^2)}{F_2^{\mathrm{HERA}}(x,Q^2)} \tag{35}$$

and by $D_{\%}$, which denotes the average of the corresponding values of $d_{\%}$. Finally, for completeness Fig. 12 shows the comparison of the model and data for the charm component of the proton structure function measured at HERA [55].

Overall, the agreement between prediction and data is within a few percent over most of the phase space. For our purposes this level of agreements is satisfactory. First, the equation we are using does not include the full angular dependence. Second, we have not needed to add any *ad hoc* component to describe data and the values of the parameters are reasonable from the point of view of the physics that is being probed. Furthermore, note that the BK equation that we are using is definitely not the last word on the subject. The full equation at NLO has already been computed [44], and a large effort is being done to use it for phenomenology [53,56–59]. There are also recent developments regarding the most adequate variable to evolve the scattering amplitude [60].

VI. PRODUCTION OF VECTOR MESONS

A. Exclusive cross section in the color-dipole approach

Similarly to the DIS process described in the previous section, the diffractive production of a vector meson as a result of the interaction of a virtual photon with the proton can be treated within the color-dipole approach. In this formalism, the exclusive cross section to produce a vector meson V is given by

$$\left.\frac{\mathrm{d}\sigma^{\gamma^* p\to \mathrm{V}p}}{\mathrm{d}|t|}\right|_{T,L} = \frac{(1+\beta^2)(R_g^{T,L})^2}{16\pi}|\mathcal{A}_{T,L}|^2, \tag{36}$$

where $\mathcal{A}_{T,L}$ is the scattering amplitude of the process. It is given as a convolution of the overlap of photon-meson wave functions with the dipole cross section given in Eq. (30) (for a detailed derivation see e.g., [61,62]) and takes the following form:

$$\mathcal{A}_{T,L}(x,Q^2,\vec{\Delta}) = i\int \mathrm{d}\vec{r}\int_0^1 \frac{\mathrm{d}z}{4\pi}\int \mathrm{d}\vec{b}|\Psi_{\mathrm{V}}^*\Psi_{\gamma^*}|_{T,L}$$
$$\times \exp\left[-i(\vec{b}-(1-z)\vec{r})\vec{\Delta}\right]\frac{\mathrm{d}\sigma^{q\bar{q}}}{\mathrm{d}\vec{b}}, \tag{37}$$

where the subscripts T, L denote the contribution from the virtual photon with transverse, respectively longitudinal, polarization, Ψ_{γ^*} is the wave function of a virtual photon

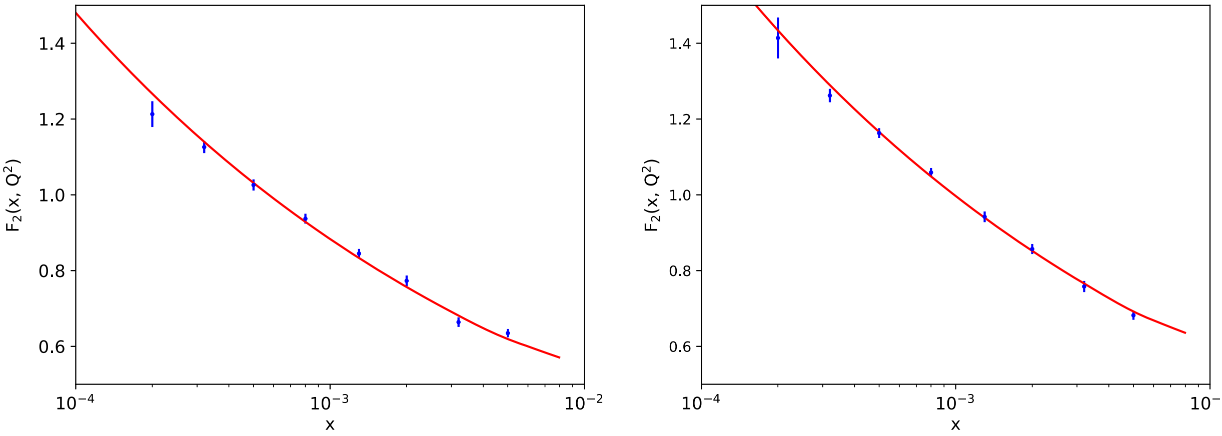

FIG. 10. Close-up comparison of the structure function data from HERA [55] (blue points) to the b-dependent prediction (red line) for $Q^2 = 8.5\ \mathrm{GeV}^2$ (left) and $Q^2 = 12\ \mathrm{GeV}^2$ (right).

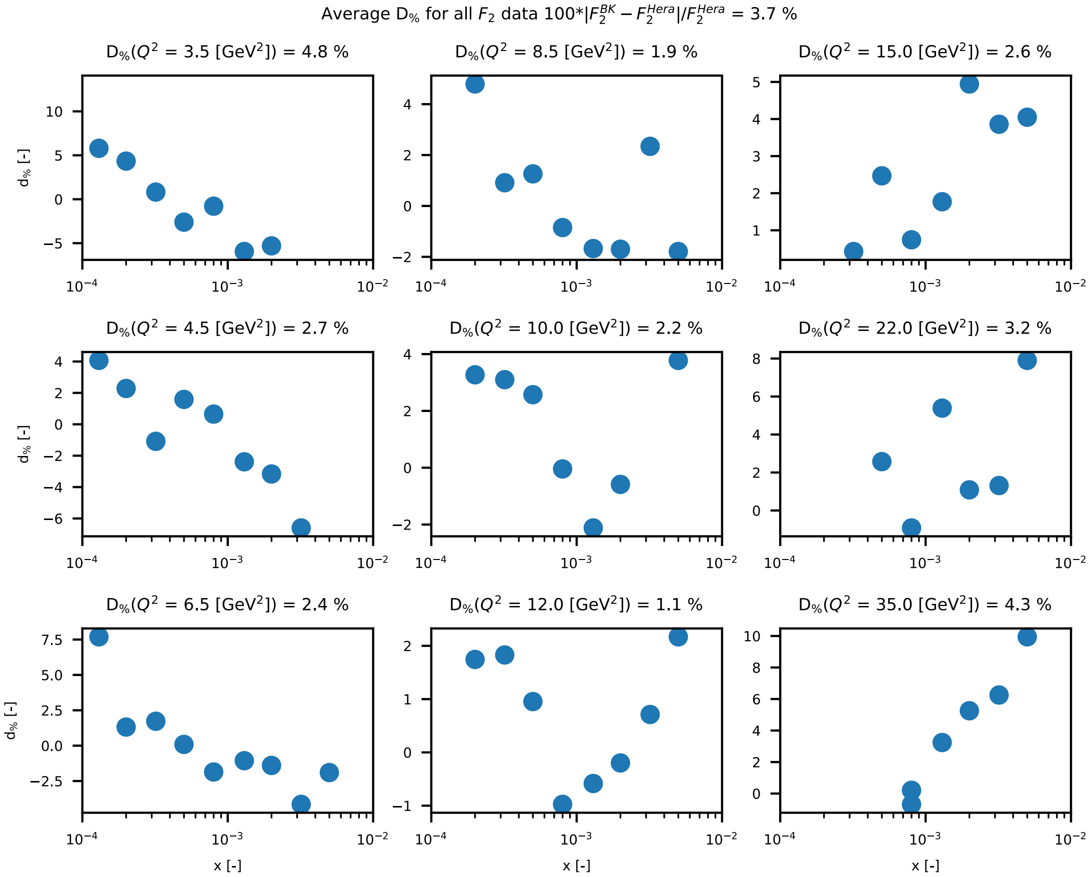

FIG. 11. The percentage pulls for various values of Q^2 and their average value.

which fluctuates into a dipole, Ψ_V represents the wave function of the vector meson, and $\vec{\Delta}^2 \equiv -t$, the square of the four momentum transferred in the proton vertex. Under the assumption of large photon-proton center-of-mass energies $W_{\gamma p}$,

$$x = \frac{Q^2 + M^2}{W_{\gamma p}^2 + Q^2}, \tag{38}$$

where M is the mass of the given vector meson.

The wave functions of a vector meson are modeled under the assumption that the vector meson is predominantly a $q\bar{q}$ pair with the same polarization and the spin structure as the original photon. The overlap of the photon-meson wave functions in Eq. (37) is given as

$$|\Psi_V^* \Psi_{\gamma^*}|_T = \hat{e}_f e \frac{N_C}{\pi z(1-z)} [m_f^2 K_0(\epsilon r)\phi_T(r,z) - (z^2 + (1-z)^2)\epsilon K_1(\epsilon r)\partial_r \phi_T(r,z)], \tag{39}$$

and

$$|\Psi_V^* \Psi_{\gamma^*}|_L = \hat{e}_f e \frac{N_C}{\pi} 2Qz(1-z) K_0(\epsilon r)\left[M\phi_L(r,z) + \delta \frac{m_f^2 - \nabla_r^2}{Mz(1-z)} \phi_L(r,z)\right], \tag{40}$$

with $\hat{e}_f$ being the effective charge of the given vector meson, ϵ defined by Eq. (28), and the parameter δ is a

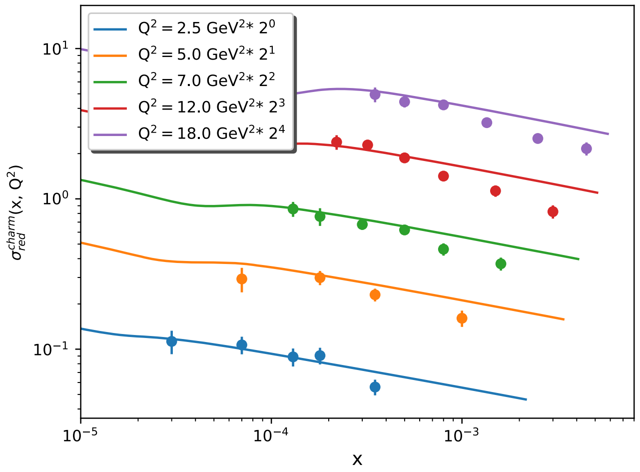

FIG. 12. The comparison of the prediction for the reduced cross section for charm to data from HERA [55].

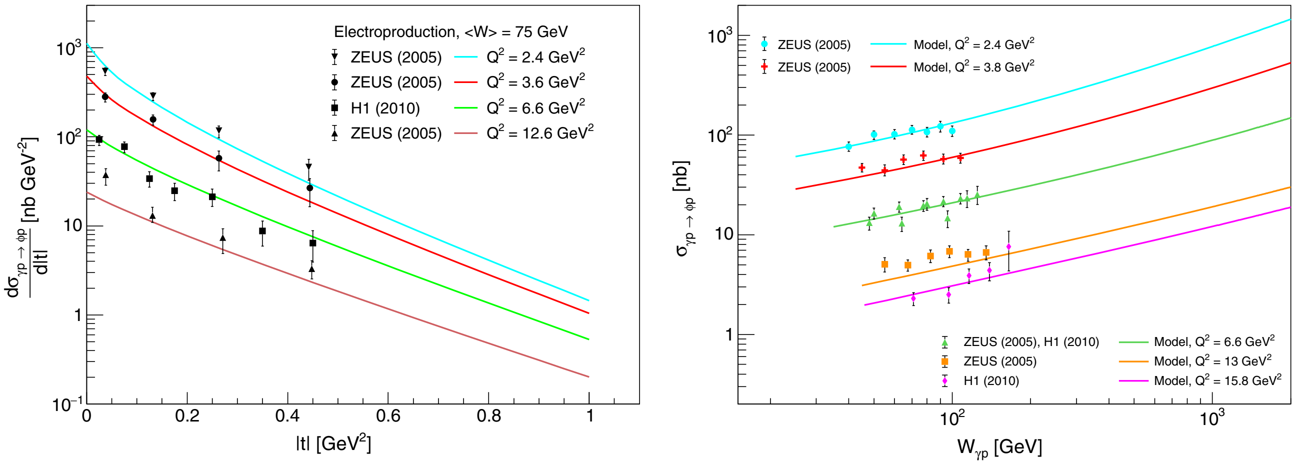

FIG. 13. Comparison of the predictions of the model (solid lines) with HERA data from H1 [68] and ZEUS [69] for the $|t|$ dependence (left) and the $W_{\gamma p}$ dependence (right) of the exclusive electroproduction cross section of the ϕ meson.

switch to include ($\delta = 1$) or exclude ($\delta = 0$) the nonlocal term in the longitudinal contribution. The scalar part $\phi_{T,L}$ of the wave function is, in general, model dependent. For our studies, we use the boosted Gaussian model [63–65] in which the δ parameter is fixed to one. The values of the parameters for the wave functions of all vector mesons are fixed according to Table I in [66].

The total exclusive cross section to produce a vector meson is given by the sum of the transverse and the longitudinal contributions defined by Eq. (36). Moreover two important corrections have to be applied. The derivation of the formula for the exclusive vector meson cross section is performed under the assumption that the scattering amplitude $\mathcal{A}_{T,L}(x, Q^2, \vec{\Delta})$ is purely imaginary. The real part of the amplitude can be accounted for by the extra term $(1 + \beta^2)$ in Eq. (37), where β is the ratio of real to imaginary parts of the scattering amplitude, for details see [61]. The other correction takes into account that there are two values of x involved in the interaction of the dipole with the proton and one should therefore use the off-diagonal gluon distribution for vector meson production. This effect can be accounted for by multiplying the scattering amplitude by a factor $R_g^{T,L}$, called the skewedness correction [67].

B. Comparison to data

Using the model described in this paper, the cross sections for exclusive photoproduction and electroproduction of ϕ, J/ψ, $\psi(2S)$, and $\Upsilon(1S)$ vector mesons are presented at different virtualities of the exchanged photon and they are compared to available experimental data. The presented results are calculated at the scales which allow perturbative treatment of the specific parts of the model.

In Fig. 13 a comparison of our predictions for the $|t|$ distributions and the total cross sections with HERA H1 [68] and ZEUS [69] data for the exclusive electroproduction of the ϕ meson for several values of Q^2 is shown. The predictions give a very good description of the available data, especially at low photon virtualities.

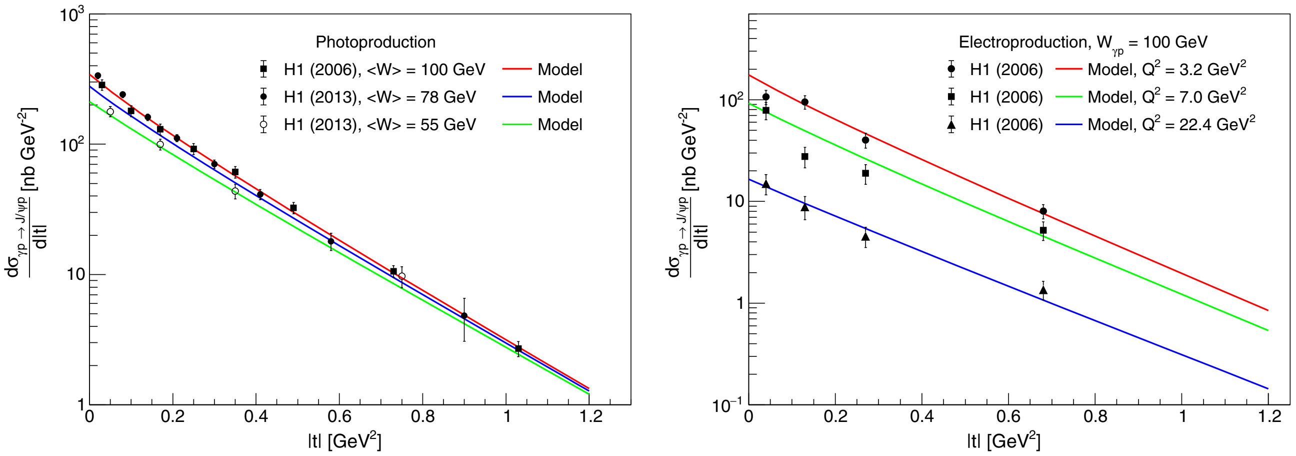

FIG. 14. Comparison of the predictions of the model (solid lines) with HERA data from H1 [70,71] for the $|t|$ dependence of the exclusive photoproduction (left) and electroproduction (right) cross sections of the J/ψ meson.

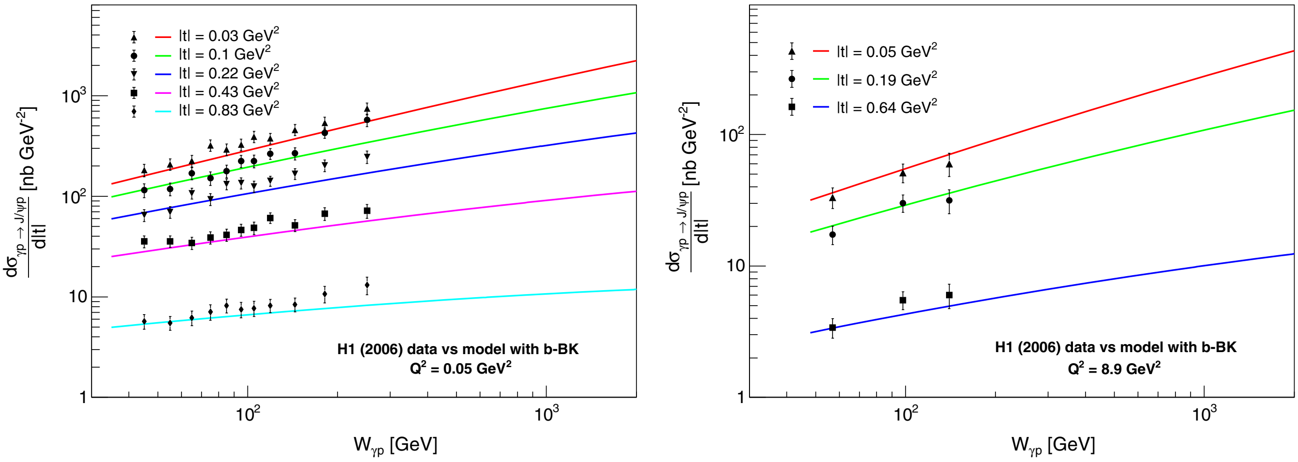

FIG. 15. Comparison of the predictions of the model (solid lines) with HERA data from H1 [70] for the W dependence of the exclusive photoproduction (left) and electroproduction (right) cross sections of the J/ψ meson at fixed $|t|$ values.

The predictions for the exclusive production of the J/ψ meson are compared with the experimental data from H1 [70,71] and ALICE [72,73] experiments in Figs. 14–16, for several different measurements of kinematic observables. In the left panel of Fig. 14, the comparison of the $|t|$ distribution of the photoproduction cross section is presented. The predictions give very good agreement with the data at energies $W_{\gamma p} = 55$ GeV and $W_{\gamma p} = 100$ GeV. The result for $W_{\gamma p} = 78$ GeV is slightly underestimated at low values of $|t|$, however one can notice the very small difference in the measured data with respect to the result for $W_{\gamma p} = 100$ GeV. Since the value of $W_{\gamma p}$ from the experimental data is a mean value estimated from a measured energy range, the result of the model can be considered satisfactory. The same comparison for the electroproduction at three different values of Q^2 can be seen in the right panel of the same figure. Although our predictions do not describe all the data points, we conclude the agreement between the data and the model to be qualitatively good. The same conclusion applies to the comparison of the model predictions with the measured $W_{\gamma p}$ dependence of the exclusive differential photoproduction and electroproduction cross sections at several fixed values of $|t|$ presented in Fig. 15. The agreement of the predictions with the data is very good at low values of $W_{\gamma p}$, however at larger values ($\sim 10^2$ GeV), the predictions are underestimated when compared to experimental photoproduction data. We have also obtained total cross section for the J/ψ production which is presented in the left panel of Fig. 16. The predictions for the electroproduction at three different values of Q^2 give a very good description of the available data. The result for photoproduction gives a

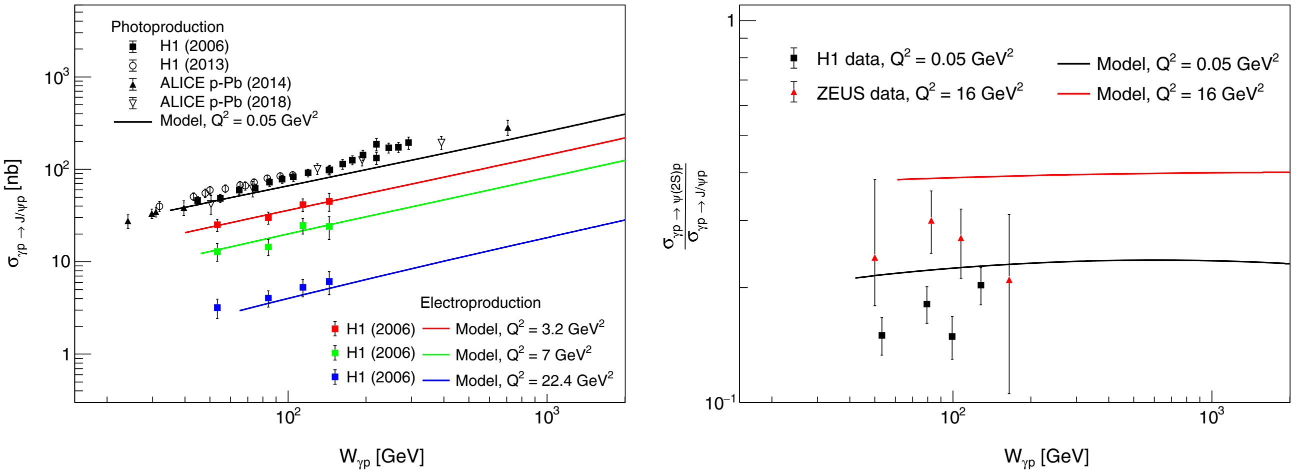

FIG. 16. Comparison of the predictions of the model (solid lines) with HERA data from H1 [70,71] and LHC data from ALICE [72,73] for the $W_{\gamma p}$ dependence of the exclusive photoproduction and electroproduction cross section of the J/ψ meson (left) and with HERA data from H1 [74] and ZEUS [75] for the $W_{\gamma p}$ dependence of the exclusive photoproduction and electroproduction cross section J/ψ/ψ(2S) ratio (right).

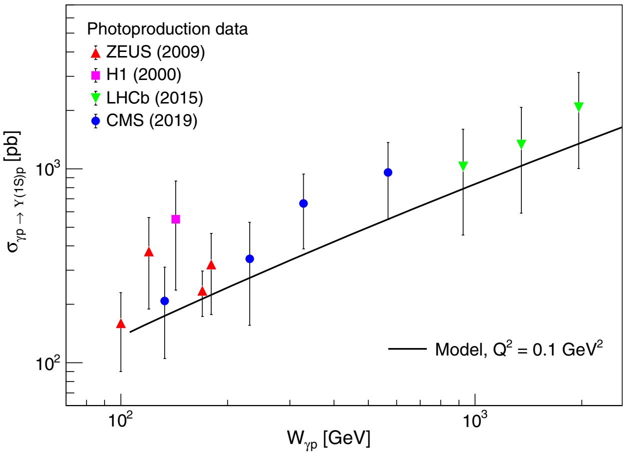

FIG. 17. Comparison of the predictions of the model (solid lines) with the HERA data from H1 [76] and ZEUS [77], and LHC data from LHCb [78] and CMS [79] for the $W_{\gamma p}$ dependence of the exclusive photoproduction cross section of the $\Upsilon(1S)$ meson.

good agreement with the data at low values of $W_{\gamma p}$, however at high energies the result is again underestimated when compared to data.

Also, the exclusive cross section of the $\psi(2S)$ meson was calculated within the model. The experimental data are not available for the total cross sections, but only for a ratio of the $\psi(2S)$ to J/ψ cross sections, the predictions for these ratios for photoproduction and electroproduction at $Q^2 = 16$ GeV^2 are calculated and compared to data from H1 [74], and ZEUS [75], respectively, in the right panel of Fig. 16. The description of the data is not very good, yet the large uncertainties of the experimental data do not allow us to make any final conclusions in this case.

To complete the set of the predictions based on the BK equation, the exclusive photoproduction of the $\Upsilon(1S)$ meson is presented in Fig. 17. The prediction is compared with experimental data obtained at HERA by H1 [76] and ZEUS [77] experiments. It is also compared with the two latest measurements—in proton-proton collisions at $\sqrt{s} = 7$ TeV and $\sqrt{s} = 8$ TeV by LHCb [78], and in proton-lead collisions at $\sqrt{s} = 5.02$ TeV by the CMS experiment [79]. The description of the data is good, although the large uncertainties prevent us from making any strong conclusions regarding the agreement of the predictions with the data.

VII. CONCLUSIONS

The solution of the Balitsky-Kovchegov equation with the collinearly improved kernel and including the impact-parameter dependence has been obtained numerically. This solution does not show the so-called Coulomb tails that have appeared in previous attempts to include the impact-parameter dependence. We have shown that the suppression at large values of the impact parameter is due to the suppression of contributions from daughter dipoles of large sizes in the terms of the collinearly improved kernel that deal with the resummation of double and single collinear logarithms.

The solutions based on a physics-inspired initial condition have been confronted with HERA and LHC data of the structure function of the proton measured in deep-inelastic scattering and of exclusive vector meson photoproduction and electroproduction. The predictions described data over a large kinematic range in scale and in energy.

The dipole scattering amplitudes computed in this work are publicly available on the website [80] along with instructions on how to use them.

ACKNOWLEDGMENTS

We would like to thank Dionysios Triantafyllopoulos for fruitful discussions regarding this paper. Our work has been partially supported from Grant No. LTC17038 of the INTER-EXCELLENCE program at the Ministry of Education, Youth and Sports of the Czech Republic, by Grant No. 17-04505S of the Czech Science Foundation, GA ČR and the European Cooperation in Science and Technology (COST) Action CA15213 Theory of hot matter and relativistic heavy-ion collisions (THOR). Computational resources were provided by the Czech Educational and Scientific NETwork (CESNET) LM2015042 grant and the Centrum vzdělávání, výzkumu a inovací v informačních a komunikačních technologiích (CERIT) Scientific Cloud LM2015085, provided under the program Projects of Large Research, Development, and Innovations Infrastructures.

---

[1] G. Altarelli, Phys. Rep. **81**, 1 (1982).
[2] L. N. Lipatov, Phys. Rep. **286**, 131 (1997).
[3] L. V. Gribov, E. M. Levin, and M. G. Ryskin, Phys. Rep. **100**, 1 (1983).
[4] P. Newman and M. Wing, Rev. Mod. Phys. **86**, 1037 (2014).
[5] K. Akiba *et al.* (LHC Forward Physics Working Group), J. Phys. G **43**, 110201 (2016).
[6] A. Accardi *et al.*, Eur. Phys. J. A **52**, 268 (2016).
[7] J. Abelleira Fernandez *et al.* (LHeC Study Group), J. Phys. G **39**, 075001 (2012).
[8] I. Balitsky, Nucl. Phys. **B463**, 99 (1996).

[9] Y. V. Kovchegov, Phys. Rev. D **60**, 034008 (1999).

[10] Y. V. Kovchegov, Phys. Rev. D **61**, 074018 (2000).

[11] A. H. Mueller, Nucl. Phys. **B335**, 115 (1990).

[12] N. N. Nikolaev and B. Zakharov, Z. Phys. C **49**, 607 (1991).

[13] A. H. Mueller, Nucl. Phys. **B415**, 373 (1994).

[14] J. Jalilian-Marian, A. Kovner, A. Leonidov, and H. Weigert, Phys. Rev. D **59**, 014014 (1998).

[15] J. Jalilian-Marian, A. Kovner, and H. Weigert, Phys. Rev. D **59**, 014015 (1998).

[16] H. Weigert, Nucl. Phys. **A703**, 823 (2002).

[17] E. Iancu, A. Leonidov, and L. D. McLerran, Nucl. Phys. **A692**, 583 (2001).

[18] E. Iancu, A. Leonidov, and L. D. McLerran, Phys. Lett. B **510**, 133 (2001).

[19] E. Ferreiro, E. Iancu, A. Leonidov, and L. McLerran, Nucl. Phys. **A703**, 489 (2002).

[20] N. N. Nikolaev and B. G. Zakharov, Z. Phys. C **64**, 631 (1994).

[21] I. Balitsky, Phys. Rev. D **75**, 014001 (2007).

[22] Y. V. Kovchegov and H. Weigert, Nucl. Phys. **A784**, 188 (2007).

[23] J. L. Albacete and Y. V. Kovchegov, Phys. Rev. D **75**, 125021 (2007).

[24] J. L. Albacete, N. Armesto, J. G. Milhano, C. A. Salgado, and U. A. Wiedemann, Phys. Rev. D **71**, 014003 (2005).

[25] J. L. Albacete, N. Armesto, J. G. Milhano, and C. A. Salgado, Phys. Rev. D **80**, 034031 (2009).

[26] J. L. Albacete, N. Armesto, J. G. Milhano, P. Quiroga-Arias, and C. A. Salgado, Eur. Phys. J. C **71**, 1705 (2011).

[27] J. Cepila and J. G. Contreras, arXiv:1501.06687.

[28] J. L. Albacete and A. Dumitru, arXiv:1011.5161.

[29] T. Lappi and H. Mantysaari, Phys. Rev. D **88**, 114020 (2013).

[30] B. Ducloue, T. Lappi, and H. Mantysaari, Phys. Rev. D **91**, 114005 (2015).

[31] J. L. Albacete, G. Giacalone, C. Marquet, and M. Matas, Phys. Rev. D **99**, 014002 (2019).

[32] J. L. Albacete, J. I. Illana, and A. Soto-Ontoso, Phys. Rev. D **92**, 014027 (2015).

[33] A. Bhattacharya, R. Enberg, Y. S. Jeong, C. S. Kim, M. H. Reno, I. Sarcevic, and A. Stasto, J. High Energy Phys. 11 (2016) 167.

[34] K. J. Golec-Biernat and A. M. Stasto, Nucl. Phys. **B668**, 345 (2003).

[35] J. Berger and A. Stasto, Phys. Rev. D **83**, 034015 (2011).

[36] J. Berger and A. M. Stasto, Phys. Rev. D **84**, 094022 (2011).

[37] H. Mantysaari and B. Schenke, Phys. Rev. D **98**, 034013 (2018).

[38] J. Berger and A. M. Stasto, J. High Energy Phys. 01 (2013) 001.

[39] E. Iancu, J. D. Madrigal, A. H. Mueller, G. Soyez, and D. N. Triantafyllopoulos, Phys. Lett. B **744**, 293 (2015).

[40] E. Iancu, J. D. Madrigal, A. H. Mueller, G. Soyez, and D. N. Triantafyllopoulos, Phys. Lett. B **750**, 643 (2015).

[41] A. Sabio Vera, Nucl. Phys. **B722**, 65 (2005).

[42] J. Cepila, J. G. Contreras, and M. Matas, Phys. Rev. D **99**, 051502 (2019).

[43] L. Motyka and A. M. Stasto, Phys. Rev. D **79**, 085016 (2009).

[44] I. Balitsky and G. A. Chirilli, Phys. Rev. D **77**, 014019 (2008).

[45] K. A. Olive *et al.* (Particle Data Group), Chin. Phys. C **38**, 090001 (2014).

[46] K. J. Golec-Biernat and M. Wusthoff, Phys. Rev. D **59**, 014017 (1998).

[47] H. Kowalski and D. Teaney, Phys. Rev. D **68**, 114005 (2003).

[48] G. Watt and H. Kowalski, Phys. Rev. D **78**, 014016 (2008).

[49] C. Marquet, Phys. Rev. D **76**, 094017 (2007).

[50] H. Mantysaari and B. Schenke, Phys. Rev. Lett. **117**, 052301 (2016).

[51] J. Cepila, J. G. Contreras, and J. D. Tapia Takaki, Phys. Lett. B **766**, 186 (2017).

[52] M. Matas, J. Cepila, and J. Guillermo Contreras Nuno, EPJ Web Conf. **112**, 02008 (2016).

[53] G. Beuf, Phys. Rev. D **89**, 074039 (2014).

[54] C. Contreras, E. Levin, and R. Meneses, arXiv:1906.09603.

[55] F. D. Aaron *et al.* (ZEUS and H1 Collaborations), J. High Energy Phys. 01 (2010) 109.

[56] T. Lappi and H. Mantysaari, Phys. Rev. D **93**, 094004 (2016).

[57] G. Beuf, Phys. Rev. D **96**, 074033 (2017).

[58] B. Ducloue, H. Hanninen, T. Lappi, and Y. Zhu, Phys. Rev. D **96**, 094017 (2017).

[59] H. Hanninen, T. Lappi, and R. Paatelainen, Ann. Phys. (Amsterdam) **393**, 358 (2018).

[60] B. Ducloue, E. Iancu, A. H. Mueller, G. Soyez, and D. N. Triantafyllopoulos, J. High Energy Phys. 04 (2019) 081.

[61] H. Kowalski, L. Motyka, and G. Watt, Phys. Rev. D **74**, 074016 (2006).

[62] I. P. Ivanov, N. N. Nikolaev, and A. A. Savin, Phys. Part. Nucl. **37**, 1 (2006).

[63] J. Nemchik, N. N. Nikolaev, and B. G. Zakharov, Phys. Lett. B **341**, 228 (1994).

[64] J. Nemchik, N. N. Nikolaev, E. Predazzi, and B. G. Zakharov, Z. Phys. C **75**, 71 (1997).

[65] J. R. Forshaw, R. Sandapen, and G. Shaw, Phys. Rev. D **69**, 094013 (2004).

[66] D. Bendova, J. Cepila, and J. G. Contreras, Phys. Rev. D **99**, 034025 (2019).

[67] A. G. Shuvaev, K. J. Golec-Biernat, A. D. Martin, and M. G. Ryskin, Phys. Rev. D **60**, 014015 (1999).

[68] F. D. Aaron *et al.* (H1 Collaboration), J. High Energy Phys. 05 (2010) 032.

[69] S. Chekanov *et al.* (ZEUS Collaboration), Nucl. Phys. **B718**, 3 (2005).

[70] A. Aktas *et al.* (H1 Collaboration), Eur. Phys. J. C **46**, 585 (2006).

[71] C. Alexa *et al.* (H1 Collaboration), Eur. Phys. J. C **73**, 2466 (2013).

[72] B. B. Abelev *et al.* (ALICE Collaboration), Phys. Rev. Lett. **113**, 232504 (2014).

[73] S. Acharya *et al.* (ALICE Collaboration), Eur. Phys. J. C **79**, 402 (2019).

[74] C. Adloff *et al.* (H1 Collaboration), Phys. Lett. B **541**, 251 (2002).

[75] H. Abramowicz *et al.* (ZEUS Collaboration), Nucl. Phys. **B909**, 934 (2016).
[76] C. Adloff *et al.* (H1 Collaboration), Phys. Lett. B **483**, 23 (2000).
[77] S. Chekanov *et al.* (ZEUS Collaboration), Phys. Lett. B **680**, 4 (2009).
[78] R. Aaij *et al.* (LHCb Collaboration), J. High Energy Phys. 09 (2015) 084.
[79] A. M. Sirunyan *et al.* (CMS Collaboration), Eur. Phys. J. C **79**, 277 (2019).
[80] https://hep.fjfi.cvut.cz/

Predictions for nuclear structure functions from the impact-parameter dependent Balitsky-Kovchegov equation

J. Cepila, J. G. Contreras, and M. Matas
Faculty of Nuclear Sciences and Physical Engineering,
Czech Technical University in Prague, Czech Republic

(Dated: February 26, 2020)

Abstract

In this work we present dipole scattering amplitudes, including the dependence on the impact-parameter, for a variety of nuclear targets of interest for the electron-ion colliders (EICs) being currently designed. These amplitudes are obtained by numerically solving the Balitsky-Kovchegov equation with the collinearly improved kernel. Two different cases are studied: initial conditions representing the nucleus under consideration and the solutions based on an initial condition representing a proton complemented by a Glauber-Gribov prescription to obtain dipole-nucleus amplitudes. We find that the energy evolution of these two approaches differ. We use the obtained dipole scattering amplitudes to predict (*i*) nuclear structure functions that can be measured in deep-inelastic scattering at EICs and (*ii*) nuclear suppression factors that reveal the energy evolution of shadowing for the different cases we studied. We compare our predictions with the available data.

I. INTRODUCTION

Feasibility studies for electron-ion colliders (EICs), like those proposed in the USA [1] or at CERN [2], are an essential ingredient towards the design of these machines. Inclusive measurements are among the most important observables in this context. In particular, the study of the structure function $F_2^A(x, Q^2)$ at small Bjorken-x for photons of virtuality Q^2 at a pertubative scale, and for a variety of nuclei A, is expected to yield a new understanding of the high-energy limit of quantum chromodynamics (QCD). Comparison of these measurements with those reported by H1 and ZEUS [3] for the corresponding structure function of the proton, $F_2^p(x, Q^2)$, promise to shed new light on the origin of shadowing, the phenomenon that the parton distributions of nucleons bounded in a nucleus are suppressed with respect to those of free nucleons [4].

At small values of x, the dominant parton distribution is that of gluons; thus the case of gluon shadowing has been the focus of attention for theorists since a long time; e.g., [5, 6]. A process expected to occur in this kinematic regime is saturation, namely the fact that the density of gluons is so high that they start to interact with each other, even in the domain of perturbative QCD. (For a recent review see [7].) An early equation to describe saturation was introduced in the seminal work [8], while nowadays it is common to use the Balitsky-Kovchegov (BK) equation for this type of studies. The leading order BK equation, discussed in Sec II, was derived in [9] and [10] using two independent approaches. Later on, corrections to account for the running of the coupling [11, 12] as well as the resummation of other logarithmic contributions [13, 14] were incorporated into this formalism. In the approximation of considering a large homogeneous target, that is, disregarding the impact parameter dependence, this equation has been successfully used to describe the existing $F_2^p(x, Q^2)$ data, e.g. in [14, 15].

The first attempt at solving the BK equation including the impact-parameter dependence [16] found that the solutions developed so-called Coulomb tails: an unphysical grow of the amplitude at large impact parameters. Nonetheless, using some extra ad hoc corrections it was possible to describe the structure function data of the proton [17, 18]. Recently, our group discovered that using the collinearly-improved kernel introduced in [14] the problem of Coulomb tails is tamed such that a successful phenomenology using the BK equation is possible [19, 20].

In this article, we solve the BK equation with the collinearly improved kernel for different nuclei of importance for future EICs and predict their structure functions as well as the corresponding nuclear suppression factors, which are a direct measurement of shadowing. We study two cases: solutions obtained from an initial condition representing the nuclei (denoted as b-BK-A below), and solutions of the proton case coupled to a Glauber-Gribov prescription to obtain the nuclear structure functions (denoted as b-BK-GG). Other approaches to the computation of nuclear structure functions can be found for example in [21–25]

The rest of the text is organised as follows: Sec. II contains a brief review of the formalism, including the definition of the initial conditions and the values of the parameters used in the computation. Section III discusses the behaviour of the dipole scattering amplitudes obtained by solving the BK equation for the different nuclei and the b-BK-A and b-BK-GG approaches. Section IV presents our predictions for the nuclear structure functions and nuclear suppression factors for all cases under study as well as a comparison with the available data. Finally, in Sec. V we provide a brief summary of the presented work as well as an outlook of future steps.

II. FORMALISM

A. The Balistsky-Kovchegov equation with the collinearly improved kernel

The leading order Balitsky-Kovchegov equation [9, 10] is

$$\begin{aligned}\frac{\partial N(\vec{r},\vec{b},Y)}{\partial Y} = \int d\vec{r_1} K(r,r_1,r_2)\Big(&N(\vec{r_1},\vec{b_1},Y)+N(\vec{r_2},\vec{b_2},Y)-N(\vec{r},\vec{b},Y)\\ &-N(\vec{r_1},\vec{b_1},Y)N(\vec{r_2},\vec{b_2},Y)\Big).\end{aligned} \tag{1}$$

It describes the evolution in rapidity Y of the dipole scattering amplitude $N(\vec{r},\vec{b},Y)$. Here, the sizes of the mother and daughter dipoles are $r \equiv |\vec{r}|$, $r_1 \equiv |\vec{r_1}|$, and $r_2 \equiv |\vec{r_2}| \equiv |\vec{r}-\vec{r_1}|$, respectively. The magnitudes of the corresponding impact parameters between these dipoles and the hadronic target are $b \equiv |\vec{b}|$, $b_1 \equiv |\vec{b_1}|$, $b_2 \equiv |\vec{b_2}|$. All these vectors are two-dimensional and live in the impact-parameter plane.

We solve the equation for the case when the following two conditions are fulfilled, (i) the evolution depends only on the magnitude of both the dipole size and the impact-parameter vectors, and (*ii*) the angle between $\vec{r}$ and $\vec{b}$ is fixed to zero:

$$\frac{\partial N(r,b,Y)}{\partial Y} = \int d\vec{r}_1 K(r,r_1,r_2)\Big(N(r_1,b_1,Y) + N(r_2,b_2,Y) - N(r,b,Y) \\ - N(r_1,b_1,Y)N(r_2,b_2,Y)\Big). \tag{2}$$

For the kernel we use the recently proposed collinearly improved version [13]

$$K_{\rm ci}(r,r_1,r_2) = \frac{\overline{\alpha}_s}{2\pi}\frac{r^2}{r_1^2 r_2^2}\left[\frac{r^2}{\min(r_1^2,r_2^2)}\right]^{\pm\overline{\alpha}_s A_1} K_{\rm DLA}(\sqrt{L_{r_1 r}L_{r_2 r}}), \tag{3}$$

where (see also [26])

$$K_{\rm DLA}(\rho) = \frac{J_1(2\sqrt{\overline{\alpha}_s\rho^2})}{\sqrt{\overline{\alpha}_s}\rho}, \tag{4}$$

J_1 is the Bessel function, the anomalous dimension is $A_1 = 11/12$, and $L_{r_i r} = \ln(r_i^2/r^2)$. The sign is positive when the size of the original dipole is smaller than the size of each of the daughter dipoles and negative otherwise. The smallest dipole prescription is used for the running coupling: $\overline{\alpha}_s = \alpha_s(r_{\rm min})N_c/\pi$, where $r_{\rm min} = \min(r_1,r_2,r)$. Note that this prescription has also been put forward as the natural scale for the BK equation at next-to-leading order [27]. The variable-number-of-flavours scheme is used with the same parameters as in our previous work [19, 20].

B. Glauber-Gribov approach to the nuclear dipole amplitude

Following [21], one can use the solution of the BK equation for the case of a proton target to obtain the dipole scattering amplitude for a nuclear target by using a Glabuer-Gribov approach

$$N^A(r,b,Y) = \Big[1 - \exp\Big(-\frac{1}{2}T_A(b)\sigma_{q\bar{q}}(Y,r)\Big)\Big], \tag{5}$$

with

$$\sigma_{q\bar{q}}(Y,r) = \int {\rm d}^2\vec{b}2N^p(r,b,Y). \tag{6}$$

This approach has been used in other studies, e.g. those reported in [21, 22] (see also [24] for a more general approach that reduces to the Glabuer-Gribov case for large nuclei). The nuclear thickness function $T_A(b)$ is obtained from a Woods-Saxon distribution for the nuclear matter density

$$\rho_A(x,y,z) = \rho_0\frac{1}{\exp\left[(r-{\rm R})/{\rm a}\right]+1}, \tag{7}$$

TABLE I. Values of the parameters of the Wood-Saxon distribution, see Eq. (7), used in the computations reported in this text, and the value of the $Q_{s0}^2(A)$ parameter obtained as explained in the text. The Wood-Saxon parameters are taken from [29].

Nucleus	A	R (fm)	a (fm)	ρ_0 (fm^{-3})	$Q_{s0}^2(A)$ (GeV^2)
Al	27	2.84	0.569	0.2015	0.315
Ca	40	3.51	0.563	0.17611	0.341
Fe	56	3.980	0.569	0.17655	0.390
Cu	64	4.2	0.569	0.1746	0.409
W	184	6.510	0.535	0.1493	0.553
Pb	208	6.624	0.549	0.16	0.609

(where $r \equiv \sqrt{x^2+y^2+z^2}$) by integrating it over the longitudinal coordinate z

$$T_A(b) = \int_{-\infty}^{+\infty} dz \rho_A(x,y,z), \tag{8}$$

with the x and y coordinates in the impact-parameter plane. It is normalised according to $\int \mathrm{d}^2\vec{b}\ T_A(b) = A$. (See for example [28] for full details on the formalism.) The values of the Woods-Saxon parameters are given in Table I. This approach is denoted as b-BK-GG in what follows.

C. Initial conditions for the nuclear targets

To solve the BK equation an initial condition is needed. In our previous work [19, 20] we introduced a new functional form for the initial condition given by

$$N^p(r,b,Y=0) = 1 - \exp\left(-\frac{1}{2}\frac{Q_{s0}^2}{4} r^2 T_p(b_{q_1}, b_{q_2})\right), \tag{9}$$

where Q_{s0}^2 is a free parameter representing the saturation scale at a zero impact parameter, and b_{q_i} are the impact parameters of the quark and anti-quark forming the dipole.

For the case of the proton, we assumed a Gaussian like distribution which leads to

$$T_p(b_{q_1}, b_{q_2}) = \left[\exp\left(-\frac{b_{q_1}^2}{2B_G}\right) + \exp\left(-\frac{b_{q_2}^2}{2B_G}\right)\right]. \tag{10}$$

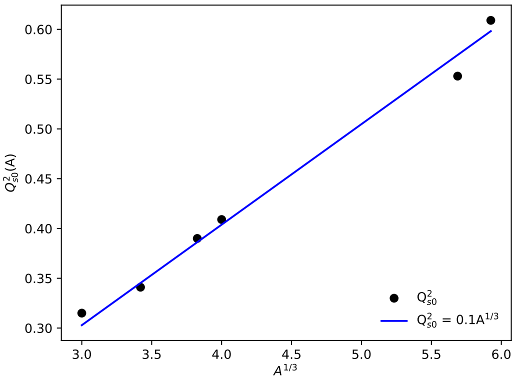

FIG. 1. Dependence of the $Q^2_{s0}(A)$ parameter as a function of $A^{1/3}$ (solid bullets) compared with a linear function (blue line). See text for details.

The parameter B_G was set to 3.2258 GeV^{-2}, while Q^2_{s0} took the value 0.496 GeV^2. With these values a satisfactory description of HERA and LHC data on the proton structure functions and exclusive production of vector mesons is achieved [19, 20].

Here, we follow a similar approach for the nuclear case, but assuming a Woods-Saxon instead of a Gaussian distribution:

$$N^A(r, b, Y = 0) = 1 - \exp\left(-\frac{1}{2}\frac{Q^2_{s0}(A)}{4} r^2 T_A(b_{q_1}, b_{q_2})\right), \tag{11}$$

with

$$T_A(b_{q_1}, b_{q_2}) = k\left[T_A(b_{q_1}) + T_A(b_{q_2})\right]. \tag{12}$$

where the factor k ensures that $kT_A(0) = 1$. This approach is denoted as b-BK-A in what follows.

As the nuclear parameters are already fixed, the only free parameter is $Q^2_{s0}(A)$. We have fixed these parameters using $N(r, b, Y = 0)$ where $Y = \ln(x_0/x)$ with $x_0 \equiv 0.008$. This dipole scattering amplitude at the initial rapidity is used to compute structure functions and to compare them with the predictions obtained using the EPPS16 nuclear parton distributions [30].

In detail, we have varied the value of the $Q^2_{s0}(A)$ parameter in order to get a small relative deviation from the structure function $F_2(x = 0.008, Q^2)$ as predicted by the EPPS16 PDFs. The comparison is done for the following values of the photon virtuality: $Q^2 \in$ [3.5, 4.5, 6.5, 8.5, 10, 12, 15, 18, 22, 27] GeV^2 to avoid the nonperturbative region at very low Q^2 and to stay in the region of virtualities where the BK equation is expected to work the best. We have used LHAPDFs [31] to obtain the PDF sets and the APFEL software [32, 33] for the computation of the structure function. The values obtained for $Q^2_{s0}(A)$ by this procedure are reported in the last column of Table I.

Interestingly, this parameter follows a linear behaviour as a function of $A^{1/3}$ as shown in Fig. 1. This opens the possibility of studying other nuclei for which there is currently no information in the EPPS16 set of parton distributions.

III. BEHAVIOUR OF THE DIPOLE SCATTERING AMPLITUDE

The dipole scattering amplitude in the b-BK-A approach computed using the colinearlly improved kernel with the initial condition given by Eq. (11) is shown in Fig. 2 for two values of the rapidity and at a fixed value of r, respectively b, for three different nuclei. The chosen rapidity values are the initial condition ($Y = 0$) and $Y = 5$, which corresponds to $x \approx 5.4 \cdot 10^{-5}$ representing the case of a dipole scattering amplitude evolved to a rapidity of potential interest of future EICs. The impact parameter dependence is clearly different for the three depicted nuclei, reflecting their different sizes, while the shape of the amplitude as a function of r is similar for the three cases. The main effects of the evolution are the growth of the profile in impact parameter, the softening of the large r behaviour, and a small advancement of the wave front towards smaller dipoles.

Figure 3 shows a comparison of the two methods, b-BK-A and b-BK-GG, to compute the nuclear dipole scattering amplitude presented above. The differences are remarkable. The absolute value of the amplitude for dipoles of size 1/GeV is substantially smaller for b-BK-A. Regarding the dependence on the dipole size at an impact parameter of 0.1/GeV the b-BK-GG approach samples dipole sizes around one order of magnitude smaller than those sampled in the b-BK-A case for large dipoles.

These differences between the dipole scattering amplitudes in the two approaches reflect themselves in one of the most important parameters that can be obtained from these objects: the saturation scale and its evolution. As it is standard, we define the saturation scale at a given rapidity and a fixed impact parameter as the dipole size that produces a scattering amplitude equal to a constant that commonly is chosen to be one half. Figure 4 shows the behaviour of the saturation scale at an impact parameter of 0.01/GeV for two rapidities as a

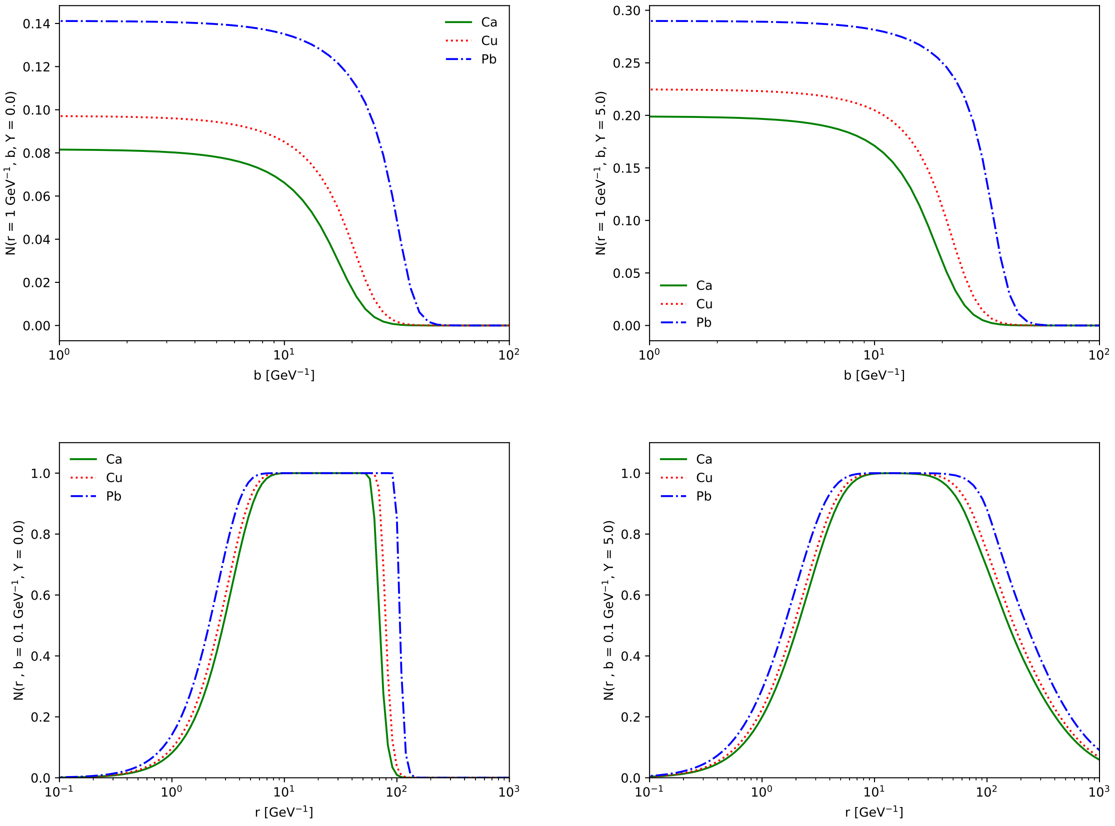

FIG. 2. Dipole scattering amplitude in the b-BK-A approach at the initial condition (left) and after evolution to $Y = 5$ (right) as a function of the impact parameter for a dipole size $r = 1/\mathrm{GeV}$ (upper panels), and as a function of the dipole size for an impact parameter $b = 0.1/\mathrm{GeV}$ (lower panels).

function of $A^{1/3}$. The saturation scale shows a linear behaviour in this representation. The intercept is larger for b-BK-A with respect to b-BK-GG, while the slope is smaller. The evolution of both the intercept and the slope seems to be different in both cases. For all values of A the saturation scale at $Y = 5$ is smaller for b-BK-A than for b-BK-GG predictions. Note that the figure would look the same at other values of the impact parameter due to the flat form of the dipole scattering amplitude as shown in Fig. 3. Only for larger values of the impact parameter, around 4 to 5/GeV, the drop at the border of the nuclei changes the behaviour of Fig. 4.

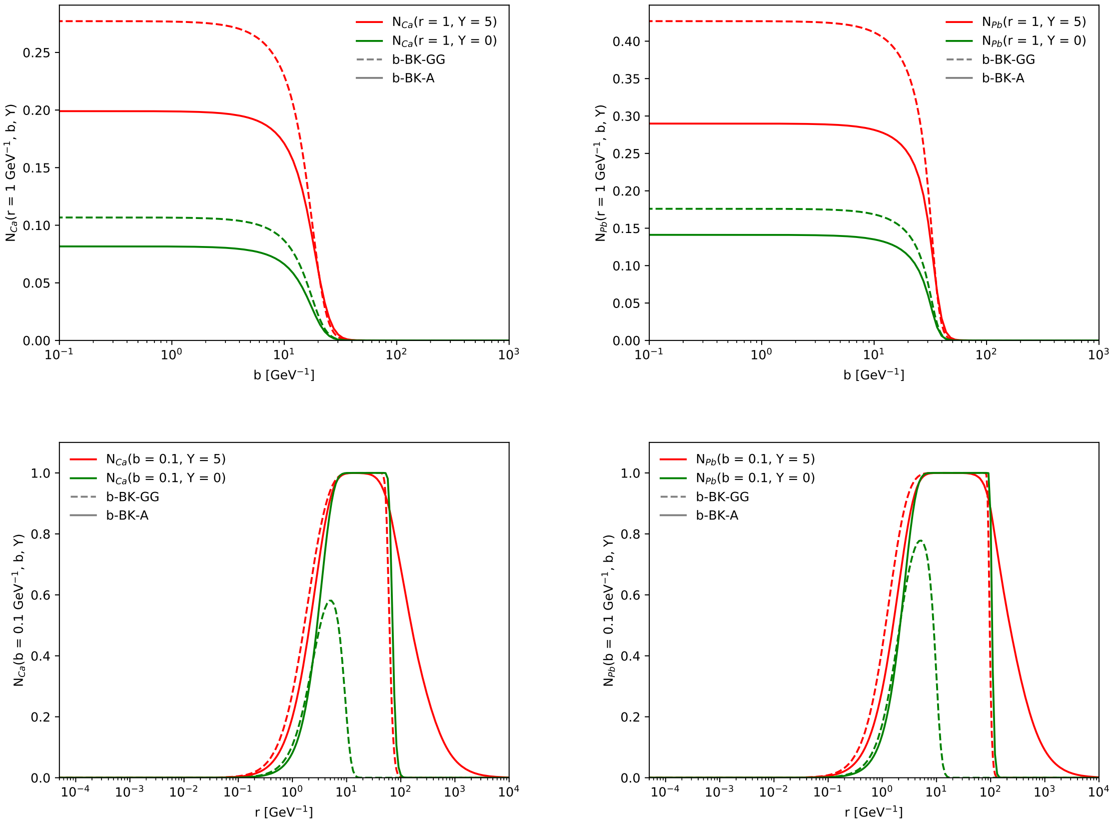

FIG. 3. Comparison of the dipole scattering amplitudes computed for b-BK-A (solid line) with the b-BK-GG approach (dashed line). The comparisons are done at $Y = 0$ and $Y = 5$ for two nuclei, Ca (left) and Pb (right) as a function of the impact parameter for a dipole size $r = 1/\mathrm{GeV}$ (upper panels), and as a function of the dipole size for an impact parameter $b = 0.1/\mathrm{GeV}$ (lower panels).

IV. PREDICTIONS FOR NUCLEAR STRUCTURE FUNCTIONS AND NUCLEAR SUPPRESSION FACTORS

A. Relation between the dipole scattering amplitude and the structure function

Using as input the dipole scattering amplitudes, the structure function $F_2^A(x, Q^2)$ is computed as

$$F_2^A(x, Q^2) = \frac{Q^2}{4\pi^2 \alpha_{\mathrm{em}}} \int \sum_i d\vec{r} d\vec{b} dz \mid \Psi^i_{T,L}(z, \vec{r}) \mid^2 \frac{\mathrm{d}\sigma^{q\bar{q}}(\vec{r}, \tilde{x})}{\mathrm{d}\vec{b}}, \tag{13}$$

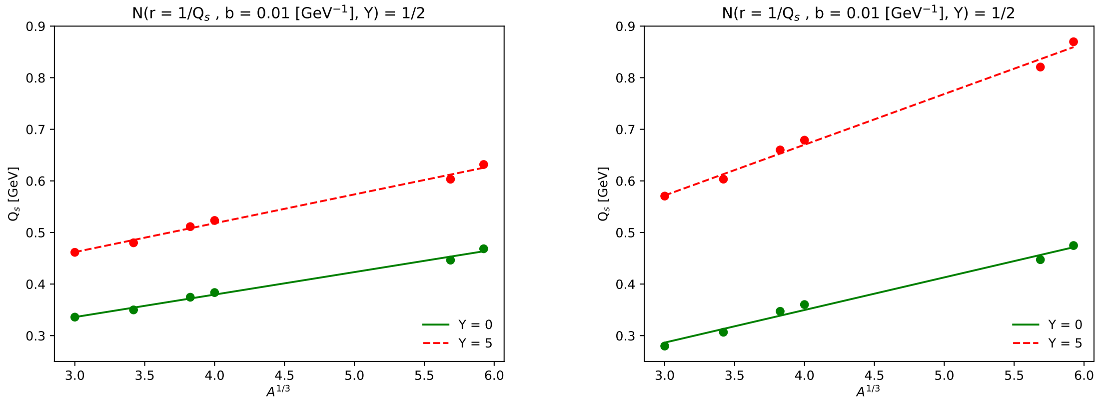

FIG. 4. Saturation scale at two different rapidities for an impact parameter of 0.01/GeV for the b-BK-A (left) and b-BK-GG (right) approaches. The solid bullets are the results from the evolution and are well described by a linear function. See text for details.

where, following [34], $\tilde{x} = x(1 + (4m_{q_i}^2)/Q^2)$ with m_{q_i} the mass of the i-quark. The dipole–target cross section is related to the dipole scattering amplitude by

$$\frac{\mathrm{d}\sigma^{q\bar{q}}(\vec{r}, x)}{\mathrm{d}\vec{b}} = 2N^A(\vec{r}, \vec{b}, x). \tag{14}$$

Finally, the wave function representing the probability of a virtual photon splitting into a quark-antiquark dipole, and following the notation of [34], is

$$\mid \Psi_T^i(z, \vec{r}, Q^2) \mid^2 = \frac{3\alpha_{\mathrm{em}}}{2\pi^2} e_{q_i}^2 \Big((z^2 + (1-z)^2)\epsilon^2 K_1^2(\epsilon r) + m_{q_i}^2 K_0^2(\epsilon r) \Big), \tag{15}$$

and

$$\mid \Psi_L^i(z, \vec{r}, Q^2) \mid^2 = \frac{3\alpha_{\mathrm{em}}}{2\pi^2} e_{q_i}^2 \Big(4Q^2 z^2 (1-z)^2 K_0^2(\epsilon r) \Big) \tag{16}$$

for the transverse and longitudinal polarisation of the incoming photon, respectively. The total wave function is

$$\mid \Psi_{T,L}^i(z, \vec{r}) \mid^2 = \mid \Psi_T^i(z, \vec{r}) \mid^2 + \mid \Psi_L^i(z, \vec{r}) \mid^2 . \tag{17}$$

In these equations K_0 and K_1 are the MacDonald functions, z is the fraction of the total longitudinal momentum of the photon carried by the quark, e_{q_i} is the fractional charge (in units of elementary charge) of quark i, $\alpha_{\mathrm{em}} = 1/137$ and $\epsilon^2 = z(1-z)Q^2 + m_{q_i}^2$. As in our previous work [19, 20] we set the quark masses to $100\,\mathrm{MeV}/c^2$ for light, $1.3\,\mathrm{GeV}/c^2$ for charm, and $4.5\,\mathrm{GeV}/c^2$ for bottom quark. As reported for example in [13] the numerical results do not depend strongly on these choices.

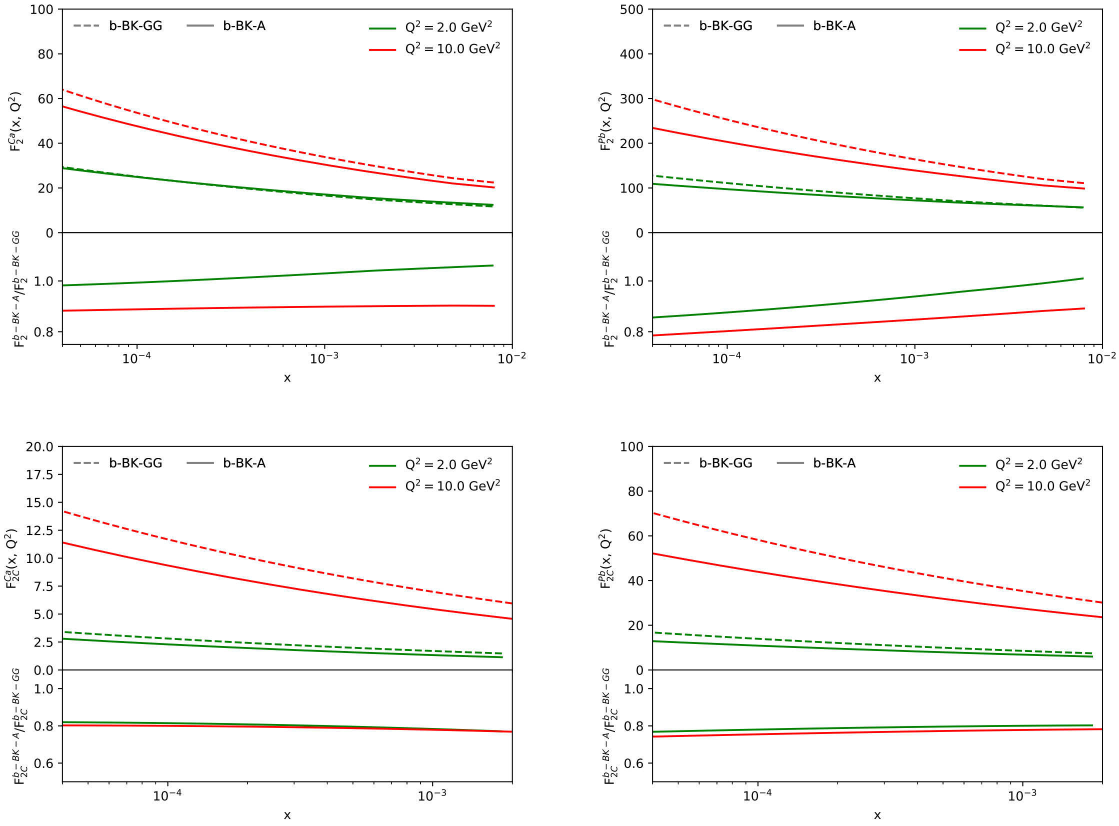

FIG. 5. The upper panels show the dependence on x of the nuclear structure function $F_2^A(x, Q^2)$ computed in the b-BK-A and b-BK-GG approaches for two values of the photon virtuality Q^2 and two nuclei: Ca (left) and Pb (right). The ratio of the structure functions in the b-BK-A and b-BK-GG approaches is shown in the lower part of those panels. The bottom panels show the contribution of charm, that is they show the structure function $F_{2C}^A(x, Q^2)$.

B. Predictions for the nuclear structure function

The nuclear structure functions $F_2^A(x, Q^2)$ for Ca and Pb are shown in the upper panels of Fig. 5 as a function of x for two values of the photon virtuality Q^2. Results in both approaches, b-BK-A and b-BK-GG, are shown in the figure which also shows the ratio of both predicted structure functions. There is a clear difference between both sets of results. Furthermore, the difference shows a dependence on x, on Q^2, and a striking dependence on A, where the difference between both approaches grows from small to large nuclei.

A measurement of this structure function is expected to be one of the first results of any future EIC. Given the precision expected from these machines, these measurements will select which of the two approaches describes better the data.

The lower panels of Fig. 5 show that the difference between the b-BK-A and b-BK-GG approaches are larger for the charm structure function, $F_{2C}^{A}(x, Q^2)$, than for the inclusive case, and that there is a very soft dependence on kinematic variables and nucleus species. A measurement of $F_{2C}^{A}(x, Q^2)$ would offer additional stringent constraints to predictions of the structure function of nuclei.

C. Predictions for the nuclear suppression factor

As a final observable we present the nuclear suppression factor, defined as the ratio $R_{pA} \equiv F_2^A(x, Q^2)/(A\ F_2^p(x, Q^2))$, which is expected to be unity if the structure of a free nucleon is equal to that of a bounded one. This ratio is the most direct way to observed nuclear shadowing, which for small x is dominated by gluon shadowing and thus may be an important tool to determine the behaviour of saturation across different nuclei.

This factor is shown in the upper panels of Fig. 6 as a function of x. Exiting data at the same Q^2 from [35] is also shown as a cross check of the procedure. For the x dependence of R_{pA} one sees a linear decrease (in logarithmic scale) towards small x for both nuclei, but the linear behaviour is reached later for the lighter nucleus, specially at higher Q^2 scales.

The b-BK-A computation predicts stronger shadowing than the b-BK-GG case with this behaviour seemingly dependent on Q^2. The same figure also shows, in the bottom panels, the A-dependence of the nuclear suppression factor for two Q^2 scales and for two values of x. As expected, shadowing becomes stronger as the size of the nucleus grows. The different behaviour of shadowing for different nuclei in the b-BK-A and b-BK-GG is clearly seen in this observable.

Figure 7 shows the comparison of our predictions with those obtained using EPPS16 which is considered a standard of our current knowledge of nuclear shadowing. The comparison is done for Ca and Pb as middle and large nuclei. The predictions are compared with data from [35]. Note that the predictions are at a Q^2 scale of 2.42 GeV^2 which we considered the lowest we would like to go to stay in a somehow perturbative scale. But the data is measured at a different Q^2 for each x value (as illustrated by the use of empty markers for data at smaller Q^2). The Q^2 values are reported in the figure.

Focusing on the predictions, the behaviour at small x is definitely different for the EPPS16 and BK computations. Note that the difference between EPPS16 and b-BK at the initial scale used for the BK evolution have two origins: one, that the parameter of the initial scale shown in Fig. 1 is chosen by comparing with larger values of Q^2 than those shown in Fig. 7, and two that the prediction for the structure of the proton is substantially different for EPPS16 and for the b-BK approach reported in [19, 20]. Given that the difference among the approaches goes beyond a normalisation factor and shows a strong x-dependence, data from future EICs are expected to be precise enough to decide which prediction is closer to reality.

Comparing with the currently available data, and taking into account (*i*) the different Q^2 in data and predictions, and (*ii*) that for measurements the values are quite low (even below what one would expect to be valid for an approach based on perturbative QCD), the b-BK-A prediction seems to do a reasonable job of describing data. The EPPS16 prediction also does quite well for Pb, but slightly worse for Ca. The b-BK-GG prediction on the other hand is good when comparing with Ca, but it suffers a bit when compared with Pb.

V. SUMMARY AND OUTLOOK

The dipole scattering amplitudes, including the impact parameter dependence, for different nuclei have been obtained by solving the BK equation with the collinearly improved kernel. These amplitudes have been used to predict structure functions and nuclear saturation factors in kinematic ranges of interest for future EICs as those currently planned in the USA and at CERN. We followed two approaches: modelling the target directly as a nucleus using Wood-Saxon parameterisations (denoted as b-BK-A above), and solving for a proton and using a Glauber-Gribov prescription to go to the nuclear level (denoted as b-BK-GG above).

We find sizable differences between these approaches. These differences show a dependence on x, Q^2 and A such that data from a future EIC will be able to select the most appropriate approach for the description of data. We also compared nuclear suppression factors with those predicted using the EPPS16 formalism which is taken as a standard of our current knowledge of nuclear shadowing. We find that all three approaches yield different predictions and that the b-BK-A computation seems to provide a better description of

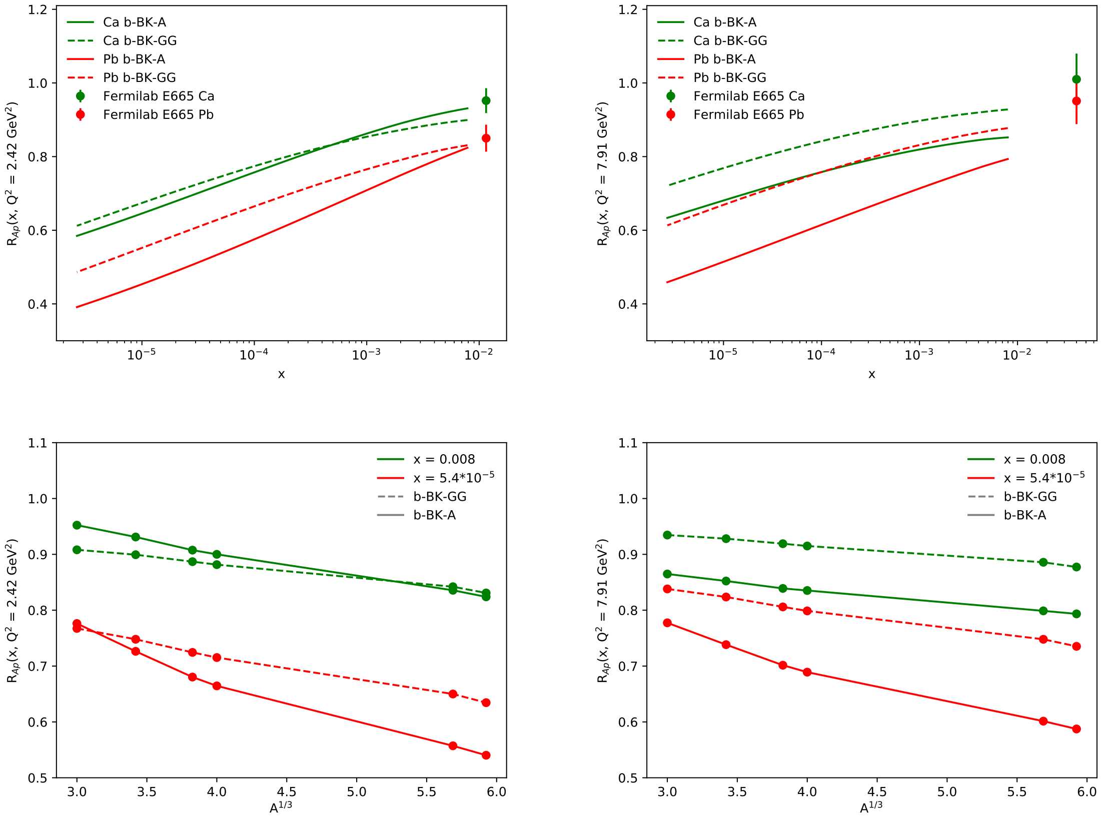

FIG. 6. Nuclear suppression factor at two values of the photon virtuality $Q^2 = 2.42$ GeV^2 (left) and $Q^2 = 7.91$ GeV^2 (right) as a function of x for Ca and Pb (upper panels) and as a function of A at different fixed values of x (lower panels). The predictions are compared with data from [35].

existing data.

These studies show that the data expected from a future EIC have the capability of select the best theoretical approach and thus to advance our understanding of the nuclear structure, of shadowing, and of the high energy limit of QCD.

The dipole scattering amplitudes computed in this work are publicly available in the website `https://hep.fjfi.cvut.cz/` along with macros and instructions to facilitate their use for anybody interested.

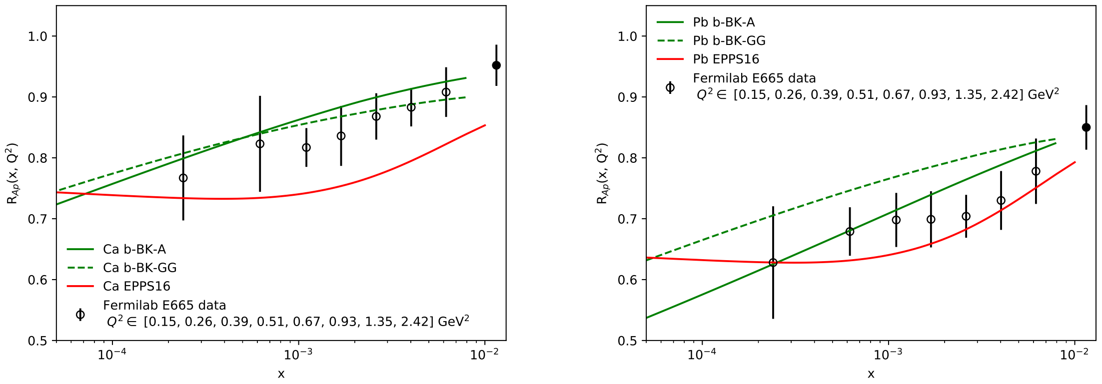

FIG. 7. Nuclear suppression factor for Ca (left) and Pb (right) for $Q^2 = 2.42\,\mathrm{GeV}^2$. The data-points correspond to Q^2 values of [0.15, 0.26, 0.39, 0.51, 0.67, 0.93, 1.35, 2.42] from left to right. Only the data point represented by a solid marker correspond to the Q^2 used for the predictions. See text for details.

ACKNOWLEDGEMENTS

This work was partially performed within the activities of the Centre of Advanced Applied Sciences with the number: CZ.02.1.01/0.0/0.0/16-019/0000778. The Centre of Advanced Applied Sciences is co-financed by the European Union. This work has also been partially supported from grant LTC17038 of the INTER-EXCELLENCE program at the Ministry of Education, Youth and Sports of the Czech Republic and the COST Action CA15213 THOR. Computational resources were provided by the CESNET LM2015042 grant and the CERIT Scientific Cloud LM2015085, provided under the program Projects of Large Research, Development, and Innovations Infrastructures.

---

[1] A. Accardi *et al.*, Eur. Phys. J. **A52**, 268 (2016), arXiv:1212.1701 [nucl-ex].

[2] J. Abelleira Fernandez *et al.* (LHeC Study Group), J.Phys. **G39**, 075001 (2012), arXiv:1206.2913 [physics.acc-ph].

[3] H. Abramowicz *et al.* (ZEUS, H1), Eur. Phys. J. **C75**, 580 (2015), arXiv:1506.06042 [hep-ex].

[4] N. Armesto, J. Phys. **G32**, R367 (2006), arXiv:hep-ph/0604108 [hep-ph].

[5] A. H. Mueller and J.-w. Qiu, Nucl. Phys. **B268**, 427 (1986).

[6] N. N. Nikolaev and B. Zakharov, Z.Phys. **C49**, 607 (1991).

[7] J. L. Albacete and C. Marquet, Prog. Part. Nucl. Phys. **76**, 1 (2014), arXiv:1401.4866 [hep-ph].

[8] L. V. Gribov, E. M. Levin, and M. G. Ryskin, Phys. Rept. **100**, 1 (1983).

[9] I. Balitsky, Nucl.Phys. **B463**, 99 (1996), arXiv:hep-ph/9509348 [hep-ph].

[10] Y. V. Kovchegov, Phys. Rev. **D60**, 034008 (1999), arXiv:hep-ph/9901281 [hep-ph].

[11] Y. V. Kovchegov and H. Weigert, Nucl.Phys. **A784**, 188 (2007), arXiv:hep-ph/0609090 [hep-ph].

[12] J. L. Albacete and Y. V. Kovchegov, Phys.Rev. **D75**, 125021 (2007), arXiv:0704.0612 [hep-ph].

[13] E. Iancu, J. D. Madrigal, A. H. Mueller, G. Soyez, and D. N. Triantafyllopoulos, Phys. Lett. **B750**, 643 (2015), arXiv:1507.03651 [hep-ph].

[14] E. Iancu, J. D. Madrigal, A. H. Mueller, G. Soyez, and D. N. Triantafyllopoulos, Phys. Lett. **B744**, 293 (2015), arXiv:1502.05642 [hep-ph].

[15] J. L. Albacete, N. Armesto, J. G. Milhano, P. Quiroga-Arias, and C. A. Salgado, Eur.Phys.J. **C71**, 1705 (2011), arXiv:1012.4408 [hep-ph].

[16] K. J. Golec-Biernat and A. Stasto, Nucl.Phys. **B668**, 345 (2003), arXiv:hep-ph/0306279 [hep-ph].

[17] J. Berger and A. Stasto, Phys. Rev. **D83**, 034015 (2011), arXiv:1010.0671 [hep-ph].

[18] J. Berger and A. M. Stasto, Phys.Rev. **D84**, 094022 (2011), arXiv:1106.5740 [hep-ph].

[19] J. Cepila, J. G. Contreras, and M. Matas, Phys. Rev. **D99**, 051502 (2019), arXiv:1812.02548 [hep-ph].

[20] D. Bendova, J. Cepila, J. G. Contreras, and M. Matas, Phys. Rev. **D100**, 054015 (2019), arXiv:1907.12123 [hep-ph].

[21] N. Armesto, Eur. Phys. J. **C26**, 35 (2002), arXiv:hep-ph/0206017 [hep-ph].

[22] E. R. Cazaroto, F. Carvalho, V. P. Goncalves, and F. S. Navarra, Phys. Lett. **B671**, 233 (2009), arXiv:0805.1255 [hep-ph].

[23] L. Agozzino, P. Castorina, and P. Colangelo, Eur. Phys. J. **C74**, 2828 (2014), arXiv:1401.0826 [hep-ph].

[24] C. Marquet, M. R. Moldes, and P. Zurita, Phys. Lett. **B772**, 607 (2017), arXiv:1702.00839 [hep-ph].

[25] E. C. Aschenauer, S. Fazio, M. A. C. Lamont, H. Paukkunen, and P. Zurita, Phys. Rev. **D96**, 114005 (2017), arXiv:1708.05654 [nucl-ex].

[26] A. Sabio Vera, Nucl. Phys. **B722**, 65 (2005), arXiv:hep-ph/0505128 [hep-ph].

[27] I. Balitsky and G. A. Chirilli, Phys.Rev. **D77**, 014019 (2008), arXiv:0710.4330 [hep-ph].

[28] C. Loizides, J. Kamin, and D. d'Enterria, Phys. Rev. **C97**, 054910 (2018), [erratum: Phys. Rev.C99,no.1,019901(2019)], arXiv:1710.07098 [nucl-ex].

[29] H. De Vries, C. De Jager, and C. De Vries, Atom.Data Nucl.Data Tabl. **36**, 495 (1987).

[30] K. J. Eskola, P. Paakkinen, H. Paukkunen, and C. A. Salgado, Eur. Phys. J. **C77**, 163 (2017), arXiv:1612.05741 [hep-ph].

[31] A. Buckley, J. Ferrando, S. Lloyd, K. Nordstrm, B. Page, M. Rfenacht, M. Schnherr, and G. Watt, Eur. Phys. J. **C75**, 132 (2015), arXiv:1412.7420 [hep-ph].

[32] V. Bertone, S. Carrazza, and J. Rojo, Comput. Phys. Commun. **185**, 1647 (2014), arXiv:1310.1394 [hep-ph].

[33] S. Carrazza, A. Ferrara, D. Palazzo, and J. Rojo, J. Phys. **G42**, 057001 (2015), arXiv:1410.5456 [hep-ph].

[34] K. J. Golec-Biernat and M. Wusthoff, Phys. Rev. **D59**, 014017 (1998), arXiv:hep-ph/9807513 [hep-ph].

[35] M. R. Adams *et al.* (E665), Z. Phys. **C67**, 403 (1995), arXiv:hep-ex/9505006 [hep-ex].

Photonuclear J/ψ production at the LHC: proton-based versus nuclear dipole scattering amplitudes

D. Bendova[a], J. Cepila[a], J. G. Contreras[a], M. Matas[a]

[a]*Faculty of Nuclear Sciences and Physical Engineering, Czech Technical University in Prague, Czech Republic*

Abstract

The coherent photonuclear production of a J/ψ vector meson at the LHC has been computed using two different sets of solutions of the impact-parameter dependent Balitsky-Kovchegov equation. The nuclear dipole scattering amplitudes are obtained either from (*i*) solutions for this process off proton targets coupled with a Glauber-Gribov prescription, or (*ii*) from solutions obtained with an initial condition representing the nucleus. These approaches predict different cross sections, which are compared with existing data from ultra-peripheral collisions at the LHC. The latter approach seems to better describe current measurements. Future LHC data should be precise enough to select one of the two approaches as the correct one.

Keywords: Impact-parameter dependent Balitsky-Kovchegov equation, coherent vector meson photoproduction, LHC

---

1. Introduction

The exclusive photoproduction of a J/ψ vector meson off a hadron has been recognised for many years as a very sensitive probe of the gluonic structure of hadrons in the perturbative regime of quantum chromodynamics (QCD) [1, 2]; thus it has been extensively studied at HERA [3, 4]. In recent years, this process has attracted renewed attention. On one hand, due to measurements at the LHC including production off protons and off Pb nuclei and reaching unprecedented energies [5, 6, 7]. On the other, because of studies related to the potential of electron-ion colliders [8, 9].

As mentioned above, there is plenty of high-quality data from HERA on production off proton targets. Therefore, many computations predicting the behaviour of this process off nuclear targets start from a description of the process off nucleons, where the parameters of the given model are fixed by HERA data, and then apply some form of Glauber formalism to predict the cross sections for photonuclear production. Such an approach has been followed for example in [10, 11, 12, 13].

The applicability of using a Glauber approach has been analysed since a long time, e.g. [14, 15], but recent advances in the understanding of saturation through the solution of the Balitsky-Kovchegov (BK) equation [16, 17, 18] allow for new insights into this question. In particular, the implementation of collinear corrections to the kernel [19, 20] together with a suitable initial condition have been used to find impact-parameter dependent solutions of the BK equation [21], which correctly describe HERA data on vector meson photo- and electroproduction off protons [22].

Recently, these advances have been extended to the case of nuclear targets [23] using two approaches: (*i*) coupling the solution of the BK equation for the case of proton targets to a Glauber-Gribov prescription to obtain the solutions to the nuclear case, and (*ii*) solving directly the impact-parameter dependent BK equation with an initial condition representing a specific nucleus. In what follows, these two set of solutions are denoted as b-BK-GG and b-BK-A, respectively.

In this Letter, both approaches are used to predict the cross section for coherent photoproduction of J/ψ vector mesons in Pb–Pb ultra-peripheral collisions (UPC) at the LHC and compare the predictions with data available at different rapidities and at two centre-of-mass energies per nucleon pair, $\sqrt{s_{\rm NN}} = 2.76$ TeV and $\sqrt{s_{\rm NN}} = 5.02$ TeV, corresponding to measurements performed during the LHC Run 1 and Run 2, respectively. It is found that Run 1 measurements at midrapidity strongly disfavour the use of b-BK-GG solutions, and that the expected precision of the measurements with Run 2 data may provide a definitive answer on the question of which approach is the valid one. The rest of this

Letter is organised as follows: the next section presents a brief overview of the formalism; Sec. 3 contains the main results, while in Sec. 4 our findings are discussed; the Letter concludes with a brief summary and outlook in Sec. 5.

2. Brief overview of the formalism

In this section a brief overview of the formalism is presented. For the full details see for example [22, 23] and references therein.

The cross section for the coherent photoproduction of a J/ψ vector meson, differential on the square of the momentum transfer t at the target vertex, is given by the sum of the contributions from transversely (T) and longitudinally (L) polarised photons:

$$\left.\frac{\mathrm{d}\sigma_{\gamma\mathrm{Pb}}}{\mathrm{d}|t|}\right|_{T,L} = \frac{\left(1+\beta^2\right)\left(R_g^{T,L}\right)^2}{16\pi}|\mathcal{A}_{T,L}|^2. \tag{1}$$

The factor $(1+\beta^2)$ accounts for contributions from the real part of the amplitude, while $(R_g^{T,L})^2$ corrects for the so-called skewedness [24]. The scattering amplitude of the process is given by

$$\mathcal{A}_{T,L}(x,Q^2,\vec{\Delta}) = i\int \mathrm{d}\vec{r}\int_0^1 \frac{\mathrm{d}z}{4\pi}\int \mathrm{d}\vec{b}|\Psi_{\mathrm{V}}^*\Psi_{\gamma^*}|_{T,L}\exp\left[-i\left(\vec{b}-(1-z)\vec{r}\right)\vec{\Delta}\right]\frac{\mathrm{d}\sigma^{q\bar{q}}}{\mathrm{d}\vec{b}}. \tag{2}$$

Here, Ψ_{γ^*} and Ψ_{V} are the wave functions of a virtual photon fluctuating into a colour dipole and of the dipole producing the vector meson. The vector $\vec{r}$ represents the dipole size and orientation, and $\vec{b}$ represents the impact parameter between the dipole and the target. Q^2 denotes the virtuality of the photon and $\vec{\Delta}^2 \equiv -t$. The variable z corresponds to the fraction of the energy of the quark-antiquark dipole carried by the quark, while

$$\frac{\mathrm{d}\sigma^{q\bar{q}}}{\mathrm{d}\vec{b}} = 2N(\vec{r},\vec{b};x), \tag{3}$$

with $N(\vec{r},\vec{b};x)$ the dipole scattering amplitude obtained as a solution of the BK equation at a rapidity $Y = \ln(x_0/x)$; here $x_0 \equiv 0.008$ corresponds to the rapidity at the initial condition.

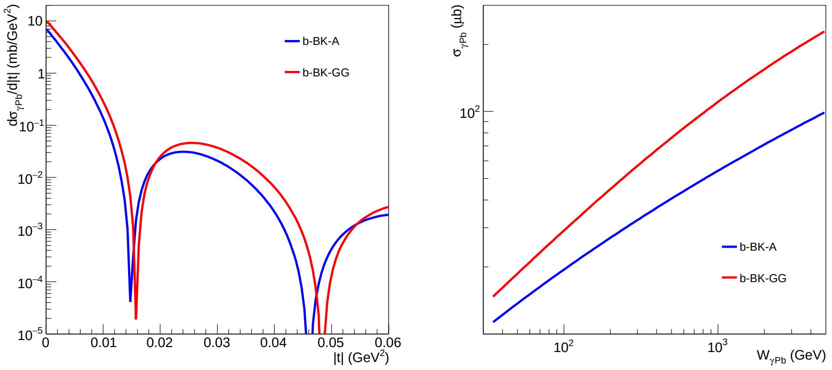

Figure 1: (Colour online) Left: Cross section for the coherent photoproduction of a J/ψ vector meson off a Pb target as a function of $|t|$ at a centre-of-mass energy of the γPb system $W_{\gamma\mathrm{Pb}} = 121$ GeV. Right: Energy dependence for the cross section integrated over $|t|$.

As mentioned before, two sets of dipole scattering amplitudes are used; both were obtained and studied in detail in our previous work [23][1]. In the b-BK-GG approach, the impact-parameter dependent BK equation is solved with an initial condition representing a proton. The solutions at each rapidity are then converted into solutions for a nucleus using the Glauber-Gribov prescription proposed in [25]. In the case of the b-BK-A approach, the initial condition represents the specific nucleus where the impact-parameter part is described with the help of the corresponding Woods-Saxon distribution.

3. Results

The cross section for the coherent photoproduction of a J/ψ vector meson off a Pb target as a function of $|t|$ is shown in Fig. 1 (left) at a centre-of-mass energy of the γPb system $W_{\gamma\mathrm{Pb}} = 121$ GeV, where $W^2_{\gamma\mathrm{Pb}} = M^2_{\mathrm{J}/\psi}/x$ with $M_{\mathrm{J}/\psi}$ the mass of the J/ψ vector meson. Note that not only the absolute magnitude of the cross section is different in the b-BK-A and b-BK-GG approaches, but

---

[1] The amplitudes are available online at `https://hep.fjfi.cvut.cz/NuclearbdepBK.php`

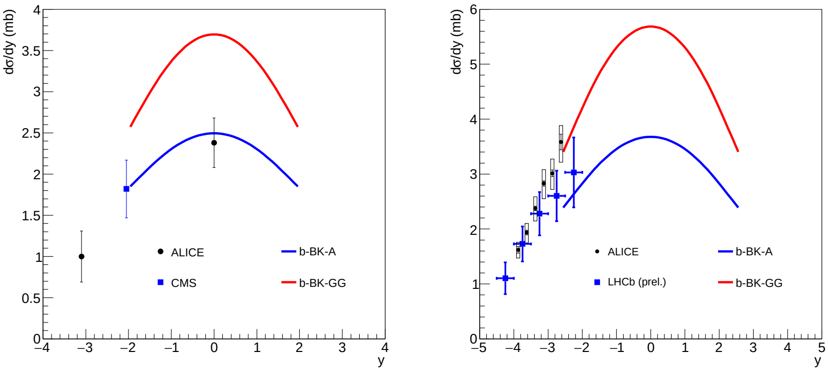

Figure 2: (Colour online) Cross section for the coherent photoproduction of a J/ψ vector meson in ultra-peripheral Pb–Pb collisions at $\sqrt{s_{\rm NN}} = 2.76$ TeV (left) and $\sqrt{s_{\rm NN}} = 5.02$ TeV (right) corresponding to LHC energies during the the Run 1 and Run 2 periods, respectively. The predictions are compared with data from the ALICE [26, 27, 28] and CMS [29] collaborations as well as with preliminary results from the LHCb collaboration [30].

also that the positions of the diffractive minima are displaced. This particular value of $W_{\gamma\rm Pb}$ has been chosen, because it corresponds to production in UPC at midrapidity for LHC Run 2 $\sqrt{s_{\rm NN}}$ energies, as explained below.

Figure 1 (right) shows the energy dependence of the total γPb cross section, that is integrated over $|t|$. The difference in the absolute value of the cross section when using b-BK-A with respect to b-BK-GG solutions increases with energy from a 30% at $W_{\gamma\rm Pb} = 35$ GeV to 54% at $W_{\gamma\rm Pb} = 121$ GeV, reaching already a factor of two at $W_{\gamma\rm Pb} = 900$ GeV.

The cross section $d\sigma/dy$ for the coherent photoproduction of a J/ψ vector meson in Pb–Pb UPC is shown in Fig. 2 for the LHC energies corresponding to the Run 1 (left) and Run 2 (right). This cross section is given by

$$\frac{d\sigma}{dy} = n_\gamma(y)\sigma_{\gamma\rm Pb}(y) + n_\gamma(-y)\sigma_{\gamma\rm Pb}(-y), \qquad (4)$$

where the rapidity y of the J/ψ at the LHC is related to $W_{\gamma\rm Pb}$ by

$$W^2_{\gamma\rm Pb} = \sqrt{s_{\rm NN}} M_{{\rm J}/\psi} e^{-y}. \qquad (5)$$

The flux of photons from the Pb nucleus $n_\gamma(y)$ is computed following the description detailed in [31]. The figure also shows a comparison with existing measurements from the ALICE [26, 27, 28] and CMS [29] collaborations as well as with preliminary results from the LHCb collaboration [30].

4. Discussion

Some comments are in order. First, those of technical nature are addressed, followed by those related to the physics insight provided by the results presented in the previous section.

There has been recent interest on the argument of the exponential term in Eq. (2). This factor, introduced in [32], originates from a Fourier Transform term modified to take into account non-forward amplitudes. In [32] the factor is written in a general form, but when used for phenomenology it has been commonly implemented as in Eq. (2). A proposal put forward in [33] and based on symmetry arguments is that the term $(1-z)$ should be $(1-2z)/2$. Using the proposal from [33] produces a 3.5% larger cross section in both the b-BK-A and the b-BK-GG scenarios. This percentage is constant within the studied energy range. Therefore, this issue does not affect significantly the results presented in this Letter.

The corrections to take into account contributions from the real part of the amplitude and the skewedness effect are computed at fixed $|t| = 0.0001$. They depend on energy decreasing slowly with increasing $W_{\gamma\text{Pb}}$. The factor $(1+\beta^2)$ is 1.07 (1.08) around 35 GeV and 1.04 (1.05) at 1 TeV, while $(R_g^{T,L})^2$ is 1.32 (1.34) around 35 GeV and 1.23 (1.27) at 1 TeV for the b-BK-A (b-BK-GG) case.

The predictions shown in Fig. 2 cover a restricted range in rapidity. The origin of this limitation is that the initial condition for the evolution of the dipole scattering amplitude in the BK equation corresponds to an initial value of $x_0 = 0.008$. Inserting this into $W^2_{\gamma\text{Pb}} = M^2_{\text{J}/\psi}/x$ and using Eq. (5) produces a lower limit in y for Eq. (4).

The approach followed here to compare the predictions from the b-BK-A and b-BK-GG is consistent in the sense that the same wave functions and the same corrections are used. The internal parameters not directly related to the targets take the same values in both cases and the subjacent QCD input, namely the BK equation with the collinear corrections, is the same. Furthermore, this implementation of the BK equation and the corresponding solutions including the impact-parameter dependence avoid the introduction of ad hoc parameters or assumptions to describe the distribution of matter in the plane transverse to the γA interaction. The solutions for the proton case used in the b-BK-GG approach described correctly photo and electroproduction data from HERA [22].

The cross sections shown in Fig. 1 (left) demonstrate the presence of diffractive dips. The location of the dips have been put forward as a signature of saturation in γp [34] and γA collision [35]. The facts that the position of the dip changes according to whether a Glauber-Gribov prescription is used or not, and that the change is larger than that observed in [35] between the saturation and the no-saturation cases, casts a warning on the use of this observable.

The flux entering Eq. (4) is fairly constant for lower $W_{\gamma \mathrm{Pb}}$ energies, but it shows a strong cut-off at large energies. As the γA cross section raises with energy as shown in Fig. 1 (right), the two terms in Eq. (4) have a different numerical value at large $|y|$ with the low $W_{\gamma \mathrm{Pb}}$ contribution being dominant. In this region, the predictions for the b-BK-A and b-BK-GG prescriptions are the closest. At midrapidity, both contributions to Eq. (4) are the same and correspond to $W_{\gamma \mathrm{Pb}} = 125$ GeV. Here, the difference in the presented UPC cross sections is the largest as shown in Fig. 2. Comparison with data from the LHC Run 1 indicates a preference for the b-BK-A approach and disagrees with b-BK-GG at a bit more than one-sigma for $|y| = 2$ and more than 3 sigmas for $y = 0$. The currently existing data from the LHC Run 2 does not provide such a clean message because of the large experimental uncertainties as well as the slight apparent discrepancy between ALICE and LHCb results. The data from LHC Run 2 at midrapidity are still being analysed; it is expected that the uncertainties will be smaller than those in the existing measurement. If so, then these new data may help to select one of the two prescriptions as the most adequate approach.

These results, specifically those shown in Fig. 1, are of interest for future electron-ion colliders [8, 9] where such a process will be precisely measured for a variety of nuclei, allowing for the study not only of the energy, but also of the A dependence of the cross section for coherent J/ψ photo and electroproduction.

5. Summary and outlook

The coherent photonuclear production off Pb nuclei in ultra-peripheral collisions at the LHC has been studied using solutions of the impact-parameter dependent BK equation. Two approaches have been compared. Starting from solutions of the proton case coupled to a Glauber-Gribov formalism, or solving directly the impact-parameter dependent BK equation with an initial condition representing the nucleus. Data from the LHC favour the latter approach. Future data at midrapidity should be precise enough to settle the question of the most valid approach in this context. These studies are of interest for the newly approved and planned future electron-ion colliders where this type of process can be studied with more precision and in a variety of ways.

Acknowledgements

This work has been partially supported by grant 18-07880S of the Czech Science Foundation (GACR), grant LTC17038 of the INTER-EXCELLENCE program at the Ministry of Education, Youth and Sports of the Czech Republic and by the Centre of Advanced Applied Sciences with the number: CZ.02.1.01/0.0/0.0/16-019/0000778. The Centre of Advanced Applied Sciences is co-financed by the European Union.

References

[1] M. G. Ryskin, Diffractive J / psi electroproduction in LLA QCD, Z. Phys. C57 (1993) 89–92. `doi:10.1007/BF01555742`.

[2] S. J. Brodsky, L. Frankfurt, J. F. Gunion, A. H. Mueller, M. Strikman, Diffractive leptoproduction of vector mesons in QCD, Phys. Rev. D50 (1994) 3134–3144. `arXiv:hep-ph/9402283`, `doi:10.1103/PhysRevD.50.3134`.

[3] I. P. Ivanov, N. N. Nikolaev, A. A. Savin, Diffractive vector meson production at HERA: From soft to hard QCD, Phys. Part. Nucl. 37 (2006) 1–85. `arXiv:hep-ph/0501034`, `doi:10.1134/S1063779606010011`.

[4] P. Newman, M. Wing, The Hadronic Final State at HERA, Rev. Mod. Phys. 86 (3) (2014) 1037. `arXiv:1308.3368`, `doi:10.1103/RevModPhys.86.1037`.

[5] A. J. Baltz, The Physics of Ultraperipheral Collisions at the LHC, Phys. Rept. 458 (2008) 1–171. `arXiv:0706.3356`, `doi:10.1016/j.physrep.2007.12.001`.

[6] J. G. Contreras, J. D. Tapia Takaki, Ultra-peripheral heavy-ion collisions at the LHC, Int. J. Mod. Phys. A30 (2015) 1542012. `doi:10.1142/S0217751X15420129`.

[7] S. R. Klein, H. Mntysaari, Imaging the nucleus with high-energy photons, Nature Rev. Phys. 1 (11) (2019) 662–674. `arXiv:1910.10858`, `doi:10.1038/s42254-019-0107-6`.

[8] A. Accardi, et al., Electron Ion Collider: The Next QCD Frontier, Eur. Phys. J. A52 (9) (2016) 268. `arXiv:1212.1701`, `doi:10.1140/epja/i2016-16268-9`.

[9] J. Abelleira Fernandez, et al., A Large Hadron Electron Collider at CERN: Report on the Physics and Design Concepts for Machine and Detector, J.Phys. G39 (2012) 075001. `arXiv:1206.2913`, `doi:10.1088/0954-3899/39/7/075001`.

[10] S. R. Klein, J. Nystrand, Exclusive vector meson production in relativistic heavy ion collisions, Phys. Rev. C60 (1999) 014903. `arXiv:hep-ph/9902259`, `doi:10.1103/PhysRevC.60.014903`.

[11] T. Lappi, H. Mantysaari, Incoherent diffractive J/Psi-production in high energy nuclear DIS, Phys. Rev. C 83 (2011) 065202. `arXiv:1011.1988`, `doi:10.1103/PhysRevC.83.065202`.

[12] V. Goncalves, B. Moreira, F. Navarra, Investigation of diffractive photoproduction of J/Ψ in hadronic collisions, Phys. Rev. C 90 (1) (2014) 015203. `arXiv:1405.6977`, `doi:10.1103/PhysRevC.90.015203`.

[13] J. Cepila, J. G. Contreras, M. Krelina, Coherent and incoherent J/ψ photonuclear production in an energy-dependent hot-spot model, Phys. Rev. C97 (2) (2018) 024901. `arXiv:1711.01855`, `doi:10.1103/PhysRevC.97.024901`.

[14] S. J. Brodsky, A. H. Mueller, Using Nuclei to Probe Hadronization in QCD, Phys. Lett. B 206 (1988) 685–690. `doi:10.1016/0370-2693(88)90719-8`.

[15] B. Kopeliovich, B. Zakharov, Quantum effects and color transparency in charmonium photoproduction on nuclei, Phys. Rev. D 44 (1991) 3466–3472. `doi:10.1103/PhysRevD.44.3466`.

[16] I. Balitsky, Operator expansion for high-energy scattering, Nucl.Phys. B463 (1996) 99–160. `arXiv:hep-ph/9509348`, `doi:10.1016/0550-3213(95)00638-9`.

[17] Y. V. Kovchegov, Small x F(2) structure function of a nucleus including multiple pomeron exchanges, Phys. Rev. D60 (1999) 034008. `arXiv:hep-ph/9901281`, `doi:10.1103/PhysRevD.60.034008`.

[18] Y. V. Kovchegov, Unitarization of the BFKL pomeron on a nucleus, Phys.Rev. D61 (2000) 074018. `arXiv:hep-ph/9905214`, `doi:10.1103/PhysRevD.61.074018`.

[19] E. Iancu, J. D. Madrigal, A. H. Mueller, G. Soyez, D. N. Triantafyllopoulos, Resumming double logarithms in the QCD evolution of color dipoles, Phys. Lett. B744 (2015) 293–302. `arXiv:1502.05642`, `doi:10.1016/j.physletb.2015.03.068`.

[20] E. Iancu, J. D. Madrigal, A. H. Mueller, G. Soyez, D. N. Triantafyllopoulos, Collinearly-improved BK evolution meets the HERA data, Phys. Lett. B750 (2015) 643–652. `arXiv:1507.03651`, `doi:10.1016/j.physletb.2015.09.071`.

[21] J. Cepila, J. G. Contreras, M. Matas, Collinearly improved kernel suppresses Coulomb tails in the impact-parameter dependent Balitsky-Kovchegov evolution, Phys. Rev. D99 (5) (2019) 051502. `arXiv:1812.02548`, `doi:10.1103/PhysRevD.99.051502`.

[22] D. Bendova, J. Cepila, J. Contreras, M. Matas, Solution to the Balitsky-Kovchegov equation with the collinearly improved kernel including impact-parameter dependence, Phys. Rev. D 100 (5) (2019) 054015. `arXiv:1907.12123`, `doi:10.1103/PhysRevD.100.054015`.

[23] J. Cepila, J. Contreras, M. Matas, Predictions for nuclear structure functions from the impact-parameter dependent Balitsky-Kovchegov equation (2 2020). `arXiv:2002.11056`.

[24] A. G. Shuvaev, K. J. Golec-Biernat, A. D. Martin, M. G. Ryskin, Off diagonal distributions fixed by diagonal partons at small x and xi, Phys. Rev. D60 (1999) 014015. `arXiv:hep-ph/9902410`, `doi:10.1103/PhysRevD.60.014015`.

[25] N. Armesto, A Simple model for nuclear structure functions at small x in the dipole picture, Eur. Phys. J. C26 (2002) 35–43. `arXiv:hep-ph/0206017`, `doi:10.1007/s10052-002-1021-z`.

[26] B. Abelev, et al., Coherent J/ψ photoproduction in ultra-peripheral Pb-

Pb collisions at $\sqrt{s_{NN}} = 2.76$ TeV, Phys. Lett. B718 (2013) 1273–1283. `arXiv:1209.3715`, `doi:10.1016/j.physletb.2012.11.059`.

[27] E. Abbas, et al., Charmonium and e^+e^- pair photoproduction at mid-rapidity in ultra-peripheral Pb-Pb collisions at $\sqrt{s_{\rm NN}}$=2.76 TeV, Eur. Phys. J. C73 (11) (2013) 2617. `arXiv:1305.1467`, `doi:10.1140/epjc/s10052-013-2617-1`.

[28] S. Acharya, et al., Coherent J/ψ photoproduction at forward rapidity in ultra-peripheral Pb-Pb collisions at $\sqrt{s_{\rm NN}} = 5.02$ TeV, Phys. Lett. B 798 (2019) 134926. `arXiv:1904.06272`, `doi:10.1016/j.physletb.2019.134926`.

[29] V. Khachatryan, et al., Coherent J/ψ photoproduction in ultra-peripheral PbPb collisions at $\sqrt{s_{NN}} = 2.76$ TeV with the CMS experiment, Phys. Lett. B772 (2017) 489–511. `arXiv:1605.06966`, `doi:10.1016/j.physletb.2017.07.001`.

[30] A. Bursche, Study of coherent J/ψ production in lead-lead collisions at $\sqrt{s_{\rm NN}} = 5$ TeV with the LHCb experiment, Nucl. Phys. A982 (2019) 247–250. `doi:10.1016/j.nuclphysa.2018.10.069`.

[31] J. G. Contreras, Small x gluon shadowing from LHC data on coherent J/ψ photoproduction, Phys. Rev. C96 (1) (2017) 015203. `arXiv:1610.03350`, `doi:10.1103/PhysRevC.96.015203`.

[32] J. Bartels, K. J. Golec-Biernat, K. Peters, On the dipole picture in the nonforward direction, Acta Phys. Polon. B 34 (2003) 3051–3068. `arXiv:hep-ph/0301192`.

[33] Y. Hatta, B.-W. Xiao, F. Yuan, Gluon Tomography from Deeply Virtual Compton Scattering at Small-x, Phys. Rev. D95 (11) (2017) 114026. `arXiv:1703.02085`, `doi:10.1103/PhysRevD.95.114026`.

[34] N. Armesto, A. H. Rezaeian, Exclusive vector meson production at high energies and gluon saturation, Phys. Rev. D 90 (5) (2014) 054003. `arXiv:1402.4831`, `doi:10.1103/PhysRevD.90.054003`.

[35] T. Toll, T. Ullrich, Exclusive diffractive processes in electron-ion collisions, Phys. Rev. C 87 (2) (2013) 024913. `arXiv:1211.3048`, `doi:10.1103/PhysRevC.87.024913`.

Contribution of the non-linear term in the Balitsky-Kovchegov equation to the nuclear structure functions

Jan Cepila and Marek Matas

Faculty of Nuclear Sciences and Physical Engineering, Czech technical University in Prague, Czech Republic

Abstract. In this paper, we present nuclear structure functions calculated from the impact-parameter dependent solution of the Balitsky-Kovchegov equation with our recently proposed set of nuclear initial conditions. We calculate the results with and without the non-linear term in the BK equation in order to study the impact of saturation effects on the measurable structure functions and nuclear modification factor. The difference of these results rises with decreasing Bjorken x and increasing scale. These predictions are of interest to the physics program at the future ep and eA colliders.

PACS. 12.40.-y Models of Strong Interactions – 12.38.Bx Perturbation theory applied to quantum chromodynamics – 21.60.-n Nuclear models

1 Introduction

With the recently approved Electron Ion Collider in the USA [1] and planned LHeC [2] at CERN, a new interest is sparked in understanding the difference between the structure function of nuclear and of proton targets. At small values of Bjorken x, the nuclear structure function per one nucleon is smaller than the nucleon structure function. This effect called shadowing may be understood qualitatively in the frame where the target is moving very fast to be a result of gluon recombination due to the overlap of the gluon wave functions from the surrounding nucleons [3,4]. In this way, the gluon density in a bound nucleon is smaller than the gluon density in a free nucleon.

This phenomenon is called saturation since at certain saturation scale the recombination processes balance gluon splitting, effectively saturating the gluon density. Quantitatively, the evolution of gluon density in this frame is described by non-linear evolution equations [3,4]. Recent review of available evolution equations can be found in e.g. [5]. The Balitsky-Kovchegov evolution equation (BK) [6,7] has been used with great success to describe the internal structure and dynamics of protons in the impact parameter independent framework [8]. This evolution equation can be schematically written as $\partial_y N = K \otimes (N - N^2)$. It incorporates non-linear dynamics via the second term proportional to N^2. Omitting this term, the BK equation becomes equivalent to BFKL equation, which has been shown to give a satisfactory description of HERA data [9].

The solution of the BK equation — the dipole scattering amplitude N — allows us to calculate a wide spectrum of observables e.g. [8,10]. In our previous work, we have lifted one of the common approximations that were needed for solving this equation and by utilizing the collinearly improved kernel, we have shown that the impact parameter dependent computation can be obtained without being spoiled by the non-perturbative effects of Coulomb tails [11]. In this work, we focus on quantitatively addressing the onset of saturation effects in nuclear targets by suppressing the non-linear term in the equation using our recently proposed initial condition. We are aware that the applicability of our model is restricted to sufficiently high energies where gluons are dominant scattering targets. The resulting signals are of interest for the physics program planned at future facilities.

2 Balitsky-Kovchegov equation

The leading order Balitsky-Kovchegov evolution equation [6,7] for the impact parameter dependent case with the assumption of identical scattering amplitude for various angles between the transverse dipole size vector $\boldsymbol{r}$ and impact parameter vector $\boldsymbol{b}$ can be written as

$$\frac{\partial N(r,b;y)}{\partial y} = \int d\boldsymbol{r_1} K(r,r_1,r_2)\big(N(r_1,b_1;y) + N(r_2,b_2;y) - N(r,b;y) - N(r_1,b_1;y)N(r_2,b_2;y)\big). \quad (1)$$

The evolution runs in rapidity $y = \log(x_0/x)$, where x is the Bjorken variable and x_0 gives the initial value of Bjorken variable for the evolution. In order to solve the BK equation with explicit impact parameter dependence and to avoid the unphysical growth of so-called Coulomb tails [12] originating from the non-perturbative region of its phase space we shall use the collinearly improved kernel [13] expressed as

$$K(r,r_1,r_2) = \frac{\overline{\alpha}_s}{2\pi}\frac{r^2}{r_1^2 r_2^2}\left[\frac{r^2}{\min(r_1^2,r_2^2)}\right]^{\pm\overline{\alpha}_s A_1}\frac{J_1(2\sqrt{\overline{\alpha}_s\rho^2})}{\sqrt{\overline{\alpha}_s}\rho}. \quad (2)$$

with the smallest-dipole prescription for its running coupling

$$\alpha_s(r) = \frac{4\pi}{\beta_{0,n_f}\ln\left(\frac{4C^2}{r^2\Lambda^2_{n_f}}\right)}, \quad (3)$$

as described in [11] with all the parameter values and in greater detail.

In order to solve the BK equation for the nuclear case, one has to start with a nuclear initial condition. We have chosen to treat individually the dependence on the transverse size of the dipole $\boldsymbol{r}$ and the dependence on the distance of the dipole from the center of the target $\boldsymbol{b}$. For the r-dependence, we have parametrized our initial condition as in the GBW model [14] and for the b-dependence, we have chosen to mimic the density profile of the target parametrized by the Woods-Saxon distribution expressed as [15]

$$\rho_A(b,z) = \rho_0\frac{1}{\exp\left[(r-\mathrm{R})/\mathrm{a}\right]+1}, \quad (4)$$

where $r \equiv \sqrt{b^2+z^2}$ and parameters are given by [16]. In order to obtain the nuclear thickness of the target, one has to integrate the Woods-Saxon distribution over the longitudinal coordinate z as

$$T_A(b) = \int\limits_{-\infty}^{+\infty} dz\rho_A(b,z). \quad (5)$$

Then we can define our nuclear initial condition (we denote this model as b-BK-A in the plots) as

$$N^A(r,b,y=0) = 1-\exp\left(-\frac{Q_{s0}^2(A)}{4}r^2\frac{T_A(b_{q_1},b_{q_2})}{2}\right) \quad (6)$$

with

$$T_A(b_{q_1},b_{q_2}) = \frac{1}{T_A(0)}\left[T_A(b_{q_1})+T_A(b_{q_2})\right] \quad (7)$$

and values of $Q_{s0}^2(Ca) = 0.341\,\mathrm{GeV}^2$ and $Q_{s0}^2(Pb) = 0.609\,\mathrm{GeV}^2$ taken from [15].

3 Nuclear structure functions

An observable that is often used to describe the onset and characteristic of nuclear effects is the so-called nuclear modification factor. This variable tells us how much a nucleus differs from a simple sum of the constituent nucleons and is obtained in our framework with the use of the structure function that can be expressed in the dipole model [4,17] as

$$F_2^A(x,Q^2) = \frac{Q^2}{4\pi^2\alpha_{\mathrm{em}}}\sum_i\int d\boldsymbol{r}dz|\Psi^i_{T,L}(z,r)|^2\sigma^A_{q\bar{q}}(r,\tilde{x}_i). \quad (8)$$

Here $\tilde{x}_i = x(1+(4m_{q_i}^2)/Q^2)$ with m_{q_i} the mass of the i-quark [14]. The cross section of the interaction of the color dipole with the target can be obtained due to the optical theorem as

$$\sigma^A_{q\bar{q}}(r,x) = 2\int \mathrm{d}\boldsymbol{b}N^A(r,b,x). \quad (9)$$

The wave function representing the probability of a virtual photon splitting into a quark-antiquark dipole can be written [17] as

$$|\Psi^i_T(z,r)|^2 = \frac{3\alpha_{\mathrm{em}}}{2\pi^2}e_{q_i}^2\left((z^2+(1-z)^2)\epsilon^2K_1^2(\epsilon r)+m_{q_i}^2K_0^2(\epsilon r)\right) \quad (10)$$

and

$$|\Psi^i_L(z,r)|^2 = \frac{3\alpha_{\mathrm{em}}}{2\pi^2}e_{q_i}^2\left(4Q^2z^2(1-z)^2K_0^2(\epsilon r)\right) \quad (11)$$

for the transverse and longitudinal polarization of the incoming photon, respectively, and $|\Psi^i_{T,L}(z,r)|^2$ is a sum of squares of both contributions. K_0 and K_1 are the MacDonald functions, z is the fraction of the total photon longitudinal momentum carried by the quark, e_{q_i} is the fractional charge in units of elementary charge of quark i, $\alpha_{\mathrm{em}} = 1/137$ and $\epsilon^2 = z(1-z)Q^2+m_{q_i}^2$. The quark masses were set to $100\,\mathrm{MeV}/c^2$ for light, $1.3\,\mathrm{GeV}/c^2$ for charm, and $4.5\,\mathrm{GeV}/c^2$ for bottom quark. After computing the structure function in such way and after taking the proton structure function calculated in a similar way (see [11,12]), one can obtain the nuclear modification factor as

$$R_{pA} \equiv \frac{F_2^A(x,Q^2)}{A\,F_2^p(x,Q^2)}. \quad (12)$$

The longitudinal structure function can be within the same model expressed as

$$F_L^A(x,Q^2) = \frac{Q^2}{4\pi^2\alpha_{\mathrm{em}}}\sum_i\int d\boldsymbol{r}dz|\Psi^i_L(z,\boldsymbol{r})|^2\sigma^A_{q\bar{q}}(\boldsymbol{r},\tilde{x}_i). \quad (13)$$

4 Results

We have solved the BK equation in the impact-parameter dependent, collinearly improved framework. We have done so with the same initial condition for two cases $i)$ with the inclusion of the saturation effects represented by the nonlinear term in Equation 1 and $ii)$ without the nonlinear term in order to understand the expected role of saturation in the solutions of this equation. The initial condition was chosen so that it resembles the transverse profile of the nucleus. Fig. 1 shows the resulting scattering amplitude at $y = 5$ for two nuclei (lead and calcium) and its dependence on the transverse dipole size r for a fixed $b = 0.1\,\mathrm{GeV}^{-1}$ and on the impact parameter b for a fixed $r = 1\,\mathrm{GeV}^{-1}$. We can see that the value of the non-saturated scattering amplitude exceeds unity. The difference between the nonlinear and linear evolution is 30%-60%. In Figs. 2 and 3 we show the computed structure functions $F_2(x,Q^2)$

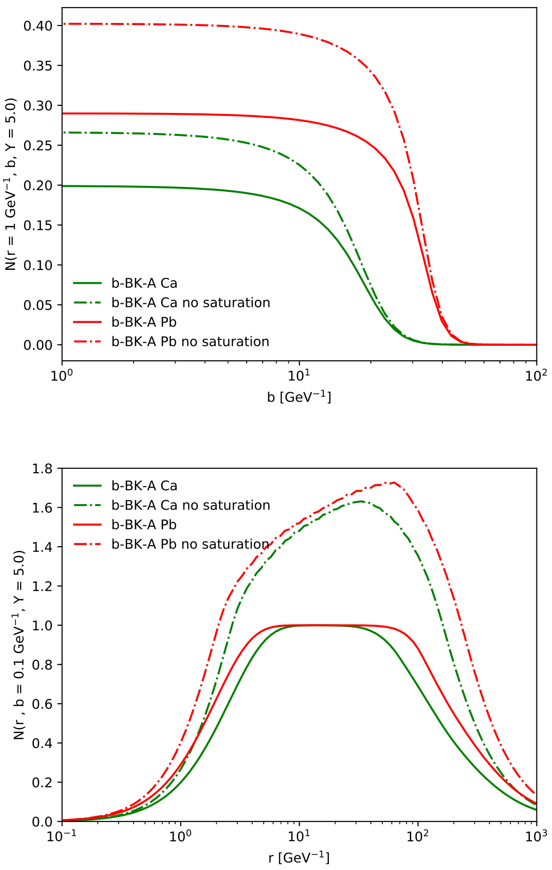

Fig. 1. The dipole scattering amplitudes computed for Ca (green) and Pb (red) with (solid) and without (dashed) saturation effects. The comparison is done at $y = 5$ as a function of the impact parameter for a dipole size $r = 1/\mathrm{GeV}$ (upper) and as a function of the dipole size for an impact parameter $b = 0.1/\mathrm{GeV}$ (lower).

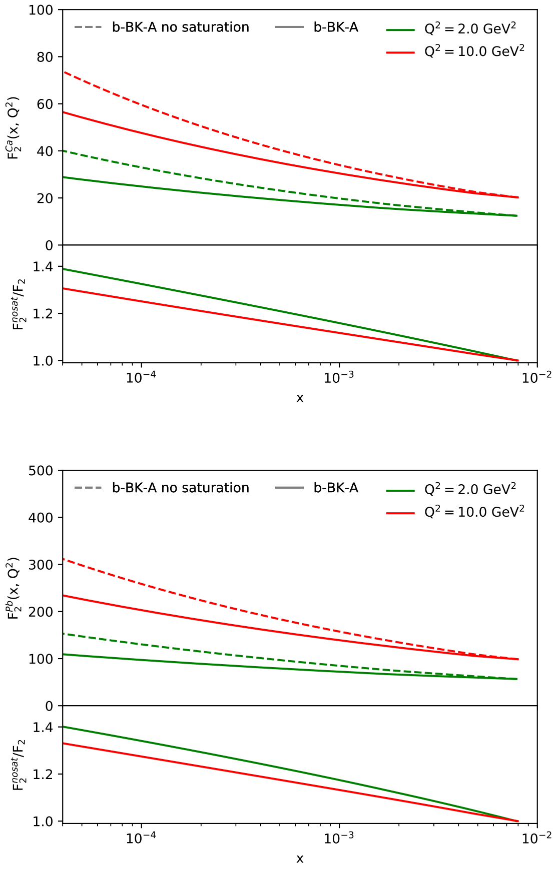

Fig. 2. The nuclear structure function $F_2^A(x, Q^2)$ w.r.t x computed with the Balitsky-Kovchegov evolution equation with and without saturation for two values of Q^2 for calcium (upper) and lead (lower). Bottom panel in the figures shows the ratio of the computation with and without saturation.

and $F_L(x, Q^2)$ for calcium and lead respectively in linear and non-linear scenario as well as their ratios for two choices of Q^2. One can see that the non-linear evolution suppresses the structure functions significantly and the difference grows with decreasing Bjorken x. At large Bjorken x the difference is very small and thus one cannot discriminate between both scenarios using available data. Also, the difference rises with increasing Q^2 both for $F_L(x, Q^2)$ and $F_2(x, Q^2)$. For $F_L(x, Q^2)$ the difference is greater than for $F_2(x, Q^2)$ at all scales and Bjorken x. In Fig. 4, we show the dependence of the nuclear modification factor on x for calcium and lead obtained with the use of Eq. (12) and compare it to data for $Q^2 = 2.42\,\mathrm{GeV}^2$ and $Q^2 = 4.45\,\mathrm{GeV}^2$. We can see, that the non-saturated scattering amplitudes produce larger nuclear modification factor implying softer nuclear effects. The difference between linear and non-linear model grows with decreasing Bjorken x and so one can clearly discriminate between saturated and non-saturated model with future data from electron ion colliders. At large Bjorken x, both models are indistinguishable and both agree quite well with measured data point from E665 from Fermilab [18].

5 Conclusions

In this paper we have presented a calculation of nuclear structure functions using the impact parameter dependent solution of the non-linear BK evolution equation. We have compared the resulting structure functions $F_2(x, Q^2)$ and $F_L(x, Q^2)$ and nuclear modification factor $R_{pA}(x, Q^2)$ with and without the non-linear term in BK evolution equation. The difference of the results with and without saturation is clearly visible and it rises with decreasing Bjorken x and with scale Q^2 indicating that we will be able to distinguish between these two models with future data from electron-ion colliders.

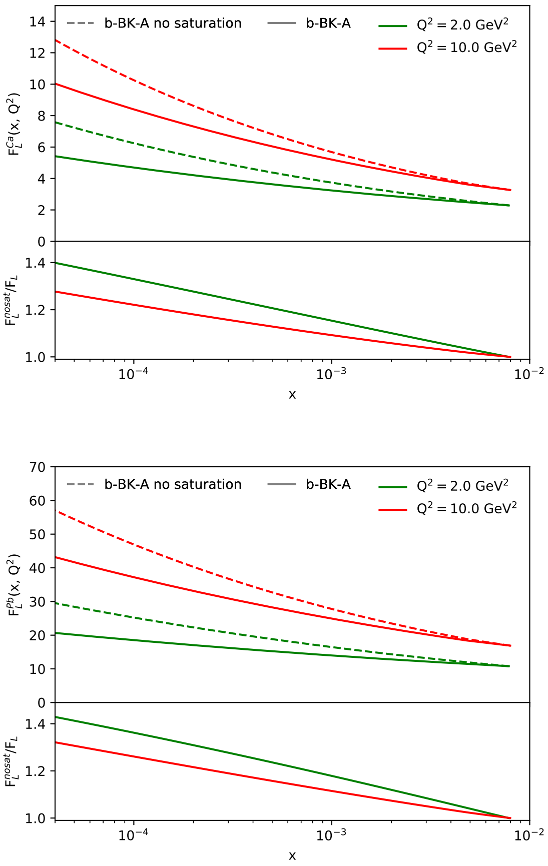

Fig. 3. The nuclear structure function $F_L^A(x, Q^2)$ w.r.t x computed with the Balitsky-Kovchegov evolution equation with and without saturation for two values of Q^2 for calcium (upper) and lead (lower). Bottom panel in the figures shows the ratio of the computation with and without saturation.

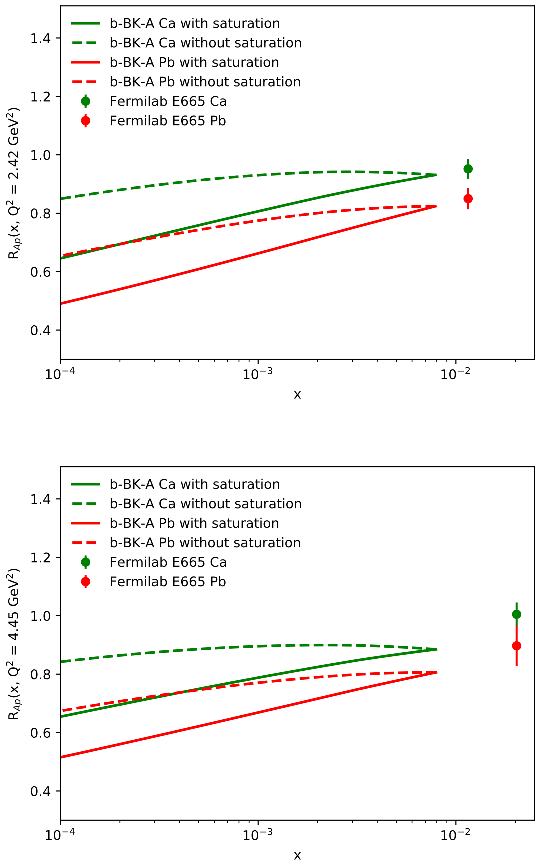

Fig. 4. Nuclear modification factor computed for Ca (green) and Pb (red) with (solid) and without (dashed) saturation effects for $Q^2 = 2.42$ GeV^2 (upper) and $Q^2 = 4.45$ GeV^2 (lower). The predictions are compared with data from [18].

6 Acknowledgements

This work has been supported from grant LTC17038 of the INTER-EXCELLENCE program at the Ministry of Education, Youth and Sports of the Czech Republic and the COST Action CA15213 THOR.

References

1. A. Accardi et al., Eur. Phys. J. **A52**, 268 (2016), `1212.1701`
2. J. Abelleira Fernandez et al. (LHeC Study Group), J.Phys. **G39**, 075001 (2012), `1206.2913`
3. L.V. Gribov, E.M. Levin, M.G. Ryskin, Phys. Rept. **100**, 1 (1983)
4. A.H. Mueller, J.w. Qiu, Nucl. Phys. **B268**, 427 (1986)
5. J.L. Albacete, C. Marquet, Prog. Part. Nucl. Phys. **76**, 1 (2014), `1401.4866`
6. I. Balitsky, Nucl.Phys. **B463**, 99 (1996), `hep-ph/9509348`
7. Y.V. Kovchegov, Phys. Rev. **D60**, 034008 (1999), `hep-ph/9901281`
8. J.L. Albacete, N. Armesto, J.G. Milhano, P. Quiroga-Arias, C.A. Salgado, Eur.Phys.J. **C71**, 1705 (2011), `1012.4408`
9. E. Avsar, E. Iancu, Phys. Lett. B **673**, 24 (2009), `0901.2873`
10. A. van Hameren, P. Kotko, K. Kutak, C. Marquet, E. Petreska, S. Sapeta, JHEP **12**, 034 (2016), [Erratum: JHEP 02, 158 (2019)], `1607.03121`
11. D. Bendova, J. Cepila, J.G. Contreras, M. Matas, Phys. Rev. **D100**, 054015 (2019), `1907.12123`
12. J. Cepila, J.G. Contreras, M. Matas, Phys. Rev. **D99**, 051502 (2019), `1812.02548`
13. E. Iancu, J.D. Madrigal, A.H. Mueller, G. Soyez, D.N. Triantafyllopoulos, Phys. Lett. **B750**, 643 (2015), `1507.03651`
14. K.J. Golec-Biernat, M. Wusthoff, Phys. Rev. **D59**, 014017 (1998), `hep-ph/9807513`
15. J. Cepila, J. Contreras, M. Matas (2020), `2002.11056`
16. H. De Vries, C. De Jager, C. De Vries, Atom.Data Nucl.Data Tabl. **36**, 495 (1987)
17. N.N. Nikolaev, B. Zakharov, Z.Phys. **C49**, 607 (1991)
18. M.R. Adams et al. (E665), Z. Phys. **C67**, 403 (1995), `hep-ex/9505006`

Bibliography

[1] David J. Gross and Frank Wilczek. Ultraviolet behavior of non-abelian gauge theories. *Phys. Rev. Lett.*, 30:1343–1346, Jun 1973.

[2] H. David Politzer. Reliable perturbative results for strong interactions? *Phys. Rev. Lett.*, 30:1346–1349, Jun 1973.

[3] Jamal Jalilian-Marian, Alex Kovner, Larry D. McLerran, and Heribert Weigert. The Intrinsic glue distribution at very small x. *Phys. Rev.*, D55:5414–5428, 1997.

[4] Jamal Jalilian-Marian, Alex Kovner, Andrei Leonidov, and Heribert Weigert. The Wilson renormalization group for low x physics: Towards the high density regime. *Phys. Rev.*, D59:014014, 1998.

[5] Jamal Jalilian-Marian, Alex Kovner, and Heribert Weigert. The Wilson renormalization group for low x physics: Gluon evolution at finite parton density. *Phys. Rev.*, D59:014015, 1998.

[6] Heribert Weigert. Unitarity at small Bjorken x. *Nucl. Phys.*, A703:823–860, 2002.

[7] Edmond Iancu, Andrei Leonidov, and Larry D. McLerran. Nonlinear gluon evolution in the color glass condensate. 1. *Nucl. Phys.*, A692:583–645, 2001.

[8] Alex Kovner, J. Guilherme Milhano, and Heribert Weigert. Relating different approaches to nonlinear QCD evolution at finite gluon density. *Phys. Rev.*, D62:114005, 2000.

[9] H. David Politzer. Asymptotic Freedom: An Approach to Strong Interactions. *Phys. Rept.*, 14:129–180, 1974.

[10] L. N. Lipatov. The parton model and perturbation theory. *Sov. J. Nucl. Phys.*, 20:94–102, 1975. [Yad. Fiz.20,181(1974)].

[11] V. N. Gribov and L. N. Lipatov. Deep inelastic e p scattering in perturbation theory. *Sov. J. Nucl. Phys.*, 15:438–450, 1972. [Yad. Fiz.15,781(1972)].

[12] Guido Altarelli and G. Parisi. Asymptotic Freedom in Parton Language. *Nucl. Phys.*, B126:298–318, 1977.

[13] Victor S. Fadin, E. A. Kuraev, and L. N. Lipatov. On the Pomeranchuk Singularity in Asymptotically Free Theories. *Phys. Lett.*, B60:50–52, 1975.

[14] L. N. Lipatov. Reggeization of the Vector Meson and the Vacuum Singularity in Nonabelian Gauge Theories. *Sov. J. Nucl. Phys.*, 23:338–345, 1976. [Yad. Fiz.23,642(1976)].

[15] I. Balitsky. Operator expansion for high-energy scattering. *Nucl. Phys.*, B463:99–160, 1996.

[16] I. Balitsky. Factorization for high-energy scattering. *Phys. Rev. Lett.*, 81:2024–2027, 1998.

[17] Ian Balitsky. Factorization and high-energy effective action. *Phys. Rev.*, D60:014020, 1999.

[18] Ian Balitsky. Effective field theory for the small x evolution. *Phys. Lett.*, B518:235–242, 2001.

[19] Yuri V. Kovchegov. Small x F(2) structure function of a nucleus including multiple pomeron exchanges. *Phys. Rev.*, D60:034008, 1999.

[20] V.N. Gribov and L.N. Lipatov. e+ e- pair annihilation and deep inelastic e p scattering in perturbation theory. *Sov. J. Nucl. Phys.*, 15:675–684, 1972.

[21] Yuri L. Dokshitzer. Calculation of the Structure Functions for Deep Inelastic Scattering and e+ e- Annihilation by Perturbation Theory in Quantum Chromodynamics. *Sov. Phys. JETP*, 46:641–653, 1977.

[22] Alfred H. Mueller. Small x Behavior and Parton Saturation: A QCD Model. *Nucl. Phys.*, B335:115–137, 1990.

[23] Nikolai N. Nikolaev and B. G. Zakharov. Color transparency and scaling properties of nuclear shadowing in deep inelastic scattering. *Z. Phys.*, C49:607–618, 1991. [,733(1990)].

[24] Alfred H. Mueller. Soft gluons in the infinite momentum wave function and the BFKL pomeron. *Nucl. Phys.*, B415:373–385, 1994.

[25] Larry D. McLerran and Raju Venugopalan. Boost covariant gluon distributions in large nuclei. *Phys. Lett.*, B424:15–24, 1998.

[26] Krzysztof J. Golec-Biernat and M. Wusthoff. Saturation effects in deep inelastic scattering at low Q**2 and its implications on diffraction. *Phys. Rev.*, D59:014017, 1998.

[27] A. van Hameren, P. Kotko, K. Kutak, C. Marquet, E. Petreska, and S. Sapeta. Forward di-jet production in p+Pb collisions in the small-x improved TMD factorization framework. *JHEP*, 12:034, 2016.

[28] E. A. Kuraev, L. N. Lipatov, and Victor S. Fadin. Multi - Reggeon Processes in the Yang-Mills Theory. *Sov. Phys. JETP*, 44:443–450, 1976. [Zh. Eksp. Teor. Fiz.71,840(1976)].

[29] E. A. Kuraev, L. N. Lipatov, and Victor S. Fadin. The Pomeranchuk Singularity in Nonabelian Gauge Theories. *Sov. Phys. JETP*, 45:199–204, 1977. [Zh. Eksp. Teor. Fiz.72,377(1977)].

[30] I. I. Balitsky and L. N. Lipatov. The Pomeranchuk Singularity in Quantum Chromodynamics. *Sov. J. Nucl. Phys.*, 28:822–829, 1978. [Yad. Fiz.28,1597(1978)].

[31] E. Iancu, J. D. Madrigal, A. H. Mueller, G. Soyez, and D. N. Triantafyllopoulos. Resumming double logarithms in the QCD evolution of color dipoles. *Phys. Lett.*, B744:293–302, 2015.

[32] E. Iancu, J. D. Madrigal, A. H. Mueller, G. Soyez, and D. N. Triantafyllopoulos. Collinearly-improved BK evolution meets the HERA data. *Phys. Lett.*, B750:643–652, 2015.

[33] D. Bendova, J. Cepila, J. G. Contreras, and M. Matas. Solution to the Balitsky-Kovchegov equation with the collinearly improved kernel including impact-parameter dependence. *Phys. Rev.*, D100(5):054015, 2019.

[34] J. Cepila, J. G. Contreras, and M. Matas. Collinearly improved kernel suppresses Coulomb tails in the impact-parameter dependent Balitsky-Kovchegov evolution. *Phys. Rev.*, D99(5):051502, 2019.

[35] J. Cepila, J.G. Contreras, and M. Matas. Predictions for nuclear structure functions from the impact-parameter dependent Balitsky-Kovchegov equation. *arXiv:2002.11056*, 2 2020.

[36] Elliott D. Bloom et al. High-Energy Inelastic e p Scattering at 6-Degrees and 10-Degrees. *Phys. Rev. Lett.*, 23:930–934, 1969.

[37] Martin Breidenbach, Jerome I. Friedman, Henry W. Kendall, Elliott D. Bloom, D. H. Coward, H. C. DeStaebler, J. Drees, Luke W. Mo, and Richard E. Taylor. Observed Behavior of Highly Inelastic electron-Proton Scattering. *Phys. Rev. Lett.*, 23:935–939, 1969.

[38] H. Abramowicz et al. Combination of measurements of inclusive deep inelastic $e^{\pm}p$ scattering cross sections and QCD analysis of HERA data. *Eur. Phys. J.*, C75(12):580, 2015.

[39] F. D. Aaron et al. Combined Measurement and QCD Analysis of the Inclusive e+- p Scattering Cross Sections at HERA. *JHEP*, 01:109, 2010.

[40] Guthrie Miller et al. Inelastic electron-Proton Scattering at Large Momentum Transfers. *Phys. Rev.*, D5:528, 1972.

[41] A. C. Benvenuti et al. A High Statistics Measurement of the Proton Structure Functions F(2) (x, Q**2) and R from Deep Inelastic Muon Scattering at High Q**2. *Phys. Lett.*, B223:485–489, 1989.

[42] Richard P. Feynman. Very high-energy collisions of hadrons. *Phys. Rev. Lett.*, 23:1415–1417, 1969. [,494(1969)].

[43] J. D. Bjorken. Asymptotic Sum Rules at Infinite Momentum. *Phys. Rev.*, 179:1547–1553, 1969.

[44] J I Friedman and H W Kendall. Deep inelastic electron scattering. *Annual Review of Nuclear Science*, 22(1):203–254, 1972.

[45] Curtis G. Callan, Jr. and David J. Gross. High-energy electroproduction and the constitution of the electric current. *Phys. Rev. Lett.*, 22:156–159, 1969.

[46] David Griffiths. *Introduction to elementary particles.* 2008.

[47] Javier L. Albacete, Nestor Armesto, Jose Guilherme Milhano, Paloma Quiroga-Arias, and Carlos A. Salgado. AAMQS: A non-linear QCD analysis of new HERA data at small-x including heavy quarks. *Eur. Phys. J.*, C71:1705, 2011.

[48] H. Kowalski, L. Motyka, and G. Watt. Exclusive diffractive processes at HERA within the dipole picture. *Phys. Rev.*, D74:074016, 2006.

[49] A. G. Shuvaev, Krzysztof J. Golec-Biernat, Alan D. Martin, and M. G. Ryskin. Off diagonal distributions fixed by diagonal partons at small x and xi. *Phys. Rev.*, D60:014015, 1999.

[50] J. Nemchik, Nikolai N. Nikolaev, and B. G. Zakharov. Scanning the BFKL pomeron in elastic production of vector mesons at HERA. *Phys. Lett.*, B341:228–237, 1994.

[51] J. Nemchik, Nikolai N. Nikolaev, E. Predazzi, and B. G. Zakharov. Color dipole phenomenology of diffractive electroproduction of light vector mesons at HERA. *Z. Phys.*, C75:71–87, 1997.

[52] Jeffrey R. Forshaw, R. Sandapen, and Graham Shaw. Color dipoles and rho, phi electroproduction. *Phys. Rev.*, D69:094013, 2004.

[53] Edmond Iancu and Raju Venugopalan. The Color glass condensate and high-energy scattering in QCD. In Rudolph C. Hwa and Xin-Nian Wang, editors, *Quark-gluon plasma 4*, pages 249–3363. 2003.

[54] Francois Gelis, Edmond Iancu, Jamal Jalilian-Marian, and Raju Venugopalan. The Color Glass Condensate. *Ann. Rev. Nucl. Part. Sci.*, 60:463–489, 2010.

[55] Javier L. Albacete and Cyrille Marquet. Gluon saturation and initial conditions for relativistic heavy ion collisions. *Prog. Part. Nucl. Phys.*, 76:1–42, 2014.

[56] Gerard 't Hooft. A Two-Dimensional Model for Mesons. *Nucl. Phys.*, B75:461–470, 1974.

[57] Alfred H. Mueller. Unitarity and the BFKL pomeron. *Nucl. Phys.*, B437:107–126, 1995.

[58] Alfred H. Mueller and Bimal Patel. Single and double BFKL pomeron exchange and a dipole picture of high-energy hard processes. *Nucl. Phys.*, B425:471–488, 1994.

[59] Yuri V. Kovchegov. Unitarization of the BFKL pomeron on a nucleus. *Phys. Rev.*, D61:074018, 2000.

[60] Daniel Boer, Andre Utermann, and Erik Wessels. Compatibility of phenomenological dipole cross sections with the Balitsky-Kovchegov equation. *Phys. Rev.*, D75:094022, 2007.

[61] Ian Balitsky. Quark contribution to the small-x evolution of color dipole. *Phys. Rev.*, D75:014001, 2007.

[62] C. Marquet and G. Soyez. The Balitsky-Kovchegov equation in full momentum space. *Nucl. Phys.*, A760:208–222, 2005.

[63] Yuri V. Kovchegov and Heribert Weigert. Triumvirate of Running Couplings in Small-x Evolution. *Nucl. Phys.*, A784:188–226, 2007.

[64] Javier L. Albacete and Yuri V. Kovchegov. Solving high energy evolution equation including running coupling corrections. *Phys. Rev.*, D75:125021, 2007.

[65] Guillaume Beuf. An Alternative scaling solution for high-energy QCD saturation with running coupling. 2008.

[66] C. Marquet, Robert B. Peschanski, and G. Soyez. QCD traveling waves at non-asymptotic energies. *Phys. Lett.*, B628:239–249, 2005.

[67] S. Munier and Robert B. Peschanski. Traveling wave fronts and the transition to saturation. *Phys. Rev.*, D69:034008, 2004.

[68] Javier L. Albacete, Nestor Armesto, Jose Guilherme Milhano, and Carlos A. Salgado. Non-linear QCD meets data: A Global analysis of lepton-proton scattering with running coupling BK evolution. *Phys. Rev.*, D80:034031, 2009.

[69] M. Matas. Study of Properties of the Dipole Scattering Amplitude Using Balitsky-Kovchegov Evolution Equation. *Master's thesis, CTU in Prague*, 2016.

[70] Marek Matas, Jan Cepila, and Jesus Guillermo Contreras Nuno. Numerical precision of the solution to the running-coupling Balitsky-Kovchegov equation. *EPJ Web Conf.*, 112:02008, 2016.

[71] Jan Cepila and Jesus Guillermo Contreras. Rapidity dependence of saturation in inclusive HERA data with the rcBK equation. *arXiv:1501.06687*, 2015.

[72] Paloma Quiroga-Arias, Javier L. Albacete, N. Armesto, Jose Guilherme Milhano, and Carlos A. Salgado. AAMQS: a non-linear QCD description of new HERA data at small-x. *J. Phys.*, G38:124124, 2011.

[73] K. A. Olive et al. Review of Particle Physics. *Chin. Phys.*, C38:090001, 2014.

[74] L. Frankfurt, G. A. Miller, and M. Strikman. Coherent nuclear diffractive production of mini - jets: Illuminating color transparency. *Phys. Lett.*, B304:1–7, 1993.

[75] H. Heiselberg, G. Baym, B. Blaettel, L. L. Frankfurt, and M. Strikman. Color transparency, color opacity, and fluctuations in nuclear collisions. *Phys. Rev. Lett.*, 67:2946–2949, 1991.

[76] B. Z. Kopeliovich, L. I. Lapidus, and A. B. Zamolodchikov. Dynamics of Color in Hadron Diffraction on Nuclei. *JETP Lett.*, 33:595–597, 1981. [Pisma Zh. Eksp. Teor. Fiz.33,612(1981)].

[77] Jeffrey Berger and Anna Stasto. Numerical solution of the nonlinear evolution equation at small x with impact parameter and beyond the LL approximation. *Phys. Rev.*, D83:034015, 2011.

[78] Jeffrey Berger and Anna M. Stasto. Small x nonlinear evolution with impact parameter and the structure function data. *Phys. Rev.*, D84:094022, 2011.

[79] Krzysztof J. Golec-Biernat and A. M. Stasto. On solutions of the Balitsky-Kovchegov equation with impact parameter. *Nucl. Phys.*, B668:345–363, 2003.

[80] Marcel Froissart. Asymptotic behavior and subtractions in the Mandelstam representation. *Phys. Rev.*, 123:1053–1057, 1961.

[81] W. Heisenberg. Mesonenerzeugung als Stosswellenproblem. *Z. Phys.*, 133:65, 1952.

[82] André Martin. Scattering Theory: Unitarity, Analyticity and Crossing. *Lect. Notes Phys.*, 3:1–117, 1969.

[83] Alexander Kovner and Urs Achim Wiedemann. Nonlinear QCD evolution: Saturation without unitarization. *Phys. Rev.*, D66:051502, 2002.

[84] Jeffrey J. Berger. Small-x evolution wih impact parameter dependence. *The Physics Department of Penn State*, 2012.

[85] B. Ducloué, E. Iancu, A. H. Mueller, G. Soyez, and D. N. Triantafyllopoulos. Non-linear evolution in QCD at high-energy beyond leading order. *JHEP*, 04:081, 2019.

[86] Javier L. Albacete. Resummation of double collinear logs in BK evolution versus HERA data. *Nucl. Phys.*, A957:71–84, 2017.

[87] Guillaume Beuf. Improving the kinematics for low-x QCD evolution equations in coordinate space. *Phys. Rev.*, D89(7):074039, 2014.

[88] Agustin Sabio Vera. An 'All-poles' approximation to collinear resummations in the Regge limit of perturbative QCD. *Nucl. Phys.*, B722:65–80, 2005.

[89] C. Alexa et al. Elastic and Proton-Dissociative Photoproduction of J/psi Mesons at HERA. *Eur. Phys. J.*, C73(6):2466, 2013.

[90] A. Aktas et al. Elastic J/psi production at HERA. *Eur. Phys. J.*, C46:585–603, 2006.

[91] Nestor Armesto. Nuclear shadowing. *J. Phys. G*, 32:R367–R394, 2006.

[92] A. Accardi et al. Electron Ion Collider: The Next QCD Frontier. *Eur. Phys. J.*, A52(9):268, 2016.

[93] J. L. Abelleira Fernandez et al. A Large Hadron Electron Collider at CERN: Report on the Physics and Design Concepts for Machine and Detector. *J. Phys.*, G39:075001, 2012.

[94] Kari J. Eskola, Petja Paakkinen, Hannu Paukkunen, and Carlos A. Salgado. EPPS16: Nuclear parton distributions with LHC data. *Eur. Phys. J.*, C77(3):163, 2017.

[95] H. De Vries, C. W. De Jager, and C. De Vries. Nuclear charge and magnetization density distribution parameters from elastic electron scattering. *Atom. Data Nucl. Data Tabl.*, 36:495–536, 1987.

[96] N. Armesto. A Simple model for nuclear structure functions at small x in the dipole picture. *Eur. Phys. J. C*, 26:35–43, 2002.

[97] M. R. Adams et al. Shadowing in inelastic scattering of muons on carbon, calcium and lead at low x(Bj). *Z. Phys.*, C67:403–410, 1995.

[98] Jan Cepila and Marek Matas. Contribution of the non-linear term in the Balitsky-Kovchegov equation to the nuclear structure functions. *arXiv:2006.16130*, 6 2020.

[99] D. Bendova, J. Cepila, J.G. Contreras, and M. Matas. Photonuclear J/ψ production at the LHC: proton-based versus nuclear dipole scattering amplitudes. *arXiv:2006.12980*, 6 2020.

[100] Néstor Armesto and Amir H. Rezaeian. Exclusive vector meson production at high energies and gluon saturation. *Phys. Rev. D*, 90(5):054003, 2014.

[101] Tobias Toll and Thomas Ullrich. Exclusive diffractive processes in electron-ion collisions. *Phys. Rev. C*, 87(2):024913, 2013.

[102] Betty Abelev et al. Coherent J/ψ photoproduction in ultra-peripheral Pb-Pb collisions at $\sqrt{s_{NN}} = 2.76$ TeV. *Phys. Lett. B*, 718:1273–1283, 2013.

[103] E. Abbas et al. Charmonium and e^+e^- pair photoproduction at mid-rapidity in ultra-peripheral Pb-Pb collisions at $\sqrt{s_{\mathrm{NN}}}$=2.76 TeV. *Eur. Phys. J. C*, 73(11):2617, 2013.

[104] Shreyasi Acharya et al. Coherent J/ψ photoproduction at forward rapidity in ultra-peripheral Pb-Pb collisions at $\sqrt{s_{\mathrm{NN}}} = 5.02$ TeV. *Phys. Lett. B*, 798:134926, 2019.

[105] Vardan Khachatryan et al. Coherent J/ψ photoproduction in ultra-peripheral PbPb collisions at $\sqrt{s_{NN}} = 2.76$ TeV with the CMS experiment. *Phys. Lett. B*, 772:489–511, 2017.

[106] J.G. Contreras. Gluon shadowing at small x from coherent J/ψ photoproduction data at energies available at the CERN Large Hadron Collider. *Phys. Rev. C*, 96(1):015203, 2017.

[107] Ermes Braidot. Suppression of Forward Pion Correlations in d+Au Interactions at STAR. In *Proceedings, 45th Rencontres de Moriond on QCD and High Energy Interactions: La Thuile, Italy, March 13-20, 2010*, pages 355–338, 2010.

[108] A. Adare et al. Suppression of back-to-back hadron pairs at forward rapidity in d+Au Collisions at $\sqrt{s_{NN}} = 200$ GeV. *Phys. Rev. Lett.*, 107:172301, 2011.

[109] Javier L. Albacete and Cyrille Marquet. Azimuthal correlations of forward di-hadrons in d+Au collisions at RHIC in the Color Glass Condensate. *Phys. Rev. Lett.*, 105:162301, 2010.

[110] Anna Stasto, Bo-Wen Xiao, and Feng Yuan. Back-to-Back Correlations of Di-hadrons in dAu Collisions at RHIC. *Phys. Lett.*, B716:430–434, 2012.

[111] T. Lappi and H. Mantysaari. Forward dihadron correlations in deuteron-gold collisions with the Gaussian approximation of JIMWLK. *Nucl. Phys.*, A908:51–72, 2013.

[112] Yuri V. Kovchegov. Brief Review of Saturation Physics. *Acta Phys. Polon.*, B45(12):2241–2256, 2014.

[113] Fabio Dominguez, Cyrille Marquet, Bo-Wen Xiao, and Feng Yuan. Universality of Unintegrated Gluon Distributions at small x. *Phys. Rev.*, D83:105005, 2011.

[114] Javier L. Albacete and Cyrille Marquet. Single and double inclusive particle production in d+Au collisions at RHIC, leading twist and beyond. *Nucl. Phys.*, A854:154–167, 2011.

[115] Javier L. Albacete, Giuliano Giacalone, Cyrille Marquet, and Marek Matas. Forward dihadron back-to-back correlations in pA collisions. *Phys. Rev.*, D99(1):014002, 2019.